



**MATERIAL  
AND MECHANICAL  
ENGINEERING  
TECHNOLOGY**

**Editorial board of the journal**

Gulnara Zhetessova (Abylkas Saginov Karaganda Technical University, Kazakhstan)  
Alexander Korsunsky (University of Oxford, England)  
Olegas Cernasejus (Vilnius Gediminas Technical University, Lithuania)  
Jaroslav Jerz (Institute of Materials & Machine Mechanics SAS, Slovakia)  
Boris Moyzes (Tomsk Polytechnic University, Russia)  
Nikolai Belov (National Research Technological University «Moscow Institute of Steel and Alloys», Russia)  
Georgi Popov (Technical University of Sofia, Bulgaria)  
Sergiy Antonyuk (University of Kaiserslautern, Germany)  
Zharkynay Christian (University of Texas at Dallas Institute of Nanotechnology, USA)  
Katica Simunovic (University of Slavonski Brod, Croatia)  
Lesley D.Frame (School of Engineering University of Connecticut, USA)  
Łukasz Gierz (Poznan University of Technology, Poland)  
Łukasz Warguła (Poznan University of Technology, Poland)  
Olga Zharkevich (Abylkas Saginov Karaganda Technical University, Kazakhstan)

Content

<b>Yurov V.M., Portnov V.S., Zhangozhin K.N., Rakhimova G.M., Rakhimova Zh.B.</b> About the Friction Mechanism in Graphite and Diamond.....	3
<b>Gierz Ł., Perz K., Wieczorek B., Peixoto Matos C., Wargula Ł.</b> Kinematic Viscosity of Engine, Gear, Hydraulic and Special Purpose Oils at Temperatures of 25°C and 50°C.....	11
<b>Buzauova T.M., Sarbaev D.A., Smailova B.K., Toleubayeva Sh. B.</b> Analysis of the Stress-Strain State of the Surfaced Tooth in the T-FLEX CAD Application Program.....	17
<b>Issabek Z.R., Kadyrov Zh. N., Kassenov A. Zh., Mussina Zh. K., Tussupova S.O.</b> A Device for Measuring the Wear of Replaceable Rotary Tool Inserts of Milling Drums of Road Milling Machines.....	24
<b>Zhetessova G.S., Zharkevich O.M., Shakhatova A.T., Khrustaleva I.N., Shkodyrev V.P.</b> Additive Optimization Method for Choosing CNC Machines for Technological Preparation of Machine-Building Production.....	32
<b>Makarov G.V., Kolchurina I.Yu., Kolchurina M.A., Plotnikova I.V., Moyzes B.B.</b> Predictive Control Systems of Product Quality .....	38
<b>Sarsembekov B.K., Kadyrov A.S., Kunayev V.A., Issabayev M.S., Kukesheva A.B.</b> Experimental Comparison of Methods for Cleaning Car Exhaust Gas by Exposure Using Ultrasound and Laser Radiation.....	44
<b>Gulyarenko A., Bembenek M., Iskakov R., Shaimuratova E., Gulyarenko A.</b> Development of a Tractor Reliability Optimization Model: a Review of Research and Rationale for the Components.....	54
<b>Berdik M., Blaginina M., Beckles Z., Laipanov R.</b> Research of the Causes of Defects Type “Dent” on the Linear Part of the Main Pipelines.....	62
<b>Avdeychik S.V., Antonov A.S., Struk V.A., Prokopchuk N.R., Zhang R.</b> Nanostate Factor in Materials Science of Functional Nanocomposite Materials .....	69
<b>Ravitej Y.P.</b> Analysis of Wear Parameters of Chill Casted LM13/Zircon/Carbon Hybrid Composites Using Experimental and Statistical Approach.....	76
<b>Ganyukov A.A., Sinelnikov K.A., Kabikenov S.Zh., Karsakova A.Zh.</b> Research and Calculation of the Deformed State of the Roadway Mobile Overpass.....	88
<b>Kondhalkar Ganesh Eknath, G. Diwakar</b> Remaining Useful Life Prediction Method for Different Types of Rolling Bearings Based on Bi-Lstm Quantification.....	96
<b>Mustafin A., Sadykov N., Kabylkaiyr D., Shaimardan A., Sadykova A.</b> Comparative Analysis of Fits of Parts with Guaranteed Interference on Shafts of Annular and Solid Sections.....	112

## About the Friction Mechanism in Graphite and Diamond

Yurov V.M.<sup>1</sup>, Portnov V.S.<sup>2</sup>, Zhangozhin K.N.<sup>1</sup>, Rakhimova G.M.<sup>2\*</sup>, Rakhimova Zh.B.<sup>2</sup>

<sup>1</sup>LLP "TSC-Vostok", Karaganda, Astana, Kazakhstan

<sup>2</sup>Abylkas Saginov Karaganda Technical University, Karaganda, Kazakhstan

\*corresponding author

**Abstract.** A model of graphite friction is proposed. In this model, the friction process is described as a process of elastoplastic deformation of the surface layer. Moreover, the nanolayer, which contains 3–5 atomic monolayers, behaves elastically and quickly collapses according to the Griffiths scheme, forming a layer like a solid lubricant. Next, the mesolayer enters into the friction process. If the friction of graphite is considered similar to the friction of a viscous liquid, then from this approach it follows that friction depends on the speed of movement, has a structure similar to Benard cells, which means self-organization and friction synergism occurs. The fact that the friction of graphite cannot be explained using the usual Amonton law or on the basis of the hydrodynamic theory of lubrication is due to the fact that it is associated with the viscosity of the solution, the theory of which has not yet been completed.

Due to the reconstruction of its surface, the surface layer of metastable diamond becomes graphite and its friction coefficient is the same value  $k \approx 0.1$ . If you remove the surface layer of metastable diamond, i.e. turning it into a diamond, then its friction coefficient will be  $k \approx 0.6$ .

**Keywords:** graphite, diamond, friction, surface, self-organization, synergetics, speed, lubrication, elasticity.

### Introduction

The performance of parts of various moving mechanisms and machines is mainly affected by friction. Currently, there are five theories that explain the processes occurring during friction: mechanical (deformation); molecular (adhesive); molecular mechanical; energy; hydrodynamic [1]. The study of the friction process is over 500 years old [2] and continues to this day, due to the emergence of extreme conditions: high processing speeds of various metal products, high pressures, high temperatures, aggressive environments, etc. [3]. In the theory of friction, it is necessary to take into account both the mesoscopic approach [4] and the nanostructural approach [5]. In [6], a mechanical friction quantum was proposed. During friction, especially under lubrication conditions, as well as in dry friction, it is necessary to take into account the self-organization and synergy of the rubbing materials [7, 8].

In this article, we will review and propose the friction mechanism of two allotropic modifications of carbon - graphite and diamond.

A graphite crystal is a layered structure consisting of graphene layers. Each layer consists of regular hexagons of carbon atoms (C) measuring 0.335 nm, between which there are strong covalent bonds with an energy of 170 J/mol. Between the layers there is a space of 0.7-1.6 nm in size, where weak Van der Waals forces act with an energy of 16.7 J/mol (Fig. 1a). These graphene layers easily slide in the longitudinal direction and represent a solid lubricant (Fig. 1b).

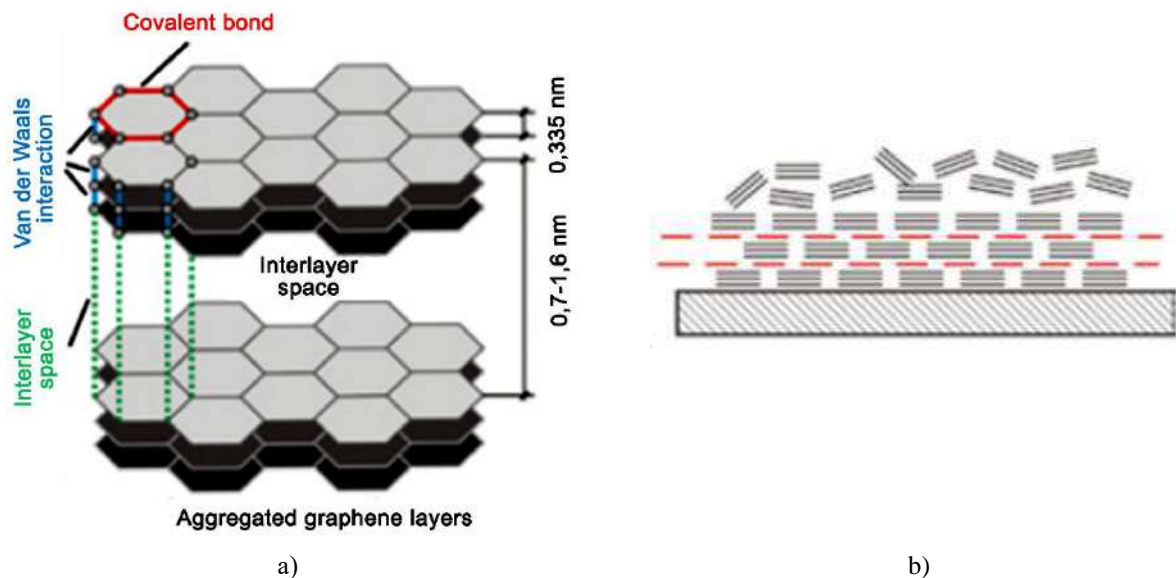


Fig. 1. Structure of graphite (a) and layer diagram on the metal (b) [9]

In work [10], graphites of various grades according to GOST [11] were used for solid lubrication. It has been shown that colloidal graphite containing dispersed particles provides the best antifriction properties of metal composite materials. Antifriction graphite and its application in industry have long been used [12]. In Kazakhstan, a monograph is devoted to carbon materials [13].

The coefficient of friction of diamond on metal materials is 0.1, which leads to high abrasion resistance of diamond, which is 90 times greater than the wear resistance of corundum, and 100 and 1000 times greater than that of various abrasive materials. Diamond powders are indispensable for processing parts made of hard alloys [14, 15]. A large amount of information on diamond is available in [16].

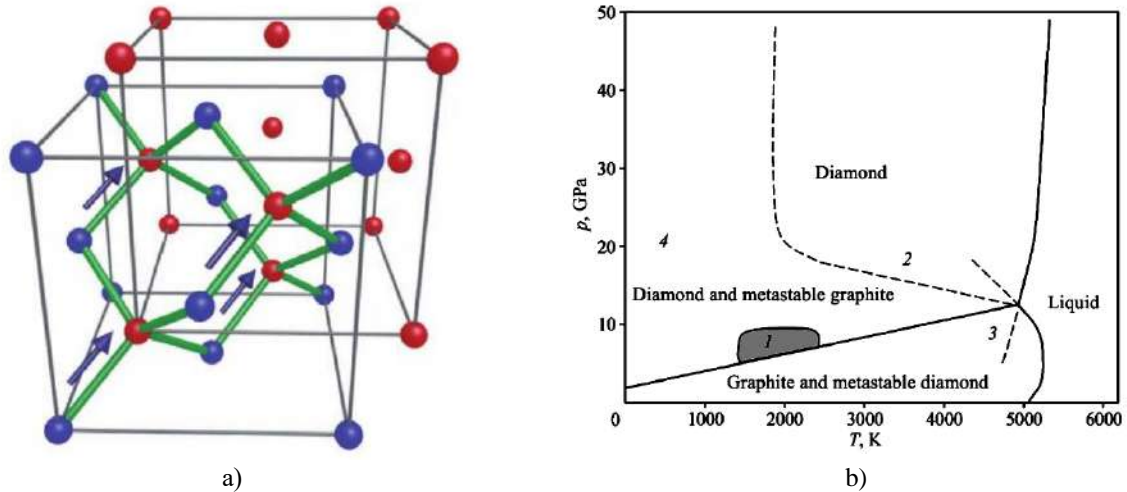


Fig. 2. Diamond lattice (a) [16]; Bundy carbon phase diagram [17]

The structure of diamond consists entirely of carbon (Fig. 2a) and belongs to the  $Fd\bar{3}m$  symmetry. Lattice parameter  $a = 0.35667$  nm, density  $\rho = 3.52$  (g/cm<sup>3</sup>), molar mass  $M = 12.01$  (g/mol) [16]. The Bundy phase diagram of carbon is shown in Fig. 2b [17]. In the periodic table of Mendeleev D.I. shows the position of carbon in the central column and top row (Fig. 3a). In the central column, carbon has the most covalent bonds per atom (4). The top position makes its atoms the smallest among all the elements in the central column. The combination of these two attributes gives diamond the highest concentration of binding energy and thereby gives it unmatched hardness and other beneficial properties [18].

In Fig. 3b shows the dependence of the friction coefficient on hardness. As you can see, diamond has a friction coefficient of about 0.1, just like graphite. As a result, diamond powder (DLC) can protect engine parts from further mechanical wear or chemical erosion. In addition, the opposing moving parts now slide on a solid surface that has a coefficient of friction much lower than that of any metal component (Fig. 3b). The movement of the engine part will receive much less resistance and less energy (such as gasoline) needed to power the engine.

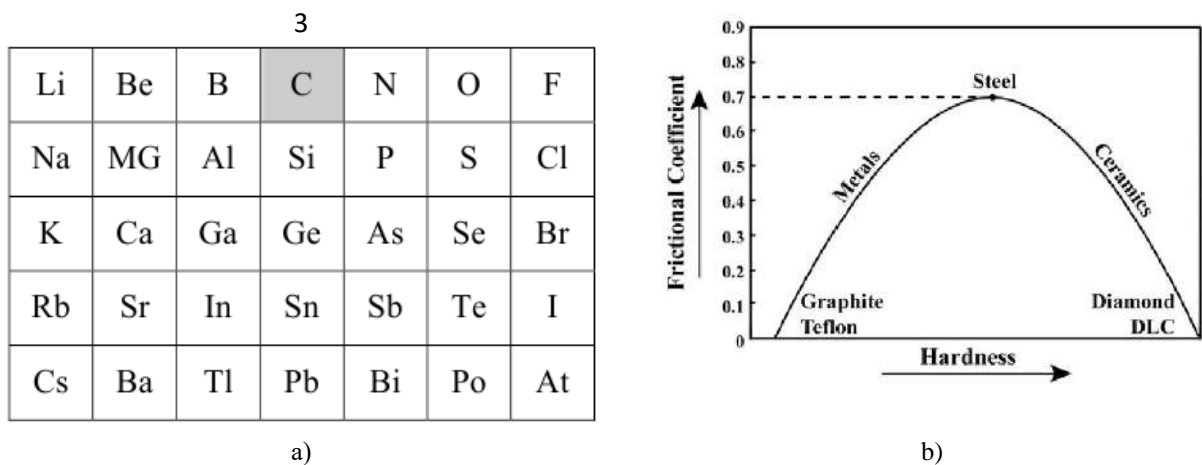
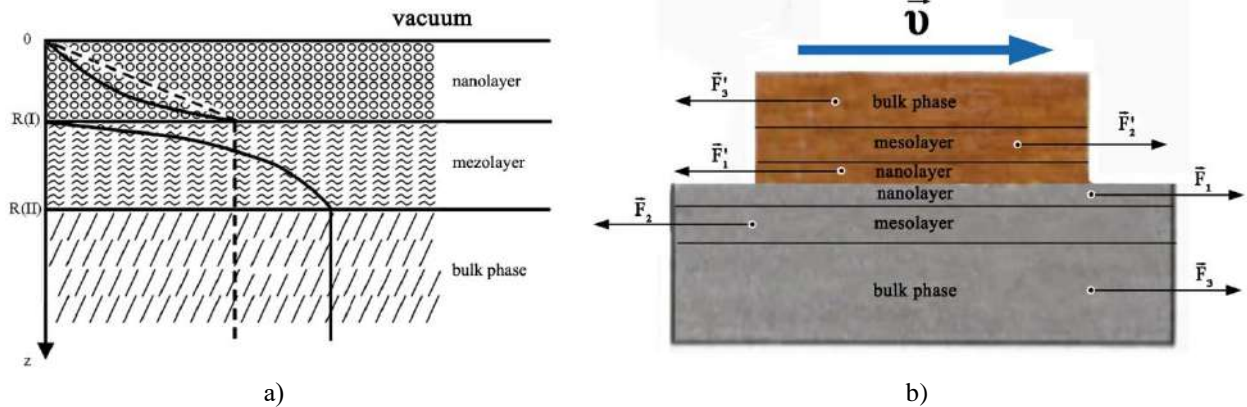


Fig. 3. Periodic table of D.I., showing solid materials with atomic bonds. This table does not include hydrogen and noble gases (a); friction coefficient as a function of hardness (b) [18]

Diamonds and diamond powder are widely used in industry [19], electronics and optics [20]. From Fig. 2b it follows that under ordinary conditions diamond is a metastable structure [17]. It becomes stable at high pressure and high temperature [21, 22] or at sizes less than 30 μm, when it becomes a nanodiamond [23, 24].

**1. Research methodology**

It has now become generally known that friction is significantly related to the surface layer of a solid [1-3]. Determining the thickness of this layer R(I) experimentally is a very difficult task, requiring ultra-high vacuum and complex equipment [25]. This problem has been solved only for a few substances. For example, for gold R(I) = 1.2 nm, and for silicon - R(I) = 3.2 nm [25], i.e. they are a nanostructure. Theoretically, we first determined the thickness of the surface layer of solids in [26-28] (Fig. 4a), and friction in [29] (Fig. 4b).



**Fig. 4.** Scheme of a solid: nanolayer → mezolayer → bulk phase [28] (a); diagram of the movement of atomically smooth diamond and graphite on atomically smooth metal surfaces with a constant speed  $u$  [29].

The thickness of the surface layer R(I) is given by the formula [26-28]:

$$R(I) = 0,17 \cdot 10^{-9} \cdot \alpha \cdot v \text{ [m]}. \tag{1}$$

In equation (1), you need to know one parameter - the molar volume of the element, which is equal to  $v = M/\rho$  ( $M$  is the molar mass,  $\rho$  is its density),  $\alpha = 1 \text{ m}^{-2}$  - a constant, so that the dimension (R(I) [m]). Using formula (1), we calculate R(I) (Table 1) for graphite parallel to the plane  $x = a = b$  and perpendicular to this plane  $x = c$  [30].

**Table 1.** Parameters R(I) of graphite.

Graphite	Structure	M, g/mol	$\rho$ , g/cm <sup>3</sup>	R(I) <sub>a</sub> , nm	R(I) <sub>c</sub> , nm
C	C6/mmc-D <sup>4</sup> <sub>6h</sub>	12,0107	2,26	0.90 (3)	2.46 (3)
			1,75	1.17 (4)	3.19 (4)
			1,65	1.24 (5)	3.39 (5)

From the table It can be seen from Fig. 1 that the thickness of the R(I)<sub>a</sub> layer varies from 0.9 to 1.24 nm in the upper plane, and the thickness of the R(I)<sub>c</sub> layer varies from 2.46 to 3.39 nm perpendicular to this plane. This is due to changes in the density of graphite and its layered structure. Natural graphite has  $\rho = 2.26 \text{ g/cm}^3$ , and artificial graphite has  $\rho = (1.75-1.65) \text{ g/cm}^3$ . The number of monolayers in graphite is given in parentheses -  $n = R(I)_a \cdot a/a$ ,  $c$  ( $a$ ,  $c$  are lattice constants). In the R(I) layer, the number of monolayers varies from 3 to 5, depending on the porosity of the graphite. It is shown in [31] that the surface energy of a bulk metal  $\gamma_2$ , with an accuracy of 3%, is equal to:

$$\gamma_2 = 0,7 \cdot 10^{-3} \cdot T_m \text{ [J/m}^2\text{]}, \tag{2}$$

where  $T_m$  is the melting temperature of the metal (K).

In the R(I) layer, it is necessary to take into account the size effect and the surface energy of the R(I) layer becomes equal to  $\gamma_1$  [32]:

$$\gamma_1 = \gamma_2(1 - R(I)/R(I) + h) \approx 0,3\gamma_2, \tag{3}$$

Equation (3) shows that the surface energy of the R(I) layer is three times less than the surface energy of the main crystal. To separate the R(I) layer from the rest of the crystal, it is necessary to expend energy, which is called adhesion energy [32]:

$$W_a = \gamma_1 + \gamma_2 - \gamma_{12} \approx \gamma_1 + \gamma_2 = 1.3\gamma_2, \quad (4)$$

where  $\gamma_{12}$  is the surface energy at the phase interface, which is negligible due to a second-order phase transition. Internal voltages  $\sigma_{is}$  between phases  $\gamma_1$  and  $\gamma_2$  can be calculated using the formula [33]:

$$\sigma_{is} = \sqrt{W_a \cdot \dot{A} / R(I)}, \quad (5)$$

where E is Young's modulus of elasticity.

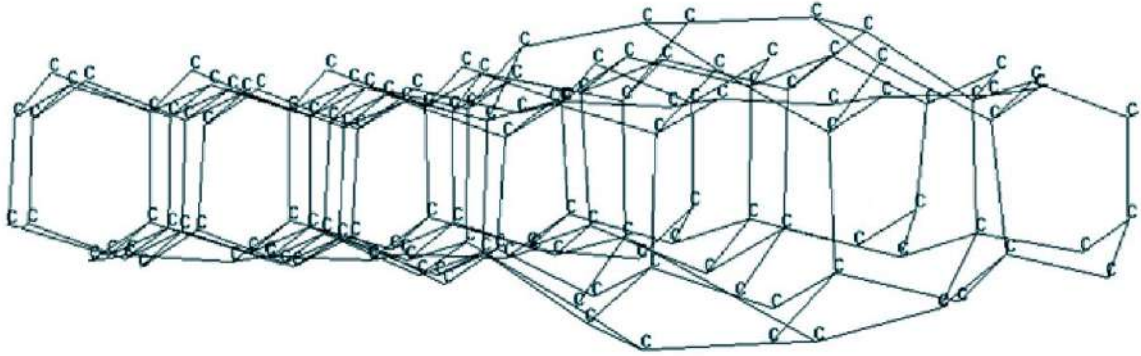
## 2. Results and discussion

Using equations (1) – (5), we calculate the elastic parameters for graphite.

**Table 2.** Elastic parameters of graphite

Graphite	$W_{aa}, J/m^2$	$W_{ac}, J/m^2$	$\sigma_{isa}, GPa$	$\sigma_{isc}, GPa$	$E_a, GPa$	$E_c, GPa$
C ( $\rho = 2,26$ )	3,613	1,323	5,74	1,37	7,59	3,48
C ( $\rho = 1,75$ )	2,801	1,026	3,75	0,93	5,88	2,70
C ( $\rho = 1,65$ )	2,637	0,966	3,44	0,87	5,55	2,55

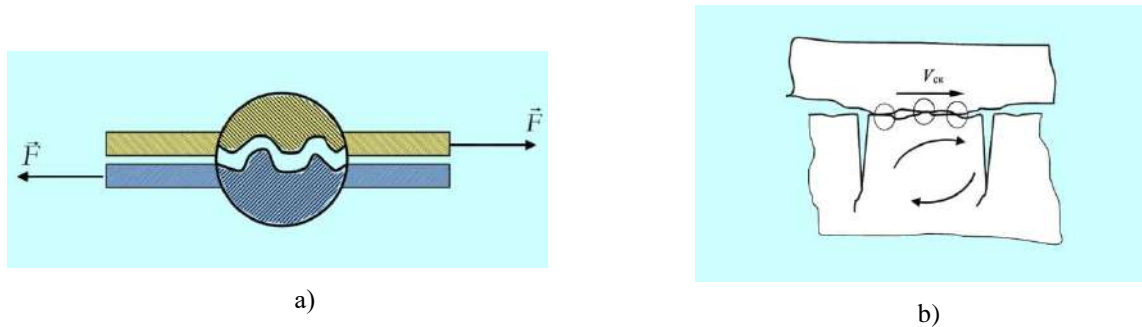
Graphite has an average value of  $T_m = 3970$  K and  $\gamma_2 = 2.779$  J/m<sup>2</sup>. Internal stresses in graphite  $\sigma_{isc}$  lead to an increase in the interplanar distance (Fig. 5), which can be easily separated from the rest of the crystal with simple tape, turning it into graphene [34]. If we look at Fig. 4b, it can be seen that the friction process itself can be described as a process of elastoplastic deformation of the surface layer. Moreover, the nanolayer, which contains 3–5 atomic monolayers, behaves elastically and quickly collapses according to the Griffiths scheme, forming a layer like a solid lubricant. Energy  $W_{ac}$  is spent on this. Next, the mesolayer (or mesoscopic layer) enters into the friction process. In mesoscopics, it has been experimentally proven that plastic flow begins in a brittle material when it loses shear stability, which is fundamentally different from the previous case.



**Fig. 5.** Increasing the interplanar distance of the surface layer.

The characteristic length for mesoscopics is the phase coherence length  $h\phi$ , which can vary within wide limits, but in mesoscopics it is always  $h\phi \leq 10^{-6}$  m = 1 micron.

As the upper graphite moves along the surface of the lower metal, a new surface of nanometer thickness is formed again. This means that friction performs an oscillatory motion (Fig. 6a). As soon as the speed exceeds a critical value and the formation of a nanolayer does not occur, friction begins to depend on speed. Layers R(I), R(II) and the bulk phase have different values of internal friction, which is proportional to the internal stresses  $\varepsilon_{isc}$  from the table. 2. When the graphite from above begins to move, a turbulent fragment appears due to friction (Fig. 6b).



**Fig. 6.** Oscillatory motion of friction during the formation of a new surface (a); diagram of the formation of a turbulent fragment (b)

This is manifested in the microstructure found on the surface of steel 20 [35] (Fig. 7a) and on our CrNiTiZrCu alloy [36] (Fig. 7b). There are many similarities between high-entropy alloys and metallic glasses [46]. A similar structure in Fig. 7 is typical for Bénard cells [37]. Bénard cells are the appearance of order in the form of convective cells in the form of cylindrical shafts or regular hexagonal figures in a layer of viscous liquid with a vertical temperature gradient. And the temperature gradient  $\text{grad}T \sim k$ , i.e. is proportional to the coefficient of internal and external friction, so friction is similar to a viscous fluid. So, the friction of graphite and layered materials on steel is similar to a viscous liquid, although there is another point of view [38]. In this paper, the distance dependence of non-contact friction on a graphite surface is studied using a quartz tuning fork with transverse vibration in the atmosphere. It is found that energy dissipation begins to increase when the distance is less than 2 nm, exhibiting a form of phonon dissipation. However, as the distance decreases further, the dissipation is different from the phonon dissipation and represents a huge friction energy dissipation peak, which is caused by the hysteretic behavior between the vibration of the surface atoms and the vibration of the tip. This work advances the understanding of the mechanism of energy dissipation in non-contact friction.

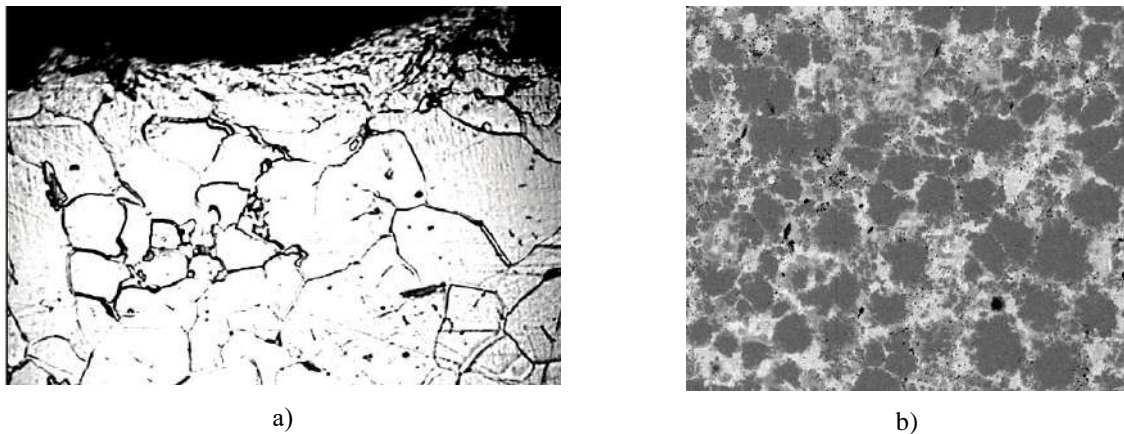


Fig. 7. Friction surface at the moment of a turbulent fragment of a sample made of steel 20 [35] (a) and CrNiTiZrCu alloy [36] (b).

If the friction of graphite is considered similar to the friction of a viscous liquid, then from this approach it follows that friction depends on the speed of movement, has a structure similar to Benard cells, which means self-organization and friction synergism occurs. The fact that the friction of graphite cannot be explained using the usual Amonton law or on the basis of the hydrodynamic theory of lubrication is due to the fact that it is associated with the viscosity of the solution (viscous liquid), the theory of which has not yet been completed [39].

Using equations (1) - (5), we calculate the parameters for diamond [40].

Table 3. Diamond structure parameters

Diamond	(hkl)	Structure	R(I), nm	R(II), nm	$\gamma$ , [41] J/m <sup>2</sup>	$\gamma$ , [42] J/m <sup>2</sup>
C	100	Fd3m	0,29 (1)	2,61 (7)	9,100	9,300
	110		0,41 (1)	3,69 (7)	6,274	6,570
	111		0,68 (1)	6,12 (7)	5,270	5,400

From the table 1 it follows that the number of carbon monolayers in the R(I) layer of diamond is equal to one, like in graphene. The total thickness of the surface layer  $H = R(I) + R(II)$  is equal to:  $H_{100} = 2.9$  nm;  $H_{110} = 4.1$  nm;  $H_{111} = 6.8$  nm. The surface energy  $\gamma$  is significantly greater than all materials known in nature, which means its friction coefficient  $k \sim \gamma L$  ( $L$  is the length of the path traveled) should also be large. However (Fig. 3b), today it is believed that the low friction of diamond is due to the fact that its surface adsorbs air atoms (nitrogen, oxygen) and the surface turns into a solid lubricant similar to graphite [16]. Here we will present a different point of view. The elastic parameters of the surface layer of diamond are shown in table. 4.

Table 4. Properties of the surface layer of diamond

Diamond	(hkl)	$H_{(hkl)}$ , nm	$W_a$ , J/m <sup>2</sup>	$\sigma_{(hkl)}$ , GPa
C	100	2,9	11,83	58
	110	4,1	8,16	41
	111	6,8	6,85	29

The internal stresses  $\sigma_{(hkl)}$  of metastable diamond are an order of magnitude greater than those of graphite and they are similar to the structure of silicon and germanium (Fig. 3a), in which covalent bonding is predominant. In



the bulk of C, Si, and Ge crystals, each atom forms four covalent bonds with its nearest neighbors located at the vertices of a regular tetrahedron. On the surface of the crystals, some of the bonds are broken, leading to its reconstruction [25]. For Si and Ge crystals, surface reconstruction and its models are presented in [43]. The Hanemann model consists of a chain of surface atoms that move up and down, but the bond length does not change compared to the bulk. In other words, the topology of the connections does not change, which has not been confirmed experimentally. Pandy's model, called the  $\pi$ -bonded atomic chain model. Here the communication topology changes completely: two six-bar rings of an idealized structure turn into five- and seven-bar rings. This model is recognized by many researchers, but it has not yet been confirmed experimentally.

In diamond, the bond between atoms is carried out by hybridized  $sp^3$  orbitals. If we assume that diamond has two bonding electrons for each orbital in the crystalline volume, they are divided in half on the surface. This hybridization is associated with the excitation of electrons to an energetically higher state (Fig. 8). A structure consisting of three  $sp^2$  orbitals and one p orbital may be more advantageous. This leads to a different distribution of electron density in space. In addition,  $sp^2$  orbitals are localized almost exactly in the same plane. It follows that the surface layer of diamond turns into graphite during reconstruction. To prove this conclusion, consider the experimental results shown in Fig. 9. Here in Fig. 9a shows the photoluminescence of diamond, which clearly shows the difference between the glow of the surface layer and the bulk of the diamond.

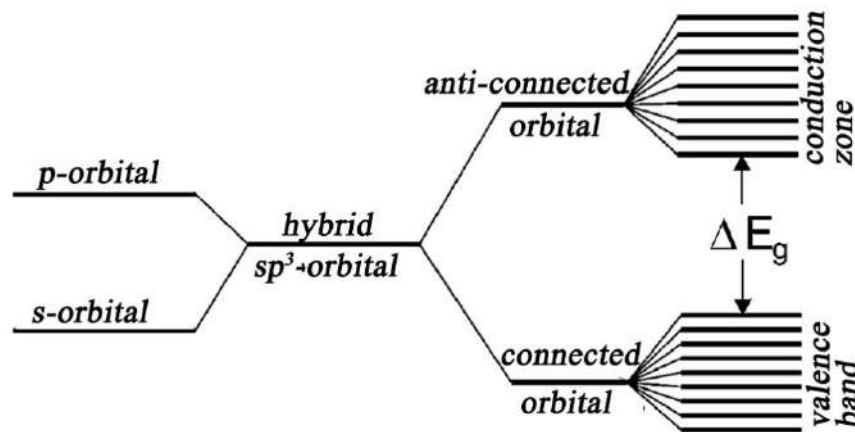


Fig. 8. Change in the energy of electronic states during hybridization of  $s$ - and  $p$ -orbitals [43]

Experimental Raman spectra of the surface layer of diamond are shown in Fig. 9b. In Fig. 9b D-peak (associated with carbons at the boundary of graphite crystallites) appears near  $1350\text{ cm}^{-1}$ . The G-peak (associated with in-plane vibrations of graphite) is located near  $1570\text{ cm}^{-1}$ . Both peaks are located against a luminescent background (Fig. 9b).

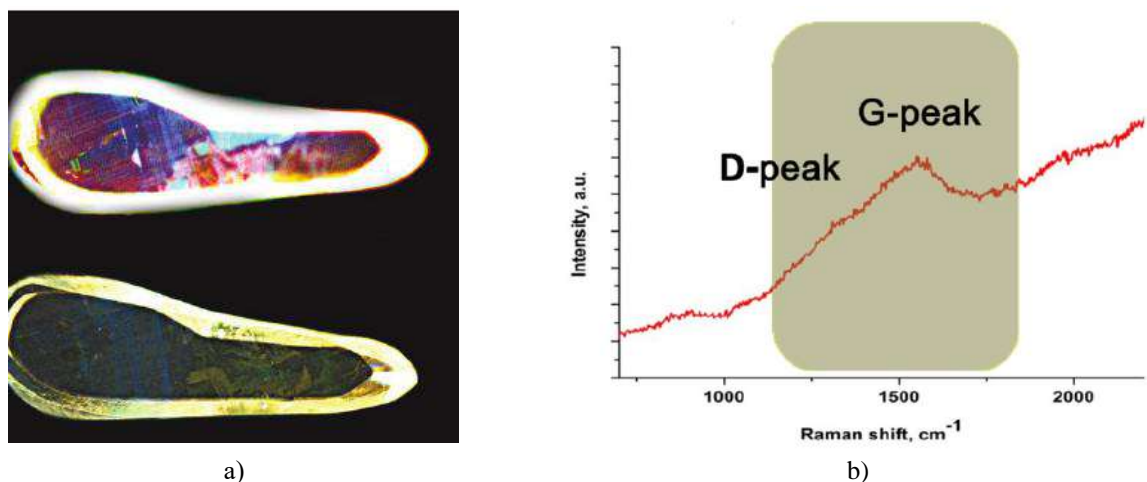


Fig. 9. Photoluminescence of diamond samples [44], Raman spectra of the upper layer of diamonds [45]

Thus, the surface layer of metastable diamond, due to the reconstruction of its surface, becomes graphite and its friction coefficient is the same value (Fig. 3b). If you remove the surface layer of metastable diamond, i.e. turning it into a diamond, its friction coefficient will be  $k \approx 0.6$  [16]. This means that our assumption about the formation of a surface layer of diamond can be considered proven.

## Conclusions

Here we considered only two allotropic modifications of carbon - graphite ( $sp^2$ ) and diamond ( $sp^3$ ). There are other modifications of carbon: carbyne ( $sp$ ); a series of fullerenes ( $sp^{2+x}$  or  $sp^{3-x}$ ). The thickness of the surface layer of fullerene  $C_{96}$  is  $R(I) = 135$  nm, which is three! order of magnitude higher than  $R(I)$  for diamond and graphite. Since friction, as shown above, is mainly determined by the surface layer, then for these modifications of carbon, determining the friction mechanism is a task for the near future.

## References

- [1] Frolov K.V. Modern tribology: Results and prospects. - M.: LKI Publishing House, 2008. - 480 p.
- [2] Zhuravlev V.F. 500 years of history of the law of dry friction // Bulletin of MSTU im. N.E. Bauman. Ser. "Natural Sciences", 2014, No. 2. - P. 21-31.
- [3] Shalygin M.G. Wear of sub-roughness of friction surfaces in a hydrogen-containing environment. - Dissertation of Doctor of Technical Sciences, Bryansk, 2017. - 235 p.
- [4] Anthony K.-H. Thermodynamics of the friction process and Lagrangian formalism: contribution to the mesoscopic approach to the theory of plasticity // Physical mesomechanics, 2001, Vol. 4, No. 4. - P. 33-46.
- [5] Yurov V.M., Guchenko S.A. Friction of high-entropy alloys and the thickness of their surface layer // Science of the XXI century, 2019, No. 8. - P. 14-16.
- [6] Fedorov S.V. Assessment of the energy potential of mechanical (nano) friction quantum // Bulletin of science and education of the North-West of Russia, 2016, Vol. 2, No. 1. - P. 1-14.
- [7] Baranov A.V., Vagner V.A., Tarasevich S.V. and others. Self-organization of tribosystems under boundary friction of metals // Polzunovsky Bulletin, 2009, No. 2. - P. 155-158.
- [8] Pavelko G.F. Synergism and antagonism of anti-wear additives as a method of confirming the mechanism of their action // Friction and Wear, 2023, V. 44, No. 1. - P. 85-92.
- [9] Grigoriev A.Ya., Myshkin N.K. Solid lubricants // Chemistry and Life, 2014, No. 1. - P. 34-42.
- [10] Bolsunovskaya T.A., Efimochkin I.Yu., Sevostyanov N.V., Burkovskaya N.P. The influence of graphite grade as a solid lubricant on the tribological properties of a metal composite material // Proceedings of VIAM, 2018, No. 7 (67). - P. 69-77.
- [11] GOST 17022-81. Graphite. Types, brands and general technical requirements. - M.: Standartinform, 2010. - 8 p.
- [12] Belogorsky V.D. Antifriction graphite and its use in industry. - M.: Knowledge, 1974. - 154 p.
- [13] Kazankapova M.K., Ermagambet B.T., Kasenov B.K., Nauryzbaeva A.T., Kasenova Zh.M., Kemelova B.A. Porous carbon materials based on carbon-mineral raw materials from Kazakhstan. Monograph. - Nur-Sultan: Institute of Coal Chemistry and Technology LLP, 2020. - 323 p.
- [14] Kozhevnikov D.V., Grechishnikov V.A., Kirsanov S.V., Kokarev V.I., Skhirtladze A.G. Cutting tool. - M.: Mechanical Engineering, 2004. - 512 p.
- [15] Vinokurov G.G., Sharin P.P., Popov O.N., Vinokurova S.G. Statistical description of the formation of microgeometry of the friction surface of a diamond drill // Friction and Wear, 2016, Vol. 37, No. 1. - P. 42-49.
- [16] Handbook of Industrial Diamonds and Diamond Films / under general editorship M Prelas, G Popovici, L K Bigelow. - New York: CRC Press, 1997. - 1232 p.
- [17] Bundy F.P., Bassett W.A., et al. The Pressure-Temperature Phase and Transformation Diagram for Carbon; Updated Through 1994 // Carbon, 1996, V. 34, No. 2. - P. 141-153.
- [18] Sung J.C. and Lin J. Diamond nanotechnology. Syntheses and Applications. - Singapore, 2010. - 252 p.
- [19] Gridin O.M., Teplova T.B., Gogotov A.A., Doronin M.A. Application of diamonds in industry and methods of their processing // Mining Information and Analytical Bulletin, 2013, No. 9 - P. 275-282.
- [20] Khmelnskiy R.A., Talipov N.Kh., Chucheva G.V. Synthetic diamond for electronics and optics. - M.: IKAR Publishing House, 2017. - 228 p.
- [21] [Stupnikov V.A., Bulychev B.M. High pressures in chemistry. diamond and diamond-like materials, technical and synthetic aspects. - M.: Moscow State University Publishing House, 2012. - 112 p.
- [22] Kaminsky F.V., Voropaev S.A. Modern ideas about the genesis of diamond // Geochemistry, 2021, vol. 66, No. 11. - P. 993-1007.
- [23] Kulakova I.I., Lisichkin G.V., Yakovlev R.Yu. Chemical modification of the surface of detonation nanodiamond. - M.: Moscow State University Publishing House, 2018. - 92 p.
- [24] Kumar S, Nehra M, Kedia D, Dilbaghi N, Tankeshwar K, Kim K-H. Nanodiamonds: Emerging face of future nanotechnology // Carbon, 2019, Vol. 143. - P. 678-699.
- [25] Oura K., Lifshits V.G., Saranin A.A., Zotov A.V., Katayama M. Introduction to surface physics. - M.: Science. 2006. - 490 p.
- [26] Yurov V.M. Thickness of the surface layer of atomically smooth crystals // Physico-chemical aspects of studying clusters, nanostructures and nanomaterials. 2019. issue. 11. - P. 389-397.
- [27] Yurov V.M., Goncharenko V.I., Oleshko V.S. Anisotropy of the surface layer of d-elements // Modern science-intensive technologies, 2021, No. 2. - P. 88-93.
- [28] Yurov V., Zhangozin K. About the mechanism of mica splitting // Sciences of Europe, 2024, No. 133. - P. 97-104.

- [29] Yurov V.M., Berdibekov A.T., Belgibekov N.A., Makhanov K.M. Friction of high-entropy coatings // Bulletin of KarU, 2021, No. 3. - P. 101-114.
- [30] Yurov V., Zhangozin K. Surface layer thickness, defects and strength of graphite // The scientific heritage, 2023, No 128. – P. 20-27.
- [31] Rekhviashvili S.Sh., Kishtikova E.V., Karmokova R.Yu. Towards the calculation of the Tolman constant // Letters to ZhTP, 2007, T. 33, Issue. 2. - P. 1–7.
- [32] Yurov V.M., Goncharenko V.I., Oleshko V.S. Study of primary nanocracks in atomically smooth metals // Letters to ZhTP, 2023, vol. 49, issue. 8. - P. 35-38.
- [33] Zimon A.D. Adhesion of films and coatings. - M.: Chemistry, 1977. – 352 p.
- [34] Novoselov K.S. Graphene: materials of Flatland // Uspekhi Fizicheskikh Nauk, 2011, T. 181, No. 12. - P. 1299-1311.
- [35] Kim V.A., Karimov Sh.A. Manifestation of physical mesomechanics during contact interaction, friction and wear // Scientific notes of KnAGTU, 2014, No. 11-1(18). – P. 5-9.
- [36] Yurov V.M., Guchenko S.A., Makhanov K.M. High-entropy CrNiTiZrCu coatings and their properties // Trends in the development of science and education, 2021, No. 75, Part 1. – P. 107-114.
- [37] Gershuni G.Z., Zhukhovnitsky E.M. Convective stability of an incompressible fluid. - M.: Nauka, 1972. - 232 p.
- [38] Wang Ch., Liu H., Wang J., Han Y., Sun Z., Xu H., Liu H., Liu D. and Luo J. Non-contact friction energy dissipation via hysteretic behavior on a graphite surface // Nanoscale Adv., 2022, Vol. 4. – P. 4782-4788.
- [39] Yurov V., Zhangozin K. Some questions of the theory of solution viscosity // German International Journal of Modern Science, 2023, No.71. – P. 34-41.
- [40] Yurov V.M., Zhangozin K.N., Goncharenko V.I., Oleshko V.S. The thickness of the surface layer of diamonds // Endless Light in Science, 2024, No. 1. – P. 218-224.
- [41] Harkins W. D. Energy Relations of surface of Solids // Journal Chem. Phys., 1942, V. 10. - P. 268-272.
- [42] Nozhkina A.V., Kostikov V.I. Surface energy of diamond and graphite // Rock cutting and metalworking tools - equipment and technology for its manufacture and application: Sat. scientific tr. - Kyiv: INM im. V.M. Bakulya NAS of Ukraine, 2017, No. 20. - P. 161-167.
- [43] Vladimirov G.G. Physics of the surface of solids. - St. Petersburg: Lan Publishing House, 2022. - 352 p.
- [44] Klepikov I.V., Vasiliev E.A. Features of luminescence of the surface of diamond crystals // Ural Mineralogical School, 2022. – P. 78-80.
- [45] Shashkov S.N. Raman microscopy of graphenes and other carbon structures // [www.solinstruments.com](http://www.solinstruments.com)
- [46] Yurov V.M., Goncharenko V.I., Portnov V.S., Sha Mingun, Oleshko V.S., Rakhimova Zh.B., Rakhimov M.A., Rakhimova G.M., Maussymbayeva A.D. Anisotropy of the Surface Energy of Steel and Nickel Alloys in Aviation //Material and Mechanical Engineering Technology, №1, 2023 – C. 10-23

#### Information of the authors

**Yurov Viktor Mikhailovich**, c.ph.m.s, leading construction manager of LLP “ TSC-Vostok”

e-mail: [exciton@list.ru](mailto:exciton@list.ru)

**Portnov Vassily Sergeevich**, d.t.s., Abylkas Saginov Karaganda Technical University

e-mail: [vs\\_portnov@mail.ru](mailto:vs_portnov@mail.ru)

**Zhangozhin Kanat Nakoshevich**, c.ph.m.s, associate professor, director of LLP “TSC-Vostok”

e-mail: [4kzh@mail.ru](mailto:4kzh@mail.ru)

**Rakhimova Galiya Mukhamedievna**, c.t.s., associate professor, Abylkas Saginov Karaganda Technical University

e-mail: [g.rakhimova@kstu.kz](mailto:g.rakhimova@kstu.kz)

**Rakhimova Zhanara**, master of technical sciences, Abylkas Saginov Karaganda Technical University

e-mail: [zhanara.rahimova.87@mail.ru](mailto:zhanara.rahimova.87@mail.ru)

## Kinematic Viscosity of Engine, Gear, Hydraulic and Special Purpose Oils at Temperatures of 25°C and 50°C

Gierz L.<sup>1\*</sup>, Perz K.<sup>2</sup>, Wieczorek B.<sup>1</sup>, Peixoto Matos C.<sup>3</sup>, Wargula L.<sup>1</sup>

Institute of Machine Design, Faculty of Mechanical Engineering, Poznan University of Technology, Poznań, Poland

<sup>2</sup>Institute of Machines and Motor Vehicles (IMRiPS), Poznan University of Technology, Poznań, Poland

<sup>3</sup>Department of Mathematics, Politécnico de Viseu, Portugal

\*corresponding author

**Abstract.** Oils are used in various lubrication systems, such as internal combustion engines, transmissions, hydraulic systems, and specialized industrial applications. The aim of this study is to show how the kinematic viscosity of oils for various applications changes with temperature. Sixteen different commercially available oils were evaluated, from the group of engine oils, transmission oils, hydraulic oils, shock absorbers, chain saw lubrication oils, air conditioning oils, hybrid vehicle internal combustion engines, and two-stroke engine fuel mixtures. Kinematic viscosity was measured for two temperatures, that is, 25 °C and 50 °C. For the purposes of the study, an Ostwald-Pinkiewicz capillary viscometer was used. According to the theory, the kinematic viscosity of all 16 oils tested decreased with increasing temperature. Knowledge of the viscosity behavior of oils in the group of engine oils, transmission oils, hydraulic oils, and specialized applications is of great importance, especially when considering the pumping resistance in gear pumps.

**Keywords:** chain saw lubrication oils, shock absorber oils, fuel mixture oils for two-stroke engines, SAE classification.

### Introduction

The kinematic viscosity of oil is one of the key parameters that determine its lubricating properties and efficiency in various applications [1]. Oils are used in various lubrication systems, such as combustion engines, gears, hydraulic systems, or specialized applications in industry [2]. Each of these applications requires appropriate oil properties, which depend on, among others, viscosity, operating temperature, and environmental conditions. In technology, the concept of kinematic viscosity, also called kinetic viscosity or absolute viscosity, is very often used. In the CGS system, the unit of kinematic viscosity is Stokes [St]. In practice, a 100 times smaller, called centistokes [cSt]. The unit of kinematic viscosity in the SI system is square meters per second [m<sup>2</sup>/s]. In practice, however, a unit 106 times smaller [mm<sup>2</sup>/s] is used, which is the equivalent of centistokes (cSt) [3]. In industrial practice, the kinematic viscosity of oils is usually measured using a capillary viscometer, most often in accordance with the national standards PN-77/C04166 or international standards such as ISO 3104. This process consists in measuring the time in which a given volume of liquid flows through a capillary under the influence of gravity, which allows for precise determination of the flow properties of the liquid at different temperatures. Kinematic viscosity has been assessed many times in the world literature, although these data are still not consistent or made at different temperatures. In one of the works, the viscosity of 6 engine oils used on motorcycles was assessed with changing temperature in the range of – 5 °C to +115 °C, which are important for the performance of combustion engines [4]. The next paper presents the results of the measurements of kinematic viscosity obtained using three different fast measuring devices and a standardized method using the Ubbelohde capillary viscometer, where the most accurate results were obtained for the Stabinger viscometer [5]. The intensive development that is happening in the fuel and oil sector, both at the legislative and technological level, encourages scientists to carry out more ambitious research [6]. One can also encounter an analysis of the nature of the action of additives in the form of POLYTRONMTC in terms of its adaptation to high-speed and high-load conditions in the aspect of ball wear on a moving disc [7]. The results of the influence of the dynamic viscosity of the lubricant material on the parameters of the adhesive bond during the re-abrasion of Steel 45 [8] cannot be omitted. To examine resistance to degradation, the oils were also subjected to the oxidation process and the most resistant groups of oils were indicated [9]. For hydraulic oils, the dynamic viscosity was determined at temperatures of 40 °C and 100 °C [10], but hydraulic oils generally operate at temperatures not exceeding 50 °C, which is why we selected the temperature of 25 °C during start-up and 50 °C during standard pump operation during measurements. The aim of this article is to examine the kinematic viscosity of 16 oils from the group of oils: engine, gear, hydraulic and oils for special applications at temperatures of 25 °C and 50 °C. Special purpose oils include shock absorber oils, chainsaw lubrication oils, air conditioning oils, hybrid vehicle combustion engine oils, and two-stroke engine fuel mixture oils. The properties of the oils at these two temperatures will allow us to assess how the lubrication properties change at the operating temperature of standard gear pumps.

## 1. Materials and Methods

Kinematic viscosity was measured using an Ostwald-Pinkiewicz capillary viscometer in accordance with the Polish standard PN-77/C04166 [11] and the international standard ISO 3104 [12], in particular procedure A, which describes how to perform the measurement using hand-held glass viscometers. Kinematic viscosity  $\nu$  is defined (1) as the ratio of the dynamic viscosity  $\eta$  of a liquid to its density  $\rho$  [12]:

$$\nu = \frac{\eta}{\rho} \quad (1)$$

The measurement of viscosity, using the flow of liquid through capillaries, is based on the Hagen-Poiseuille law [13] (2):

$$\eta = \frac{\pi r^4 \Delta p t}{8 l V} \quad (2)$$

where  $r$  – capillary radius in cm,

$l$  – capillary length in cm,

$t$  – flow time in s,

$\Delta p$  – pressure difference causing liquid flow in Pa,

$V$  – volume of liquid flowing in time  $t$  in cm<sup>3</sup>.

Taking into account the flow through the capillary only under the action of its own weight, and the formula for the capillary constant  $k$ , we obtain and, dividing by the density of the liquid, we finally obtain the kinematic viscosity formula (3) [14]:

$$\nu = k \cdot t \quad (3)$$

where  $\nu$  – kinematic viscosity

$k$  – capillary constant,

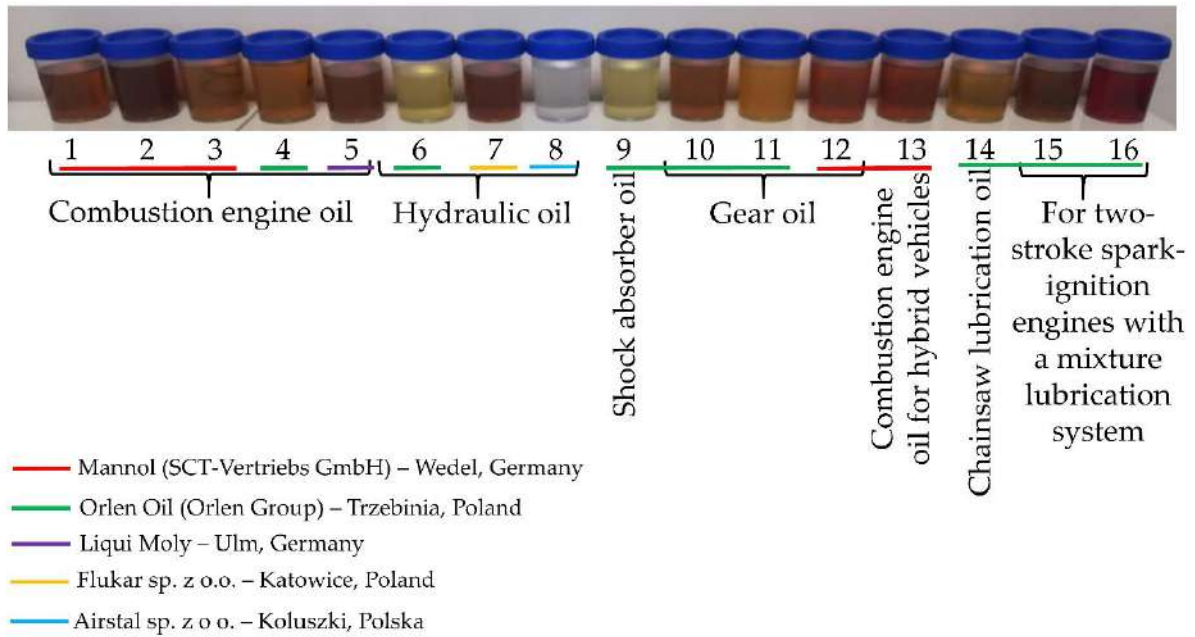
$t$  – flow time of a liquid of a given volume through the capillary.

The tests were carried out at two temperatures: 25 °C and 50 °C to assess the effect of temperature on the viscosity of the oils.

The test procedure was as follows:

1. The oils were heated successively to two temperatures, that is, 25 °C and 50 °C in a controlled chamber;
2. Kinematic viscosity  $\nu$  was measured by determining the flow time of the oil under the influence of gravity [15, 16] through the Ostwald-Pinkiewicz capillary, used many times during similar tests [17]. Then, using the capillary constant  $k$  and the measured time  $t$ , the kinematic viscosity  $\nu$  was calculated from the relationship(3);
3. Development of a database of kinematic viscosity results for the 16 different oils (3 repetitions were performed for each measurement test; then the mean and standard deviation were calculated, additionally indicating the confidence interval).

The principle of kinematic viscosity measurement using the Ostwald-Pinkiewicz capillary viscometer consists in measuring the liquid flow time of the tested from the measuring reservoir of the capillary with a volume precisely defined by measuring lines (upper and lower measuring line) [4]. Based on knowledge of the capillary constant  $k$  and the liquid flow time  $t$ , after substituting these values into formula (3), the liquid kinematic viscosity of the tested is calculated [14]. To present the tested samples, 16 oils were characterized in Figure 1.



**Fig. 1.** Samples of tested oils: 1 - 5W/20 (Energy Ultra JP), 2 - 0W/30 (Legend Extra), 3 - 15W/40 (Universal), 4 - 20W/50 (Lubro), 5 - 10W/60 (Synthoil Race Tech GT1), 6 - L-HL 32 (Hydrol), 7 - HL 46 (Revlina), 8 - PAO 68 (Hart), 9 - 15-WL 150 (Amortyzol), 10 - GL-4 80W/90 (Hipol), 11 - GL-5 85W/90 (Hipol 15F), 12 - GL-5 LS 85W/140 (Hypoid LSD), 13 - 0W/16 (Hybrid SP), 14 - VG 68 (Pilarol), 15 - 0W/12 (Mixol S), 16 - 0W/20 (2T Semisynthetic).

## 2. Results and discussion

According to the methodology indicated, the oil flow time  $t$  was determined and then the kinematic viscosity was calculated from the relationship (3). Table 1 presents the collected results of the kinematic viscosity  $\nu$  tests at a temperature of 25 °C, while Table 2 presents the collected results of the kinematic viscosity  $\nu$  tests at a temperature of 50 °C.

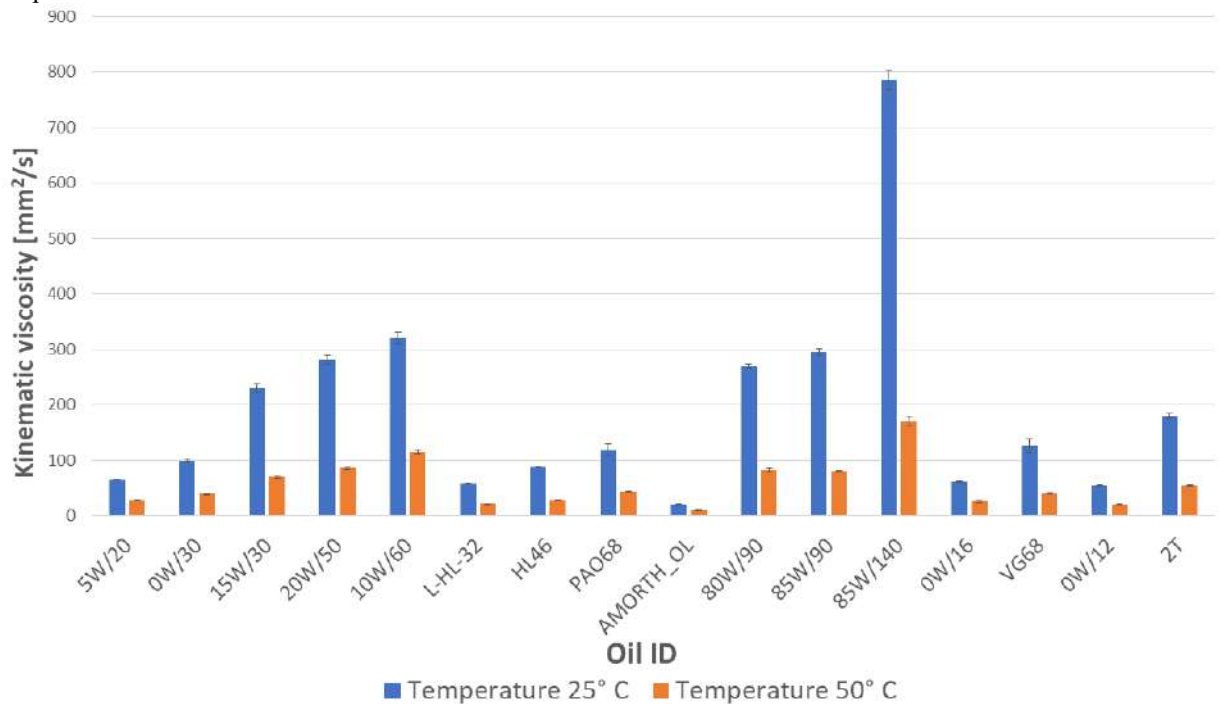
**Table 1.** Kinematic viscosity test results  $\nu$  at 25°C

Oil ID	Time $t$ [s]			Capillary constant $k$	Kinematic viscosity [mm <sup>2</sup> /s] $\nu = k \cdot t$				
	1	2	3		1	2	3	Mean	Standard deviation
5W/20	236	240	237	0,2736	64,57	65,66	64,84	65,03	0,47
0W/30	362	366	369	0,2718	98,39	99,48	100,29	99,39	0,78
15W/30	854	841	825	0,2736	233,65	230,10	225,72	229,82	3,24
20W/50	1016	1044	1036	0,2718	276,15	283,76	281,58	280,50	3,20
10W/60	1151	1192	1174	0,2736	314,91	326,13	321,21	320,75	4,59
L-HL-32	216	215	213	0,2736	59,10	58,82	58,28	58,73	0,34
HL46	324	320	325	0,2718	88,06	86,98	88,34	87,79	0,59
PAO68	456	422	423	0,2736	124,76	115,46	115,73	118,65	4,32
AMORTH_OL	80	80	81	0,2656	21,25	21,25	21,51	21,34	0,13
80W/90	985	992	980	0,2736	269,50	271,41	268,13	269,68	1,35
85W/90	1126	1105	1109	0,2656	299,07	293,49	294,55	295,70	2,42
85W/140	2879	2890	2833	0,2736	787,69	790,70	775,11	784,50	6,75
0W/16	228	230	232	0,2656	60,56	61,09	61,62	61,09	0,43
VG68	490	485	450	0,2656	130,14	128,82	119,52	126,16	4,73
0W/12	205	206	206	0,2656	54,45	54,71	54,71	54,63	0,13
2T	687	669	678	0,2656	182,47	177,69	180,08	180,08	1,95

**Table 2.** Kinematic viscosity test results  $\nu$  at 50 °C

Oil ID	Time $t$ [s]			Capillary constant $k$	Kinematic viscosity [mm <sup>2</sup> /s] $\nu = k \cdot t$				
	1	2	3		1	2	3	Mean	Standard deviation
5W/20	102	103	102	0,2736	27,91	28,18	27,91	28,00	0,13
0W/30	145	147	145	0,2718	39,41	39,95	39,41	39,59	0,26
15W/30	260	258	253	0,2736	71,14	70,59	69,22	70,32	0,81
20W/50	317	320	312	0,2718	86,16	86,98	84,80	85,98	0,90
10W/60	416	421	428	0,2736	113,82	115,19	117,10	115,37	1,35
L-HL-32	81	82	82	0,2718	22,02	22,29	22,29	22,20	0,13
HL46	105	104	104	0,2736	28,73	28,45	28,45	28,55	0,13
PAO68	162	160	161	0,2718	44,03	43,49	43,76	43,76	0,22
AMORTH_OL	40	40	39	0,2736	10,94	10,94	10,67	10,85	0,13
80W/90	297	304	306	0,2718	80,72	82,63	83,17	82,17	1,05
85W/90	298	296	297	0,2736	81,53	80,99	81,26	81,26	0,22
85W/140	620	622	646	0,2718	168,52	169,06	175,58	171,05	3,21
0W/16	96	92	92	0,2736	26,27	25,17	25,17	25,54	0,52
VG68	148	145	145	0,2718	40,23	39,41	39,41	39,68	0,38
0W/12	77	78	79	0,2736	21,07	21,34	21,61	21,34	0,22
2T	203	204	202	0,2718	55,18	55,45	54,90	55,18	0,22

In order to clearly present the measured values of the kinematic viscosity of oils, they are presented in Fig. 2, where a comparative graph for two temperatures (25 °C and 50 °C) is shown. Analysis of the test results shows that with increasing temperature, the kinematic viscosity  $\nu$  of all 16 tested oils decreased according to the theory. It should also be noted that the error bars for the temperature of 50 °C are more than twice smaller than for the temperature of 25 °C.



**Fig.2.** Dependence of kinematic viscosity of oil at two temperatures 25° C and 50° C

It should also be noted that the kinematic viscosity  $\nu$  of the 85W/90 oil for the indicated temperatures drops more intensively than for the 80W/90 oil. For a temperature of 25 °C, the difference in kinematic viscosities  $\nu$

between the indicated oils is 26 mm<sup>2</sup>/s, while for a temperature of 50 °C, this difference decreases to 2 mm<sup>2</sup>/s. On average, for all 16 oils tested, the kinematic viscosity  $\nu$  drops by about 65%. The smallest decrease in kinematic viscosity  $\nu$  was observed for the shock absorber oil (AMOTTH\_OIL), which was 49%, while the largest decrease was observed for the gear oil (85W/140), which was 78%. It has been proven that operating temperature and the quality of the hydraulic oil quality affect the volumetric efficiency of the gear pump [18], therefore the presented results are essential for the users of these devices. It should be emphasized that the kinematic viscosities  $\nu$  of the oils are determined at different temperatures. Usually according to the SAE classification [19] or according to the ISO classification [20, 21], which determines both cold and warm conditions. However, it is important to select temperatures that are as close as possible to the standard operation of the pump.

## Conclusions

This study focuses primarily on indicating the decrease in kinematic viscosity  $\nu$  of oils from the group of engine oils, transmission oils, hydraulic oils, shock absorbers, chain saw lubrication oils, air conditioning systems, hybrid vehicle combustion engines, and two-stroke engine fuel mixtures. Studies conducted at two temperatures will be helpful in making rational decisions regarding the selection of oil for pump operating conditions. The main conclusions of this study are as follows:

The kinematic viscosity  $\nu$  of the 16 oils tested for temperatures of 25 °C and 50 °C drops significantly according to the theory. Moving from lower to higher temperatures, the kinematic viscosity  $\nu$  of the oils tested dropped by an average of about 65%. The smallest decrease in kinematic viscosity  $\nu$  was noted for shock absorber oil (AMOTTH\_OIL) and the largest for 85W/140 transmission oil) was noted.

The kinematic viscosity  $\nu$  of the oil is crucial for its lubricating properties and affects the efficiency of the mechanical systems in which it is used. Choosing the right oil, adapted to the temperature conditions in which it will operate, has a direct impact on the durability of the equipment, energy consumption, and efficiency of their work.

Knowledge of the kinematic viscosity  $\nu$  behavior of oils from the group of engine, gear, hydraulic, and special-purpose oils is of great importance, especially when considering the pumping resistance in gear pumps, which we plan to study in the next stage of work.

In future studies, the analysis can also be extended to higher operating temperatures and other types of specialist oils to obtain a more complete picture of their behavior under variable thermal conditions.

## References

- [1] Tormos, B., Bermúdez, V., Ruiz, S., & Alvis-Sanchez, J. (2023). Degradation effects of base oils after thermal and electrical aging for EV thermal fluid applications. *Lubricants*, 11(6), 241.
- [2] [2] Stepień, Z. (2024). Powertrain and fuel diversification – challenges for engine oils. *Nafta - Gaz*, 80(1), pp. 45–54
- [3] Dynamic and kinematic viscosity of fluids <https://gorner.pl/aktualnosci/lepkosc-dynamiczna-a-kinematyczna-plynow/> -accessed 18/09/2024
- [4] Severa, L., Havlíček, M., & Kumbár, V. (2009). Temperature dependent kinematic viscosity of different types of engine oils. *Acta Universitatis Agriculturae et Silviculturae Mendelianae Brunensis*, 57(4), 95-102.
- [5] Wolak, A., Zając, G., & Słowik, T. (2021). Measuring kinematic viscosity of engine oils: A comparison of data obtained from four different devices. *Sensors*, 21(7), 2530.
- [6] Tucki, K.; Orynycz, O. (2021). Bioenergy and Biofuels. *Sustainability*, 13, 9972. <https://doi.org/10.3390/su13179972>
- [7] Kubich V.I., Cherneta O.G., Yurov V.M., Portnov V.S., Amangeldikyzy A., Kopobayeva A.N., Madisheva R.K., Askarova N.S. (2024) Influence of PolytronTMC Composition on the Tribological State of the System of materials “40Ch - Transmission Oil - HCh15” when Simulating Friction Modes and Lubrication Conditions. *Material and Mechanical Engineering Technology*, 2024(2), pp. 8–17
- [8] Kubich, V.I., Cherneta, O.G., Yurov, V.M. (2023) Influence of Dynamic Viscosity of a Lubricant Material on the Parameters of Adhesion Bond in the Systems of Materials 12KH2H4-STEEL 45, 45KHN2MFA-Steel 45 when Boring and Borocement Steel 45. *Material and Mechanical Engineering Technology*, 2023(1), pp. 3–9.
- [9] Krasodonski, W., Skibińska, A., & Żółty, M. (2020). Thermal Oxidation Stability of Lubricating Greases. *Advances in Science and Technology. Research Journal*, 14(3).
- [10] Stanciu, I. (2023). Some methods for determining the viscosity index of hydraulic oil. *Indian J. Sci. Technol*, 16(4), 254-258.
- [11] Polish Standard PN-77/C04166. Testing of shear resistance of lubricating oils and hydraulic fluids in an ultrasonic device.
- [12] International standard ISO ISO 3104:2023 Petroleum products — Transparent and opaque liquids — Determination of kinematic viscosity and calculation of dynamic viscosity
- [13] Paludan, M. V., Dollet, B., Marmottant, P., & Jensen, K. H. (2024). Elastohydrodynamic interactions in soft hydraulic knots. *Journal of Fluid Mechanics*, 984, A55.
- [14] Viswanath, D. S., Ghosh, T. K., Prasad, D. H., Dutt, N. V., & Rani, K. Y. (2007). *Viscosity of liquids: theory, estimation, experiment, and data*. Springer Science & Business Media.
- [15] Hebda M., Wachal A., *Tribology*. Scientific and Technical Publishing House, Warsaw 1980. (In Polish)



- [16] Zwierzycki W., Industrial oils and lubricants. ITE, Radom 1999. (In Polish)
- [17] Tilloev, L., Dustov, K., Alimov, A., Bobokulov, F., & Ruziev, F. (2021, April). Research the content of waste (yellow oil) of the shurtan gas chemical complex in Uzbekistan. In Journal of Physics: Conference Series (Vol. 1889, No. 2, p. 022057). IOP Publishing.
- [18] Novaković, B., Radovanović, L., Zuber, N., Radosav, D., Đorđević, L., & Kavalić, M. (2022). Analysis of the influence of hydraulic fluid quality on external gear pump performance. *Eksploatacja i Niezawodność*, 24(2).
- [19] Guan, L., Feng, X. L., & Xiong, G. (2008). Engine lubricating oil classification by SAE grade and source based on dielectric spectroscopy data. *Analytica Chimica Acta*, 628(1), 117-120.
- [20] Novaković, B., Radovanović, L., Zuber, N., Radosav, D., Đorđević, L., & Kavalić, M. (2022). Analysis of the influence of hydraulic fluid quality on external gear pump performance. *Eksploatacja i Niezawodność*, 24(2).
- [21] Wolak, A., & Zajac, G. (2017). The kinetics of changes in kinematic viscosity of engine oils under similar operating conditions. *Eksploatacja i Niezawodność*, 19(2), 260-267.

#### Information of the authors

**Łukasz Gierz**, PhD DSc Eng., professor, Poznan University of Technology

e-mail: [lukasz.gierz@put.poznan.pl](mailto:lukasz.gierz@put.poznan.pl)

**Karolina Perz**, PhD Eng., associate professor, Poznan University of Technology

e-mail: [karolina.perz@put.poznan.pl](mailto:karolina.perz@put.poznan.pl)

**Bartosz Wieczorek**, PhD DSc Eng., professor, Poznan University of Technology

e-mail: [bartosz.wieczorek@put.poznan.pl](mailto:bartosz.wieczorek@put.poznan.pl)

**Cristina Peixoto Matos**, PhD., professor, Politécnico de Viseu

e-mail: [cristinapeixoto@mat.estv.ipv.pt](mailto:cristinapeixoto@mat.estv.ipv.pt)

**Łukasz Warguła**, PhD DSc Eng., professor, Poznan University of Technology

e-mail: [lukasz.wargula@put.poznan.pl](mailto:lukasz.wargula@put.poznan.pl)

## Analysis of the Stress-Strain State of the Surfaced Tooth in the T-FLEX CAD Application Program

Buzauova T.M.<sup>1\*</sup>, Sarbaev D.A.<sup>1</sup>, Smailova B.K.<sup>1</sup>, Toleubayeva Sh.B.<sup>2</sup>

<sup>1</sup>Abylkas Saginov Karaganda Technical University, Karaganda, Kazakhstan

<sup>2</sup>L.N. Gumilyov Eurasian National University, Astana, Kazakhstan

\*corresponding author

**Abstract.** This work is devoted to the analysis of the stress-strain state of the surfaced gear teeth using the T-Flex CAD software. The study showed that the surfaced teeth are able to withstand workloads, as well as loads increased by 50%, demonstrating a deformation of only 2%. Zones of maximum stresses and deformations have been identified, which makes it possible to predict the durability and reliability of the surfaced teeth. The conducted studies confirm the effectiveness of the electroslag surfacing method for restoring gears and its application to improve the performance of gears under high loads.

**Keywords:** stress-strain state, analysis, T-Flex CAD, gear tooth, surfaced tooth, material, finite element method.

### Introduction

The restoration of gear teeth is an important task in mechanical engineering, especially in conditions of intensive operation and high loads. One of the effective methods of tooth restoration is electroslag surfacing, which allows to restore the geometry and properties of the teeth, ensuring their long-term operation [1, 2]. As part of this study, a laboratory installation for electroslag surfacing of gear teeth was developed. This installation was designed taking into account all necessary technical requirements and tested in a laboratory [3, 4].

The quality of the tooth sample was assessed using visual, capillary, ultrasound, micro- and macrostructural analyses. The results of the analyses showed that the surfaced tooth has high performance characteristics and can be effectively used in real conditions [5, 6].

To analyze the stress-strain state of a gear with a surfaced tooth, the T-Flex application program was used, which allows mathematical modeling of common physical phenomena and solving important practical problems that arise in everyday design practice. All calculations are performed using the finite element method (FEM). At the same time, an associative relationship is maintained between the three-dimensional model of the product and the calculated finite element model. Parametric changes of the initial solid-state model are automatically transferred to the grid finite element model [7].

In this paper, the finite element method using T-Flex software is used to analyze the stress-strain state of a surfaced tooth. A comprehensive analysis of the surfaced teeth allows to identify possible defects and helps prevent premature failures and wear of the gear.

The purpose of this study is to analyze the stress-strain state of the surfaced teeth in order to assess their performance characteristics.

The object of the study is a model of a surfaced gear tooth.

The relevance of the study is due to the need for effective methods of restoring gears that are subjected to high loads and intensive operation. Electroslag surfacing significantly extends the service life of gear teeth, which is important for the engineering industry and other industries where the reliability and durability of gears play a key role.

The novelty of the research lies in the use of T-Flex software for detailed analysis of the stress-strain state of the surfaced teeth, as well as modeling with an increased load by 50%.

Research method: literary review, modeling, analysis.

Research methodology: simulation modeling of the stress-strain state, creation of a three-dimensional model of surfaced teeth in T-Flex software, static analysis by the finite element method (FEM) to determine the distribution of stresses and deformations; analysis of simulation results under workloads and under loads increased by 50%; comparison of the results of the analysis of surfaced teeth with the results for non-surfaced teeth; determination of maximum stress and strain zones and assessment of the performance characteristics of surfaced teeth.

### 1. Research methodology

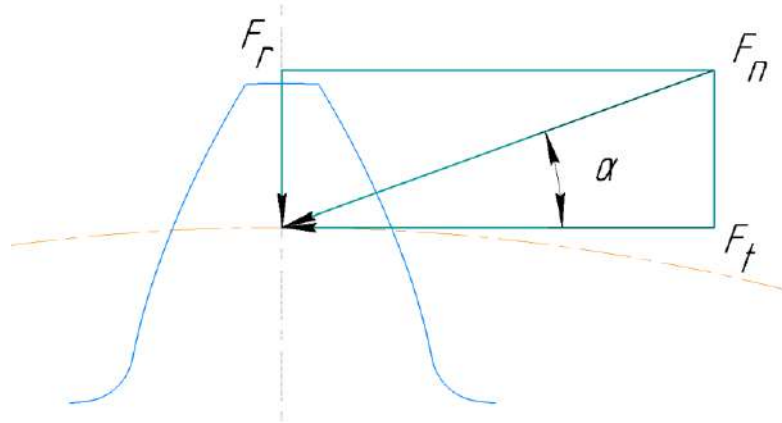
To simulate a surfaced tooth, the following parameters were used as initial data: module  $m = 20$ , number of teeth  $z = 29$ , pitch diameter  $d = 580$  mm, material of the surfaced tooth - steel 70 (GOST 14959-79).

Characteristics of the objects of study, such as strength, modulus of elasticity, shear modulus, density, tensile strength, compressive strength are shown in Table 1.

**Table 1.** Initial data for modeling

Physical and mechanical properties	Steel 70 (GOST 14959-79)
Modulus of elasticity	206000 N/mm <sup>2</sup>
Poisson's ratio	0,29
The shear modulus	79844.96 N/mm <sup>2</sup>
Density	7810 kg/m <sup>3</sup>
Yield strength	834 N/mm <sup>2</sup>
Tensile strength	1030 N/mm <sup>2</sup>
Compressive strength	1030 N/mm <sup>2</sup>

The static analysis in the program is carried out by calculating the stress-strain state of structures under the action of forces applied to the system constant in time. To determine the forces acting in cylindrical gears, using the "Analysis" tab, three main forces were used (Fig.1): circumferential, radial and normal.



**Fig. 1.** – Diagram of the force in the engagement of cylindrical gears

The circumferential force  $F_t$  is directed tangentially to the dividing circle of the gear tooth and is responsible for the transfer of power between the teeth, which is determined from the following equation [8]:

$$F_t = \frac{2T_{\max}}{d}, \quad (1)$$

where  $d$  – pitch diameter;

$T_{\max}$  – the greatest moment of a normally flowing technological process ( $T_{\max} = 39226$  N/m).

$$F_t = \frac{2 \cdot 39226 \cdot 10^3}{580} = 135262 N.$$

The radial force  $F_r$  acting perpendicular to the circumferential force is directed from the center of the gear to the point of contact of the teeth and affects the bearings, creating a radial load [8]:

$$F_r = F_t \frac{\tan \alpha}{\cos \beta}, \quad (2)$$

where  $\alpha$  – angular correction;

$\beta$  - helix angle.

There is no angular correction for the gear tooth under study,  $\tan \alpha = \tan 20^\circ = 0.36$ . In straight tooth gears  $\cos \beta = 1$ .

$$F_r = 135262 \frac{0,36}{1} = 49235 N.$$

The normal force  $F_n$  is determined by the formula [8]:

$$F_n = \frac{F_t}{\cos \alpha \cos \beta}. \quad (3)$$

In straight tooth gears  $\text{tg} \beta = 0$ .

$$F_n = \frac{135262}{\cos 20^\circ \cdot 1} = 143942 N.$$

When the normal force is distributed to all teeth of the gear, the normal force is set according to the formula [8]:

$$F_n' = \frac{F_n}{z}, \quad (4)$$

where  $z$  – number of teeth.

$$F_n' = \frac{143942}{29} = 4963 N.$$

It is also possible to take into account the expansion/compression stresses of the material or deformation of the structure by the amount of known displacements. Displacements are the value of the absolute displacements of the model at the measurement points (sensors) determined at each point 1, 2, 3, etc. (Fig. 2). The points are fixed along the involute of the tooth surface [9, 10, 11, 12, 13], and the surfaced tooth (A) is highlighted taking into account the depth of penetration [14].

The displacement is determined by the formula:

$$\Delta = \sqrt{x_i^2 + y_i^2 + z_i^2}, \quad (5)$$

where  $x, y, z$  - the components of the displacement vector of a certain  $i$  node of the finite element grid.

The equivalent stress in the surfaced tooth is analyzed to determine the distribution of internal forces arising in the material under the influence of external loads. This analysis allows us to identify stress concentrations that can become potential zones of the onset of cracks or other defects. The equivalent stress is calculated using the formula [8]:

$$\sigma_U = \frac{1}{\sqrt{2}} \sqrt{(\sigma_x - \sigma_y)^2 + (\sigma_y - \sigma_z)^2 + (\sigma_z - \sigma_x)^2 + 6(\tau_{xy}^2 + \tau_{yz}^2 + \tau_{xz}^2)}, \quad (6)$$

where  $\sigma_{x,y,z}$  - stress in the direction of the corresponding axis OX, OY, OZ of the global coordinate system;

$\tau_{xy}, \tau_{xz}, \tau_{yz}$  - the stress in the direction of the OX, OY, OZ axis of the global coordinate system acting on a site with a normal parallel to the OX, OY, OZ axis.

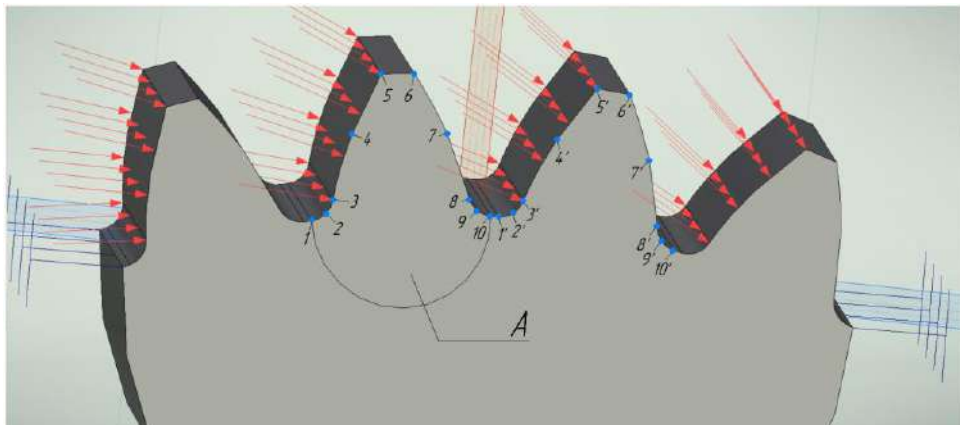


Fig. 2. – Fixing points along the tooth involute: A-surfaced tooth (the arrows indicate the applied forces).

The design sequence (Fig.3) includes the creation of a model of a gear with a surfaced tooth (A), a grid for the finite element method, fastening, applied forces and measurement points of the calculation result of finite element analysis. The grid type is absolute, the grid size is 10, the minimum curve size is 5, the number of finite elements is 142805 (Fig.4).

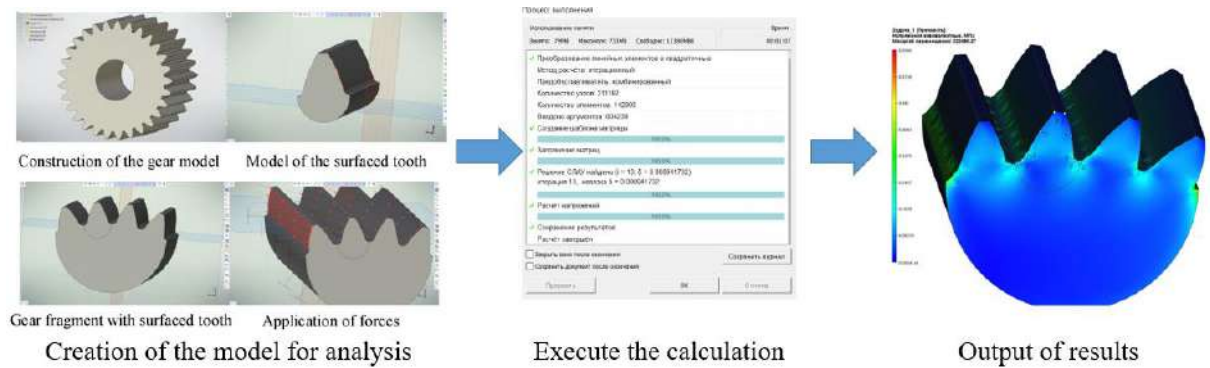
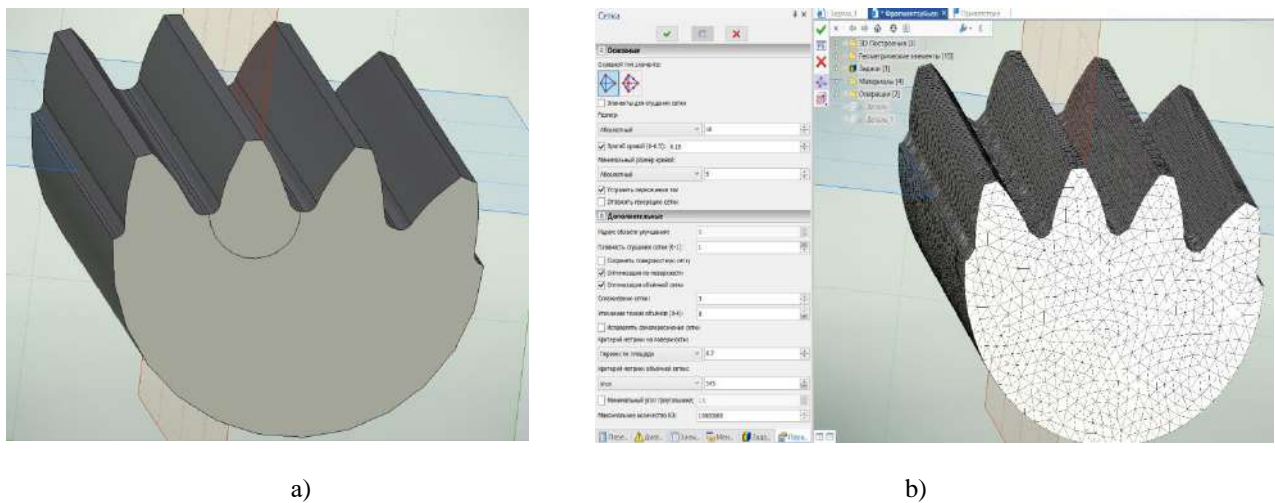


Fig. 3. – Modeling steps in the T-Flex program

As part of the study, the surfaced tooth will be tested for tensile strength by increasing the applied force by 50%. This will allow assessment of how the tooth material endures with increased loads and identify possible limits of its stability. A 50% increase in strength will give a more complete picture of the behavior of the surfaced tooth in extreme operating conditions, predicting its durability and reliability.



a – gear fragment with surfaced tooth; b – finite element grid

Fig. 4. – Preprocessing preparation of the problem solution

The results of this test will help determine how effectively the surfaced material is able to withstand additional loads, and identify potential points of failure or vulnerabilities in the gear design.

After completion of the preprocessing preparation, the calculation is started, which allows to visually assess the stress-strain state of both the surfaced and other gear teeth.

2. Results and discussion

The results of static analysis under workloads of the stress-strain state of the fragment are shown in Figure 5.

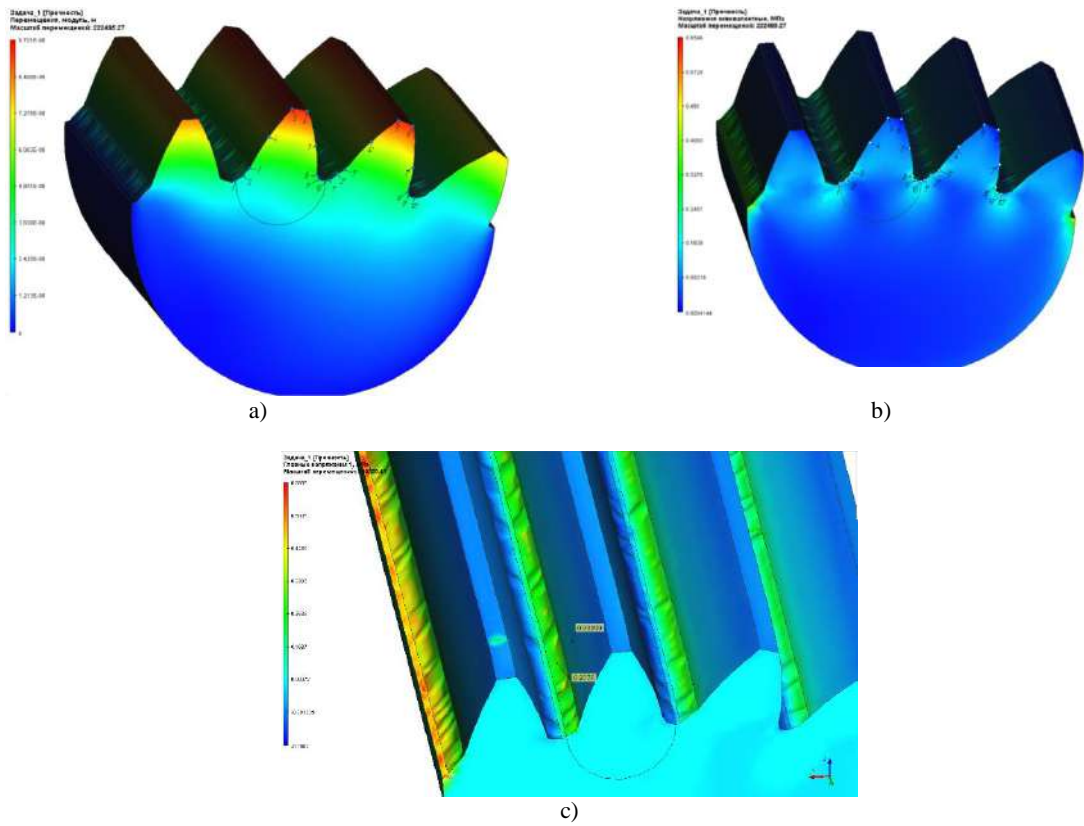


Fig. 5. – Simulation results of the stress-strain state: displacement (a), stress (b), stress concentration zones (c)

The results of modeling the stress-strain state with a load increased by 50% are shown in Figure 6.

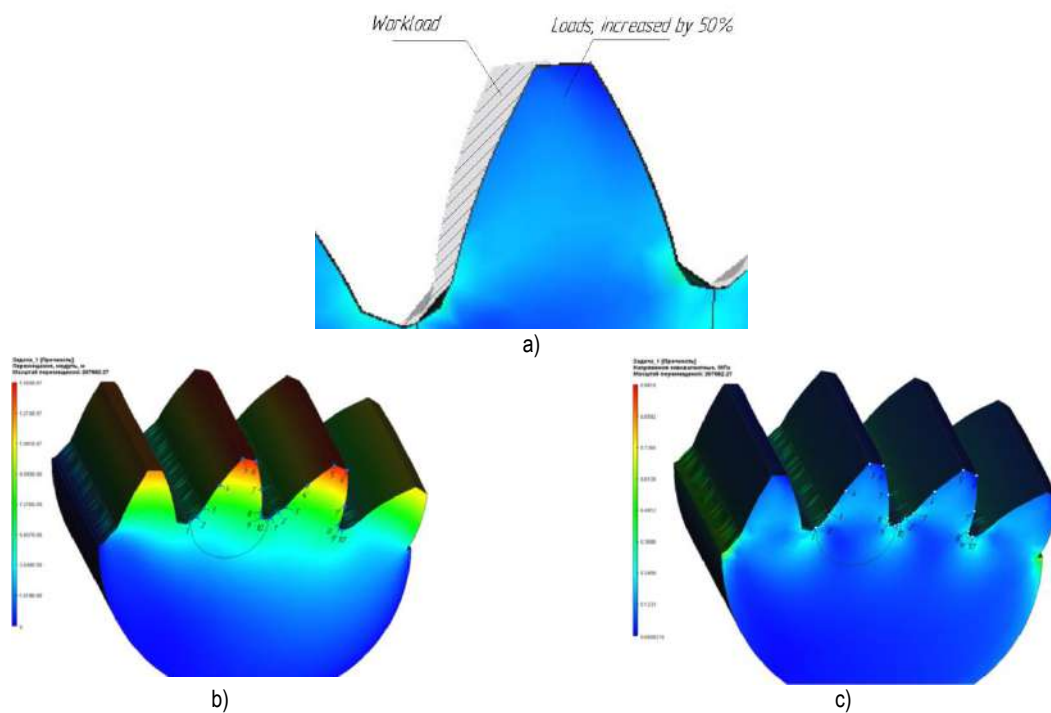
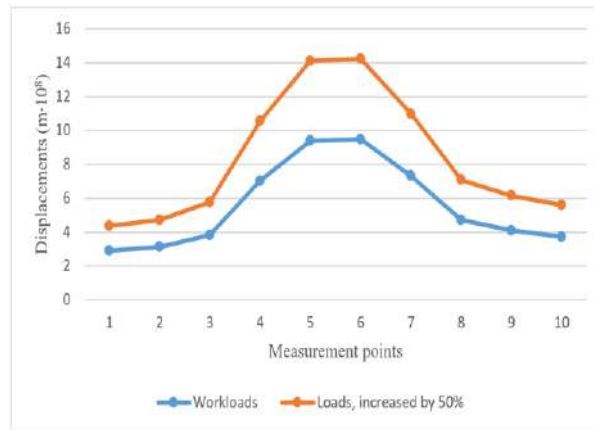
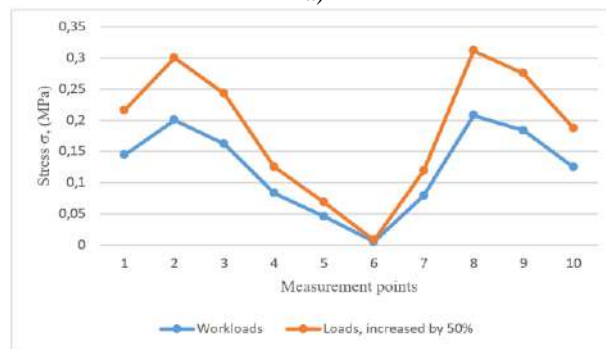


Fig. 6. - Simulation results of the stress-strain state with increased loads by 50%: in comparison (a); displacement (b), stress (c)

Displacements and stress values are recorded at the measurement points (Fig.7, 8).

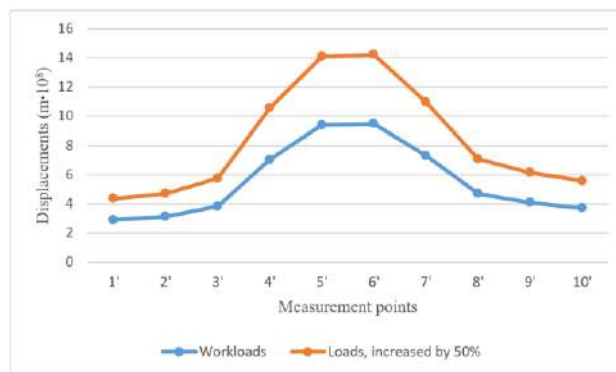


a)



b)

Fig. 7. – Graphs of displacements (a) and stresses (b) of the surfaced tooth



a)



b)

Fig. 8. – Graphs of displacements (a) and stresses (b) of the gear tooth

According to the results of the analysis, it can be clearly seen that the surfaced tooth withstands working deformations and stresses (Fig. 5, 6, 7, 8). Stress is concentrated on the roots of the tooth (Fig. 5, c). With an increased load of 50%, the surfaced tooth is deformed by 2% (Fig. 6, a) compared to the rest of the gear teeth, while the maximum stress is fixed at the measurement points – 0.3116 MPa (Fig. 7, 8).

### Conclusions

- 1) A qualitative and quantitative analysis of the surfaced tooth was carried out.
- 2) The stress-strain state of the surfaced tooth has been developed. The analysis allows to determine the stress zones and deformation of the surfaced gear tooth.
- 3) The surfaced tooth withstands workloads (Fig. 5).
- 4) The degree of deformation of the surfaced tooth with an increase in the workload by 50% is 2% (Fig. 6, a).
- 5) The high loads at points 2, 8 and 2', 8' (Fig. 7, 8) are explained by the fact that tensile and compressive loads are concentrated on these zones.

### References

- [1] Kuskov, Yu. M. i dr. E`lektroshlakovaya naplavka. - M.: AO "Nauka i texnologii", 2001. - 180 p.
- [2] Paton, B.E. E`lektroshlakovaya svarka i naplavka. - M.: Mashinostroenie: 1980. - 512p.
- [3] Smailova B.K., Buzauova T.M., Bartenev I.A., Davletova K. Restoration of large modular teeth of ball mill gears by electro-slag surface// Journal of applied engineering science, Vol. 22, No. 2 (2024), P.483-491.
- [4] Buzauova, T., Bartenev, I., Smailova, B. Kristallizator dlya e`lektroshlakovoj naplavki krupnomodul`ny`x zub`ev. Patent RK na poleznuyu model`. №9186. 31.05.2024.
- [5] Smailova1 B.K., Buzauova T.M., Bartenev I.A., Škamat J. Analysis of the quality of the restored gear tooth of large-module gears// Science and technology of Kazakhstan, Issue 1, 2024, P.16-24.
- [6] Buzauova T.M., Sarbaev D.A. Optimizaciya rezhimov svarki dlya vosstanovleniya krupnomodul`ny`x zubchaty`x koles s ispol`zovaniem e`lektroshlakovoj naplavki// Trudy` Respublikanskoj studencheskoj nauchnoj konferencii. -Karaganda: Izd-vo KarTU, 2024.- P.147-148.
- [7] T-Flex CAD. URL: [https://www.tflex.ru/downloads/products/tfanalysis\\_documentation.pdf](https://www.tflex.ru/downloads/products/tfanalysis_documentation.pdf) (date of application: 20.06.2024).
- [8] Reshetov D. N., Gusenkov A.P., Drozdov Yu.N. Mashinostroenie. E`nciklopediya / Red. sovet: Frolov V. K. (pred.) i dr. – M.: Mashinostroenie. Detali mashin. Konstrukcionnaya prochnost`. Trenie, iznos, smazka. T. Sh-4; Pod red. Reshetova D. N. 1995. – 864 p.
- [9] Sánchez-Majano A. R. et al. Accurate stress analysis of variable angle tow shells by high-order equivalent-single-layer and layer-wise finite element models //Materials, 2021, T. 14, №. 21, P. 6486.
- [10] Mohammed J. K., Khdir Y. K., Kasab S. Y. Contact stress analysis of spur gear under the different rotational speed by theoretical and finite element method //Academic Journal of Nawroz University. – 2018. – T. 7. – №. 4. – S. 213-222.
- [11] Hwang S. C. et al. Contact stress analysis for a pair of mating gears //Mathematical and Computer Modelling. – 2013. – T. 57. – №. 1-2. – S. 40-49.
- [12] David Müzel S. et al. Application of the finite element method in the analysis of composite materials: A review //Polymers. – 2020, T. 12, №. 4. – P. 818.
- [13] Muhammad A., Ali M. A. H., Shanono I. H. Finite Element Analysis of a connecting rod in ANSYS: An overview //IOP Conference Series: Materials Science and Engineering. – IOP Publishing, 2020, T. 736, №. 2, P. 022119.
- [14] Smailova B.K., Buzauova T.M., Sarbaev D.A. Issledovaniya vliyanie rezhimov e`lektroshlakovoj naplavki na glubinu proplavlenniy`x zub`ev// Trudy` Respublikanskoj studencheskoj nauchnoj konferencii. - Karaganda: Izd-vo KarTU.-2023. - P.347-348.

### Information of the authors

**Buzauova Toty Meirbekovna**, c.t.s., associate professor , Abylkas Saginov Karaganda Technical University  
e-mail: [toty\\_77@mail.ru](mailto:toty_77@mail.ru)

**SarbaevDalelehan Ardakovich**, master's student, Abylkas Saginov Karaganda Technical University  
e-mail: [dalelehan20002@gmail.com](mailto:dalelehan20002@gmail.com)

**Smailova Baglan Kabdullaevna**, PhD student, PhD student, Abylkas Saginov Karaganda Technical University  
e-mail: [bahlan@mail.ru](mailto:bahlan@mail.ru)

**Toleubayeva Shamsygaiyn Bolatkyzy**, PhD, senior lecturer, L.N. Gumilyov Eurasian National University  
e-mail: [shamsygaiyn@mail.ru](mailto:shamsygaiyn@mail.ru)



## A Device for Measuring the Wear of Replaceable Rotary Tool Inserts of Milling Drums of Road Milling Machines

Issabek Z.R.<sup>1</sup>, Kadyrov Zh. N.<sup>2</sup>, Kassenov A. Zh.<sup>1</sup>, Mussina Zh. K.<sup>1</sup>, Tussupova S.O.<sup>1\*</sup>

<sup>1</sup>Toraighyrov University, Pavlodar, Kazakhstan

<sup>2</sup>Office of the patent attorney «Kadyrov and Partners», Almaty, Kazakhstan

\*corresponding author

**Abstract.** In the article, based on studies of the wear of the cutting surfaces of the incisor inserts of road cutters, an original device is proposed that allows measuring all wear elements of the cutting inserts of road cutters, including the kinematic profile of the wear site proposed for the first time. Experimental studies of prototypes of assemblies with elastic elements embedded in them have been carried out and a decrease in noise content in the general flow of measuring information has been achieved due to the simplicity of the design and the absence of destabilizing complex-profile and kinematically dependent mechanisms and assemblies in it. For the first time, the proposed solutions made it possible to increase the efficiency of road milling machines (RMM), including expanding their operational, technological, economic, and design and mechanical capabilities.

**Keywords:** measurement, tool inserts, wear elements, kinematic profile, wear site, road milling machines.

### Introduction

The operation of milling drums of road milling machines is accompanied by intensive wear of replaceable rotary tool inserts. At the same time, depending on the operating conditions, the size of the wear pads, as well as the shape of the worn surface, vary greatly. In these conditions, the development of a device for mobile measurement of all wear elements of replaceable rotary cutter rates of milling drums of road milling machines is relevant. Improving the efficiency of road milling machines by considering them as an object of management and creating automatic milling process control systems based on standard components of road milling machines.

### 1. Methodology

It is established that from the moment of embedding a round replaceable tool insert into the surface to be processed and until they come out of contact with this surface, chips with a thickening at the end are formed, the size of which depends on the speed and depth of milling. Figure 1 shows a prefabricated cutter with a round shank used in milling drums.

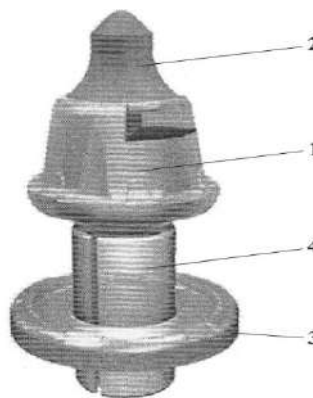


Fig.1. - A prefabricated cutter with a round shank

The body 1 (Figure 1) of the cutter consists of a head and a cylindrical shank. A replaceable carbide tip 2 is attached to the head using high-temperature solder. With the help of a wear washer 3 and a clamping sleeve fitting the shank 4, the assembly structure of the tool insert in the tool holder is based with the possibility of periodically turning it at an angle of  $10^\circ$  (per revolution of the rotating milling drum). This rotation is performed in the absence of chip removal by this cutting plate [1]. The rotation of the tool insert is facilitated by low-amplitude "swinging" of the shank with a sleeve inside the washer and minor dynamic vibrations of the tool holder body. All this creates a precessional movement of the tool insert inside the base hole of the tool holder, provides conditions for uniform wear of the cutting and contacting surfaces of prefabricated tool inserts. With uniform (along the arc of the circle) wear of the cutting part of the head of the tool insert, the effect of self-sharpening of the cutting parts occurs, which increases the service life of the tool insert as a whole.

Tip 2 is made of tungsten-cobalt hard alloys for example, (VK6 with 94% tungsten carbide and 6% cobalt) cap-shaped (three versions), or cylindrical shape [1] Tungsten carbide (WC) with a hardness of 9 according to the Mohs school is close to the hardness of diamond (hardness 10), while cobalt, as a more viscous malleable material, provides cementing properties to this two-component alloy [2].

For tangential rotating cutting inserts with metal-ceramic tungsten-cobalt alloys, the cutting angle is reduced compared to radial ones, which leads to a 20-25% reduction in cutting force and a reduction in the energy intensity of the process.

Research [3] based on statistical processing of 1470 pieces of worn cutting inserts on Wirtgen W500 and Wirtgen DC200 milling drums has established that 63% of assembled cutting inserts are subject to uniform wear; 19% are subject to intense wear of the cutter body (when using them as scoring tool holders (item 2 in Figure 1.2), or when working in a viscous environment, for example, in viscous asphalt); 13% are subject to uneven wear due to jamming in the tool holder and 5% of cutting inserts fail due to chipping and destruction of carbide tips (item 2 in Figure 1).

The operation of milling drums with prefabricated rotary cutting inserts is characterized by [3, 4]: frequency of operation of the cutting inserts, variable area of the removed layer with one cutting insert, a variable (changing) number of cutting inserts in operation, which causes variations in the forces, moments and cutting power required for milling.

The total path length in the asphalt concrete pavement of one cutting insert is determined as [5]:

$$L = \frac{S}{6} \cdot \arccos\left(1 - \frac{P}{R}\right) \quad (1)$$

where L – is the path length of the cutting insert 3 per one revolution of the milling drum 2 from point «b» to point «a», passed in asphalt concrete pavement 1, Figure 1.6;

S – the area of the worn-out coating;

P – depth of cut (depth of cut) of the cutting insert;

R – milling drum radius;

$\alpha$  – the angle between the points of contact of the cutting insert with the asphalt concrete pavement;

$\omega$  and  $v$  – respectively, the angular velocity and the speed of relative movement (feed) of the milling drum.

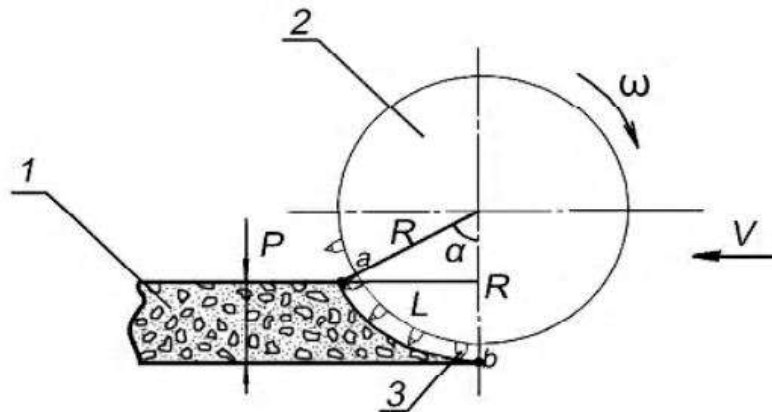


Fig. 2. - Path length of the cutting insert in an asphalt concrete road surface

To ensure the performance of incisal inserts, dry or wet cooling is used [7].

In the first case, the road milling machine (milling drum) is removed from contact with the asphalt concrete surface and rotated idle for 1-2 minutes. The wet method uses a forced supply of coolant under pressure from nozzles to the surface of the milling drum.

Periodic preventive control of cutters for rotation around their axis (usually manually) also creates conditions for uniform wear over the entire surface (the circumference of the contact surface).

The wear of rotary cutting inserts is negatively affected by various factors [1, 7]:

**A. Operational:**

1 – physical and mechanical characteristics of the treated surface (its hardness, composition and type of the treated layer, temperature).

2 – presence of coolant in the cutting zone.

3 – type and characteristics of road milling machines.

**B. Technological:**

1 – milling modes (milling depth, milling drum rotation speed);

2 – adjustment parameters (angles of attack, rotation and tilt in the milling drum coordinate system [1]).

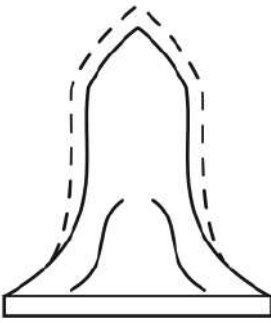
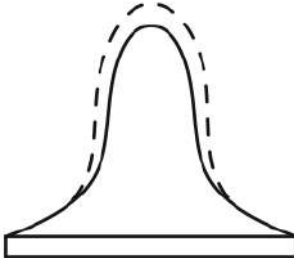

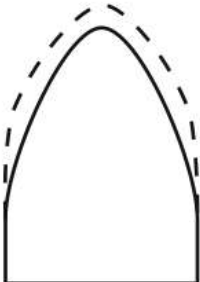
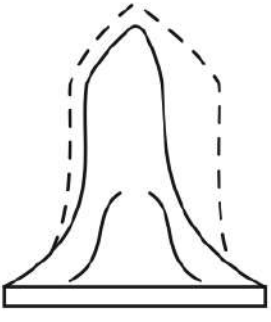
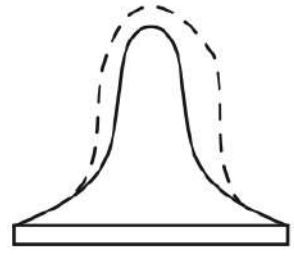

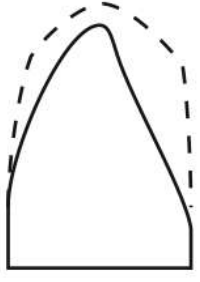
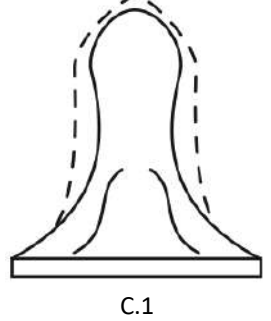
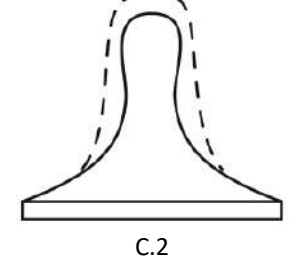
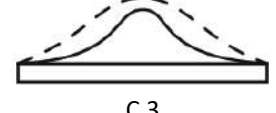
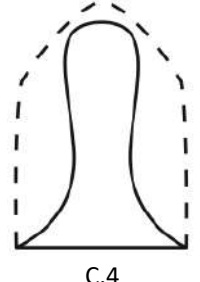
**C. Design:**

- 1 – shape of the carbide tips used;
- 2 – type of solder;
- 3 – location of the cutting inserts on the milling drum;
- 4 – step of arrangement of cutting inserts on the drum;
- 5 – inclination and pitch of the spirals of the locations of the cutting inserts on the drum;
- 6 – presence of chip ejectors and their angle of inclination relative to the spiral direction of the location of the cutting inserts on the drum.

Table 1 shows the shapes of worn surfaces of different types of tips, where:

- 1) A1-A4 – correctly worn cutting inserts. Such wear occurs when the milling technological regimes are observed, periodic preventive inspections of the milling drum are carried out, and the cutting inserts are rotated.
- 2) B1-B4 – incorrect operation of the cutting insert, when milling was carried out while the cutting insert was blocked (jammed) in the tool holder.
- 3) C1-C4 – incorrect operation of the cutting insert, when milling was carried out with free rotation (with a gap) movement of the cutting inserts in the tool holder.

**Table 1.** Shape of worn surfaces of different types of tips

Cap-shaped in a massive design	Long cap-shaped	Cap-shaped flat design	Cylindrical
 A.1	 A.2	 A.3	 A.4
 B.1	 B.2	 B.3	 B.3
 C.1	 C.2	 C.3	 C.4

In Table 1, the dotted line shows the shape of the unworn (initial) surfaces of different types of tips.

There are other forms of worn surfaces of the tips of cutting inserts (for example, wear of only the upper end part, which occurs during radial indentation in the direction of the machined surface during fluctuations in the milling depth) and others.

**2. Results and discussion**

To study the nature of wear of rotary, replaceable cutting inserts, the author was the first to develop a stationary device for measuring the wear of these inserts [8], Figure 3.

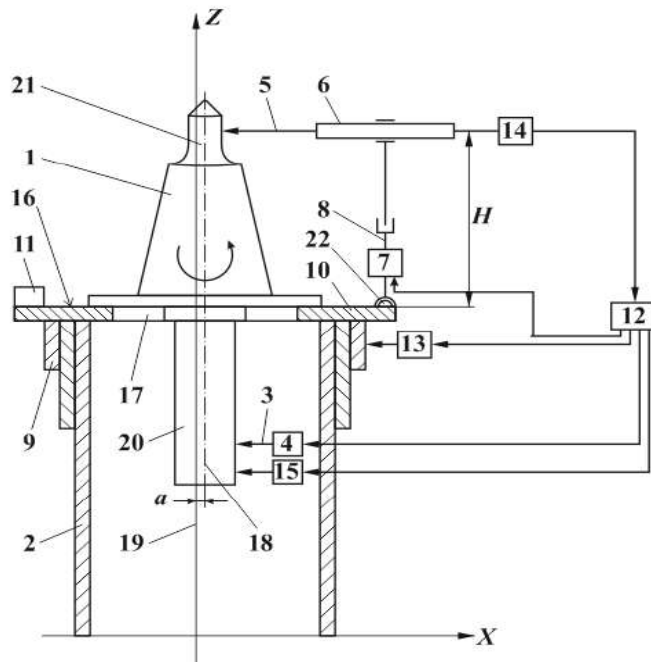


Fig. 3. - Device for measuring wear of replaceable rotary cutter inserts of milling drums

A device for measuring the wear of replaceable rotary cutting inserts 1 of milling drums contains a housing 2, a rotation drive of the cutting insert and a measuring transducer for determining the position and condition of the cutting edges of the cutting inserts.

In accordance with the proposed technical solution, the rotation drive is made prefabricated and consists of a three-detector (three-contact) clamping device with three circumferentially located cams 3 with autonomous drives 4 of their radial adjustment movements.

The measuring transducer of the position and condition of the cutting edges of the cutting inserts is made as a prefabricated device and consists of a contact tip 5 and a wide-range linear measuring transducer 6 interacting with it, for example, a linear inductosyn. The measuring transducer itself is installed on a stand 8 telescopically extendable from the drive 7 of vertical movements in such a way that the measuring transducer has the possibility of both installation radial movement and further precision measurement of deviations from roundness with fixed radial (along the X axis) and vertical (along the Z axis) positions of the measuring transducer.

The rack 8 of the measuring transducer is attached to the edge of a rotating disk 10 resting on the sleeve 9, which is additionally equipped with a counterweight 11 located opposite the rack 9.

The device additionally includes a microprocessor control device 12 and a rotation drive 13 of the sleeve 9 with the disk 10, while the output of the measuring transducer 6 is connected through the amplification-converter unit 14 to the input of the microprocessor control device 12, the output of which is connected to the input of the rotation drive 15 of the cutting insert 1, the inputs of the autonomous drives 4 of the radial adjustment movements of the cams 3, the input of the drive 7 of the vertical movements of the rack 8 and the input of the rotation drive 13 of the sleeve with the disk. In block 14 it is possible to visually control the amount of movement of the tip 5 per revolution of the cutting insert.

The device is used as follows.

The replaceable rotary cutting insert 1 to be measured is installed with its flat supporting surface of the head on the base surface 16 of the rotary disk 10, while the shank of the cutting insert 1 passes through the hole 17 in the disk, and its lower console part is at the level of the cams 3 and the rotation drive 15. Cams 3 synchronously moving towards the center are in contact with the cylindrical surface of the shank 20 of the cutting insert.

At the first stage, the axis 18 of the shank 20 of the cutting insert is aligned with the axis 19 of the rotary disk 10 (the algorithm for determining the center of the hole by three points of contact located at  $120^\circ$  intervals is not disclosed in the materials of this application). The existing mismatch in the position of the axes 18 and 19 is compensated by the drives of 4 radial adjustment movements of the cams 3 (the drives are built into each cam, are autonomously controlled and move independently of each other in the radial direction until the axes 18 and 19 are aligned, while the design of the drives in the materials of this application not disclosed). In Figure 1, the mismatch is indicated as "a".

After combining the axes 18 and 19, upon command from the microprocessor control device 12, the rotation drive 13 of the sleeve with the disk is activated, making one full revolution. In this case, the contact tip 5 comes into contact with the working (worn) surface of the carbide tip 21, and the linear inductosyn 6 records the actual radial movement of the tip 5 per revolution of the cutting insert. A circular diagram of the cross-section of the tip 21 at height "H" is reproduced.

Upon command from the microprocessor control device 12, the drive 7 periodically moves the measuring transducer in the vertical direction, reproducing the cross section at an intermediate local level. The totality of such circular patterns (processed in device 12) gives a real picture of the wear of the working surfaces (carbide tip 21 of the cutting insert).

Experience in operating milling drums with replaceable cutting inserts has shown that the nature of wear of the carbide tip 21 can be anything - from uniformly symmetrically correctly worn - to a one-sided worn position of the working edges of the tip, for example, when the cutting insert is blocked (jammed) in the tool holder, or when it is freely -rotational (with clearance) movement of the cutting inserts in the tool holder

Real objective data on tip wear allows us to develop recommendations for their restoration, for example, by surfacing.

The device is effective in operation, allows you to identify the degree of wear and the possibility of restoring each incisal insert. The procedure for diagnosing and measuring the wear of one replaceable cutting insert takes up to 3 minutes.

The rack 8 has the possibility of installation and/or adjustment angular movement within  $\pm 20^\circ$  relative to the vertical position, for which a part-rotary spherical hinge 22 is introduced into the design of the device. Such actions are necessary for monitoring complex-profile cutting inserts, for example, cap-shaped ones in a flat design

Previously, the main design features of prefabricated cutters with round shanks were noted and the main factors influencing their wear were identified and technical means for measuring the wear of the cutting surface of cutter inserts of road milling machines were disclosed.

Let us highlight individual elements of wear of the cutting surfaces of cutting inserts: dimensional U1, height of the wear area U2 and kinematic profile of the wear area U3. In Figure 4, the positions indicate: 1 – the original unworn profile of the cutting surface of the cutting insert; 2 – kinematic profile of the wear area on the cutting surface of the cutting insert.

The kinematic profile of the wear area was proposed by the authors for the first time and was constructed based on the average of thirty repeated measurements on each of the measured sections  $H_i$  (using the drive 7 of the vertical movements of the rack 8, the pitch of the measured sections  $\Delta H$  was set to 2.35 mm). For comparative analysis, the original unworn profile of the cutting surface of the cutting insert was also recorded (curve 1, Figure 4).

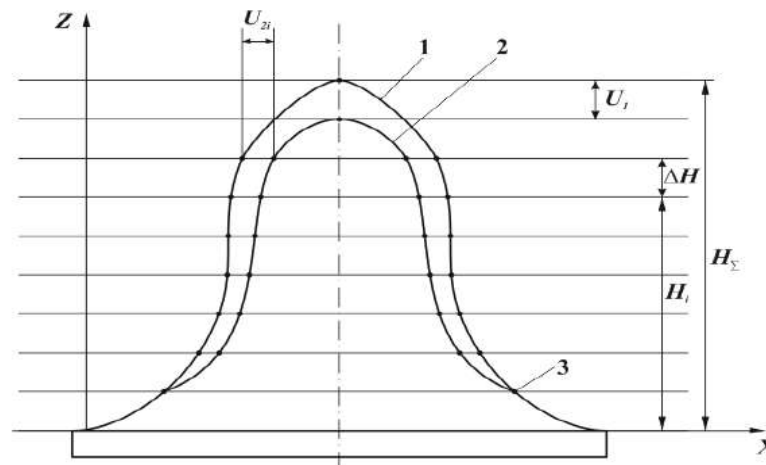


Fig. 4. - Profiles of cutting surfaces of cutting inserts

When the contact tip 5 (Figure 3) goes beyond the wear area, the readings of the measuring transducer 6 coincide (for the original (new) and used (worn) cutting inserts - point 3, Figure 4). Having fixed the boundary point of transition from the worn to the original (unworn) surfaces of the cutting surface of the cutting insert, all wear elements of the cutting inserts were found – U1, U2 and U3.

The result of measuring an individual wear element is taken to be the average of thirty repeated measurements [9], which previously included corrections to compensate for systematic errors:

$$\tilde{A} = \frac{\sum_{i=1}^n x_i}{n} \quad (2)$$

where  $x_i$  – the  $i$ -th measurement result;

$n$  – number of repeated measurements ( $n=30$ ).

The measurement error is assessed by indicating the confidence interval corresponding to a certain confidence probability value [10].

Confidence limits of random error are established for measurement results belonging to a normal distribution. In this case, to test the main hypothesis (belonging to a normal distribution), we use a composite criterion, according

to which [7] they determine that the relation  $\tilde{d}$  at a significance level of 2% belongs to the interval  $[d_{1-q_{1/2}}, d_{q_{1/2}}]$  and checking whether differences are exceeded  $(x_i - \bar{A})$  values  $Z_{P/2} \cdot S$ , where

$d_{1-q_{1/2}}$  и  $d_{q_{1/2}}$  – quantiles of distribution [9, table 1];

$Z_{P/2}$  – upper quantile of the distribution of the normalized Laplace function corresponding to the probability  $P/2$  [11, tables II-2];

$S$  – estimate of standard deviation.

$\tilde{d}$  and  $S$  were calculated using the formulas:

$$\tilde{d} = \frac{\sum_{i=1}^n |x_i - \bar{A}|}{n \cdot S^*}, \quad (3)$$

$$S^* = \sqrt{\frac{\sum_{i=1}^n (x_i - \bar{A})^2}{n}}, \quad (4)$$

$$S = \sqrt{\frac{\sum_{i=1}^n (x_i - \bar{A})^2}{n-1}}, \quad (5)$$

where  $S^*$  is a biased estimate of the standard deviation.

Received values:

$$S^* = \sqrt{\frac{39,1}{30}} = 1,14 \text{ мкм}, S = \sqrt{\frac{39,1}{29}} = 1,16 \text{ мкм}, d = \frac{27,8}{30 \cdot 1,14} = 0,8129, \quad (6)$$

$$Z_{P/2} \cdot S = 2,33 \cdot 1,16 = 2,7 \text{ мкм}$$

confirm compliance with two conditions of the composite criterion:

$$0,7110 < 0,8129 < 0,8827$$

and that none of the differences  $(x_i - \bar{A})$  exceeds 2,7 мкм.

The above confirms that the distribution of the measurement results of the wear elements of the cutting surface of the cutting inserts corresponds to the normal distribution law.

Confidence limits  $\pm \varepsilon$  of the random error of the measurement result are determined by the formula:  $\varepsilon = t \cdot S$ , where  $t$  is the Student coefficient.

Since the proportion of systematic errors in the total measurement error of wear elements (dimensional wear) of the cutting surface of cutting inserts is small, in accordance with [10], the measurement accuracy can be expressed as:

$$UI = 5,9 \text{ мкм}, \Delta \text{ from } -2,4 \text{ мкм to } +2,4 \text{ мкм}, \text{ at } P = 0,95.$$

The measurement accuracy of  $U_2$  is determined by the measurement discreteness and the size of the measurement interval of the transducer 6, as well as the positioning accuracy of the rack 8.

When measuring  $U_2$  we can distinguish:

1 – methodological error (error in fixing the moment of transition from worn to unworn cutting surface of the cutting insert  $\Delta_1$ );

2 – instrumental errors (2-1 – manufacturing error of hemispherical surfaces of the part-turn hinge 22 interacting with each other –  $\Delta_2$ ; 2-2 – manufacturing error of guides for linear movements of tip 5 along the X axis and post 8 along the Z axis –  $\Delta_3$ ; 2-3 – manufacturing error of synchronously moved cams 3, including their radial displacement drive –  $\Delta_4$ ).

3 – counting errors (subject to visual reading in block 14), including the error due to parallax –  $\Delta_5$ .

According to the patterns of occurrence, these errors are divided into systematic ( $\Delta_2, \Delta_3$  and  $\Delta_4$ ) and random ( $\Delta_1, \Delta_5$ ).

After certification of the device, systematic errors identified a priori were excluded.

Total measurement error  $U_2$ :  $\Delta_{\Sigma U_2} \in \Delta_1, \Delta_5$ .

It has been experimentally established that the standard deviation of the total measurement error  $U_2$  ( $\sigma_{\Sigma U_2}$ ) does not exceed 2.9  $\mu\text{m}$ .

The accuracy of measuring the kinematic profile of the wear area is influenced by the same factors as the accuracy of measuring  $U_2$ . It has been established that the variation of standard deviations based on the results of repeated measurements of cutter wear (at different levels of position of the rack 8) is insignificant, and the standard deviation of the total error in measuring the kinematic profile  $\sigma_{\Sigma_{\text{кин}}}$  does not exceed 3.5  $\mu\text{m}$ .

For a comparative analysis of the device we developed with known similar ones, we used a criterion that directly reflects their main purpose - obtaining measurement information. Thus, from the point of view of information theory [11], the measurement accuracy is determined by the value (magnitude) of the entropy measurement error, calculated by the formula [8]:

$$\Delta = K \cdot \sigma = \frac{d}{2} \cdot \frac{n}{10^n \cdot \sum_{i=1}^m n_i \cdot \ln n_i}, \quad (7)$$

where  $K$  – is the entropy coefficient depending on the type of error distribution law;

$\sigma$  – root mean square value of measurement error deviation,  $\mu\text{m}$ ;

$d$  – width of the local interval of the distribution histogram,  $\mu\text{m}$ ;

$n$  – number of measurements;

$n_i$  – number of measurements in the  $i$ -th column;

$m$  – number of columns of the distribution histogram.

For the developed device, the value of the entropy measurement error was:

$$\Delta = \frac{30}{2 \cdot 10^{30} \sum (2 \cdot 1,4313 + 5,9157 + 7,2248 + 8,5878)} = \frac{15}{10^{0,819}} = \frac{15}{6,7} = 2,24 \text{ MKM}$$

$$K = \frac{\Delta}{\sigma_{30}} = \frac{2,24}{1,16} = 1,93$$

## Conclusions

Based on the research carried out on the wear of the cutting surfaces of cutter inserts in road milling machines, the following conclusions can be drawn:

1) measurement of selected wear elements of the cutting surfaces of cutting inserts can be carried out with sufficient accuracy to solve practical problems;

2) the accuracy of measuring wear elements of the cutting surfaces of cutting inserts using the developed device, determined by the value of the entropy measurement error, is higher than the accuracy of measuring the same wear elements using known devices;

3) reduction of noise content in the general flow of measurement information was achieved due to the simplicity of the design and the absence of destabilizing complex-profile and kinematically dependent mechanisms and assemblies;

4) according to the results of the study, all certified cutting inserts are classified as suitable, repairable and not subject to restoration with the consumption of a minimum amount of additional material to create a restored wear-resistant coating using technological methods of surfacing on repairable cutting inserts.

## References

- [1] Guide to Wirtgen cold milling machines. /[https://media.wirtgen-droup.com/media/02\\_wirtgen/media\\_1/\\_archiv\\_zu\\_loeschen/cold\\_milling/kaltfrsenhandbuch\\_technologieundanwendung/BR\\_Manual-cold-milling-machines\\_RU.pdf/](https://media.wirtgen-droup.com/media/02_wirtgen/media_1/_archiv_zu_loeschen/cold_milling/kaltfrsenhandbuch_technologieundanwendung/BR_Manual-cold-milling-machines_RU.pdf/).
- [2] Perelygin V. Carbide tools for cold milling cutters. /<https://os1.ru/article/6613-tverdosplavniy-instrument-dlya-holodnyh-frez/>.
- [3] Kini, C., Sharma, N., Shenoy B., S., Fluid Structure Interaction Study of High Pressure Stage Gas Turbine Blade Having Grooved Cooling Channels, (2017) International Review of Mechanical Engineering (IREME), 11 (11), pp. 825-830. doi: <http://dx.doi.org/10.15866/ireme.v11i11.12465>
- [4] Popov S.N., Antonyuk D.A. Optimization of the service life of road milling cutters based on technologies for preliminary and restorative wear resistance of surfacing // New materials and technologies in metallurgy and machinery. – 2007.-№1.-P.69-77.
- [5] Popov S.N., Antonyuk D.A. Study of the influence of external wear conditions on the wear resistance of road milling cutters. //New materials and technologies in metallurgy and mechanical engineering. – 2008.-№1.-P.25-29.
- [6] Shah, A., Gurav, S., Joshi, S., Fatigue Life Prediction of Steering Axle for Heavy Duty Truck Under Variable Amplitude Loading, (2017) International Review of Mechanical Engineering (IREME), 11 (7), pp. 499-504.
- [7] And yet they spin! Mounted road milling machines for pothole repair. /<https://os1.ru/article/4255-navesnyedorojnye-frezy-dlya-yamochnogo-remonta-i-vse-taki-oni-krutyatsya/>.
- [8] Application for assumptions. image No. 2020/0745.1. Device for measuring wear of replaceable rotary cutting inserts of milling drums / Kadyrov Zh.N., Isabek Z.R., dated 10.26.2020
- [9]. GOST 8.207-76. Direct measurements with multiple observations. Methods for processing observation results.
- [10] GOST 8.011-72. Indicators of measurement accuracy and forms of presentation of measurement results
- [11] Novitsky P.V. Fundamentals of information theory of measuring devices. – L.: Energy, Leningrad department, 1968. – 248 p.

[12] Rabinovich S.G. Measurement errors. – L.: Energy, Leningrad department, 1978. – 262 p.

[13] Nurzhanova O., Zharkevich O., Berg A., Zhukova A., Mussayev M, Buzauova T., Abdugaliyeva G., Shakhmatova A. Evaluation of the Structural Strength of a Prefabricated Milling Cutter with Replaceable inserts During Machining // Material and Mechanical Engineering Technology, 2023, №4. – P.10-18.

**Information of the authors**

**Issabek Zarina Ramazanovna**, PhD, Toraighyrov University

e-mail: [zarinachina@mail.ru](mailto:zarinachina@mail.ru)

**Kadyrov Zhannat Nurgalieovich**, d.t. s., professor, Office of the patent attorney «Kadyrov and Partners»

e-mail: [kadyrov.1954@mail.ru](mailto:kadyrov.1954@mail.ru)

**Kassenov Assylbek Zhumabekovich**, c.t.s, associate professor, Toraighyrov University

e-mail: [assylbek\\_kasenov@mail.ru](mailto:assylbek_kasenov@mail.ru)

**Mussina Zhanara Kereyovna**, c.t.s., associate professor, Toraighyrov University

e-mail: [mussina\\_zhanara@mail.ru](mailto:mussina_zhanara@mail.ru)

**Tussupova Sayagul Oralovna**, PhD, Toraighyrov University

e-mail: [suleeva.s@inbox.ru](mailto:suleeva.s@inbox.ru)



## Additive Optimization Method for Choosing CNC Machines for Technological Preparation of Machine-Building Production

Zhetessova G.S.<sup>1</sup>, Zharkevich O.M.<sup>1\*</sup>, Shakhatova A.T.<sup>1</sup>, Khrustaleva I.N.<sup>2</sup>, Shkodyrev V.P.<sup>2</sup>

Abylkas Saginov Karaganda Technical University, Karaganda, Kazakhstan

Peter the Great St. Petersburg Polytechnic University, St. Petersburg, Russia

\* corresponding author

**Abstract.** The introduction of Industry 4.0 into the technological preparation of production leads to the optimization of processes, including the processes of selecting equipment and tools, reducing cycle time, and reducing costs. Technological preparation of production involves a set of works that make it possible to start manufacturing a new product in a given volume. Features of technological preparation of production when using CNC machines follow from the fact that a significant part of the work from the sphere of direct production is transferred to the area of its technological preparation. Technological preparation of production plays an important role in the successful functioning of a machine-building enterprise. Optimization of equipment selection allows you to increase productivity, reduce costs and improve product quality. The use of modern optimization methods and information technology allows you to make this process more efficient and accurate. The article provides a methodology for calculating the additive criterion for optimizing the selection of the best option for CNC machines.

**Keywords:** CNC machines, industry 4.0, mechanical engineering, mathematical model, production optimization.

### Introduction

The selection of CNC machines is one of the key stages of technological preparation of mechanical engineering production [1]. The efficiency of production, product quality and competitiveness of the enterprise depend on the correctness of this choice [2]. Traditionally, various expert methods and software products based on a comparative analysis of the technical characteristics of the machines were used to solve this problem [3]. CNC machines are capable of performing operations with high accuracy and repeatability, which is especially important in the production of parts with complex geometry and high requirements for surface quality [4]. Automation of processes for processing parts on CNC machines can significantly reduce production time and increase the volume of manufactured products. The ability to quickly reconfigure machines for the production of new products ensures high flexibility of production and allows you to quickly respond to changes in the market situation [5]. Automation of manual operations leads to a decrease in labor costs and an increase in productivity. CNC machines allow you to obtain products with higher surface quality and dimensional accuracy, which reduces the amount of defects and increases the competitiveness of products. Due to the high accuracy of CNC machine processing, the amount of material waste is reduced. CNC machines allow processing parts with complex geometry, which are impossible to manufacture on universal machines [6].

Selecting the best option under a variety of conditions is a problem of multi-criteria optimization under conditions of complete certainty [7]. Mathematical models describing the systems under study can be presented in the form of tables containing the values of individual criteria for various strategies under strictly defined external conditions [8]. In such a situation, a decision can be made either based on one most significant criterion, or taking into account a set of several criteria [9].

One of the approaches to solving multi-criteria control problems is associated with the procedure for forming a generalized function  $F_i$ , monotonically dependent on a number of criteria [10]. This procedure is called the procedure (method) of criteria folding [11]. There are several folding methods, but the most commonly used is the additive optimization method [12].

The additive optimization method allows, when selecting CNC machines during the technological preparation of mechanical engineering production:

- to take into account a wide range of factors influencing the choice of machines;
- minimizes the subjectivity of decision-making;
- can be adapted to various production conditions and product ranges;
- allows finding the optimal solution in the shortest possible time.

The purpose of the article is to select the best five-axis CNC machine based on the criteria of performance, cost, memory capacity, reliability and using the additive optimization method.

### 1. Research Methodology

The additive optimization criterion (generalized objective function) is determined by the formula [13]:

$$F_i(\alpha_{ij}) = \sum_{j=1}^n \partial_i \alpha_{ij} \quad (1)$$

where  $\partial_i$  – weight coefficient;

$\alpha_{ij}$  – private criteria.

The values  $\delta_i$  are weighting coefficients that quantify the degree of preference of the  $i$ -th criterion over other criteria. In other words, the coefficients  $\delta_i$  determine the importance of the  $i$ -th optimality criterion. In this case, the more important criterion is assigned a higher weight, and the total importance of all criteria is equal to one, i.e. [14]:

$$\sum_{i=1}^n \delta_i = 1, \delta \geq 0, i = \overline{1, n}$$

The generalized objective function (1) can be used to convolve private optimality criteria if [15]:

- private (local) criteria have equal quantitative importance, i.e., each of them can be assigned to some number  $\delta_i$ , which numerically characterizes its importance with respect to other criteria;
- private criteria are homogeneous (have the same dimensionality).

In this case, the application of the additive optimality criterion is valid for solving the multicriteria optimization problem. If the given local criteria are not homogeneous, i.e., they have different units of dimension, in this case, the application of the additive optimality criterion is valid.

have different units of dimensionality, in this case normalization of criteria is required.

Criterion normalization means such a sequence of procedures, by means of which all criteria are brought to a single, dimensionless scale of measurement.

For normalization it is necessary to determine the maximum and minimum of each local criterion, i.e.:

$$\alpha_j^+ = \max \alpha_{ij}, i = \overline{1, m},$$

$$\alpha_j^- = \min \alpha_{ij}, i = \overline{1, m}.$$

We distinguish a group of criteria  $\alpha_j, j = \overline{1, 1}$ , which are maximized when solving the problem, and a group of criteria  $\alpha_j, j = \overline{1+1, n}$ , which are minimized when solving the problem. Then, in accordance with the principle of maximum efficiency, the normalized criteria are determined from the following relations:

$$\widehat{\alpha}_{1j} = \frac{\alpha_{ij}}{\alpha_j^+}, j = \overline{1, 1},$$

$$\widehat{\alpha}_{1j} = 1 - \frac{\alpha_{ij}}{\alpha_j^+}, j = \overline{1+1, n},$$

$$\widehat{\alpha}_{1j} = \frac{\alpha_{ij} - \alpha_j^-}{\alpha_j^+}, j = \overline{1, 1},$$

$$\widehat{\alpha}_{1j} = \frac{\alpha_j^+ - \alpha_{ij}}{\alpha_j^+ - \alpha_j^-}, j = \overline{1+1, n}.$$

The optimal option (strategy) is the one that maximizes the value of the objective function (1):

$$F_i = \sum_{j=1}^n \delta_j \cdot \widehat{\alpha}_{1j}, j = \overline{1, m} \quad (2)$$

According to the principle of minimum loss, the normalized criteria are determined from the relation:

$$\widehat{\alpha}_{1j} = 1 - \frac{\alpha_{ij}}{\alpha_j^+}, j = \overline{1, t},$$

$$\widehat{\alpha}_{1j} = \frac{\alpha_{ij}}{\alpha_j^+}, j = \overline{t+1, n},$$

$$\widehat{\alpha}_{1j} = \frac{\alpha_j^+ - \alpha_{ij}}{\alpha_j^+ - \alpha_j^-}, j = \overline{1, t},$$

$$\widehat{\alpha}_{1j} = \frac{\alpha_{ij} - \alpha_j^-}{\alpha_j^+ - \alpha_j^-}, j = \overline{t+1, n}.$$

In this case, the optimal option (strategy) will be the one that provides the minimum value of the objective function (2).

The considered approach to solving multicriteria problems is often used in solving technical and economic problems related to technological preparation of production

**2. Results and discussion**

Suppose that in the conditions of a machine-building enterprise engaged in manufacturing of complex-shaped parts, it is required to choose an optimal strategy for providing new production with five-axis CNC machines. The following equipment was chosen as analogs:

- NL635T (SL6315T) CNC turning machining center, SOLEX, China (equipment 1);
- CNC turning machining center LT 30/1000, Ace Micromatic, Germany (equipment 2);
- turning machining center with CNC VR 8, HAAS, USA (equipment 3);
- CNC turning machining centers TAKISAWA EX, Japan (equipment 4).

With the help of statistical data and information of the relevant manufacturing plants having such equipment, local criteria for the functioning of the required equipment were determined.

By means of experimental observations, the values of private criteria of functioning of the corresponding equipment ( $\alpha_{ij}$ ) were determined, which are shown in Table 1.

The data for choosing the optimal strategy are considered under conditions of full certainty.

**Table 1.** Partial criteria of CNC machine tool utilization efficiency

Equipment options (solution strategies)	Partial criteria of equipment efficiency			
	Performance, f.u	Cost of equipment, f.u	Memory capacity, c.u.	Reliability, c.u
Equipment 1 ( $X_1$ )	$\alpha_{11} = 100$	$\alpha_{12} = 5$	$\alpha_{13} = 5$	$\alpha_{14} = 8$
Equipment 2 ( $X_2$ )	$\alpha_{21} = 150$	$\alpha_{22} = 6$	$\alpha_{23} = 8$	$\alpha_{24} = 5$
Equipment 3 ( $X_3$ )	$\alpha_{31} = 120$	$\alpha_{32} = 4$	$\alpha_{33} = 7$	$\alpha_{34} = 6$
Equipment 4 ( $X_4$ )	$\alpha_{41} = 200$	$\alpha_{42} = 7$	$\alpha_{43} = 6$	$\alpha_{44} = 4$

Note: f.u. – fraction of units; c.u. – conventional units

The weighting coefficients of private criteria were also determined on the basis of expert assessments  $\partial_i, i = \overline{1, n}$ :

$$\partial_1 = 0,25; \partial_2 = 0,2; \partial_3 = 0,32; \partial_4 = 0,23.$$

Obviously, the choice of the optimal strategy (equipment variant) by one criterion in the task is not difficult. For example, if we evaluate the equipment by reliability, the best is equipment 1 (strategy  $X_1$ ).

If it is necessary to choose the optimal equipment variant by two homogeneous local criteria:

- productivity (f.u.);
- equipment cost (f.u.).

Let the weight coefficients of these two partial criteria have been determined on the basis of expert evaluations:  $\partial_1 = 0.665, \partial_2 = 0.335$ . Let us calculate the additive optimality criterion for the three variants:

$$F_i(\alpha_{1j}) = \partial_1\alpha_{11} + \partial_2\alpha_{12} = 0,665 \cdot 100 + 0,335 \cdot 5 = 68,175$$

$$F_i(\alpha_{2j}) = \partial_1\alpha_{21} + \partial_2\alpha_{22} = 0,665 \cdot 150 + 0,335 \cdot 6 = 103,09$$

$$F_i(\alpha_{3j}) = \partial_1\alpha_{31} + \partial_2\alpha_{32} = 0,665 \cdot 120 + 0,335 \cdot 4 = 81,15$$

$$F_i(\alpha_{4j}) = \partial_1\alpha_{41} + \partial_2\alpha_{42} = 0,665 \cdot 200 + 0,335 \cdot 7 = 135,345$$

Obviously, the fourth variant of equipment according to the two private cost criteria will be optimal, since  $F_{max} = F_4(\alpha_{ij}) = 135.345$ .

In the problem under consideration, the four local criteria are not homogeneous, that is, they have different units of measurement.

In this case, it is necessary to determine the optimal strategy of equipment selection from four possible ( $m = 3$ ) taking into account the four local criteria ( $n = 4$ ).

The evaluation of the choice of the optimal variant is carried out according to the algorithm (Figure 1).

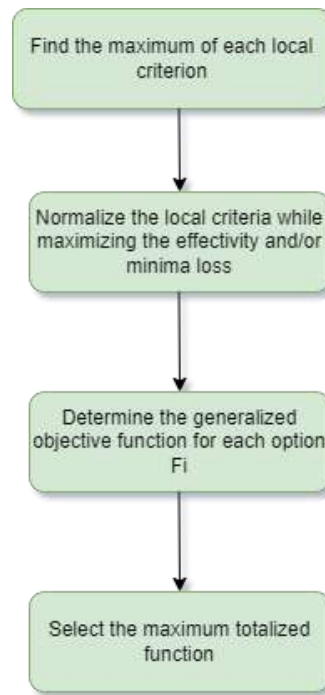


Fig. 1. - Selection of the optimal option based on the additive criterion

1. Determine the maximum of each local criterion:

$$\partial_1^+ = 200; \partial_2^+ = 7; \partial_3^+ = 8; \partial_4^+ = 8$$

2. When solving the problem, the first criterion (productivity), the third criterion (memory capacity) and the fourth criterion (reliability) are maximized. The second criterion (equipment cost) is minimized.

3. Based on the principle of efficiency maximization, we normalize the criteria:

Productivity

$$\widehat{\alpha}_{i1} = \frac{\alpha_{i1}}{\alpha_1^+}$$

$$\widehat{\alpha}_{11} = \frac{\alpha_{11}}{\alpha_1^+} = \frac{100}{200} = 0,5$$

$$\widehat{\alpha}_{21} = \frac{\alpha_{21}}{\alpha_1^+} = \frac{150}{200} = 0,75$$

$$\widehat{\alpha}_{31} = \frac{\alpha_{31}}{\alpha_1^+} = \frac{120}{200} = 0,6$$

$$\widehat{\alpha}_{41} = \frac{\alpha_{41}}{\alpha_1^+} = \frac{200}{200} = 1$$

Memory capacity

$$\widehat{\alpha}_{i3} = \frac{\alpha_{i3}}{\alpha_3^+}$$

$$\widehat{\alpha}_{13} = \frac{\alpha_{13}}{\alpha_3^+} = \frac{5}{8} = 0,625$$

$$\widehat{\alpha}_{23} = \frac{\alpha_{23}}{\alpha_3^+} = \frac{8}{8} = 1$$

$$\widehat{\alpha}_{33} = \frac{\alpha_{33}}{\alpha_3^+} = \frac{8}{8} = 0,875$$

$$\widehat{\alpha}_{43} = \frac{\alpha_{43}}{\alpha_3^+} = \frac{6}{8} = 0,75$$

Reliability

$$\widehat{\alpha}_{i4} = \frac{\alpha_{i4}}{\alpha_4^+}$$

$$\widehat{\alpha}_{14} = \frac{\alpha_{14}}{\alpha_4^+} = \frac{8}{8} = 1$$

$$\widehat{\alpha}_{24} = \frac{\alpha_{24}}{\alpha_4^+} = \frac{5}{8} = 0,625$$

$$\widehat{\alpha}_{34} = \frac{\alpha_{34}}{\alpha_4^+} = \frac{6}{8} = 0,75$$

$$\widehat{\alpha}_{44} = \frac{\alpha_{44}}{\alpha_4^+} = \frac{4}{8} = 0,5$$

4. Based on the minimum loss, we normalize the Equipment cost criterion:

$$\widehat{\alpha}_{i2} = 1 - \frac{\alpha_{i2}}{\alpha_2^+}$$

$$\widehat{\alpha}_{12} = 1 - \frac{\alpha_{12}}{\alpha_2^+} = 1 - \frac{5}{7} = 0,285$$

$$\widehat{\alpha}_{22} = \frac{\alpha_{22}}{\alpha_2^+} = 1 - \frac{6}{7} = 0,142$$

$$\widehat{\alpha}_{32} = \frac{\alpha_{32}}{\alpha_2^+} = \frac{4}{7} = 0,428$$

$$\widehat{\alpha}_{42} = \frac{\alpha_{42}}{\alpha_2^+} = 1 - \frac{7}{7} = 0$$

5. Determine the generalized objective function by formula (1) for each equipment selection variant:

$$F_1 = 0,25 \cdot 0,5 + 0,2 \cdot 0,285 + 0,32 \cdot 0,625 + 0,23 \cdot 1 = 0,612$$

$$F_2 = 0,25 \cdot 0,75 + 0,2 \cdot 0,142 + 0,32 \cdot 0,428 + 0,23 \cdot 0 = 0,3538$$

$$F_3 = 0,25 \cdot 0,625 + 0,2 \cdot 1 + 0,32 \cdot 0,875 + 0,23 \cdot 0,75 = 0,8085$$

$$F_4 = 0,25 \cdot 1 + 0,2 \cdot 0,625 + 0,32 \cdot 0,75 + 0,23 \cdot 0,5 = 0,6625$$

Thus it is necessary to choose equipment 3 (turning machining center with CNC VR 8, HAAS, USA), since  $F_{\max} = 0,8085$ .

In the technological preparation of production of machine-building enterprise methods as optimization methods can also be applied ideal point method, the method of the main criterion, the method of hierarchy analysis, the Pareto method and others.

These methods can be used when working with large data on processes, equipment and tools that ensure the readiness of the enterprise to produce products of the required quality at the established time, output volume and costs.

When working with a large number of criteria in selecting the optimal solution (strategy) it is possible to use specialized software packages for optimization: MATLAB, GAMS, Python with libraries, R, CPLEX, GUROBI and others.

### Conclusions

1) The additive optimization method is a powerful tool for the selection of CNC machines in the technological preparation of machine-building production. It allows to make informed decisions, increase production efficiency and reduce costs.

2) The additive optimization method is used when it is necessary to consider several contradictory criteria when selecting equipment.

3) The limitation of the research of the article is the conditions of complete certainty. They assume that all parameters of the problem are exactly known. That is, the values of all coefficients, constraints and target functions are known exactly. However, in real optimization problems it is possible to encounter uncertainty conditions. In this case, such a problem should be solved using stochastic programming, robust optimization and multi-criteria optimization with uncertainty.

### Acknowledgements

This research is funded by the Committee of Science of the Ministry of Science and Higher Education of the Republic of Kazakhstan (grant under the theme IRN AP23490796 “Development of digital models of the production process based on multi-criteria analysis of BigData management within the framework of technological preparation of production of machine-building enterprises” (2024 - 2026).

### References:

- [1] Zhetessova G., Yurchenko V., Nikonova T., Zharkevich O. The development of the computer-aided design system for production processes of component part machining for single-piece production and repair conditions //Journal of Applied Engineering Science, 2019, 17(4), P. 599–609
- [2] Berg A.S., Nurzhanova O.A., Vytaitas T., Berg A.A., Vitushenko D.V. Improvement of Base Sets for Complex Configuration Parts when Assessing their Manufacturability within Industry 4.0 //Material and Mechanical Engineering Technology, №2, 2024. – P.25 - 35
- [3] Casal-Guisande M., Comesaña-Campos A., Pereira A., Bouza-Rodríguez J.-B., Cerqueiro-Pequeno J. A Decision-Making Methodology Based on Expert Systems Applied to Machining Tools Condition Monitoring. //Mathematics 2022, 10, 520.
- [4] Soori M., Joughb F.K.G., Dastres R., Arezoo B. Sustainable CNC machining operations, a review Sustainable Operations and Computers //Sustainable Operations and Computers, Volume 5, 2024, P. 73-87
- [5] Thapaliya S., Valilai O.F., Wicaksono H. Power Consumption and Processing Time Estimation of CNC Machines Using Explainable Artificial Intelligence (XAI) //Procedia Computer Science 232, 2024, P. 861–870
- [6] Hou J., Liu H., Zhou H., Wang Yu. A new linear measurement method for the geometric error of CNC machine tools - Normal measurement method //Measurement, Volume 222, 2023, 113610
- [7] Statnikov R., Matusov J., Statnikov A. Multicriteria Engineering Optimization Problems: Statement, Solution and Applications //Journal of Optimization Theory and Applications, 155(2), 2012. – P. Volume 155, Issue 2. - P. 355 - 375
- [8] Dodgson J.S., Spackman M., Pearman A.D., Lawrence D. Ph. Multi-Criteria Analysis: A Manual. – London: OAI, 2009. – 168 p.

- [9] Zharkevich O., Nikonova T., Gierz Ł., Berg A., Berg A., Zhunuspekov D., Warguła Ł., Łykowski W., Fryczyński K. Parametric Optimization of a New Gear Pump Casing Based on Weight Using a Finite Element Method" Applied Sciences 13, no. 22, 2023,12154
- [10] Odu G. O., Charles-Owaba O. E. Review of Multi-criteria Optimization Methods – Theory and Applications // IOSR Journal of Engineering (IOSRJEN), Vol. 3, Issue 1, 2013, P. 1-14
- [11] Dering C., König I.R., Ramsey L.B., Relling M.V., Yang W., Ziegler A. A comprehensive evaluation of collapsing methods using simulated and real data: excellent annotation of functionality and large sample sizes required // Front Genet. 2014; 5: 323.
- [12] Mikoni S.V. System Analysis of Multi-Criteria Optimization Methods on a Finite Set of Alternatives SPIIRAS Proceedings //SPIIRAS Proceedings, 2015, 4(41):180
- [13] Gilli M., Maringer D., Schumann E. Chapter 10 - Optimization problems in finance. Numerical Methods and Optimization in Finance (Second Edition). - NY: Academic Press, 2019. - P. 219-228
- [14] Yang Xin-She Chapter 14 - Multi-Objective Optimization, Nature-Inspired Optimization Algorithms, Elsevier, 2014, P. 197-211
- [15] Martínez-Frutos J., Ortigosa R. Robust topology optimization of continuum structures under uncertain partial collapses, Computers & Structures, Volume 257, 2021, 106677

#### **Information of the authors**

**Zhetessova Gulnara Santayevna**, d.t.s., professor, Abylkas Saginov Karaganda Technical University  
e-mail: [zhetessova@mail.ru](mailto:zhetessova@mail.ru)

**Zharkevich Olga Mikhailovna**, c.t.s., professor, Abylkas Saginov Karaganda Technical University  
e-mail: [zharkevich82@mail.ru](mailto:zharkevich82@mail.ru)

**Shakhatova Alia Talgatovna**, m.e.s., Abylkas Saginov Karaganda Technical University  
e-mail: [shakhatovaa@list.ru](mailto:shakhatovaa@list.ru)

**Khrustaleva Irina Nikolaevna**, c.t.s., docent, Peter the Great St. Petersburg Polytechnic University  
e-mail: [hkrustaleva\\_in@spbstu.ru](mailto:hkrustaleva_in@spbstu.ru)

**Shkodyrev Vyacheslav Petrovich**, d.t.s., professor, Peter the Great St. Petersburg Polytechnic University  
e-mail: [shkodyrev@spbstu](mailto:shkodyrev@spbstu)

## Predictive Control Systems of Product Quality

Makarov G.V.<sup>1</sup>, Kolchurina I.Yu.<sup>1\*</sup>, Kolchurina M.A.<sup>1</sup>, Plotnikova I.V.<sup>2</sup>, Moyzes B.B.<sup>3</sup>

<sup>1</sup>Siberian State Industrial University, Novokuznetsk, Russia

<sup>2</sup>National Research Tomsk Polytechnic University, Tomsk, Russia

<sup>3</sup>National Research Tomsk State University, Tomsk, Russia

\*corresponding author

**Abstract.** A natural stage in the development of automated systems is their digital transformation. This process is aimed at optimizing and improving production efficiency, one of the indicators of which is the stabilization and improvement of the quality of products while reducing losses. Advanced control Systems assume the presence of predictive models, but they often cannot or are not used in operational control tasks. These models are quite widely used in the petrochemical and mechanical engineering industries, a little less in the metallurgical industry, and are almost completely absent in the coal-processing industry. Thus, the development of structures and models suitable for predictive quality management is an urgent task. Models based on the full-scale model approach and multivariate structures have shown high efficiency in such tasks. An example of one of the possible integration structures of predictive product quality analysis models is given in this article.

**Keywords:** quality, predictive control systems, digital transformation

### Introduction

Forecasting the quality of products is always given considerable attention, because it is better to prevent a defect than to state it. GOST 15467-79 defines quality forecasting as "determining the likely values of product quality indicators that can be achieved by a given time or within a given time interval" [1]. Well-known methods of predicting quality include statistical methods, neural networks, digital twins. These methods have areas of their effective application and are relevant only in some cases, and each task requires a separate study and a heuristic solution.

One of the examples of predictive quality control [2], based on the methods of machine image processing, statistical estimates, cluster analysis of connected components, the results of metallographic studies, as well as estimates of the quality of workpieces, is intended for automated verification of the planned dynamics of changes and the formation of the necessary correction of key casting parameters. The proposed assistant performs the role of an adviser and a digital model for research and experiments, but is not tied into automatic process control.

The second example also based on machine learning methods, talks about the methodology for obtaining formal models linking bitumen quality indicators with technological parameters of their production, both for classical regression equations and for formal neural networks [3]. The authors indicate that the methodology for obtaining such models is worked out on abstract dependencies, however, in the automated process control system, the use of such dependencies is impossible in a direct form, since the existing control and regulation circuits constantly influence the processes and without eliminating their effects, obtaining any adequate model is impossible both by classical identification methods and statistical methods, since it is not possible to their prerequisites are fulfilled [4].

For processes that take place in complex chains of technological units that produce physico-chemical transformations [5-7], it is especially important to evaluate and predict the output quality after each of transformations, since even a small deviation, albeit within acceptable limits at the very beginning of the chain, can lead to a large deviation at the end, leading to defect. Thus, the task of predictive quality management of processes and products [8], based on quality forecasting, arises. An example of such processes is coal enrichment processes.

### 1 Theoretical Part

In the coal enrichment industry, there is a method of long-term forecasting of the quality (ash content) of coal products [9]. This technique is designed to determine the quantitative values of the ash content of coal extracted, processed at concentrating plants and shipped (according to various brands and grades) of production associations, mines (sections) and factories for up to 25 years. The methodology is based on the apparatus of mathematical statistics and the theory of random processes, which are not suitable for forecasting in control systems [10].

The use of predictive models in management tasks is not a new approach. The American researcher R. Kalman started development such systems in the early 1960s. Nowadays, such models based on physical, chemical or empirical dependencies are one of the main elements of advanced control systems – Advanced Process Control (APC) [11].

An example of an advanced process control system from T-Soft LLC is presented in the Figure 1.

In general, the management approach with predictive models is called as "MPC". The approach involves the use of a predictive model (PM) – an explicit model of the technological process as an element of the regulator in order to compensate for the dynamics of an open object and the description of the observed and unobservable

variables of the object, thereby improving the properties of a closed control system. Many well-known companies (Rockwell, Siemens, Emerson, Yokogawa/Shell, etc.) develop their MPC products, allowing them to be used both for their own equipment and for third-party equipment.

Most commercial products do not disclose the underlying principles of forecasting, and the inability to refine models and algorithms without the involvement of foreign specialists significantly limits the possibilities of their using.

Among the developments of scientists from Russia, the following examples of systems with predictive models can be distinguished – both physical [12, 13] and mathematical [14, 15]. In the mineral processing industry, an example can be given of a control system for the ore grinding complex with a ball mill [16].



Fig 1. – Interface of the advanced process control system

The author builds a predictive model based on a neural network that uses sensor data to indirectly control the overload of the mill with ore according to the calculated parameter of the mass of the material in the mill. In general, there are practically no competitive integrated products on the domestic market that implement the MPC approach, both for industry and for general industrial solutions.

By presenting such systems in the symbols of the theory of automatic control, in general, for a circuit consisting of a single unit and its inputs/outputs, the following SAR structure can be formed on the basis of a modified Smith SAR (figure 2). In figure 2  $Y^*$  denotes specified values of quality indicators;  $\varepsilon$  – deviation of the specified values of quality indicators from the predicted ones;  $\varepsilon^2$  – deviation taking into account the effect of regulation without taking into account the delay in the system;  $U$  – controlling influence;  $W$  – disturbances;  $Y$  – output quality indicators;  $Y^M$  – model values of quality indicators without taking into account disturbances;  $\delta U^M$  – deviation of quality indicators caused by disturbances;  $f^{QAS}$  – predictive quality analysis subsystem;  $\Omega$  – parameters required for forecasting;  $\varphi_\tau$ ,  $\varphi_0$  – lag and object models. In this case, the extrapolation operator is a quality prediction model for a certain contour of different nature and type.

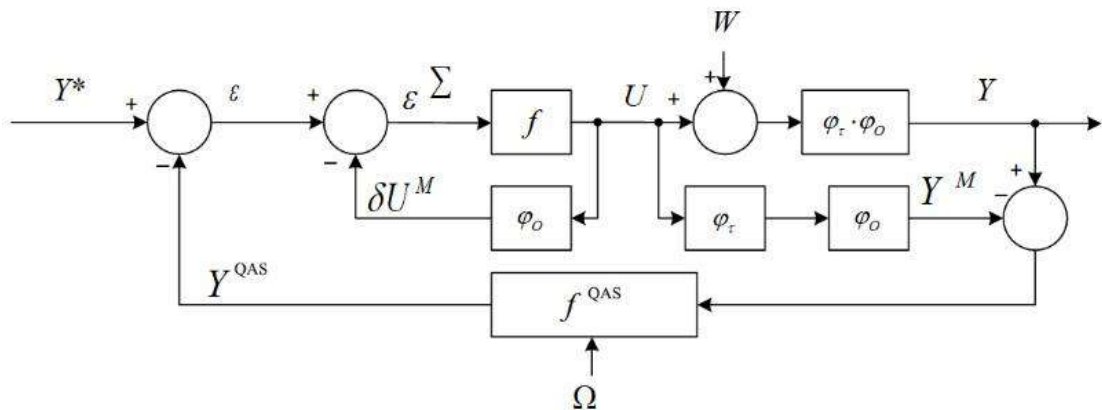


Fig 2. – SAR scheme with forecasting

Unlike the extrapolator in Smith's SAR, any predictive quality analysis system can be used for forecasting. It can rely on various models, methods and algorithms, and as input data it accepts not only the values of deviations of the actual output variable from the model, but also additional parameters that are somehow tied in forecasting: variables of the object and the system as a whole; inputs and outputs; system parameters that are not tied explicitly in regulation, but having an impact on quality; the properties of the input material obtained from the data of regulatory maps and/or laboratory analyses; various datasets, if the trained neural network is the basis for forecasting; etc.



To form model values of quality indicators, normative quality models can be taken as a mathematical model, obtained on the basis of "ideal" regime maps that do not take into account possible deviations in the initial quality of products and disturbances.

Integration of such predictive quality management subsystems is advisable to use both in digital adviser modes and to tie directly into automatic control and regulation if the system shows its high efficiency based on test results.

## 2 Experimental Part

In the existing control automation systems, the complexity of evaluating the effectiveness of predictive analytics systems lies in the fact that the built-in control circuits apply continuous control actions on the object to stabilize the quality. To assess the effectiveness in this case, you can use the methods of a full-scale model approach [17]. In this case, the use of the apparatus of recalculation models allows you to exclude the effects of control actions and adjust the system of predictive analysis on the object itself.

The full-scale mathematical approach for creating predictive models in control systems has proven its effectiveness and has developed historically in parallel with the MPC approach. The adaptation of its methods and algorithms for quality management is a strong alternative to systems of well-known manufacturers, since they are not rigidly tied to computer technology and can be embedded both at the level of workstations and in programmable logic controllers, which solves the problems of synchronization in time and sampling step, as well as integration with the domestic software and hardware complex automated control system.

If there are several predictive quality analytics systems, the effectiveness of each of them may depend on the situation and production conditions, then it is difficult to choose one of them as a predictor. The implementation of the multivariate mode [18] allows to choose the most effective system at the moment and implement management based on its results.

The introduction of advanced control systems has become widespread in such industries as petrochemical, machine-building. Slightly less common, but they are in demand in the metallurgy industry. The coal-processing industry often surpasses those mentioned above in terms of automation [19], however, the introduction of APC technologies is extremely rare, and at the moment it is also difficult, since few domestic manufacturers offer "boxed" solutions in this direction, and in the coal industry there are none at all.

A typical circuit for which such a system may be relevant is the enrichment of coal in a heavy-medium separator. The scheme of the section of the technological chain is shown in Figure 3. Control of this circuit is carried out by changing the density of the heavy medium by diluting the valve on water or increasing it by feeding fresh magnetite suspension.

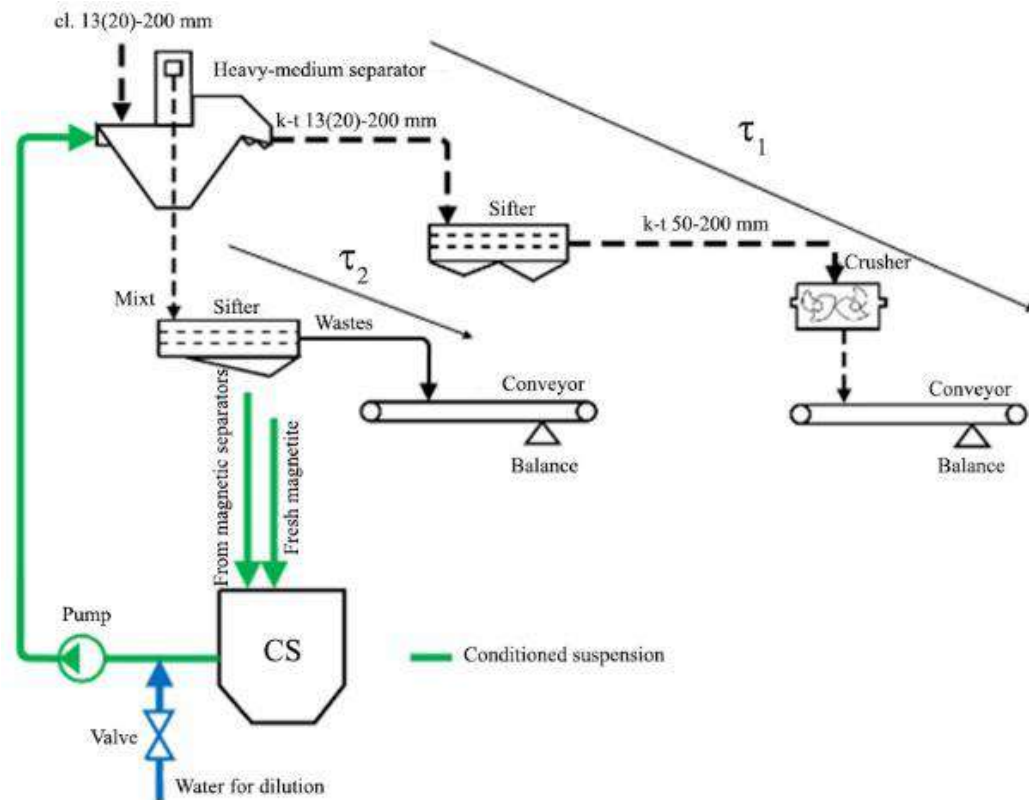


Fig 3. – Simplified diagram of a section of the technological chain of coal enrichment in a heavy-medium separator

As a rule, it is not accepted to equip such contours with in-line ash and moisture meters. Laboratory tests are spot-based and the delay in them can range from half an hour to several hours. It is advisable to apply an indirect assessment of the enrichment process according to the available data:

- grade and available characteristics of the formation;
- the actual value of the density of the heavy medium from the density meter;
- actual indications of coal and rock separation by conveyor scales.

The application of classical approaches to process management in this case is not effective, since the delay in the evaluation channels ( $\tau_1$  and  $\tau_2$ ) is better than the dynamics of the process. In this case, it is possible to make a model of indirect estimation and forecasting of coal quality based on the difference between the expected (normative) separation of ordinary coal from the actual one. In this case, it would be advisable to use systems with predictive models, as, for example, in figure 3.

The development of the direction of predictive quality control of coal will increase the economic efficiency of production, solving the problem of "pumping" (associated with excessive costs and wear of equipment) and defects (associated with penalties). Improving the quality of coking coal grades is a necessary condition for the development and activation of the metallurgical industry, which is necessary for the development, in turn, of the machine-building industry.

### 3 Predictive control of coal preparation

The achievable quality of coal preparation is initially determined at the stage of process chain design, when enlarged enrichment blocks are defined: enrichment with heavy media in separators and hydro cyclones, in spiral separators, in flotation machines, etc. The chains are designed flexible and switchable so that, depending on the characteristics of the input raw materials, it is possible to obtain the specified quality due to combination and sequential inclusion of units and processing units to obtain the required enrichment depth. These chains are designed to be flexible and switchable so that, depending on the characteristics of the incoming raw material, a given quality can be obtained by combining and sequentially switching on units and stages to obtain the desired depth of enrichment. In such an environment of constant switching, which is often dynamic, it is virtually impossible to build adequate enrichment models based on physicochemical patterns suitable for prediction.

In order to solve the problem of quality management, the technologists use the results of laboratory studies that combine particle size distribution and fractional analysis. So called "sieve-fractional" analysis allows to construct coal enrichment curves for each separate class in the heavy medium density grid. In this way it is possible to determine the required structure of the process chain for a given enrichment and density settings for each circuit.

An example of enrichment curves of coal grade "Zh" for +13 mm class is presented in Figure 4. The shape of the curves is rather heterogeneous and does not allow approximating the curve with acceptable accuracy. This is caused by measurement errors, heterogeneity of sampling for analysis, non-stationarity of characteristics of one and the same grade and other reasons. To construct a more accurate enrichment curve, many laboratory statistics are required to eliminate errors and minimize them to construct an adequate approximating curve.

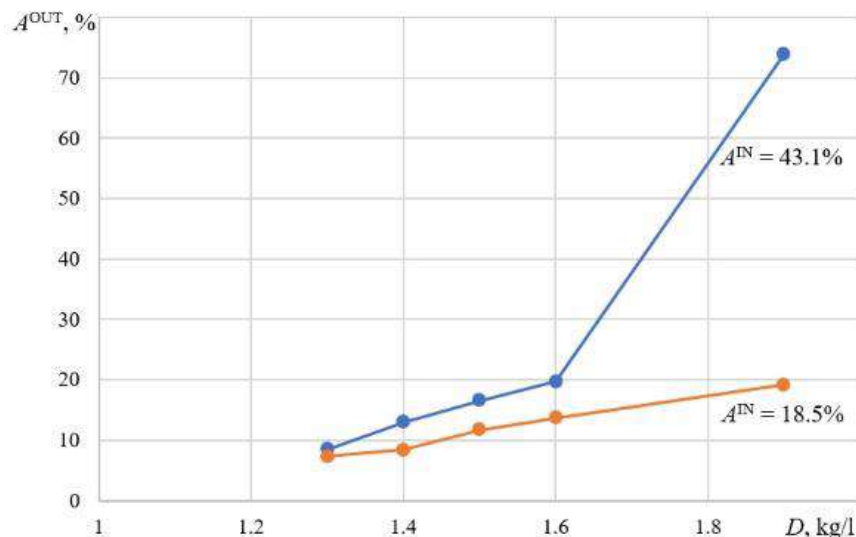


Fig 4. – Examples of enrichment curves

A large volume of laboratory studies allowed us to construct sufficiently accurate realizations of enrichment curves in the form of exponents with the following mathematical description:

$$A^{OUT} = a \cdot e^{b \cdot D}, \quad (1)$$

where  $A^{\text{OUT}}$  is the output ash content;  $D$  is the density;  $a$ ,  $b$  are curve parameters.

To find the coefficients  $a$  and  $b$ , we apply the Nelder-Mead method of search optimization by mean-modulus deviation.

Based on this expression, we obtain the solution of the equation with respect to  $D$ :

$$D^* = \frac{\ln\left(\frac{A^{\text{OUT}*}}{a}\right)}{b},$$

where  $A^{\text{OUT}*}$  is the specified ash content;  $D^*$  is the required density specification.

The curve of a given input ash content is determined by interpolation between neighboring curves and further approximation by expression (1). Figure 5 shows the curve for coal with input ash content of 25%. Set ash content  $A^{\text{OUT}*} = 17\%$ , the found set density is  $D^* = 1.63 \text{ kg/l}$ .

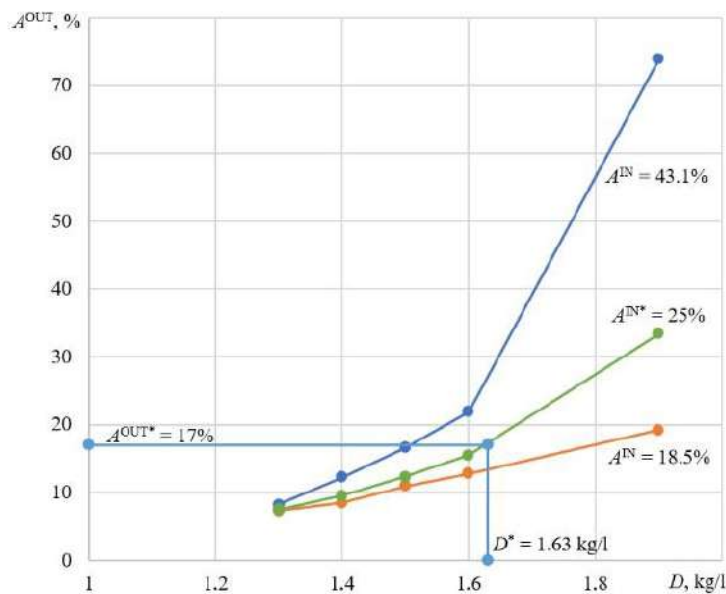


Fig 5. – Enrichment curves and set parameters

The proposed system works as a digital tipster in the beneficiation plant in semi-automatic mode. The technologist sets the setpoint parameters and decides whether to accept the results of the tipster or set his own. The setpoint is then transmitted by the control system to the magnetite slurry density control loop, which begins to maintain the new level.

At present, most production facilities can realize such systems only in the form of semi-automatic digital advisors. For full realization in the form of automatic predictive control systems, a serious digital transformation of all systems is required – process control systems, laboratories, warehouses, loading, etc. to integrate them into overall information space [20-23].

#### 4 Conclusion

Summarizing, it is worth noting that the model of indirect assessment and forecasting of coal quality presented in the work, based on the assessment of the difference between the expected (normative) separation of ordinary coal from the actual, allows for more effective management of the quality of finished products, which further contributes to improving the position of the organization in the market and the development of the economy as a whole. In the future, the model should be improved to reduce the probability of errors.

#### References

- [1] GOST 15467-79. Product-quality control. Basic concepts. Terms and definitions.
- [2] Goryainov S., Krasilnikov A. Predictive assistant for quality control for the casting machine. In Foundry and metallurgy // 25th International Scientific and Technical Conference, BNTU, 2017. – P. 1-14.
- [3] Stashkov S.I., Shumikhin A.G., Sokolchik P.Yu., Shirkunov A.S., Yurkov D.A. Bitumen quality forecasting and management based on formal models // Engineering Bulletin of the Don, 2019. – P. 1-15.
- [4] Emelyanov S.V., Korovin S.K., Rykov A.S. – Kemerovo: Kuzbassvuzizdat Publ., 2007. – 307 p.
- [5] Surzhikov A.P., Lysenko E.N., Malyshev A.V., Vlasov V.A., Suslyayev V. I., Zhuravlev V.A., Korovin E.Y., Dotsenko O.A. Study of the Radio-Wave Absorbing Properties of a Lithium-Zinc Ferrite Based Composite // Russian Physics Journal, 2014, Vol. 57(5), P. 621-626 (2014). doi: 10.1007/s11182-014-0284-9.

- [6] Lysenko E.N., Surzhikov A.P., Vlasov V.A., Malyshev A.V., Nikolaev E.V. Thermal analysis study of solid-phase synthesis of zinc- and titanium-substituted lithium ferrites from mechanically activated reagents // Journal of Thermal Analysis and Calorimetry, 2015, Vol. 122. – P. 1347-1353. doi: 10.1007/s10973-015-4849-9.
- [7] Surzhikov A.P., Ghyngazov S.A., Frangulyan, T.S., Vasil'ev, I.P., Chernyavskii, A.V. Investigation of sintering behavior of ZrO<sub>2</sub> (Y) ceramic green body by means of non-isothermal dilatometry and thermokinetic analysis // Journal of Thermal Analysis and Calorimetry, 2017, Vol. 128, no 2. – P. 787-794. doi: 10.1007/s10973-016-5966-9.
- [8] Plotnikova I., Vedyashkin M., Mustafina R., Plotnikov I., Tchaikovskaya O., Bastida J., Verpeta M. Optimization of the Stabilization System for Electromagnetic Suspension in Active Vibration Isolation Devices // MATEC Web of Conferences, 2016, Vol. 79. – 01019. <https://doi.org/10.1051/mateconf/20167901019>.
- [9] Ministry of Coal Industry of the USSR. Methodology of long-term forecasting of the quality (ash content) of coal products. – M№: TSNIEIugol, 1984. – 21 p.
- [10] Emelyanov S.V., Korovin S.K., Myshlyayev L.P. Theory and practice of prediction in control systems. – Kemerovo: Kuzbassizdat, 2008. – 259 p.
- [11] Amrit, R. Platform for Advanced Control and Estimation (PACE): Shell's and Yokogawa's Next Generation Advanced Process Control Technology // IFAC-PapersOnLine, 2015, Vol. 48, no 8. – P. 1-5
- [12] Krasovsky A.A. Optimal control by means of a physical predictive model // Automation and telemechanics. – Moscow, publishing house "Science", 2003. – 613 c.
- [13] Evtushenko V.F., Myshlyayev L.P., Makarov G.V. Adjustment of automatic control systems of production facilities at coal processing plants using multivariant physico-mathematical models // IOP Conference Series: Earth and Environmental Science, 2016. – Vol. 45. – P. 1-9 (012010)
- [14] Avdeev V.P. The restorative and predictive regulation of technological processes // News of higher educational institutions. – Ferrous metallurgy, publishing house of SMI. 1978
- [15] Gomboeva S.G., Shishkin I.F., Hamhanova D.N., Vasendina E.A., Plotnikova I.V., Efremova O.N. Sampling control planning on the base of operating characteristics and with a grapho-analytical method // Key Engineering Materials: Scientific Journal, 2016, Vol. 685. – P. 463-466. <http://dx.doi.org/10.4028/www.scientific.net/KEM.685.463>.
- [16] Zakamaldin A.A., Shilin A.A. Neural simulation of ball mill grinding process // IOP Conference Series: Materials Science and Engineering, Vol. 795. – 012010.
- [17] Yevtushenko V.F. The full-scale model approach and the theory of similarity in relation to control systems // Automation systems in education, science and production AS2019. – Novokuznetsk: publishing house of SibSIU, 2019. – P. 21-24.
- [18] Gulevich T.M. On multivariate tasks of engineering activity in the presence of a market of automation tools and systems // Management of large systems. – Moscow: IPU, 1997. – 432 p.
- [19] Makarov G.V., Myshlyayev L.P., Salamatin A.S., Vdovichenko V.V. Integration features of control systems in multicomplex distributed production // E3S Web of Conferences, 2021, Vol. 330. – 03002.
- [20] Geary Rob, Cosgrove John. Manufacturing Reliability and Cost Improvements through Data Analytics: An Industry Case Study // Procedia Computer Science, 2023, Vol. 217. – P. 395-402. doi: 10.1016/j.procs.2022.12.235.
- [21] Gavrilin A., Moyzes B., Kuvshinov K., Vedyashkin M., Surzhikova O. Determination of optimal milling modes by means of shock-vibration load reduction on tool and peak-factor equipment // Materials Science Forum, 2019, Vol. 942. – P. 87-96. doi: 10.4028/www.scientific.net/MSF.942.87.
- [22] Gavrilin A.N., Moyzes B.B., Kuvshinov K.A., Smyshlyayev A.S., Koksharova I. Using the Vibration Recorder Mobile Diagnostic Complex for Studying Vibration Processes // Material and Mechanical Engineering Technology, 2022, Vol. 3. – P. 50-57. doi: 10.52209/2706-977X\_2022\_3\_50
- [23] Sikhimbaev M.R., Sherov K.T., Zharkevich O.M., Sherov A.K., Tkachyova Y.O. Experimental studies of stabilization of boring cutter form - building top oscillation // Journal of Vibroengineering, 2012, Vol. 14, no 2. – P. 661-670

#### Information of the authors

**Makarov Georgy Valentinovich**, c.t.s., associate professor, Siberian State Industrial University  
e-mail: [gmakarov@nicsu.ru](mailto:gmakarov@nicsu.ru)

**Kolchurina Irina Yurievna**, c.t.s., director of the Institute of Advanced Engineering Technologies, Siberian State Industrial University  
e-mail: [ira-kolchurina@yandex.ru](mailto:ira-kolchurina@yandex.ru)

**Kolchurina Maria Andreevna**, graduate student, Siberian State Industrial University  
e-mail: [kolchurina.masha@yandex.ru](mailto:kolchurina.masha@yandex.ru)

**Plotnikova Inna Vasilevna**, c.t.s., associate professor, National Research Tomsk Polytechnic University  
e-mail: [inna@tpu.ru](mailto:inna@tpu.ru)

**Moyzes Boris Borisovich**, c.t.s., associate professor, National Research Tomsk State University  
e-mail: [mbb@tpu.ru](mailto:mbb@tpu.ru)

## Experimental Comparison of Methods for Cleaning Car Exhaust Gas by Exposure Using Ultrasound and Laser Radiation

Sarsembekov B.K.<sup>1</sup>, Kadyrov A.S.<sup>1</sup>, Kunayev V.A.<sup>2</sup>, Issabayev M.S.<sup>1</sup>, Kukeshva A.B.<sup>1\*</sup>

<sup>1</sup>Karaganda Technical University, Karaganda, 100027, Kazakhstan

<sup>2</sup> Karaganda Industrial University, Temirtau, 101400, Kazakhstan

\* corresponding author

**Abstract.** The article offers a comparison of the use of ultrasonic and laser exposure in a device for cleaning exhaust gases of internal combustion engines, in order to determine the most effective method to reduce their toxicity and improve the environmental safety of cities. The scheme of an experimental combined ultrasound-laser automobile muffler and the results of the experiment are presented, proving the possibility and effectiveness of using the process of ultrasonic coagulation of solid particles and photo-chemical reaction for cleaning exhaust gases of diesel cars. Dependences confirming the effectiveness of the ultrasound-laser car muffler were obtained. A comparison of methods for cleaning car exhaust gas by ultrasound, laser radiation and the combined effects of both methods is presented.

**Keywords:** car; internal combustion engine; ultrasonic cleaning; laser cleaning; car exhaust gases; coagulation.

### Introduction

Toxic emissions in modern mufflers are reduced by installing exhaust gas purification and neutralization systems that operate on vehicles; devices operating on absorption, thermocatalytic methods, and thermal afterburning have become widespread [1].

An increase in the concentration of exhaust gases leads to an increase in diseases of the cardiovascular system and lungs. Reducing harmful emissions from automobile exhaust gases is an important task in solving the environmental problem of environmental pollution [2]. Prolonged contact with an environment poisoned by car exhaust gases weakens the human body. In addition, exhaust gases can cause the development of various diseases, such as: respiratory failure; sinusitis; bronchitis; lung cancer [3-6].

The authors propose an experimental comparison of methods for ultrasonic and laser cleaning of automobile exhaust gases, including installation of an ultrasonic emitter and laser inside the muffler. Research has been carried out on the purification and utilization of exhaust gases from motor vehicles, which have shown positive results [7-16].

Patents have been registered on the use of ultrasonic influence on vehicle exhaust gas, which have shown their effectiveness [17-19]. To conduct and prove research on exhaust gas purification with ultrasound, full-size ultrasonic stands in a polypropylene housing were developed and studies were carried out [7, 10].

The research hypothesis is the possibility of cleaning exhaust gases from an internal combustion engine with ultrasonic emitters and a laser built into the car muffler housing.

The goal is to substantiate the possibility of using ultrasonic influence, laser radiation or joint work to clean car exhaust gases.

The objectives of the research include: development of an experimental stand; research methodology; experimental study and analysis of the results obtained.

The option of creating a car muffler with the combined effect of ultrasound and laser radiation has a significant advantage: it can be equipped with both new and existing cars. The importance of the environmental problem of air purification, the level of technical solutions and patents, the results of theoretical and experimental studies on ultrasonic and laser effects on media allow us to consider the task of creating automobile mufflers with the complex effect of ultrasonic and laser radiation as relevant [20-39].

### 1. Methods and Experiments

To achieve the set goals, a full-scale experiment was conducted on the developed combined ultrasonic-laser automobile muffler (Figures 1-3). During the experiment, at the first stage, the degree of exhaust gas purification from harmful impurities was determined using a gas analyzer.

During the experiment, at the first stage, the content of CH, CO, CO<sub>2</sub>, O<sub>2</sub> in the exhaust gas of a car was determined depending on the engine speed without ultrasound, under the influence of ultrasound at the frequencies of the ultrasonic generator 40, 25, 28 kHz, as well as under the influence of laser radiation and complex exposure to ultrasound and laser. At the second stage of the experiment, the smoke, temperature and humidity inside the muffler, the speed of the exhaust gas, the frequency in the ultrasonic laser car muffler measured by a frequency meter installed at a distance of 150 mm from the entrance to the muffler, as well as fuel consumption depending on the crankshaft speed of the car's internal combustion engine were determined.

The experimental study was carried out as follows:

- tests were carried out without turning on and with turning on ultrasonic and laser equipment for one minute each;
- the study was carried out at engine crankshaft speeds of 1000, 1200, 1400 rpm. A laboratory diesel internal combustion engine "D245" was used (Fig. 1), engine capacity 4750 cc. cm., engine power 245 hp, automobile 4-component gas analyzer "Infrakar M-1.01", smoke meter "INFRAKAR-D 1-3.01", anemometer "UNI-T UT363" and digital frequency meter.

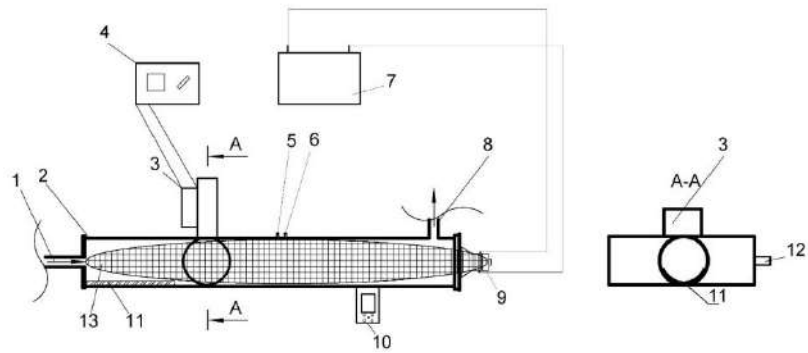


Fig. 1. – Laboratory diesel internal combustion engine "D245"

The exhaust gas from the car was supplied to the ultrasonic laser car muffler (further see Figures 2-3) through the inlet pipe 1 under pressure depending on the speed of the car's crankshaft. In the muffler, with the ultrasonic equipment turned on, for one minute at an ultrasonic generator frequency of 40, 25, 28 kHz, the exhaust gas was exposed to ultrasonic waves in the longitudinal direction 13, and laser radiation 3 also occurred. In the muffler, ultrasonic intensification of coagulation processes occurred [19, 20] and purification of exhaust gases due to sedimentation of enlarged particles of exhaust gas at the soot collection site 11, as well as photo-chemical processes occurred under the influence of a laser. The purified exhaust gas was discharged through the outlet pipe 8.



Fig. 2. – Ultrasound-laser car muffler



1 – inlet pipe; 2 – muffler body; 3 – laser; 4 – 12V rectifier;  
 5 – temperature sensor; 6 – moisture meter; 7 – ultrasonic generator; 8 – outlet pipe;  
 9 – longitudinal ultrasonic emitter; 10 – thermometer-hygrometer; 11 – removable tray;  
 12 – microscope

Fig. 3. – Diagram of an ultrasonic laser car muffler

When the ultrasonic laser muffler was operating, readings were taken from a gas analyzer, smoke meter, thermometer-hygrometer, anemometer, and frequency meter. Also, the fuel consumption of the internal combustion engine was previously measured at speeds of 1000, 1200 and 1400 (Fig. 4-8) by supplying fuel from a measuring container. Photos and video recordings were made inside the ultrasonic silencer using a digital microscope 12. Photos are not shown due to unclear images during transfer.



Fig. 4. – Indications of the automobile 4-component gas analyzer "Infrakar M-1.01"



Fig. 5. – Readings of the smoke meter "INFRAKAR-D 1-3.01"



Fig. 6. – Electronic frequency meter readings



Fig. 7. – Process of measuring fuel consumption



Fig. 8. – Process of measuring exhaust gas velocity



### 3. Experimental Studies

Tables 1-3 show the experimental results, and Figures 9-12 show the dependences of the CO<sub>2</sub>, O<sub>2</sub> content, smoke and frequency in the muffler on the engine speed without exposure, under the influence of ultrasound at frequencies of 40, 25, 28 kHz, as well as under the influence of a laser and the complex effect of ultrasound and laser at 1000, 1200, 1400 rpm of the internal combustion engine crankshaft.

**Table 1.** Experimental readings without exposure, under the influence of ultrasound and laser at 1000 rpm

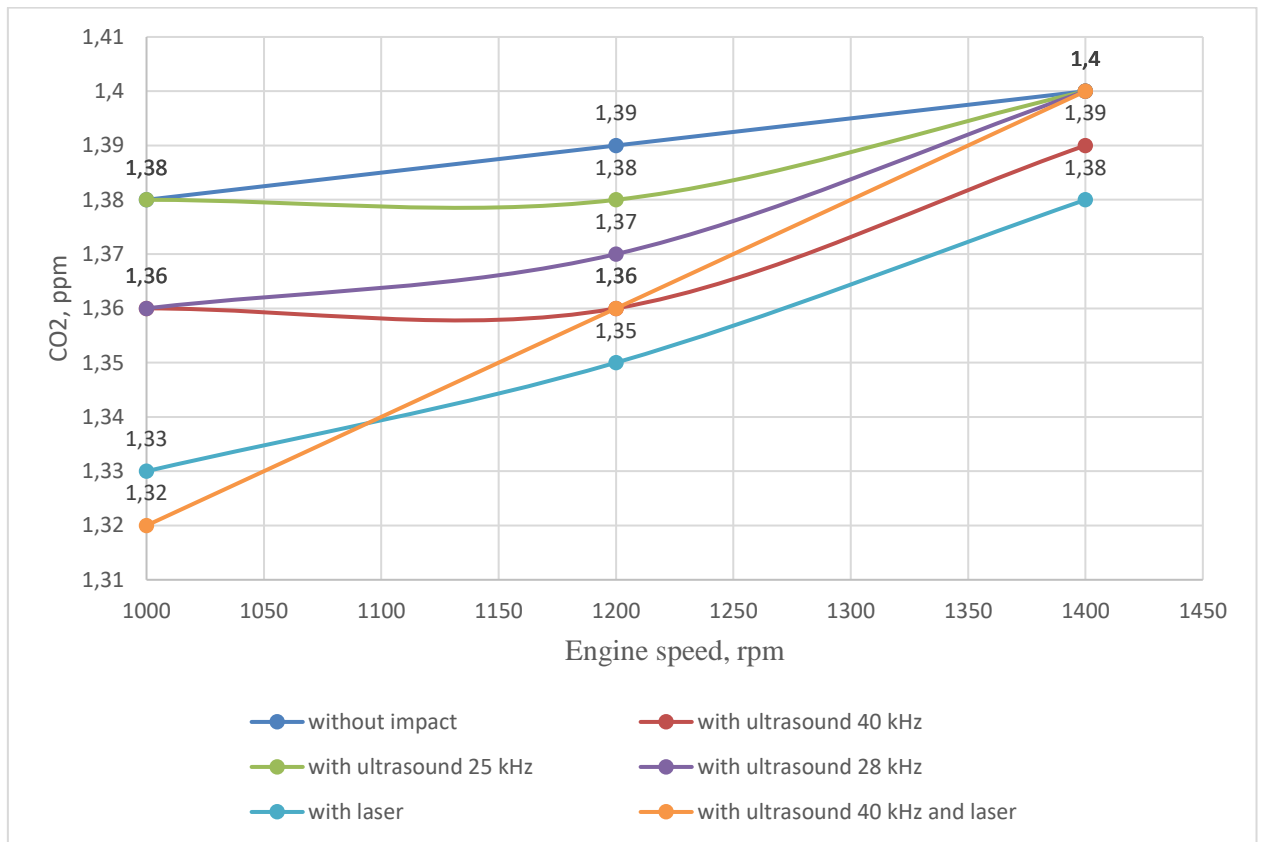
Measurements time=60 sec	without impact	with ultrasound f= 25kHz	with ultrasound f= 28 kHz	with ultrasound f= 40 kHz	with laser	with laser and ultrasound
CH (ppm)	0,00	0,00	0,00	0,00	0,00	0,00
CO (%)	0,02	0,01	0,02	0,02	0,02	0,02
CO <sub>2</sub> (%)	1,38	1,36	1,38	1,36	1,33	1,32
O <sub>2</sub> (%)	18,66	18,63	18,67	18,70	18,87	18,87
Smokiness (%)	0,9	0,7	0,7	0,8	0,6	0,8
Temperature (°C)	47,6	48	43	43,1	48,2	48
Humidity (%)	10%	10%	15%	15%	10%	10%
Gas velocity (m/s)	Input 18 Output 10.3	Input 18 Output 10.3	Input 18 Output 10.3	Input 18 Output 10.3	Input 18 Output 10.3	Input 18 Output 10.3
f in the muffler at a distance of 150 mm from the input ( Hz)	66-141	2100-2570	2400-2438	2800-2909	219-180	3600-3700
Fuel consumption (ml/min)	35	35	35	35	35	35

**Table 2.** Experimental readings without exposure, under the influence of ultrasound and laser at 1200 rpm

Measurements time=60 sec	without impact	with ultrasound f= 25kHz	with ultrasound f= 28 kHz	with ultrasound f= 40 kHz	with laser	with laser and ultrasound
CH (ppm)	0,00	0,00	0,00	0,00	0,00	0,00
CO (%)	0,02	0,02	0,02	0,02	0,02	0,02
CO <sub>2</sub> (%)	1,39	1,36	1,38	1,37	1,35	1,36
O <sub>2</sub> (%)	18,97	18,98	18,97	18,97	19,01	19,01
Smokiness (%)	3,1	2,9	2,8	2,9	2,5	2,5
Temperature (°C)	49	49,1	51,2	48,7	48,9	47,8
Humidity (%)	10%	10%	12%	13%	10%	10%
Gas velocity (m/s)	Input 20,8 Output 11	Input 20,8 Output 11	Input 20,8 Output 11	Input 20,8 Output 11	Input 20,8 Output 11	Input 20,8 Output 11
f in the muffler at a distance of 150 mm from the input ( Hz)	117-151	2200-2615	2450-2465	2915-2930	220-350	3650-3700
Fuel consumption (ml/min)	50	50	50	50	50	50

**Table 3.** Experimental readings without exposure, under the influence of ultrasound and laser at 1400 rpm

Measurements time=60 sec	without impact	with ultrasound f= 25kHz	with ultrasound f= 28 kHz	with ultrasound f= 40 kHz	with laser	with laser and ultrasound
CH (ppm)	0,02	0,02	0,02	0,02	0,04	0,04
CO (%)	0,01	0,01	0,01	0,01	0,01	0,01
CO <sub>2</sub> (%)	1,40	1,39	1,40	1,40	1,38	1,4
O <sub>2</sub> (%)	18,56	18,50	18,56	18,53	18,43	18,36
Smokiness (%)	0,8	0,7	0,7	0,5	0,6	0,6
Temperature (°C)	49,2	45,8	48	48,1	48	49,2
Humidity (%)	12%	12%	12%	12%	12%	12%
Gas velocity (m/s)	Input 21,5 Output 12,9	Input 21,5 Output 12,9	Input 21,5 Output 12,9	Input 21,5 Output 12,9	Input 21,5 Output 12,9	Input 21,5 Output 12,9
f in the muffler at a distance of 150 mm from the input (Hz)	130-185	2351-2300	2455-2465	2920-2935	250-451	3750-3960
Fuel consumption (ml/min)	65	65	65	65	65	65



**Fig. 9.** – Dependence of CO<sub>2</sub> content on engine speed without impact and under the influence of ultrasound at frequencies of 40, 25, 28 kHz and laser

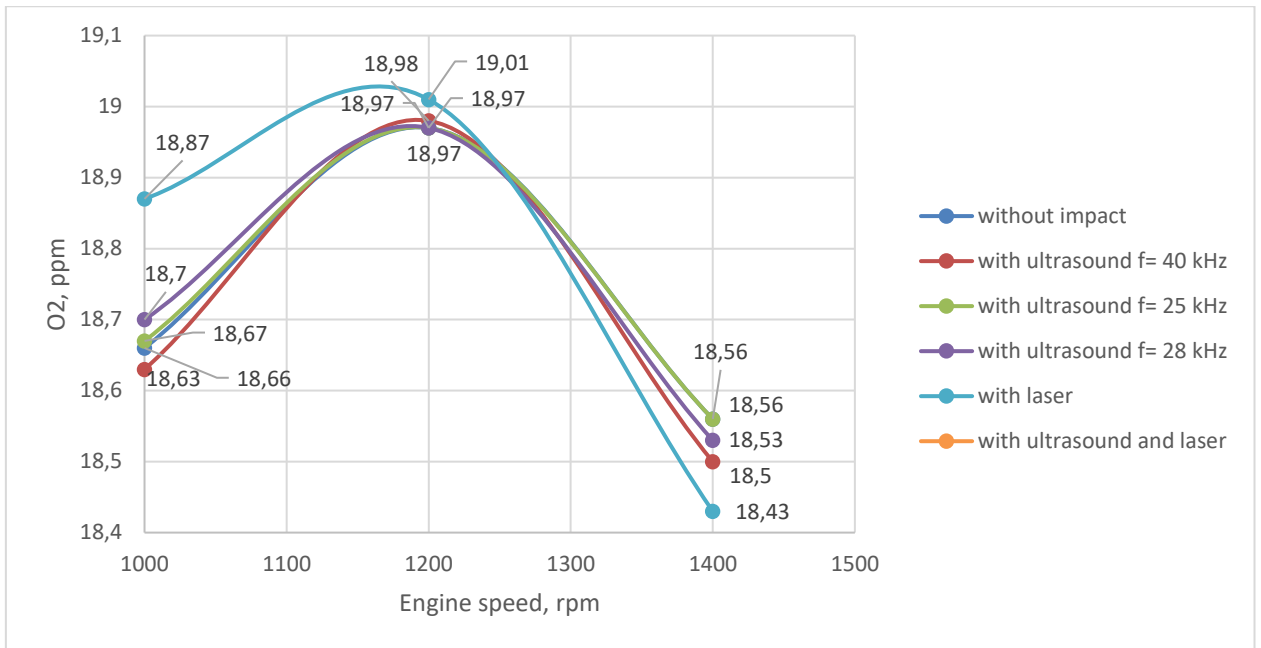


Fig. 10. – Dependence of oxygen content on engine speed without impact and under the influence of ultrasound at frequencies of 40, 25, 28 kHz and laser

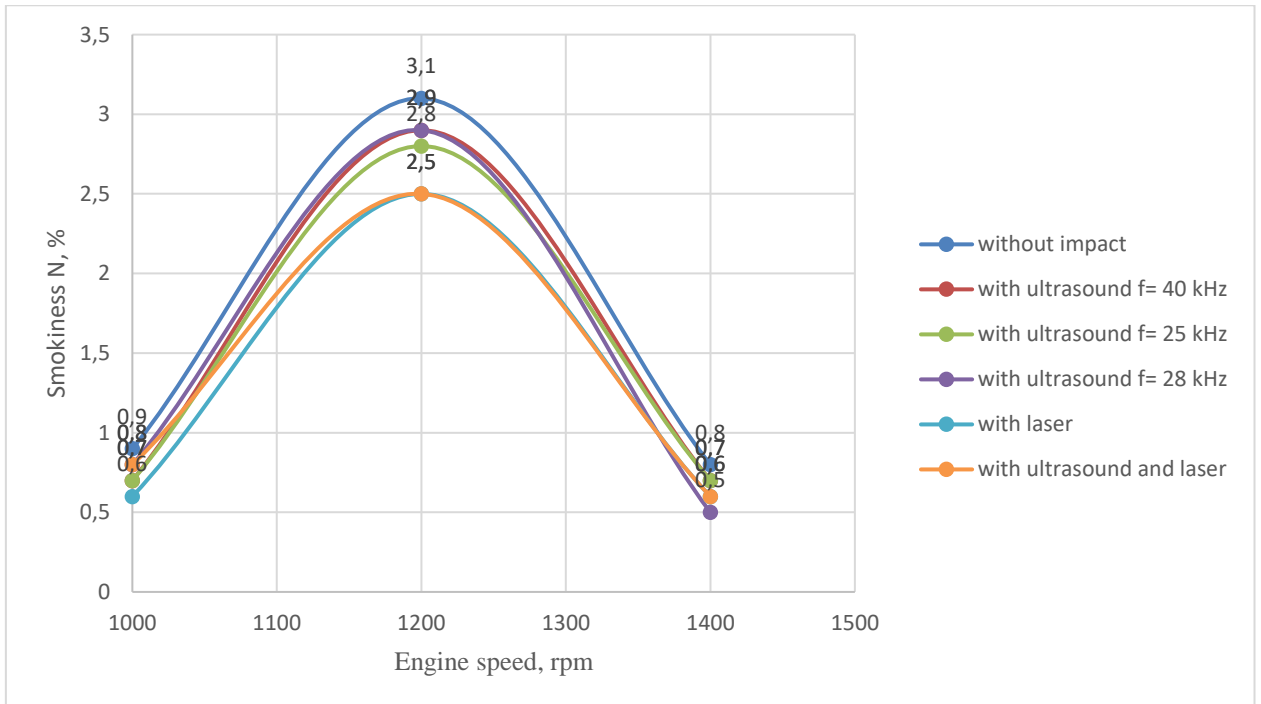


Fig.11. – Dependence of exhaust gas smokiness on engine speed without impact and under the influence of ultrasound at frequencies of 40, 25, 28 kHz and laser

As can be seen from the given dependencies, the decrease in CO<sub>2</sub> concentration and smoke, with an increase in O<sub>2</sub> confirms the hypothesis about the effective operation of ultrasonic and laser cleaning of exhaust gas. Laser radiation works more effectively than ultrasound, since the speed of light is faster than the speed of sound. The energy transmitted by the laser is instantly transferred to solid particles in the exhaust gas and there is a decrease in smoke, as well as an increase in oxygen. The combined operation of ultrasound and laser provides the maximum reduction of CO<sub>2</sub>. This complex process has not been fully studied and requires additional theoretical and experimental research.

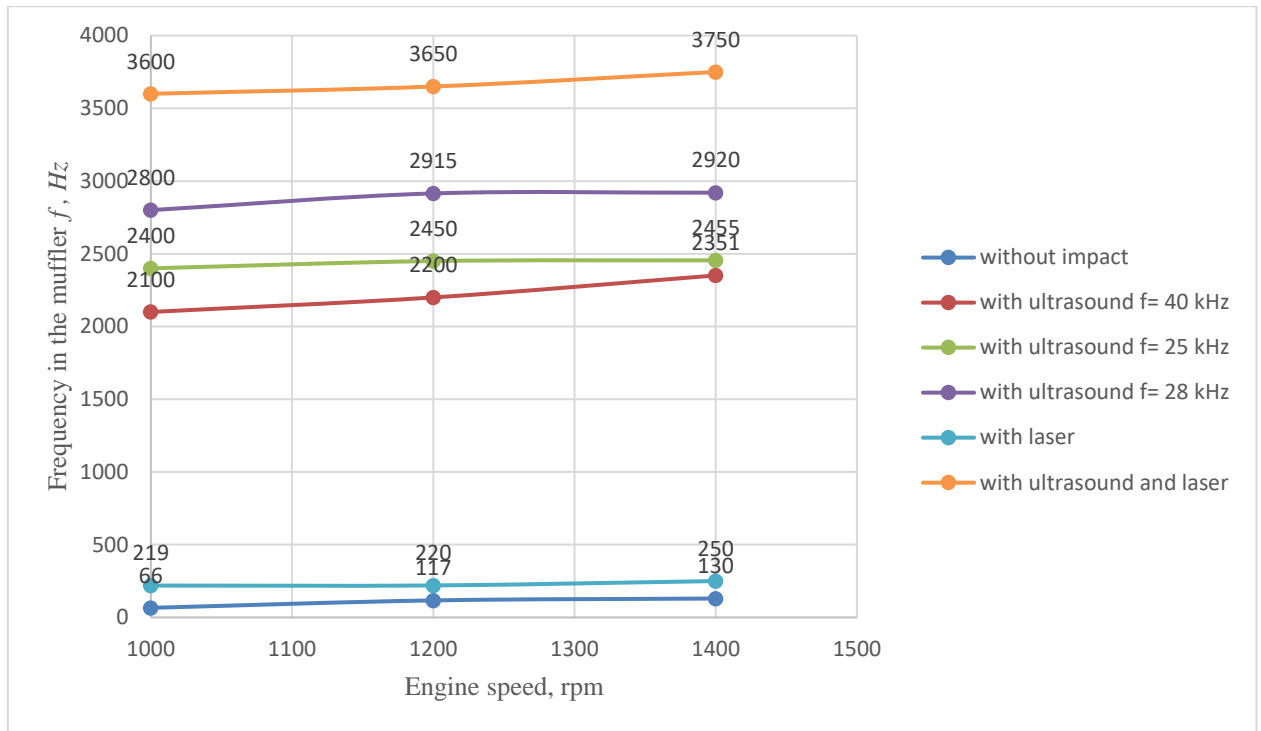


Fig. 12 – Dependence of frequency in an ultrasonic muffler on engine speed without impact and under the influence of ultrasound at frequencies of 40, 25, 28 kHz and laser

#### 4. Conclusion

In order to reduce harmful emissions from motor vehicle engines, with minimal costs and maximum efficiency of the complex effect of ultrasound and laser radiation for cleaning from solid soot particles and harmful impurities, an experimental study was conducted on the developed ultrasound-laser automobile muffler. The efficiency of the complex effect on the exhaust gases of motor vehicles was proven during the experiment and has promising development of this direction of cleaning aerosols from harmful impurities by the proposed method.

Hydrodynamic coagulation is superior in efficiency to orthokinetic cleaning, and laser cleaning is superior to ultrasound. The experimental study showed an increase in the mass of coagulated particles (soot) under the influence of ultrasound by more than 2 times.

The article proves the hypothesis of reducing harmful emissions due to the use of ultrasound and laser radiation. The direction of complex effects on the exhaust gas of cars has promising development and requires additional research. The conducted experimental studies are the basis for the creation of an engineering calculation method during the development of experimental samples of combined ultrasonic-laser mufflers.

#### References

- [1] Shamim T. Effect of engine exhaust gas modulation on the cold start emissions. *International Journal of Automotive Technology*, Vol. 12, Issue. 4, pp. 2011. – p.475–487.
- [2] Yessenbayeva A., Apsalikov B., Massabayeva M., Kazymov M., Shakhanova A., Mussazhanova Zh., Kadyrova I., Aukenov N., Shaimardanov N. Biomarkers of immunothrombosis and polymorphisms of IL2, IL6, and IL10 genes as predictors of the severity of COVID-19 in a Kazakh population. // *PLoS ONE*, Vol. 18, Issue 6, 2023. – p. 61-67. doi: <https://doi.org/10.1371/journal.pone.0288139>
- [3] Yegorov S., Kadyrova I., Korshukov I., Sultanbekova A., Kolesnikova Y., Barkhanskaya V., Bashirova T., Zhunusov Y., Li Y., Parakhina V., Kolesnichenko S., Baiken Y. Application of MALDI-TOF MS and machine learning for the detection of SARS-CoV-2 and non-SARS-CoV-2 respiratory infections // *Microbiology Spectrum*, Vol. 12, Issue 5, 2024. – p.1-11. doi: <https://doi.org/10.1128/spectrum.04068-23>
- [4] Kadyrova I.A., Mindubaeva F.A., Grzhibowski A.M. Prediction of outcomes after stroke: A systematic review. // *Ekologiya Cheloveka (Human Ecology)*. Vol. 22, Issue 10, 2015. – p.55-64. doi: <http://dx.doi.org/10.17816/humecol16983>
- [5] Akhmaltdinova L., Kolesnichenko S., Lavrinenko A., Kadyrova I., Avdienko O., Panibratov L. Influence of Pathogen Type on Neonatal Sepsis Biomarkers. *Wiley // International Journal of Inflammation*. Vol. 2021, Issue 2. – p.1- 7. doi: <http://dx.doi.org/10.1155/2021/1009231>
- [6] Mindubayeva F., Niyazova Y., Nigmatullina R., Sadykova D., Akhmaltdinova L., Salikhova Y., Kadyrova I., Akhmetova M., Sabirova D. Membrane serotonin transporter as a Biomarker of Pulmonary arterial hypertension in children with Congenital Heart Defect. // *Research Journal of Pharmacy and Technology*. Vol. 13, Issue 5, 2020. – p.2435-2438. doi: <http://dx.doi.org/10.5958/0974-360X.2020.00436.9>

- [7] Kadyrov A., Sarsembekov B., Ganyukov A., Zhunusbekova Z., Alikarimov K. Experimental research of the coagulation process of exhaust gases under the influence of ultrasound. *Communications – Scientific Letters of the University of Zilina*, 2021, Vol.23, Issue 4, 2021. – p. 288-298. doi: <https://doi.org/10.26552/com.C.2021.4.B288-B298>
- [8] Kadyrov A., Sarsembekov B., Ganyukov A., Suyunbaev Sh., Sinelnikov K. Ultrasonic unit for reducing the toxicity of diesel vehicle exhaust gases. // *Communications - Scientific Letters of the University of Zilina*, Vol. 24, Issue 3, 2022. – p. 189-198, doi: <https://doi.org/10.26552/com>.
- [9] Kadyrov A., Ganyukov A., Pak I., Suleyev B., Balabekova K. Theoretical and experimental study of operation of the tank equipment for ultrasonic purification of the internal combustion engine exhaust gases (2021) *Communications - Scientific Letters of the University of Žilina*, Vol.23, Issue 3, 2021. – p. 219-226. doi:
- [10] Kadyrov A., Bembenek M., Sarsembekov B., Kukeshva A., Nurkusheva S. The Influence of the Frequency of Ultrasound on the Exhaust Gas Purification Process in a Diesel Car Muffler. // *Appl. Sci.* Vol.14, Issue 12, 2024. – p. 1-19. <https://doi.org/10.3390/app14125027>
- [11] Pak I., Kadyrov A., Askarov B., Suleyev B., Karsakova A. Developing and studying the method of ultrasonic purification and utilization of internal combustion engine exhaust gases. // *Communications - Scientific Letters of the University of Žilina*. Vol. 25, Issue 3, 2023 – pp. 245 – 258. doi: 10.26552/com.C.2023.060
- [12] Kukeshva A., Kadyrov A., Kryuchkov Y. Establishing the parameters of the operation mode of the electric pulse automobile muffler. // *Journal of Applied Engineering Science*. Vol. 22, Issue 1, 2024. – p.89–99. doi: 10.5937/jaes0-45196
- [13] Kadyrov A., Kukeshva A., Kryuchkov Ye., Pak I., Kurmasheva B., Kabikenov S. Development of Calculation Methodology for Optimizing the Operating Mode of an Electric Pulse Unit for Cleaning Exhaust Gases. // *Communications - Scientific Letters of the University of Žilina*, Vol. 26, Issue 1, 2024. – p. 41-53, doi: <https://doi.org/10.26552/com.C.2024.011>
- [14] Kadyrov A., Kryuchkov Y., Sinelnikov K., Ganyukov A., Sakhapov R., Kukeshva A. Studying the process of the internal combustion engine exhaust gas purification by an electric pulse. // *Communications - Scientific Letters of the University of Zilina*, Vol. 24, Issue 4, 2022. – p. 275-287, doi: <https://doi.org/10.26552/com.C.2022.4.B275-B287>
- [15] Ibatov M.K., Kadyrov A.S., Pak I.A., Kadyrova I.A., Askarov B.S. The results of experimental studies of the capacitive equipment of ultrasonic cleaning of exhaust gases of vehicles // *Ugol*, (2), 2020. – pp. 73–78.
- [16] Kadyrov A., Sarsembekov B., Kukeshva A., Sinelnikov K. «Application of electric pulse and ultrasonic mufflers for increasing the degree of exhaust gas purification in car engines». //«*International Journal of Innovative Research and Scientific Studies*» 2024.
- [17] Savinykh Y.A., Logachev V.G., Logachev S.V., Vasilyeva A.Y. Device for cleaning automobile exhaust gases from particles. *Patent RU*, No. 2 373 409 C2, 2009.
- [18] Savinykh Y.A., Logachev V.G., Logachev S.V., Vasilyeva A.Y. Method for cleaning automobile exhaust gases from particles. *Patent RU*, No. 2 364 736 C2, 2009.
- [19] Ibatov M.K., Kadyrov A.S., Balabayev O.T., Askarov B.S., Pak I.A. Device for ultrasonic cleaning of exhaust gases. *Patent of the Republic of Kazakhstan* No. 3194., 2018.
- [20] Bergman L. Ultrasound and its application in science and technology. Moscow: Publishing house of foreign literature, 1957. - 726 p.
- [21] Baldev R., Rajendran V., Palanichami P. Applications of ultrasound. Moscow: Tekhnosfera, 2006. - 576 p.
- [22] Riera-Franco de Sarabia, Elvira-Segura, González-Gómez, Rodríguez-Maroto, Muñoz-Bueno, Dorronsoro-Areal. Investigation of the influence of humidity on the ultrasonic agglomeration of submicron particles in diesel exhausts. // *Ultrasonics*, Vol. 41, Issue 4, 2003. – p. 277-281.
- [23] Dong S., Lipkens B., Cameron T.V. The effects of orthokinetic collision, acoustic wake, and gravity on acoustic agglomeration of polydisperse aerosols. // *Journal of Aerosol Science*, Vol. 37, Issue 4, 2006. – p. 540-553.
- [24] Kadyrov A., Zhunusbekova Z., Ganyukov A., Kadyrova I., Kukeshva A. General characteristics for loading the working elements of drilling and milling machines when moving in the clay solution. // *Communications – Scientific Letters of the University of Zilina*, Vol. 23, Issue 2, 2021 – p.97–105.
- [25] Kadyrov A.S., Kunaev V.A., Georgiadi I.V. Ferrous metallurgy waste and waste technical fluids for obtaining the material of road bases. // *Ecology and Industry of Russia*, Vol. 21, Issue 12, 2017 – p. 44–48.
- [26] Kadyrov A.S., Kunaev V.A., Georgiadi I.V. Prospects for Processing of Ferrous Metallurgical Waste Based on Arcelormittal Temirtau Experience. // *Metallurgist*, Vol. 62, Issue 1-2, pp. 22–28.
- [27] Sherov K.T., Mardonov B.T., Kurmangaliyev T.B., Elemes D.E., Tusupova S.O., Izotova A.S., Smakova N.S., R. Gabdysalik, Buzauova T.M. The research of micro-hardness of side surfaces of teeth cylindrical wheels processed by “shaver-rolling device”. // *Journal of Theoretical and Applied Mechanics*, Sofia, Vol. 50, Issue 1, 2020, p.50-56.
- [28] Kadyrov A., Balabekova K., Ganyukov A., Akhmediyev S. The constructive solution and calculation of elements of the unified module of the mobile bridge overcrossing. // *Transport Problems*, Vol. 12, Issue 3, 2017. – p. 59–69.
- [29] Nasad T.G., Sherov K.T., Absadykov B.N., Tusupova S.O., Sagitov A.A. Abdugaliyeva G.B., Okimbayeva, A.E. Formation management in parts processing regenerated by surfacing // *News of the National Academy of*

- Sciences of the Republic of Kazakhstan, Series of Geology and Technical Sciences, Vol.3, Issue 435,2019. – p. 102–108.
- [30] Kadyrov A.A., Ganyukov A.A., Balabekova K.G., Zhunusbekova Z.Z., Suleev B.D. Scientific and engineering bases for development of mobile overpasses. *Material and Mechanical Engineering Technology*, Vol. 2, Issue 2, 2020. – pp. 7 – 13
- [31] Kyzylbaeva E.Zh., Kukeshva A.B., Kunaev V.A. Mathematical model of plate movement in thixotropic mud. // *Material and Mechanical Engineering Technology*, Vol. 2, Issue 2, 2020. – p. 26-30.
- [32] Kadyrov A., Sakhapov R., Ganyukov A., Sinelnikov K., Kurmasheva B., Suyunbaev Sh. Studying the process of transport equipment cooling system ultrasonic cleaning. // *Communications - Scientific Letters of the University of Zilina*, Vol. 24, Issue 4, 2022. – p. 288-300, doi: <https://doi.org/10.26552/com>
- [33] Menon G., Pego R.L. Approach to self-similarity in Smoluchowski's coagulation equations. // *Communications on pure and applied mathematics*, Vol. 57, Issue 9, 2004. – p. 1197-1232, doi: <https://doi.org/10.1002/cpa.3048>
- [34] Kadyrov A.S., Ganyukov A.A., Amanbayev S.Sh., Bogdanova A.A. Development of Mobile Communal Overpasses Applied During Repairing of Urban Communal Networks. // *Material and Mechanical Engineering Technology*, Vol. 5, Issue 3, 2023, - p.11-14. doi: [https://doi.org/10.52209/2706-977X\\_2023\\_3\\_1](https://doi.org/10.52209/2706-977X_2023_3_1)
- [35] Isagulov A., Akberdin A., Sultangazyev R., Kim A., Kulikov V., Isagulova D. Diagram of equilibrium phase composition of Fe – C – Si – B system // *Metalurgija*. Vol. 55, Issue 3 2016. – p. 305-308
- [36] Ilesaliev D.I. Design of Ultrasonic Technology to Improve the Efficiency of Car Exhaust Gas Cleaning System // *Material and Mechanical Engineering Technology*, Vol. 6. Issue 2, 2024. – p. 3-7
- [37] Sakhapov R. L. Method of Cleaning Internal Combustion Engine Radiator Tubes with Ultrasound/ *Material and Mechanical Engineering Technology*, Vol. 6. Issue 2, 2024. – p. 18-24.
- [38] Pak I. Experimental Study of the Ultrasonic Muffler Efficiency for Improving the Exhaust Gas Cleaning System of Internal Combustion Engines of Automobile // *Material and Mechanical Engineering Technology*, Vol. 6. Issue 2, 2024. – p. 53-63.
- [39] Aliev S.B., Suleev B.D. Study and calculation of the disk-milling tool. // *Ugol*, Vol.19. Issue 11, 2018 – p. 32 - 34 DOI: 10.18796/0041-5790-2018-11-32-34

**Funding:** This research has been funded by the Science Committee of the Ministry of Science and Higher Education of the Republic of Kazakhstan (Grant No. AP15473335 "Development and research of ultrasonic method of exhaust gas purification of internal combustion engines of transport equipment ")

**Acknowledgments:** We express our gratitude to the Science Committee of the Ministry of Science and Higher Education of the Republic of Kazakhstan for the grant provided.

**Conflicts of Interest:** The authors declare no conflict of interest.

#### Information of the authors

**Sarsembekov Bauyrzhan Koblanovich**, PhD, senior teacher, Abylkas Saginov Karaganda Technical University  
e-mail: [baurask@mail.ru](mailto:baurask@mail.ru)

**Kadyrov Adil Suratovich**, d.t.s., professor, Abylkas Saginov Karaganda Technical University  
e-mail: [ludmila77025@mail.ru](mailto:ludmila77025@mail.ru)

**Kunayev Vyacheslav Alexandrovich**, PhD, senior teacher, Karaganda industrial university  
e-mail: [v.kunaev@ttu.edu.kz](mailto:v.kunaev@ttu.edu.kz)

**Issabayev Madi Sansyzbaevich**, doctoral student, Abylkas Saginov Karaganda Technical University  
e-mail: [isabaev-madi@mail.ru](mailto:isabaev-madi@mail.ru)

**Kukeshva Aliya Bakibaevna**, PhD, Abylkas Saginov Karaganda Technical University  
e-mail: [aliya.kukeshva@bk.ru](mailto:aliya.kukeshva@bk.ru)

## Development of a Tractor Reliability Optimization Model: a Review of Research and Rationale for the Components

Gulyarenko A.A.<sup>1</sup>, Bembenek M.<sup>1,2\*</sup>, Iskakov R.M.<sup>1</sup>, Shaimuratova E.S.<sup>1</sup>, Gulyarenko A.V.<sup>1</sup>

<sup>1</sup>S. Seifullin Kazakh Agrotechnical University, Astana, Kazakhstan

<sup>2</sup>AGH University of Krakow, Krakow, Poland

\*corresponding author

**Abstract.** This study reviews existing research on optimizing the reliability of agricultural tractors, with a focus on identifying the most critical factors influencing tractor performance. The methodological approach involved an expert assessment of factors affecting tractor reliability, which highlighted three key elements: the factory (inherent) reliability of tractors, the effectiveness of repair and maintenance practices, and the losses incurred from tractor downtime. The consistency of expert opinions was validated using an agreement coefficient. Based on these findings, the development of a mathematical model is proposed, enabling agricultural enterprises to make informed decisions when selecting tractors based on reliability and cost-efficiency indicators. This research represents the initial phase of a broader project, with future plans to create software that automates the optimization of tractor reliability and costs, ultimately improving the profitability of agricultural enterprises.

**Keywords:** tractor reliability, cost optimization, maintenance, failure-free operation, maintainability

### 1. Introduction

The purpose of acquiring technical equipment for agricultural producers is to maximize the effectiveness of their functional capabilities. Among these, the operational reliability of machine-tractor units is crucial, especially given the stringent requirements for both the duration and the quality of technological processes in crop production. Key indicators of reliability include the dependability and ease of maintenance of the machinery [1–3]. However, frequent tractor failures—tractors being the energy foundation of these units - along with the high labor demands for repair and maintenance, often result in a technical utilization rate of just 60 - 70% during peak fieldwork cycles. This makes the process of maintaining operability, with tractors as the central focus, the primary challenge in their acquisition.

Additionally, the substantial resources required for routine technical maintenance (TM) and repair activities lead to significant increases in the overall cost of maintaining tractor reliability. Over the standard operational period, these costs, which include labor, materials, and infrastructure development, often are several times higher than the initial manufacturing costs of the machinery itself [4–6].

Standards for mean time between failures (MTBF) and the labor intensity of repairs should align with the agronomic requirements for the duration and quality of crop production processes [7]. This underscores the need for deploying tractors with varying levels of reliability and maintainability, allowing for differentiation in these performance metrics within machine-tractor units.

The existence of an entire field of scientific research highlights the importance of this topic on both national and international scales. In English-language literature, the solution to this practical optimization problem falls under the field known as “life cycle engineering,” which focuses on optimizing the life cycle costs of technical systems [8–10]. Another commonly used concept is the “Total Cost of Ownership” (TCO), which evaluates the comprehensive costs associated with owning a product [11–13].

Several specialized international journals are dedicated to publishing the latest research in this area, such as *The International Journal of Life Cycle Assessment* [14], *Reliability, Availability, and Maintainability Aspects of Automobiles* [15], and book series like *Sustainable Production, Life Cycle Engineering, and Management (SPLCEM)* [16]. The emphasis on evaluating total costs of acquisition and usage arises from the fact that, for certain machines like agricultural tractors, the cumulative expenses for maintenance, repairs, fuel, and other operational needs over the machine’s lifetime can far exceed the initial purchase cost [17]. This gap widens further when factoring in downtime losses, which is particularly critical for tractors in crop production.

Unfortunately, these problems have not been adequately addressed to date. The outdated GOST R 53056-2008 [18], which closely mirrors GOST 23729-88 [19] from the planned economy era, remains in use. Many researchers are still forced to rely on these obsolete standards [18, 19] when calculating the economic performance of specialized machinery [20–23]. Consequently, Kazakhstan lacks modern methodologies for assembling machine-tractor units based on reliability, productivity, and efficiency metrics. As a result, agricultural enterprises often select equipment based on intuition, without a well-founded approach to minimizing costs and maximizing profitability.

More accurate guidelines for accounting cost components, including for tractors, can be found in earlier works, such as a detailed practical guide published in 1997 by Kansas State University [24]. This guide offers extensive reference data and methodologies for conducting such calculations. Similar approaches to evaluating the cost of ownership and operating expenses for agricultural tractors were presented in a 2009 publication by Iowa State University, which was reissued in 2011 and 2015 [25]. A shorter, more pragmatic guide by the University of

South Dakota [26], along with other works by international agricultural business experts, provides further insights. These studies emphasize that determining key components for calculating an optimal level of reliability requires forecasting changes in a machine's technical and economic characteristics over its entire lifespan, as highlighted in these foreign publications.

The relevance of this study lies in its potential to generalize and adapt existing international research for agricultural enterprises in Northern Kazakhstan, while incorporating the work of local scientists [27–29], including the authors of this publication [30–32]. The first study on this topic was authored by Gulyarenko A. A. in 2008, following research conducted since 2007, with over 50 related publications during this period [33]. An analysis of the literature shows that similar studies are conducted in other countries [9, 12–14, 17, 24–26, 34], but they largely contain statistical data and scattered mathematical models, lacking a comprehensive solution tailored to specific enterprises—particularly agricultural ones. This makes the hypothesis and objectives of this study both original and highly relevant, not only for Kazakhstan but also internationally. Moreover, this research aims to automate the calculation process by developing specialized software, allowing these models to be adapted for various agricultural enterprises across the Republic of Kazakhstan.

The most important factor in improving the efficiency of agricultural production is the increase of the quantity and quality of output. Producers around the world strive to ensure that their products meet high quality standards and are in demand by consumers. It is essential to remember that the quality of products affects demand, competitiveness, and their final price. To achieve growth in both quantity and quality, scientifically sound cultivation techniques, reliable high-performance equipment, and highly skilled personnel are required, which inevitably raises the price of the final product. However, despite these increased costs, it remains crucial to seek optimal solutions for achieving the best results, particularly in crop production. One such solution involves developing a model that ensures the reliability and maintainability of tractors, enabling the achievement of necessary performance metrics in mechanized processes.

In Kazakhstan, the available range of tractors varies significantly in terms of MTBF and the labor intensity of repair and maintenance. This variety allows for the selection of tractors with economically feasible levels of reliability and maintainability, tailored to the specific requirements of different crop production processes. In other words, it is possible to assemble machine-tractor units with differentiated values for reliability and maintenance needs. However, as the reliability of tractors increases, so does their price, making it essential to address this issue within the context of farm income and profitability [35]. Given the practical significance of this challenge, its scientific relevance is clear. Furthermore, improving the profitability of both small and large agricultural enterprises will have a profound impact on the agricultural sector, which is crucial to Kazakhstan's economy.

## **2. Materials and Methods**

The methodological foundation of this study is based on the premise that a relationship exists between the MTBF, the labor intensity of repair and maintenance actions in machine-tractor units, and key factors such as the duration of technological processes in crop production, product losses, and resource costs required to maintain tractor operability. By studying and generalizing these dependencies, the goal is to solve this optimization problem for the specific conditions of agricultural enterprises in the Republic of Kazakhstan.

Given the wide range of factors influencing tractor reliability, the initial stage of the study focuses on identifying the most significant ones affecting tractor performance in crop production. The complexity of these interrelated factors is the main challenge in optimizing tractor reliability. This challenge can be effectively addressed using the expert assessment method.

To this end, an expert survey was conducted using a structured questionnaire that listed the key generalized factors affecting the reliability of mechanized processes on farms. Experts provided their understanding of each factor, clarifying any uncertainties if needed. They were then tasked with evaluating the weight of each factor and ranking them by significance. The questionnaire also allowed for the addition and ranking of unaccounted factors where necessary.

In our study, we interviewed 35 experts to assess the impact of various factors on the reliability of mechanized technological processes. As a result, eight key factors were identified as having the most significant influence on tractor performance during these processes. The factors, weighted by expert opinion, are as follows: tractor's factory reliability (X1), quality of maintenance (X2), quality of repairs (X3), availability of material and technical resources for maintenance and repair (X4), tractor workload (X5), operator proficiency (X6), storage and quality of fuel and lubricants (X7), and unfavorable environmental conditions (X8).

Once the survey was completed, it was necessary to analyze the results to determine whether the experts' responses were consistent and non-random. This involved calculating indicators that measure the degree of agreement among the experts. The primary metric used to assess this agreement was the concordance coefficient [37–39], which reflects the level of consensus across all the identified factors.



**Table 1.** The influence of individual factors on the reliability of the implementation of a mechanized technological process and their significance according to expert survey data

Expert number	The weight of the factor, assigned by the <i>i</i> -th expert within the range from 0 to 1							
	Tractor's factory reliability	Quality of maintenance	Quality of repairs	Availability of material and technical resources for maintenance and repair	Tractor workload	Operator proficiency	Storage and quality of fuel and lubricants	Unfavorable environmental conditions
1	2	3	4	5	6	7	8	9
1	0.9	0.8	0.9	0.7	0.9	0.6	0.8	0.6
2	0.6	0.8	0.3	0.4	0.2	0.4	0.3	0.2
3	0.9	0.7	0.6	0.8	0.4	0.5	0.9	0.4
4	0.8	0.3	0.4	0.5	0.4	0.5	0.2	0,1
5	0.8	0.7	0.5	1.0	0.9	0.6	0.4	0.3
6	0.7	1.0	0.5	0.6	0.8	0.8	0.5	0.2
7	0.8	0.9	0.9	0.7	0.8	0.5	0.5	0.7
8	0.8	0.6	0.7	0.6	0.7	0.5	0.6	0.7
9	0.7	0.7	0.6	0.5	0.9	0.3	0.3	0.7
10	0.8	1.0	0.7	0.6	0.5	0.4	0.4	0.2
11	0.8	0.9	0.7	0.8	0.5	0.8	0.5	0.6
12	0.8	0.8	1.0	0.6	0.5	0.4	0.4	0.3
13	0.8	0.8	0.9	0.6	0.7	0.5	0.6	0.5
14	1.0	1.0	1.0	0.5	0.8	0.5	0.5	0,0
15	0.9	0.7	0.8	0.7	0.9	0.5	0.4	0.5
16	1.0	0.5	0.5	0.2	0.5	0.8	0.5	0.7
17	0.8	1.0	0.5	0.4	0.6	0.3	0.4	0.3
18	0.6	1.0	0.5	0.5	0.5	0.6	0.7	0.4
19	0.6	1.0	0.8	0.6	0.3	0.7	0.5	0.5
20	0.9	0.9	0.6	0.5	0.8	0.5	0.6	0.7
21	0.9	0.8	0.8	0.3	0.5	0.5	0.6	0.4
22	0.6	0.5	0.5	0.4	0.4	0.4	0.3	0.5
23	0.8	0.9	0.8	0.5	0.5	0.7	0.5	0.2
24	0.8	1.0	1.0	0.6	0.6	0.8	0.6	0.2
25	0.8	0.9	0.8	0.9	0.5	0.9	0.5	0.3
26	1.0	0.8	0.9	0.7	0.6	0.4	0.4	0,0
27	0.7	0.5	0.4	0.6	0.5	0.3	0.3	0.5
28	1.0	0.5	0.7	1.0	0.3	0.7	0.9	0.5
29	0.9	0.3	0.3	0.4	0.2	0.5	0.5	0.2
30	0.7	1.0	0.5	0.7	0.8	0.4	0.5	0.2
31	0.8	0.7	0.8	0.8	0.8	0.7	0.7	0.2
32	1.0	0.4	0.8	0.8	0.6	0.3	0.6	0.2
33	0.9	1.0	0.6	0.8	0.2	0.4	0.4	0.2
34	0.7	0.8	0.5	0.7	0.6	0.5	0.7	0.4
35	1.0	0.6	0.5	1.0	0.7	1.0	0.4	0.3

To calculate the value of the concordance coefficient, we first find the sum of the ratings (ranks) for each factor  $\sum_{j=1}^m X_{ij}$ , obtained from all experts, and then the difference between this sum and the average sum of the ranks ( $\bar{X}$ ) using the formula:

$$\Delta_i = \sum_{j=1}^m X_{ij} - \bar{X} \tag{1}$$

The average sum of ranks is determined by the expression:

$$\bar{X} = \frac{\sum_{i=1}^n \sum_{j=1}^m X_{ij}}{n} \tag{2}$$

where  $m$  is the number of experts;  
 $n$  is the number of factors.

Next, the sum of the squares of the differences (deviations)  $S$  is calculated:

$$S = \sum_{i=1}^n \left( \sum_{j=1}^m X_{ij} - \frac{1}{2}m(n+1) \right)^2 \tag{3}$$

The value of  $S$  has a maximum value in the case when all experts give the same estimates. After this, we directly calculate the concordance coefficient using the following formula:

$$W = \frac{12S}{m^2(n^3 - n) - m \sum_{j=1}^m T_j} \tag{4}$$

where

$$T_j = \sum_{j=1}^J t_j^3 - t_j \tag{5}$$

where  $J$  is the number of groups of related ranks;  
 $t_j$  is the number of identical ranks in the  $j$ -th row.

To assess the significance of the coefficient of concordance  $W$ , we use the Pearson criterion:

$$x_p^2 = \frac{S}{\frac{1}{2}mn(n+1) - \frac{1}{n-1} \sum_{j=1}^m T_j} \tag{6}$$

For the agreement of expert opinions to be considered significant, it is necessary that the calculated value of the criterion  $x_p^2$  was greater than the tabular  $x_m^2$  [21], determined by the number of degrees of freedom  $f = n - 1$  and the confidence level  $y = 0.95$ .

### 3. Results and Discussion

Table 2 presents the results of calculating the consistency of expert opinions regarding the impact of individual factors on the technical performance of tractors.

**Table 2.** Assessment of the agreement of expert opinions

Index of expert consensus	The weight of the factor, assigned by the $i$ -th expert within the range from 0 to 1							
	Tractor's factory reliability	Quality of maintenance	Quality of repairs	Availability of material and technical resources for maintenance and repair	Tractor workload	Operator proficiency	Storage and quality of fuel and lubricants	Unfavorable environmental conditions
Sum of ranks $X_{ij}$	78	101	136	152	164	202	185	240
Deviations from the average sum of ranks $\Delta_i$	-79	-56	-21	-5	7	45	28	83
Squares of deviations $S$	6241	3136	441	25	49	2025	784	6889
Tied ranks index $T_i$	2923	1368	1272	1128	1197	1764	1860	1428
The weight of the factor $\varphi$	0.82	0.76	0.67	0.62	0.58	0.50	0.55	0.36

Based on the obtained data, the concordance coefficient for the entire set of factors ( $n = 8$ ) was  $W = 0.40$ . This positive value, distinct from zero, indicates a significant level of agreement among the expert opinions. The actual value of  $x^2$  ( $x_p^2 = 17.22$ ) is much greater than the critical table value ( $x_m^2 = 2.17$ ), further confirming sufficient agreement across all factors.

The analysis of the survey results shows that among the eight factors, the greatest impact on the reliability of mechanized processes comes from the factory reliability of tractors ( $\varphi = 0.82$ ), followed by the quality of maintenance ( $\varphi = 0.76$ ), and the quality of repairs ( $\varphi = 0.67$ ). Future research should prioritize these key components, as they have the most significant influence on tractor reliability.

Existing methods for determining optimal tractor reliability indicators can be categorized based on the types of operational costs they account for:

- 1) Methods that consider both repair and maintenance (MOT) costs as well as the costs of energy materials (fuel, lubricants, electricity, etc.).
- 2) Methods that account only for the repair and maintenance costs of machines.
- 3) Methods that focus solely on the costs of spare parts, metal consumption, and related materials.
- 4) Methods that account for losses due to unplanned machine downtime caused by technical faults, alongside the costs of repair and maintenance.

An analysis of the methods leads to the conclusion that, when using tractors in crop production, their reliability should generally be justified by minimizing the total cost function:

$$\sum C = C_F + C_{repair} + C_{maintenance} + C_{salary} + C_{fuel/lubricants} + C_{PR} \rightarrow \min \quad (7)$$

where  $C_F$  represents the cost of purchasing the tractor (first-order indirect costs of manufacturing at the factory, in tenge);

$C_{repair}$  are the costs of repairing the machine, in tenge;

$C_{maintenance}$  includes maintenance and storage costs, in tenge;

$C_{salary}$  is the wage expenditure for tractor operators, in tenge;

$C_{fuel/lubricants}$  are the fuel and lubricant costs, in tenge;

$C_{PR}$  represents the complex costs from production losses and underutilization of labor due to machine downtime, in tenge.

The analysis of research materials and expert survey results shows that, to determine the required level of factory reliability for tractors within machine-tractor units, it is sufficient to account for the following: the initial purchase cost of tractors, the costs of maintaining and restoring operability, and the costs arising from mechanized process disruptions due to downtime. The behavior of these costs is highly influenced by the initial reliability of the machine and the conditions under which it is operated. Therefore, the cost function can be simplified as:

$$\sum C = C_F + C_{PMA} + C_{PR} \rightarrow \min \quad (8)$$

where  $C_{PMA}$  represents the costs of preventive maintenance and repairs.

Each component of the total costs consists of variables that are characterized by their variability and the presence of numerous price-determining factors. To identify the priority indicators of the objective function, it is necessary to examine the mechanisms that influence the formation of these cost components. However, based on current findings, we can assert that the initial cost of purchasing the machine, particularly the investment in higher factory reliability, is critical. This initial expense significantly impacts the other cost components during the machine's operation and forms the foundation for optimizing the total cost function (Figure 1).

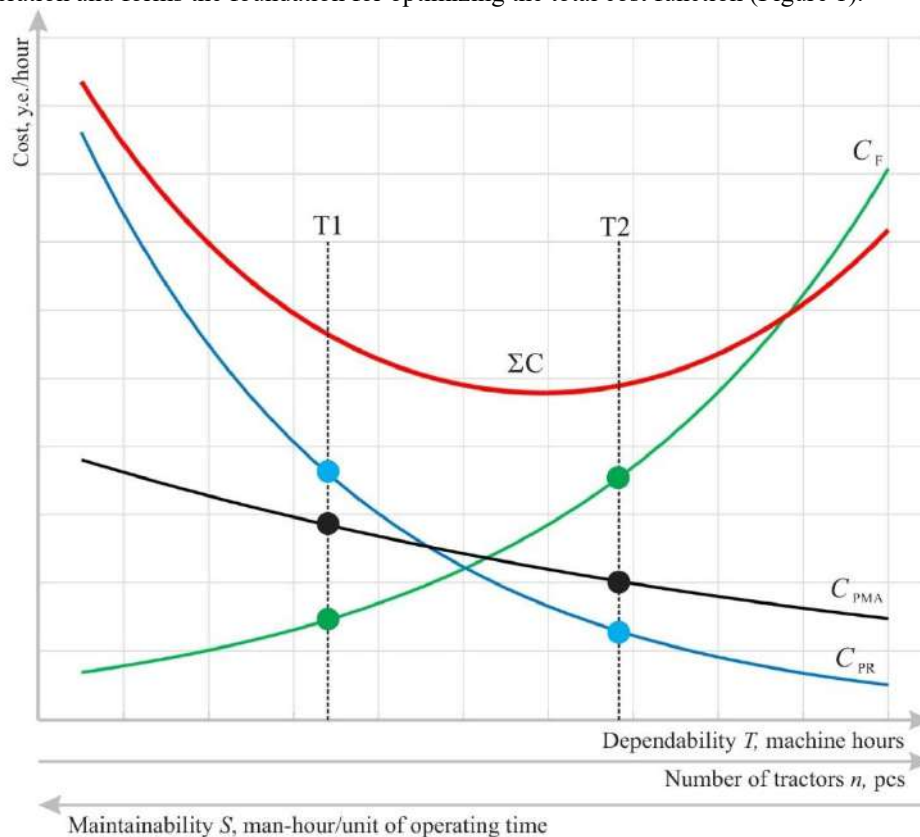


Fig. 1. - Change in the minimum of the total cost function depending on the costs of increasing the level of factory reliability of agricultural tractors  $C_F$ , the costs of maintaining and restoring their operability in operation  $C_{PMA}$  and complex costs due to losses of crop production  $C_{PR}$ .

In Figure 1, two hypothetical tractors are depicted: T1, a cheaper but less reliable tractor, and T2, a more expensive tractor with excessive reliability. This comparison illustrates the balance between cost components. The key to maximizing profit in crop production lies in minimizing total costs ( $\sum C \rightarrow \min$ ). When viewed from a profitability standpoint, delays in crop production (as shown in Figure 1) can lead to losses in both the quantity and the quality of the harvest, resulting in financial losses. At the same time, the reliability of tractors directly correlates with financial costs for manufacturing and maintaining equipment in working condition.

### Conclusions

The essence of determining the optimal levels of reliability and maintainability for agricultural tractors lies in identifying rational operational indicators where the total costs - including acquisition, operation, and downtime losses due to malfunctions - are minimized over a given service life (e.g., per 1,000 engine hours, work cycle, etc.). The goal is to achieve the lowest possible cost per unit of work performed.

Increasing factory reliability reduces product losses  $C_{PR}$ , but it also raises manufacturing costs and the price of tractors. Product losses depend on factors such as workload, crop yield, and the tractor's factory reliability level. During operation, various reliability and maintainability indicators can be used to assess tractor performance. For instance, tractors of the same class from different manufacturers may be compared using metrics such as mean time between failures and specific labor intensity of maintenance. The point at which the curves of increased factory reliability costs intersect with the cost of losses indicates the minimum total cost function ( $\sum C$ ) and helps determine the optimal range of reliability indicators on the  $x$ -axis.

### Prospects for Further Development

This article represents the first stage in substantiating the key components of a mathematical model to differentiate tractor reliability indicators. In the next stage, theoretical dependencies will be established, and the three main components of the objective function (from Formula 8) will be analyzed. This will be followed by collecting and evaluating data on tractor performance under real-world operating conditions. In the third stage, experimental data will be used to refine the theoretical models. Ultimately, this will result in a reliable mathematical model for optimizing tractor reliability indicators, tailored to the specific operational conditions of agricultural enterprises.

### Foundings

This research was funded by the Science Committee of the Ministry of Science and Higher Education of the Republic of Kazakhstan (Grant No. AP23487301)

### References

- [1] Gulyarenko A.A. Calculation method of the reasonable reliability level based on the cost criteria. //Journal of Machinery Manufacture and Reliability, Vol. 47, No. 1, 2018. - p. 96-103. <https://doi.org/10.3103/s1052618817060085>
- [2] Redreev G.V., Kachurin V.V., Myalo O.V. Efficiency Increase of Sowing Complexes. //IOP Conference Series: Materials Science and Engineering, Vol. 1079, No. 6, 2021. - p. 062067. <https://doi.org/10.1088/1757-899X/1079/6/062067>
- [3] Mishra D., Satapathy S. Reliability and maintenance of agricultural machinery by MCDM approach. //International Journal of System Assurance Engineering and Management, Vol. 14, No. 1, 2023. - p. 135-146. <https://doi.org/10.1007/s13198-021-01256-y>
- [4] Renius K.T. Fundamentals of tractor design. Cham, Switzerland: Springer, 2020. <https://doi.org/10.1007/978-3-030-32804-7>
- [5] Harianton I., Saefudin A.S., Suparman M.A. Design and manufacture of four wheel tractor for medium size work rice farming. //International Journal of Advanced Applied Science, Vol. 12, No. 1, 2022. - p. 82-92. <https://doi.org/10.11591/ijaas.v12.i1.pp82-92>
- [6] Conant M. Competition in the Farm-Machinery Industry. //The Journal of Business of the University of Chicago, Vol. 26, No. 1, 1953. - p. 26-36. <https://www.jstor.org/stable/2350224>
- [7] Redreev G.V., Chervenчук V.D., Kiyko P.V. Modeling and Study of Maintenance Service System. //International Russian Automation Conference, Cham: Springer International Publishing, 2022. - p. 262-268. [https://doi.org/10.1007/978-3-031-22311-2\\_26](https://doi.org/10.1007/978-3-031-22311-2_26)
- [8] Kambanou M.L. Life cycle costing: understanding how it is practised and its relationship to life cycle management—a case study. //Sustainability, Vol. 12, No. 8, 2020. - p. 3252. <https://doi.org/10.3390/su12083252>
- [9] Pradel M. Life cycle inventory data of agricultural tractors. //Data in Brief, Vol. 48, 2023. - p. 109174. <https://doi.org/10.1016/j.dib.2023.109174>
- [10] Cadena E., Thomassen G. Life cycle costing. //Handbook on Life Cycle Sustainability Assessment, Edward Elgar Publishing, 2024. - p. 77-88. <https://doi.org/10.4337/9781800378650.00017>
- [11] Ellram L.M. Total cost of ownership: an analysis approach for purchasing. //International Journal of Physical Distribution & Logistics Management, Vol. 25, No. 8, 1995. - p. 4-23. <https://doi.org/10.1108/09600039510099928>

- [12] Namdev S.K., et al. Estimation and Comparative Study of Operational Costs of Various Combined Tillage and Sowing Implements. //International Journal of Plant & Soil Science, Vol. 36, No. 5, 2024. - p. 553-562. <https://doi.org/10.9734/ijpss/2024/v36i54552>
- [13] Kostomakhin M., et al. Proposals for reduction of the cost of ownership of agricultural machinery due to increase controllability and adaptability to diagnosis. //E3S Web of Conferences, Vol. 402, 2023. - p. 13003. <https://doi.org/10.1051/e3sconf/202340213003>
- [14] Tassielli G., et al. Quantifying life cycle inventories of agricultural field operations by considering different operational parameters. //The International Journal of Life Cycle Assessment, Vol. 24, 2019. - p. 1075-1092. <https://doi.org/10.1007/s11367-018-1553-6>
- [15] James A.T. Reliability, availability and maintainability aspects of automobiles. //Life Cycle Reliability and Safety Engineering, Vol. 10, No. 1, 2021. - p. 81-89.
- [16] Progress in Life Cycle Assessment 2021. //Sustainable Production, Life Cycle Engineering and Management (SPLCEM). <https://doi.org/10.1007/978-3-031-29294-1>
- [17] Arhipov V.S. Ocenka stoimosti life-giving cikla traktorov. //Traktory i sel'hozmashiny, No. 5, 2014. - p. 3-9. <https://elibrary.ru/item.asp?id=21507457>
- [18] GOST R 53056-2010 Technology agricultural. Economic methods ochenki. Moscow: Standartinform, 2009. - 20 p. [https://rosgosts.ru/file/gost/65/060/gost\\_r\\_53056-2008.pdf](https://rosgosts.ru/file/gost/65/060/gost_r_53056-2008.pdf)
- [19] GOST 23729-88 Agricultural machinery. Methods of economic evaluation of specialized machines. Moscow: Standartinform, 1988. - 12 p. [https://rosgosts.ru/file/gost/03/120/gost\\_23729-88.pdf](https://rosgosts.ru/file/gost/03/120/gost_23729-88.pdf)
- [20] Starostin I.A., et al. Ocenka sebestoimosti exploitation unpiloted rural agregatov. //Vestnik Kazanskogo GAU, Vol. 2, 2024. - p. 74. <https://naukaru.ru/temp/b59bc63e29516be21fef9427e93c0454.pdf>
- [21] Gulyarenko A., Bembenek M. The method of calculating ploughshares durability in agricultural machines verified on plasma-hardened parts. //Agriculture, Vol. 12, No. 6, 2022. - p. 841. <https://doi.org/10.3390/agriculture12060841>
- [22] Shepelev S.D., et al. Theoretical and experimental studies of the tractive resistance of the sowing complex for the no-till technology. //International Conference on Industrial Engineering, Cham: Springer International Publishing, 2022. - p. 341-350. [https://doi.org/10.1007/978-3-031-14125-6\\_34](https://doi.org/10.1007/978-3-031-14125-6_34)
- [23] Koshumbaev M., et al. Development of a vortex wind device. //Eastern-European Journal of Enterprise Technologies, Vol. 121, No. 8, 2023. <https://doi.org/10.15587/1729-4061.2023.274199>
- [24] Kastens T.L. Farm machinery operation cost calculations. Manhattan, KS, USA: Kansas State University, Agricultural Experiment Station and Cooperative Extension Service, 1997. [http://extension.msstate.edu/sites/default/files/publications/publications/P3543\\_web.pdf](http://extension.msstate.edu/sites/default/files/publications/publications/P3543_web.pdf)
- [25] Edwards W.M. Estimating farm machinery costs. Iowa State University, Department of Economics, 2015. <https://www.extension.iastate.edu/agdm/crops/html/a3-29.html>
- [26] Dietmann P. Figuring the cost to own and operate farm machinery. University of Wisconsin-Extension, 2017. - p. 248. <http://128.104.248.62/ces/agmarkets/publications/documents/FiguringtheCosttoOwnandOperateFarm.pdf>
- [27] Bobkov S.I. Analysis of factors influencing on the efficiency of functioning of tractor fleet of the north region of Kazakhstan. //Tractors and Agricultural Machinery, Vol. 82, No. 8, 2015. - p. 49-51. <https://doi.org/10.17816/0321-4443-66095>
- [28] Mizanbekov I., Bekbosynov S., Lytkina L. Analysis of the state of the machine and tractor fleet of Northern Kazakhstan. //Bulletin of LN Gumilyov Eurasian National University Technical Science and Technology Series, Vol. 140, No. 3, 2022. - p. 89-103. <https://doi.org/10.32523/2616-7263-2022-140-3-89-103>
- [29] Babchenko L.A., Gulyarenko A.A. Data control for reliability of agricultural tractors. //Journal of Machinery Manufacture and Reliability, Vol. 49, 2020. - p. 900-906. <https://doi.org/10.3103/S1052618820100039>
- [30] Goryk O., Buchynskiy A., Romanyshyn L., Nurkusheva S., Bembenek M. Evaluation of the state of innovative activity of machine-building enterprise. //Management Systems in Production Engineering, Vol. 32, No. 1, 2024. - p. 1-11. <https://doi.org/10.2478/mspe-2024-0001>
- [31] Iskakov R.M., et al. Improved hammers for crushers in feed production. //Russian Engineering Research, Vol. 42, No. 10, 2022. - p. 987-992. <https://doi.org/10.3103/S1068798X22100124>
- [32] Shajmuratova E.S., Babchenko L.A. Uroven' bezotkaznosti energy-sucking tractors. //International Scientific Journal-Application Republics Kazakhstan. «Poisk», Vol. 4, 2013. - p. 46-47. <https://drive.google.com/drive/folders/1nEMS8P2tgsixcEhoRkETHC1cAgNzENTJ>
- [33] Gulyarenko A.A. Influence factory hopes in the process of provision bezotkaznosti tractors in stock machine-tractor agregatov. //Vestnik Chelyabinsky State-Owned Agroinzhenernogo University, Vol. 53, 2008. - p. 46-47.

- [34] Plaksin A.M., Kachurin V.V., Vlasov D.B., Nedovodin M.A. Methodology calculations, basic management increases technical preparations agregatov v rastenievodstve. //APK Rossii, Vol. 23, No. 2, 2016. - p. 408-416. <https://elibrary.ru/item.asp?id=26239585>
- [35] Przywara A., et al. The analysis of the new farm tractors market in Poland in 2010-2020 in the context of income generated by farmers' households. //Agricultural Engineering, Vol. 26, No. 1, 2022. - p. 65-79. <https://doi.org/10.2478/agriceng-2022-0006>
- [36] GOST 23554.0-79 Control system quality products. Expert methodology ocenki quality industrial products. Main polozheniya. Moscow: Izdatel'stvo Standartov, 1979. - 22 p. <https://files.stroyinf.ru/Index2/1/4294741/4294741906.htm>
- [37] GOST 24294-80. Definitions koefficientov weights at complex ocenke technical level and quality products. Moscow: Izdatel'stvo Standartov, 1980. - 9 p. <https://files.stroyinf.ru/Data2/1/4294741/4294741765.pdf>
- [38] Liaskos S., Khan S.M., Mylopoulos J. Modeling and reasoning about uncertainty in goal models: a decision-theoretic approach. //Software and Systems Modeling, Vol. 21, No. 6, 2022. - p. 1-24. <https://doi.org/10.1007/s10270-021-00968-w>
- [39] Hanea A.M., Hemming V., Nane G.F. Uncertainty quantification with experts: Present status and research needs. //Risk Analysis, Vol. 42, No. 2, 2022. - p. 254-263. <https://doi.org/10.1111/risa.13718>
- Dhillon B.S. Applied reliability for engineers. CRC Press, 2021. <https://doi.org/10.1201/9781003132103>

#### **Information of the authors**

**Gulyarenko Alexandr Alexandrovich**, PhD, associate professor, S. Seifullin Kazakh Agrotechnical University  
e-mail: [gulyarenko@mail.ru](mailto:gulyarenko@mail.ru)

**Bembenek Michal**, d.t.s., professor, AGH University of Krakow, S. Seifullin Kazakh Agrotechnical University  
e-mail: [bembenek@agh.edu.pl](mailto:bembenek@agh.edu.pl)

**Iskakov Ruslan Maratbekovich**, c.t.s., acting Professor, S. Seifullin Kazakh Agrotechnical University  
e-mail: [rus.iskakov79@mail.ru](mailto:rus.iskakov79@mail.ru)

**Shaimuratova Elmira Serikovna**, doctoral student, S. Seifullin Kazakh Agrotechnical University  
e-mail: [emi\\_2009@mail.ru](mailto:emi_2009@mail.ru)

**Gulyarenko Anna Viktorovna**, software engineer, S. Seifullin Kazakh Agrotechnical University  
e-mail: [9103170@mail.ru](mailto:9103170@mail.ru)

## Research of the Causes of Defects Type “Dent” on the Linear Part of the Main Pipelines

**Berdik M.\*, Blaginina M., Beckles Z., Laipanov R.**  
Peoples' Friendship University of Russia, Moscow, Russia  
\*corresponding author

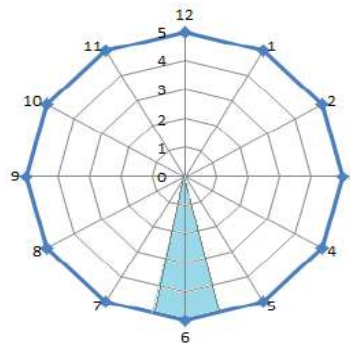
**Abstract.** This article discusses the main reasons for the formation of defects such as dents on the main pipelines. As a rule, the presence of dents is typical for laying in conditions of rocky soil or permafrost. In this case, fairly large rock fragments appear at the base of the trench, which act on the pipe with a force equal to the weight of the pipe and the weight of the back fill soil. This is why most of the dents form on the bottom surface of the pipe. As a method of combating the formation of dents, back filling of soft soil at the base of the trench is usually used, but these measures lose their effectiveness because over time the soil from the base of the trench is washed away and the metal of the pipe comes into contact with the stone fragment. This article examines the process of dent formation through numerical simulation. The procedure for modeling is considered, and the results obtained are analyzed. The dimensions and shape of the dents obtained during numerical modeling coincide with the parameters of the dents recorded on real objects. The purpose is to study the mechanism of dent formation on large diameter pipes under the influence of static load caused by external force factors. The scientific novelty lies in the refutation of the theory suggesting the possibility of dents on large diameter steel pipelines solely as a result of dynamic action from moving parts of the construction equipment or pipe impact during a fall. The study proved that a dent can form under the influence of static load. The parameters of the dent obtained during the simulation coincide in shape and size with the dents found on real pipelines, which confirms the nature of the formation of dents due to the static effect of the pipe's own weight and the weight of the filling soil.

**Keywords:** rocky soil, defects, numerical model, dents, pipeline, static load.

### Introduction

When inspecting the linear part of the main oil and gas pipelines, geometry defects often occur, which include dents. A dent is a local change in the shape of the pipe surface that is not accompanied by a thinning of the wall. A dent is formed as a result of the interaction of a pipe with a solid body that does not have sharp edges, and this interaction is usually dynamic in nature [1 - 10].

According to diagnostic data carried out by specialized organizations, similar defects in the shape of pipe sections were recorded during in-line flaw detection (ILFD) on a section of the linear part of the main gas pipeline (MG) with a total length of 450 km. A total of 14 dents were found on the investigated section of the route. All detected dents were located in the lower part of the pipe. The hourly orientation of the locations of detected defects along the pipe cross-section is presented in Figure 1. The depth of the detected dents varies from 15 to 33 mm, which is 1.1 – 2.4% of the outer diameter of the pipe, the length of the dent along the longitudinal axis of the pipe ranges from 390 to 1830 mm. A similar situation is revealed during diagnostics of the linear part of oil pipelines. To a greater extent, this problem manifests itself in sections located in mountainous areas, as well as in areas characterized by permafrost. Thus, we can say that the problem of the formation of defects in the shape of a pipe section is a pressing issue for both the oil and gas industries



**Fig. 1.** - Clockwise orientation of the dent locations, discovered during the technical inspection of a section of the main pipeline (compiled by the authors)

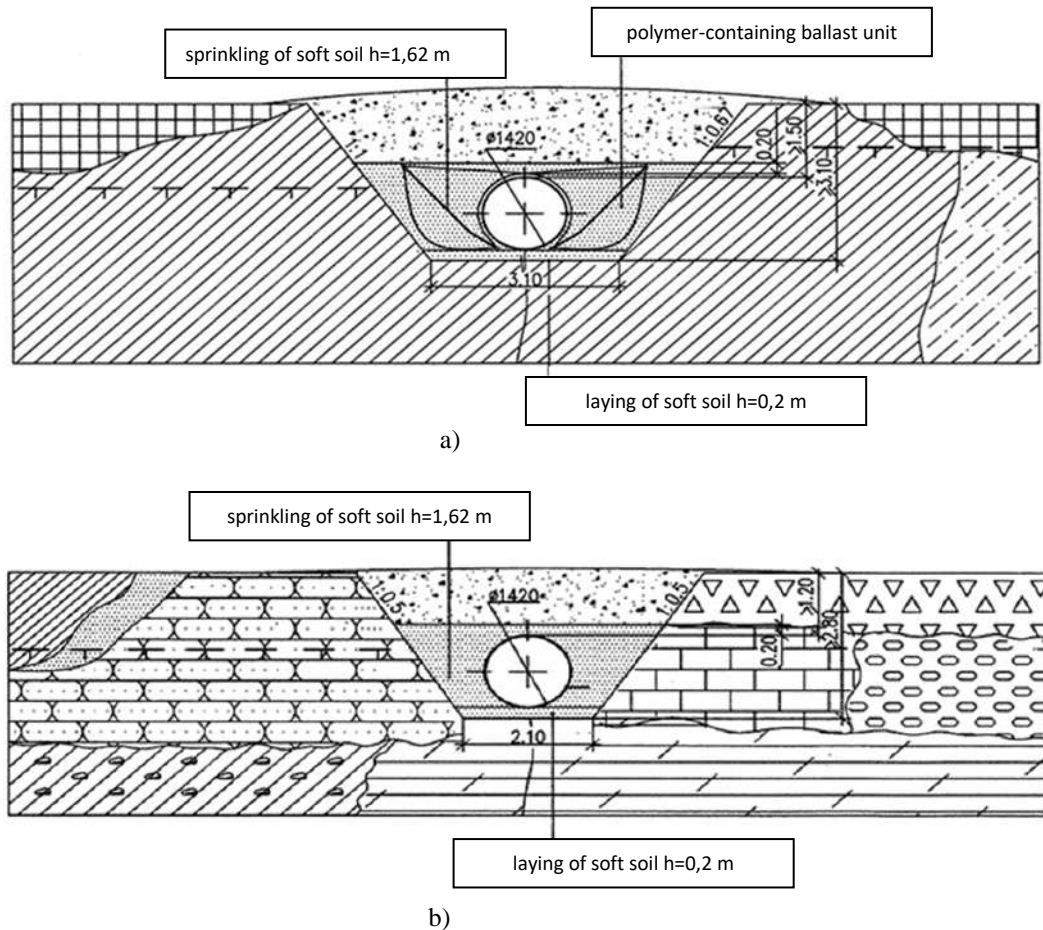
The purpose of this work was to identify the causes of the formation of such defects while complying with all design decisions made by the project.

The study was carried out using the example of individual areas with identified defects. Based on the results

of an analysis of soil conditions in the areas under consideration with recorded violations, it was established that the trench was laid either in icy frozen soil containing coarse material (pebbles and gravel) or in rocky soil. Both cases of the project assume the presence of a leveling layer of sand 0.2 m high (Figure 2).

Thus, taking into account the peculiarities of laying MG in rocky and frozen icy soils, taking into account this definition, it was assumed that the formation of dents is possible with the simultaneous presence of the following factors:

- in the soil of the base of the MG there are large rock fragments or protruding fragments of underground rock masses;
- the MG route passes through rough terrain with successive alternation of ascents and descents, which can lead to the washing out of the leveling layer.



a - in frozen, icy soils; b - in rocky soils

Fig. 2. - Trench execution schemes (Instructions for evaluating the operability and rejection of pipes with corrugations (dents), 2002)

In addition, an analysis of the conditions for the formation of dents showed that some of the detected defects are located at the border of rocky and frozen soils. This fact can be explained by the fact that during the seasonal thawing of frozen soils, significant settlement occurs, as a result of which rock ledges are formed at the border with non-subsidence rocky soil. Such ledges can also lead to dents.

### 1. Materials and Methods

The assumptions made were verified by computer modeling of the interaction of the pipeline with a rock fragment. The modeling was carried out using the ANSYS universal calculation complex. The problem was solved in a static formulation.

During the solution, two main models of dent occurrence were considered:

- the presence of large rock fragments under the pipe (size up to 0.2 m);
- the presence of a protruding fragment of a rock mass at the border with frozen loam.

Thus, in both cases under consideration, the contact problem of interaction of a pipeline with an absolutely rigid body is solved. The loads were set by the pipe's own weight, as well as vertical pressure corresponding to the weight of the back fill soil. In order to solve this problem, the length of the modeled section was taken to be 30 m. The choice of length was carried out based on the condition that the value of free loss from the action of external



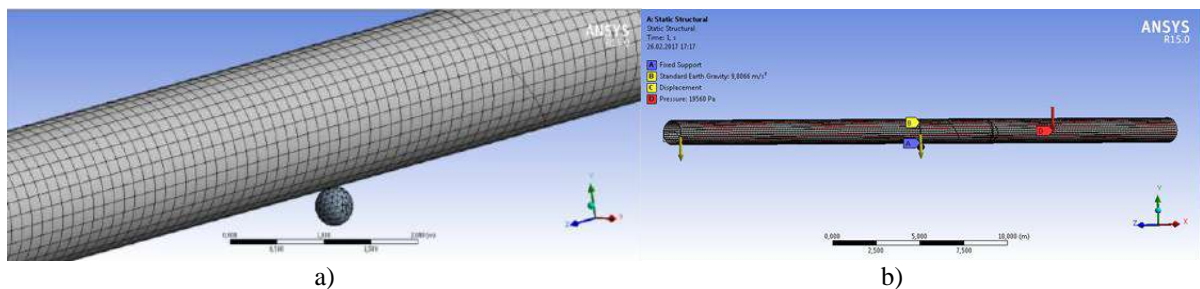
load should exceed 0.2 m.

The vertical pressure from the weight of the soil was taken equal to 27,220 Pa. This value was obtained under the assumption that the back fill soil is loam with a density of 1630 kg/m<sup>3</sup>, the height of the back fill above the upper pipe formation is 1.2 m.

During the modeling, it was assumed that a large fragment was exposed as a result of erosion of the leveling layer. Within the framework of the model, it was assumed that the foundation soil is not subject to deformation and erosion, that is, pipeline movements are limited by the thickness of the leveling layer and, according to the condition, should not exceed 0.2 m. This limitation allows us to simulate the gentlest situation. If the movement of the edges of the modeled area is greater due to the compliance of the foundation soil under certain conditions, then the load on the point of contact between the MG and the rock fragment will be even higher, which will lead to more significant deformations in the contact area.

A large rock fragment was modeled in the form of a solid body having the regular shape of a ball with a diameter of 0.2 m (Figure 3, a). The size of the rock fragment was determined by the size of the bedding layer of soft soil, which was assumed to be 20 cm in accordance with the design. Since the presence of sharp corners increases the perceived load due to the small contact area, the use of a solid body in the shape of a ball when modeling a rock fragment artificially “softens” the contact conditions pipeline. Thus, the occurrence of a dent upon contact with an absolutely solid ball will indicate that the formation of a dent is inevitable upon contact with a solid body of some other shape.

The boundary conditions of the model were determined by limiting the vertical movement of the edges of the modeled pipeline section (0.2 m), as well as by prohibiting the movement of the end sections of the section along the pipeline axis (Perelmuter & Slivker, 2002; Kuzbozhev, Birillo & Shishkin, 2014; Alexander & Kiefner, 1997). A solid body that imitates a large rock fragment is considered rigidly fixed. When modeling the loading, the weight components of the external load were considered. The weight of the pipeline itself was determined by its parameters (external diameter and wall thickness), as well as the properties of the material from which the pipe was made. The back fill soil was not modeled and was taken into account by additional impact in the form of vertical pressure on the surface of the pipeline, Figure 3, b.



a – finite element model; b – loading diagram of the pipeline model

**Fig. 3.** - Computer modeling of a pipeline and a large rock fragment (compiled by the authors)

As part of the creation of the second possible model for the occurrence of dents, it was assumed that a protruding fragment of the rock mass formed at the border of rocky soil and frozen loam due to significant settlement of the loam during the period of seasonal thawing or soil thawing for some other reason. In this case, as in the first case, it was assumed that contact of the pipeline with a rock fragment is possible only if the leveling layer is washed out.

When modeling the base of the pipeline section, it was assumed that a protrusion formed at the boundary between rocky soil and frozen loam, represented in the model as a difference in heights of the upper boundary of the base of the pipeline (Figure 4). Moreover, within the framework of this model, the difference in heights was taken to be equal to the thickness of the leveling layer (0.2 m). In fact, the amount of settlement can be significantly higher, which, accordingly, will lead to an increase in pressure at the point of contact of the pipeline with the protruding part of the rock mass.

The base along the entire length of the modeled section is assumed to be absolutely rigid.

When solving, two contact pairs were specified: “pipeline - protruding fragment of the rock mass” and “pipeline - section of the base corresponding to frozen loam.” Thus, when solving, the pipeline model will not “fall” through the base, but will come into contact with it.

As boundary conditions, the fastening of the lower surfaces of both parts of the base, as well as symmetry on the end surfaces of the modeled section of the pipeline, are accepted. As in the previous case, the loads were taken to be the pipe’s own weight and the vertical pressure on the pipe surface, numerically corresponding to the weight of the back fill soil.

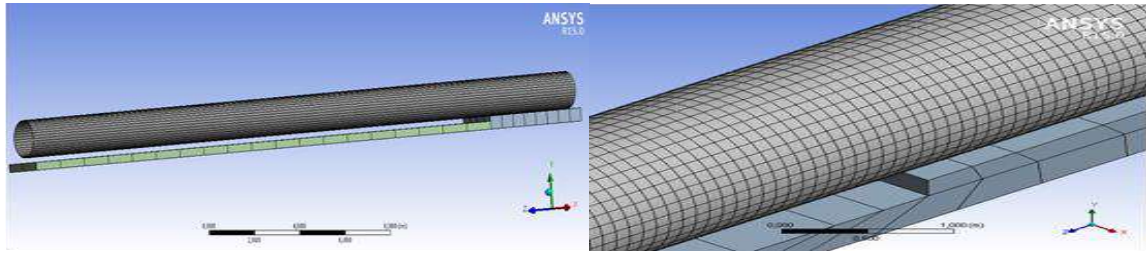


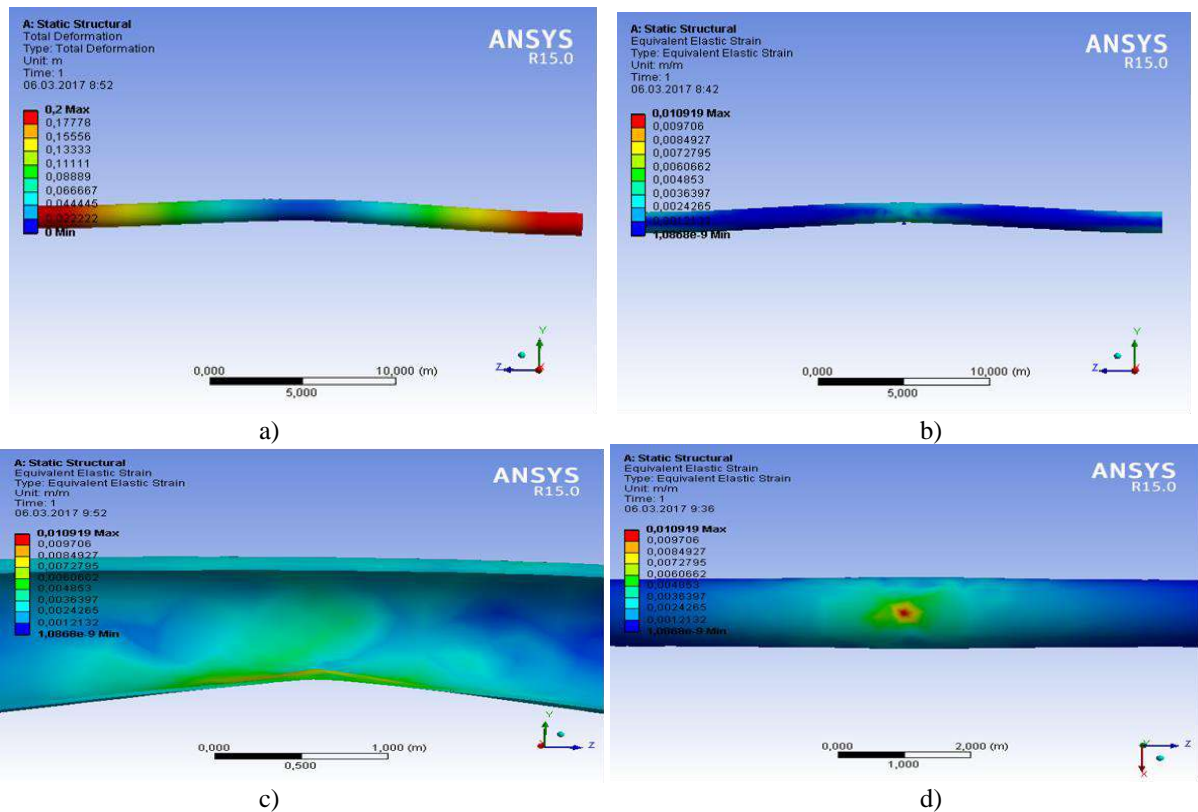
Fig. 4. - Finite element model of the pipeline and its foundation (compiled by the authors)

## 1. Results

As a result of the given loads, a solution was obtained that included pipeline movements, as well as deformations in the contact zone. The solution to the first problem is presented in Figure 5.

Figure 5a indicates that the boundary conditions are set correctly and the edges of the modeled area do not “sink” into the foundation soil. The maximum pipeline movements do not exceed 0.2 m. In this case, the contact area does not move due to the rigid fastening of a solid body simulating a large rock fragment. The simulation showed that under the given conditions, the maximum deformation is observed at the point of contact and is 10.9 mm. The resulting dent is oval in shape and stretched along the axis of the pipeline. The length of the dent is about 2 m. The shape of the resulting dent is shown on an enlarged scale in the section shown in Figure 5, c, d.

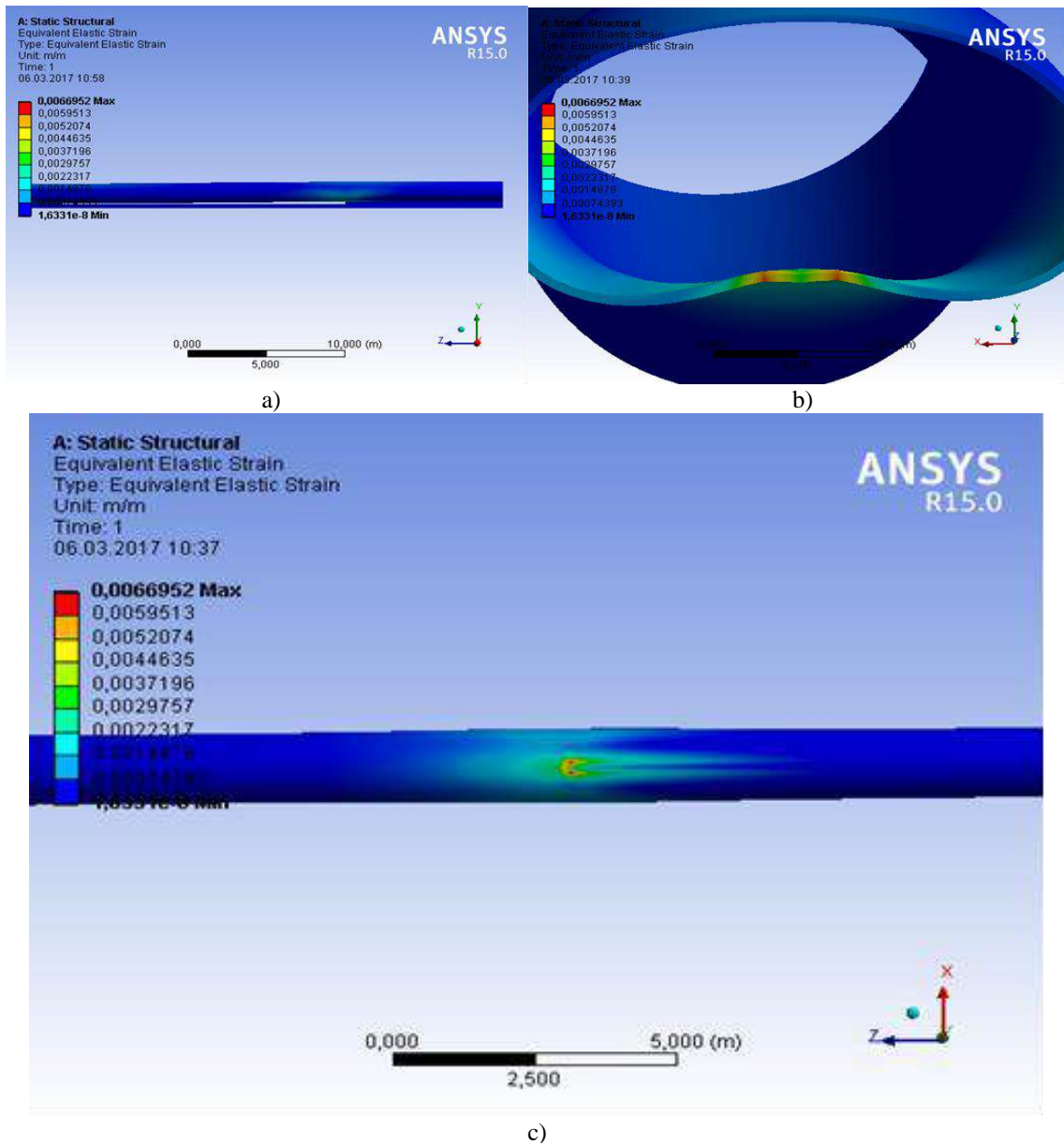
Thus, the results of the modeling show that at the point of contact of a large rock fragment with a pipe, caused by settlement or washout of the leveling layer of sandy back fill soil, a dent may form under the influence of the weight of the pipe and the back fill soil. At the same time, the shape and dimensions of the dent obtained during modeling correspond to the in-line diagnostic data.



a – pipeline movements; b – deformation of the simulated pipeline section; c – deformation of the simulated pipeline section (view of the contact point, display of a solid body simulating a large rock fragment is disabled); d – shape of the dent formed as a result of contact of the pipeline with a separate rock fragment

Fig. 5. Results of the interaction of the pipeline with a rock fragment under specified loads (compiled by the authors)

When solving the second problem, the resulting solution differs in both the size and shape of the dent. The result of the contact of the pipe with the protruding rock mass is presented in detail in Figure 6.



a) deformation of the pipeline metal at the point of contact with a protruding fragment of the rock mass; b) shape of the dent in plan; c) stresses at the point of contact with a protruding fragment of the rock mass

**Fig. 6.** Results of interaction of the pipeline with the speaker fragment of a rock mass.  
(compiled by the authors)

From Figure 6 it can be seen that the maximum displacements correspond to the left end of the modeled section. For a pipeline section 30 m long, which is under its own weight and the weight of the back fill soil, the maximum displacement is 0.17 m. That is, the maximum displacement did not reach the maximum permissible value, accepted according to the conditions of this problem as 0.2 m. Thus, in real life conditions where the length of the pipe is not limited, when frozen soil subsides by 0.2 m, the pressure on the area of contact of the pipeline with the protruding rock mass will be higher than in the adopted model due to the greater length of the sagging section.

The metal deformations are presented in Figure 6. As can be seen, the presence of deformations is observed only in the area of contact between the pipeline and the protruding rock fragment.

The simulation showed that under the given conditions, the maximum deformation is observed at the point of contact and is 6.7 mm. The resulting dent is oval in shape and stretched along the axis of the pipeline. The length of the dent is about 2 m. It should be noted that the dent obtained during computer modeling has an atypical shape; it is elongated along the axis and has two centers.

The shape of the resulting dent in plan is shown in Figure 6c. The wall deformation is shown on an enlarged scale in the section shown in Figure 6b.

Thus, the results of the simulation show that at the boundary of rocky soil and frozen loam on the pipe, a dent may form under the influence of the weight of the pipe and the back fill soil. The formation of a dent is possible

when there is significant settlement of loam caused by its thawing, and in the absence of a leveling layer at the bottom of the trench.

## **2. Discussion**

The results obtained have important practical significance. Today, many researchers argue that the formation of a dent is possible solely as a result of the dynamic impact on the main pipelines from the moving parts of construction machines or in case of violation of the laying technology, when the formation of a dent occurs as a result of a falling pipe [14-16].

This assumption was indirectly refuted by the results of statistics on detected defects such as dents. Since most of them were located on the lower surface of the pipe, then each such dent should have been formed during the fall, however, such a violation of technology, repeated many times, is very doubtful. In this case, static loads caused by the weight of the pipe and the weight of the back fill soil led to the occurrence of a reaction at the points of contact of the metal with a fragment of rocky soil, and the maximum values of such reactions correspond precisely to the lower surface, since in this case the load consists simultaneously of both the weight of the pipe and the back fill weight.

Thus, the results obtained confirmed the possibility of dent formation on pipelines during long-term static exposure. In this case, formation is possible only in the case of direct contact of the pipe with a protruding solid fragment. If you exclude the possibility of such contact, then the formation of dents will not occur.

Measures to prevent contact of the pipe body with hard fragments of soil include the use of supports for laying the pipeline in a trench, the use of synthetic non-woven material to hold the bedding soil at the base of the pipe, the use of wooden lining or any other protective structure [17-20].

## **Conclusions**

As a result of numerical modeling, confirmation was obtained of the possibility of dents occurring under the influence of static load from the pipe's own weight and the weight of the back fill soil. Moreover, in both cases considered, one of the prerequisites is the erosion of the leveling layer and, as a consequence, the exposure of fragments of rocky soil. Thus, we can say that the presence of protruding hard fragments at the base of the MG is fraught with the occurrence of dents if the laying conditions suggest the possibility of their exposure.

As measures to reduce the likelihood of dents occurring, we can recommend measures to prevent erosion of the leveling layer or to prevent contact of the MG metal with possible protruding fragments.

## **References**

- [1] Instructions for evaluating the operability and rejection of pipes with corrugations (dents) (2002). Directive document of Gazprom 39-1.10-063-2002 from June 17, 2002. Gazprom, Russia.
- [2] Błachut, J. & Iflefel, I. Experimental and Numerical Investigation of Plain and Gouged Dents in Steel Pipes Subjected to Pressure and Moment Loading. *Journal of Pressure Vessel Technology-transactions of The Asme*, 2008, 130(2). DOI: 10.1115/1.2891913.
- [3] Błachut, J. & Iflefel, I.B. Analysis of pipes containing plain and gouged dents. *Strain*, 47, 2011, e34–e51. DOI: 10.1111/j.1475-1305.2008.00478.x
- [4] Dawson, J., Murray, I. & Hedger, J. Methods of extended assessment of dents on pipelines. *Journal of Pipeline Engineering*, 17, 2018
- [5] Rinehart, A. J., & Keating, P. B. Forecasting the fatigue life of extended dents in oil pipelines. In *International Conference on Marine Mechanics and Arctic Engineering*, 36142, 2002, 1–9. DOI: 10.1115/PVP2002-1268
- [6] Zhu, L., Wu, G., Li, L., Luo, J., Tian, Y., Xu, C., & Lin, R. Deformation characteristics of X80 linear discs with smooth surfaces. *Natural Gas Industry B*, 7(1), 2020, 49–55.
- [7] Zhao, J., Lv, Y.R. & Cheng, Y.F. (2022). Standards and methods for assessing dents and predicting pipeline failures: a critical review. *The science of oil*, 19(6), 2022 DOI:10.1016/j.petsci.2022.10.003
- [8] Zhu, X. K., & Wang, R. (2018, September). The effect of residual stresses or plastic deformation history on modeling the fatigue life of dents in pipelines. At the *International Conference on Pipelines*, 51869, V001T03A080. DOI: 10.1115/IPC2018-78805
- [9] Dinovitzer, A., Lazor, R., Carroll, L.B., Zhou, J., McCarver, F., Ironside, S. & Keith, K. Geometric dent characterization. In *International Pipeline Conference*, 36207, 2002, 1589–1598. DOI: 10.1115/IPC2002-27076
- [10] Ahmad, R., Banerjee, S. & Kundu, T. (2009). Pipe Wall Damage Detection in Buried Pipes Using Guided Waves. *Journal of Pressure Vessel Technology, Transactions of the ASME*, 131(1). 2009 DOI: 10.1115/1.3027460
- [11] Perelmuter, A.V. & Slivker, V.I. Design models of structures and the possibility of their analysis. Kiev, Stal Publishing House, 2002, 600.
- [12] Kuzbozhev, A.S., Birillo, I.N. & Shishkin, I.V. (2014). Deformation of the gas pipeline from frost heaving of the soil. *News of higher educational institutions. Oil and Gas*, 2, 56–60.
- [13] Alexander, C. R. & Kiefner, J. F. The effect of dents from smooth surfaces and stones on pipelines for liquid petroleum products. At the *API Pipeline Conference in 1997*, Dallas, Texas.
- [14] Yakovlev, A.Ya., Alennikov, S.G., Romantsov, S.V., Elfimov, A.V., Kuzbozhev, A.S., Birillo, I.N. & Shishkin, I.V. Calculation model of ascent and precipitation of the Bovanenkovo – Ukhta main gas pipeline during

thawing of permafrost soils. Gas industry, 2014, 2(702), 39–43.

[15] Kuzbozhev, A.S., Birillo, I.N. & Berdnik, M.M. Investigation of the influence of the step of measuring the profile of a gas pipeline on the accuracy of calculating the bending radii of its axis. Scientific works of NIPI Neftegaz SOCAR, 4, 2014, 43–49. DOI 10.5510/OGP20180400370.

[16] Alashti, R.A., Jafari, S. & Hosseinipour, S.J. Experimental and numerical investigation of ductile damage effect on load bearing capacity of a dented API XB pipe subjected to internal pressure. Engineering Failure Analysis, 47, 2015, 208–228 DOI: 10.1016/j.engfailanal.2014.10.011

[17] Berdnik, M.M., Terentyeva, M.V., Semitkina, E.V. & Semitkin, I.V. Composite or steel: modeling of the construction of a non-metallic protective case of the IHL at a crossing over a highway. *Business Magazine Neftegaz.RU*, 12(132), 2022, 54–62.

[18] Tian, X., & Lu, M. Failure mechanism of long-distance pipelines having gouged dents. Engineering Failure Analysis, 140, 2022, 106579. DOI: 10.1016/j.engfailanal.2022.106579

[19] Ghaednia, H., & Das, S. Structural performance of oil and gas pipe with dent defect. Journal of Pipeline Systems Engineering and Practice, 9(1), 2018, 04017031. DOI: 10.1061/(asce)ps.1949

[20] Alexander, C. R. Analysis of dented pipeline considering constrained and unconstrained dent configurations. At the Conference and Exhibition on Energy Source Technologies, Texas, 1999. - 1204.0000301

### Information of the authors

**Berdik Maria**, PhD, associate professor, Peoples' Friendship University of Russia  
e-mail: [berdnik.rudn@list.ru](mailto:berdnik.rudn@list.ru)

**Blaginina Maria**, assistant, Peoples' Friendship University of Russia  
e-mail: [blaginina.rudn@mail.ru](mailto:blaginina.rudn@mail.ru)

**Beckles Zefanja**, assistant, Peoples' Friendship University of Russia  
e-mail: [beckles.rudn@mail.ru](mailto:beckles.rudn@mail.ru)

**Laipanov Radmir**, assistant, Peoples' Friendship University of Russia  
e-mail: [laipanov.rudn@mail.ru](mailto:laipanov.rudn@mail.ru)

## Nanostate Factor in Materials Science of Functional Nanocomposite Materials

Avdeychik S.V.<sup>1</sup>, Antonov A.S.<sup>2\*</sup>, Struk V.A.<sup>2</sup>, Prokopchuk N.R.<sup>3</sup>, Zhang R.<sup>4</sup>

<sup>1</sup>Francisk Skorina Gomel State University, Gomel, Belarus

<sup>2</sup>Yanka Kupala State University of Grodno, Grodno, Belarus

<sup>3</sup>Belarusian State Technological University, Minsk, Belarus

<sup>4</sup>Zhejiang International Scientific and Technological Cooperative Base of Biomedical Materials and Technology, Zhejiang Engineering Research Center for Biomedical Materials, Laboratory of Advanced Theranostic Materials and Technology, Ningbo Institute of Materials Technology and Engineering, Chinese Academy of Sciences, Ningbo, People's Republic of China

\*corresponding author

**Abstract.** Based on the system analysis of the features of the morphological and energy parameters of dispersed components of condensed matter of various compositions, their structure and production technology, methodological approaches to the implementation of the nanostate phenomenon in the formation of the optimal structure of composite materials and metal-polymer systems at different levels of organization have been developed. The concept of energy and technological compliance of the components of functional composite materials and systems has been developed, consisting in the implementation of the parameters of their energy characteristics adequate to the value of the activation energy of the prevailing structural process, which determines the optimal parameters of stress-strain, adhesive and tribological characteristics, under technological effects on the components in the process of obtaining a composite and its processing. Scientifically based principles for the creation of nanocomposite materials with high parameters of stress-strain, adhesive and tribological characteristics based on industrial thermoplastics for functional metal-polymer systems and effective technologies for their manufacture and processing into products, the novelty of which is confirmed by patents for inventions are proposed.

**Keywords:** nanostate phenomenon, nanocomposite structure, concept of energy and technological compliance of components, principles of obtaining and processing nanocomposites, industrial thermoplastics

### Introduction

In the brand range of modern engineering materials, a special place belongs to nanocomposites based on polymer, oligomeric and combined matrices, which, according to a number of performance characteristics, are the non-alternative materials in the production of automotive, special, agricultural machinery and technological equipment for thermal power plants, petrochemical and processing complexes. At the same time, the potential of such matrices produced by the domestic industry in the creation of functional nanocomposites is not fully realized, despite the developed base of their large-tonnage production and the equipping of enterprises with modern technological equipment [1–5].

The mechanism and kinetics of the processes of structure formation of composite materials at different levels of the organization are determined by the activation energy, which depends on the parameters of the energy characteristics of the components under a given technological impact. Studies by domestic and foreign specialists have established the effect of the transition of a material particle upon reaching a certain size range into a state with special parameters of energy characteristics, which is called a nanostate according to the established terminology [6–10]. It is obvious that the achievement of the nanostate by the component will have a significant impact on the structural processes in the composite material at different levels of organization, which determine the parameters of stress-strain, tribological, adhesive and other characteristics of products in metal-polymer systems.

At the same time, despite the experimentally established influence of energy parameters on structuring processes, there are no systematic studies of methodological approaches to the implementation of the nanostate phenomenon in materials science and technology of nanocomposite materials based on industrial polymers.

The purpose of this work was to develop methodological approaches to the implementation of the phenomenon of nanostate at various levels of organization of the structure of nanocomposites for the creation of functional materials based on industrial thermoplastics with high performance parameters.

### 1. Research methodology

Nanodispersed particles of carbon-containing (graphite, detonation synthesis ultra-dispersed diamonds (UDD), carbon nanotubes (CNT), shungite, carbon fibers (CF)), metal-containing (oxides, salts of organic acids) and silicon-containing (mica, tripoli, opal, clay) compounds obtained by technological effects on natural and synthetic semi-finished products produced at industrial enterprises in Belarus and the Russian Federation were chosen as the main objects of the study. Nanoscale components were obtained by mechanical crushing and heat treatment of dispersed semi-finished products at temperatures of 673–1473 K.

Two main types of thermoplastic materials were used as polymer matrices: the first are with hereditary high melt viscosity (HHMV) due to the chemical structure of the chain and molecular weight: polytetrafluoroethylene (PTFE) and ultra-high molecular weight polyethylene (UHMWPE); the second are materials with acquired high melt viscosity (AHMV): industrial thermoplastic polymers such as polyamide PA6, low density polyethylene (LDPE), ethylene vinyl acetate (EVA) copolymer, polypropylene (PP), thermoplastic polyurethane (TPU), etc., with characteristic parameters of rheological properties that were changed by the introduction of nanoscale modifiers.

The structure and properties of nanocomposite materials and products made of them were studied using modern methods of physical and chemical analysis: IR transmission spectroscopy and attenuated total reflectance (ATR) technique (Specord), spectroscopy of electron paramagnetic resonance (EPR) (PЭ 1306, Bruker), X-ray diffraction (Drone 3.0), differential thermal analysis (Q-1500), optical (MF-2), scanning electron (ISM-50A) and atomic force (Nanotope III) microscopy. The energy state of nanoscale modifiers and composite materials was evaluated using EPR spectra and temperature-stimulated current (TSC) spectra at the original facility of the V.A. Belyi Metal-Polymer Research Institute of National Academy of Sciences of Belarus. The regulation of the nanorelief of the surface layer of polymer samples and fillers was carried out using short-pulse laser and accelerated ionic action with a given power density.

The parameters of the stress-strain characteristics of the developed materials were evaluated on standard samples according to the relevant Russian standards. Tribological characteristics were determined on universal or original friction machines according to the schemes "indenter – disk", "shaft – partial liner". Assessment of the performance of products made of developed nanomaterials in the structures of automotive units for various purposes and technological equipment was carried out on stands and in the process of virtual tests using the SKIF supercomputer and full-scale tests.

## 2. Results and discussion

Multicomponent materials based on high-molecular matrices are systems, the parameters of characteristics (stress-strain, tribological, adhesive, thermophysical, etc.) are determined by the structure at various levels of organization, formed by physical and physicochemical processes, the mechanisms and kinetics of the flow of which depend on the composition of components and the parameters of technological characteristics. In the interfacial region of the system, a complex of physical and physicochemical reactions takes place simultaneously with a predominance of one or several, for which the most favorable conditions are realized, determined by the value of the activation energy. Such a prevailing reaction, the kinetics of which is in accordance with the conditions of formation and operation of the system, determines the resistance of an element made of a composite or metal-polymer system to the impact of operational factors.

A methodological approach to the formation of composites, based on the establishment of the prevailing physicochemical reaction, made it possible to establish a correlation between the parameters of the structure and energy characteristics of the components (energy state) [11, 12].

To characterize *the energy state*, a complex parameter was used, which is a cumulative result of the transformation of the initial individual parameters of the components (structure, composition, morphology, shape, size) under the influence of technological and operational factors. A characteristic feature of the proposed methodological approach is the possibility of purposeful intensification of prevailing interfacial reactions by forming the energy state of components with certain parameters of electrophysical characteristics.

Using the concepts of condensed matter physics, the conditions for the acquisition of a nanostate by a material object are determined, which can manifest itself when the dimensional parameter  $L_0$  is reached by both a single particle and the components of the surface layer of a particle or substrate of the micro- and macro-range. To analyze various types of interfacial interactions in systems based on the energy factor, the definition of "nanostate" is proposed, which makes it possible to identify the main forms of its manifestation [13–19].

The concept of energy and technological compliance of components has been developed for the formation of systems with optimized parameters of structural characteristics at various levels of the organization.

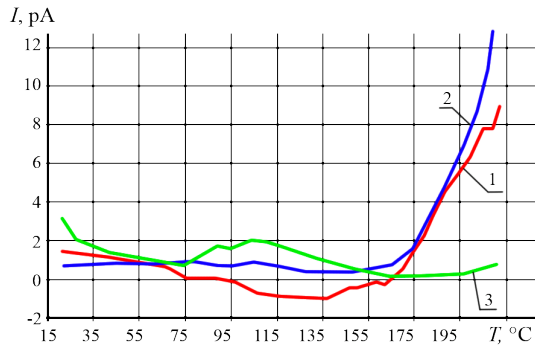
*The energy compliance of components* assumes the possibility of achieving an aggregate energy state that corresponds to the activation energy of the prevailing physicochemical process that ensures the formation of an optimal structure at the intermolecular, supramolecular, and interphase levels of organization in composites or metal-polymer systems.

The formation of the interfacial (boundary) layer of the optimal structure indicates the *technological compliance of the components* of functional materials and metal-polymer systems, which is understood as the possibility of their achieving the specified energy parameters at a certain stage of the formation of a composite, product or structure that ensures the flow of the prevailing mechanism of interfacial interaction.

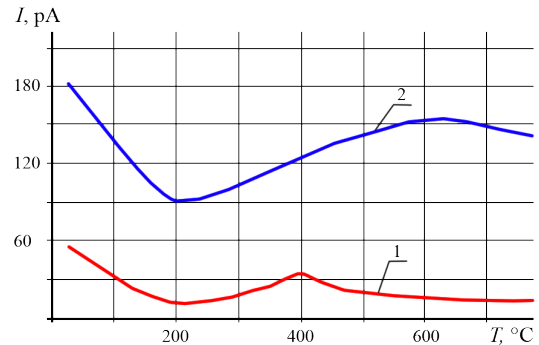
Physical and physicochemical processes are due to the transfer of electrons during the formation of intermolecular, supramolecular, interfacial structures, which determined the choice of the maximum value of the thermostimulated current (TSC) in the temperature range adequate to the technological modes of production, processing of composites and the operation of metal-polymer units as a determining parameter for assessing the energy state of the components of the systems.

The analysis of the parameters of the energy state of dispersed particles of various composition, structure and production technology, which are widely used in materials science of polymer nanocomposites (silicon-

containing – clay, mica, talc, tripoli, carbon-containing – UDD, CNT, CF, shungite, colloidal graphite product (CGP), metal-containing – particles of metals and oxides), indicates the nonlinearity of the dependence of the TSC value on temperature, the presence of extremes in the temperature ranges characteristic of each type modifier, and instability  $I = f(T)$  when changing dimensional parameters, dispersion modes, intensity of the impact of temperature, mechanical and other energy and technological factors. The characteristic type of TST spectra of particles of products of thermogasdynamic synthesis (ultradispersed polytetrafluoroethylene UPTFE), silicon, shungite with a size of 50–100  $\mu\text{m}$  is shown in Fig. 1 and 2. The nonlinearity of the dependence  $I = f(T)$  is also characteristic of other objects of organic and inorganic nature, of different composition, structure, and molecular weight.

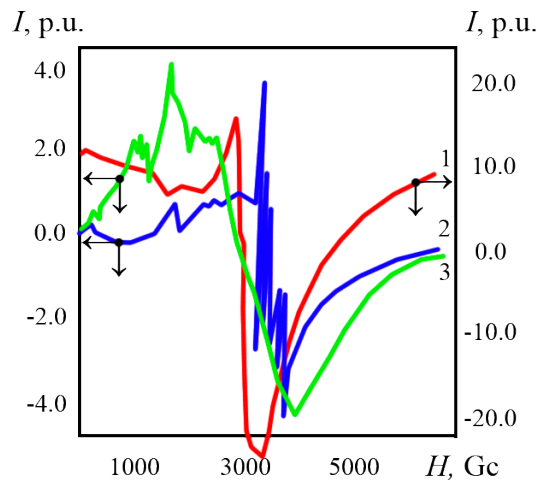


**Fig. 1.** – Characteristic TSC spectrum of products of thermogasdynamic synthesis (UPTFE) initial (1) and heat-treated at 373 K (2), 473 K (3)



**Fig. 2.** – Dependence of the value of the maximum thermally stimulated current (TSC) on the temperature for particles of silicon (1), shungite (2). Particle dispersion 50–100  $\mu\text{m}$

A characteristic feature of dispersed particles of common modifiers of high-molecular matrices is the presence of an uncompensated charge with a long relaxation time, which is confirmed by the data of EPR spectroscopy (Fig. 3).



**Fig. 3.** – EPR spectra of opal (1) and clay minerals of various compositions (2, 3). Sample dispersion is 100–200  $\mu\text{m}$

Along with special parameters of electrophysical characteristics due to the peculiarities of composition and structure, material particles can be in a nanostate, the concepts of which were proposed by Prof. P. von Weimarn, P. M. Ajan, I. P. Suzdalev, A. I. Gusev, and others, under certain types of technological action that change the size, geometric characteristics, and morphology of the surface layer. The size range of the transition of material objects into the nanostate is individual for particles of different composition and structure and is determined by the analytical expression proposed by V. A. Liopo, according to which the limiting size of  $L_0 = 230 \cdot \theta_D^{-1/2}$ , where  $\theta_D$  is Debye temperature. The validity of using this expression to analyze the structure of polymer nanocomposites is confirmed by system studies, the results of which are summarized in monographs [11, 12].

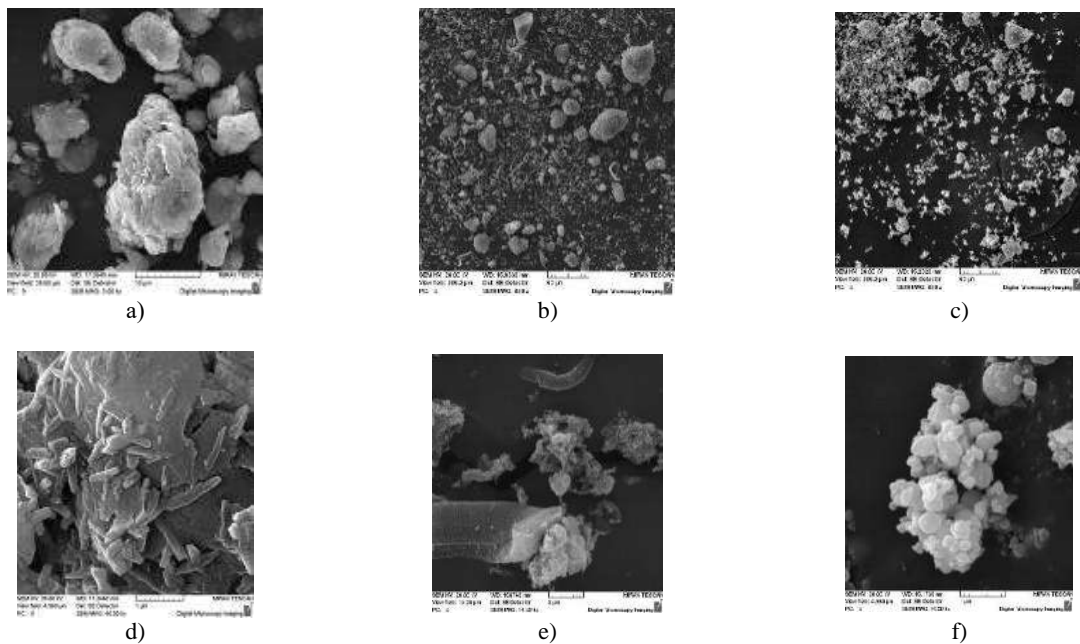
The analysis of the morphological features of dispersed particles widely used in the materials science of polymer composites using the SEM and AFM methods indicates the presence of nanoscale components in objects of the micron range that form the morphology of the surface layer (Fig. 4).

The presence of such components is the most important factor determining the activity of modifiers in the processes of formation of polymer composites at various structural levels (intermolecular, supramolecular, interphase) due to the manifestation of energy parameters characteristic of the nanostate by the surface layer of particles. Therefore, the technologies for activating polymer matrix modifiers should ensure the formation of



nanoscale components in quantities sufficient to implement the determining process of the required intensity, by establishing mechanisms for their formation under various types of technological impact on the semi-finished product.

Using the fundamental principles of condensed matter physics based on the barrier model of juvenile surface formation, mechanisms for dispersion of layered minerals such as mica, talc, kaolin with the formation of nanoscale components of lamellar shape are proposed. It has been established that the determining processes of degradation of particles in the micrometer range are dehydration and dehydroxylation, which cause the destruction of the original layered structure and the formation of nanoscale elements of the lamellar form in an active state with a long relaxation time sufficient for implementation in the technology of polymer nanocomposites [1, 2]. It has been experimentally established that the activity of such elements in the processes of interaction with the environment (components of the system) depends on its composition, temperature and time characteristics. To intensify the process of dispersion of layered minerals, it is advisable to use thermal shock at temperatures of 800–1000 K or diffusion saturation of interlayer regions with low-molecular and oligomeric media based on carbon-containing products with low resistance to thermal degradation.



**Fig. 4.** – Characteristic morphology of dispersed clay particles (a, d), carbon nanotubes CNT (b, e), metal oxides (c, f)

Model studies of the dispersion of layered minerals such as mica (muscovite) have shown the possibility of forming nanoparticles with a size of 30–50 nm under the impact thermal effect on the initial semi-finished product at 1073 K for 5–20 min. The formed lamellar particles have high adsorption activity in the processes of interaction with the environment, including polymer matrices in a viscous state, and intensify the intermolecular structuring of the composite.

Dispersion of particles of layered silicates can be implemented directly in the process of obtaining or processing composite materials under thermomechanical action on the components of screws of mixers, extruders or injection molding machines. The formation of an intercalated or exfoliated nanocomposite structure provides a technically significant effect of increasing the parameters of stress-strain and tribological characteristics even with a doping content (0.1–1.0 wt.%) of the modifier.

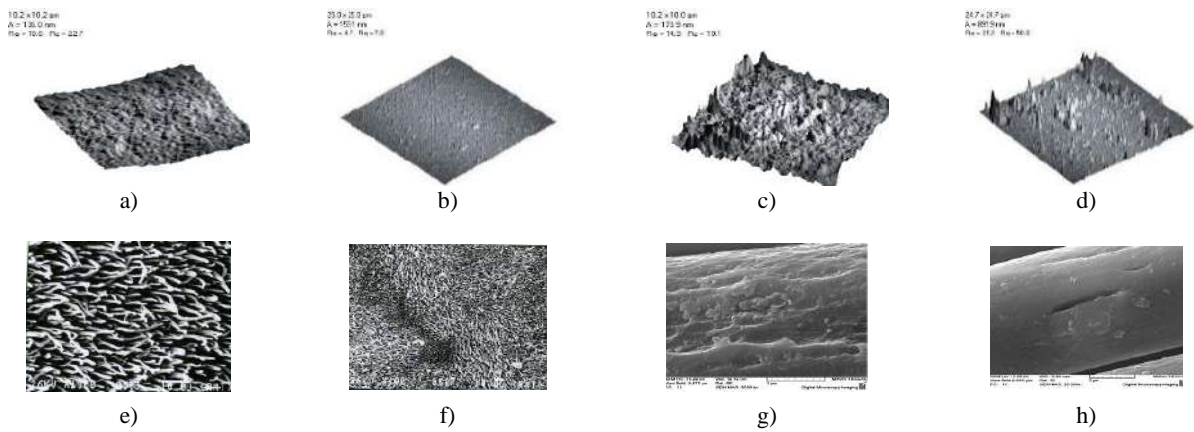
Thermal action on dispersed particles changes the energy parameters not only of layered silicates (clays, talc), but also of framework and chain (flints, zeolites) and multiphase natural (tripoli, shungite) products (Fig. 1 and 2).

An effective technology for activating dispersed particles is their dispersion under mechanical or mechanochemical action. Not only an increase in the specific surface area, but also the formation of nanoscale components in the surface layer of particles has been experimentally established. Modifiers activated in this way remain active for a technologically significant time (up to a year).

Nanoscale components of the structure of the surface layer can also be formed as a result of the impact of energy flows on the semi-finished product, i.e. ionizing, laser radiation. At the same time, not only the specific surface area of the particle, which provides the mechanical component of interfacial interaction, increases, but also the parameters of the characteristics that determine its nanostate, which affect the supramolecular structure and adsorption capacity of the surface layers of modified substrates (PET, PTFE, PP, HDPE, CF) (Fig. 5).

An energy assessment of the nanostate of polycrystalline particles is carried out to establish the temperature equivalent of geometric parameters. It is shown that for a nanoparticle, due to the increased role of surface energy in

comparison with a massive sample, there is a correlation between the size of the particle and its energy state, which can be estimated by the temperature factor.

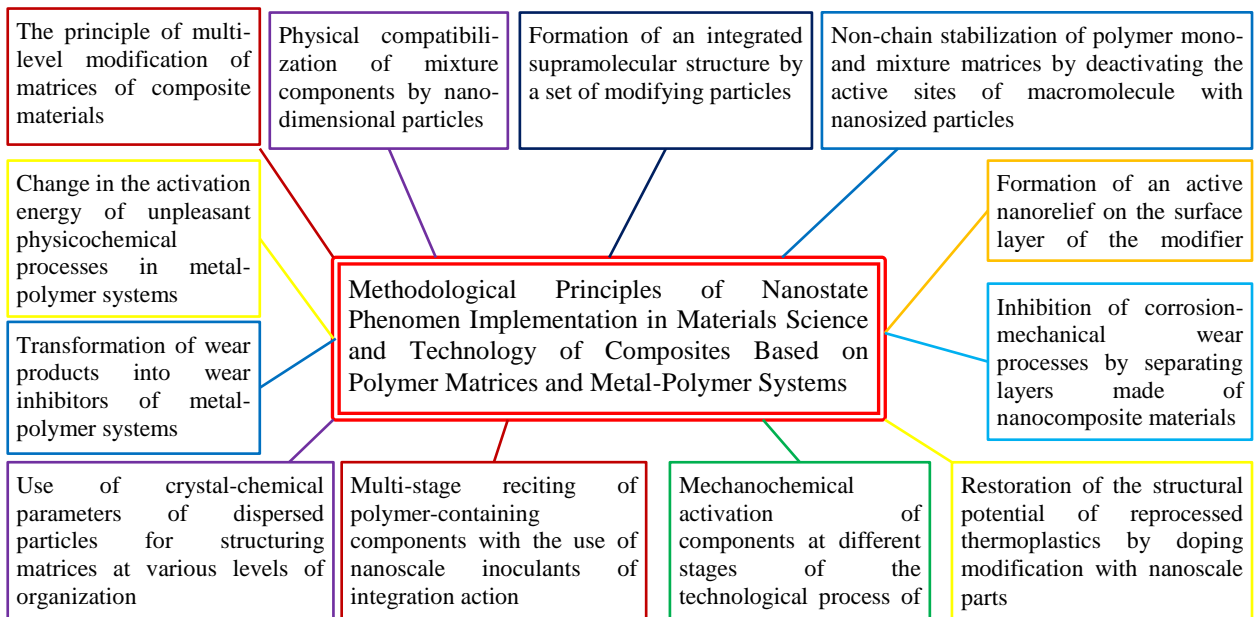


**Fig. 5.** – Characteristic morphology of the surface layer of the substrate of PTFE (e, f), PET (b, d), HDPE (a, c), carbon fiber (g, h), initial (a, b) and exposed to nitrogen ions at a dose of 1016 ion/cm<sup>2</sup> (g, h), pulsed laser radiation with a power density of 2.0 W/cm<sup>2</sup> (c, d). AFM data (a–d) and SEM (e–h)

With a decrease in the size of the  $\delta$  particle by 1%, there is an increase in energy parameters by the amount of  $\delta t = k(\delta T) \approx 3,5 \cdot 10^{-28} \text{ J}$  [20]. Therefore, the formation of nanoscale particles or nanoscale components in the structure of the surface layer of a macroparticle (substrate) is accompanied by an increase in the parameters of energy characteristics estimated by the maximum value of the thermally stimulated current and the intensity of interfacial processes in the systems.

The conducted set of studies on modeling the processes of formation of the structure of material objects with a pronounced manifestation of the nanostate made it possible to determine effective ways to achieve it in the technological processes of obtaining and processing nanocomposite materials based on matrix polymers of industrial production. The choice of the conceptual direction of the technological embodiment of the phenomenon of the nanostate is determined by a set of materials science, technological, economic, and operational factors. An algorithm for the implementation of the methodological approach has been developed, which allows, on the basis of factors that determine the nanostate of the components of the system for a specific purpose and design, to choose the technology for their implementation at a specific stage of the process, taking into account material, economic, ergonomic, environmental and other aspects.

Methodological principles for the implementation of the phenomenon of nanostate in materials science and technology of functional nanocomposites based on industrial polymer matrices and metal-polymer systems with their application, focused on the state of the domestic technological base of industrial enterprises, related mainly to the IV and V modes, are proposed (Fig. 6).



**Fig. 6.** – Methodological principles of implementation of the nanostate phenomenon in materials science and technology of composites based on polymer matrices and metal-polymer systems [15–19]

The developed principles made it possible to optimize the structure of nanocomposite materials based on polymer, oligomeric and mixed matrices of industrial production intended for the manufacture of structural elements (bearings, seals, fasteners, coatings) of static and dynamic (tribological) metal-polymer systems used in the structures of machines, mechanisms, technological equipment of domestic machine-building, chemical, processing industry, construction industry, which determine the strategy of innovative development of the economy.

The results of experimental testing of the developed methodological approaches to controlling the structural parameters of nanocomposite materials based on industrial thermoplastics are presented in Part 2 of the article.

### Conclusion

On the basis of a system analysis of the features of morphological and energy parameters of dispersed components of condensed matter of various compositions, their structure and production technology, methodological approaches to the implementation of the nanostate phenomenon in the formation of the optimal structure of composite materials and metal-polymer systems at different levels of organization have been developed. Scientifically based principles for the creation of nanocomposite materials with high parameters of stress-strain, adhesion and tribological characteristics based on industrial thermoplastics for functional metal-polymer systems and effective technologies for their manufacture and processing into products are proposed, which consist of the following:

1) The concept of energy and technological compliance of the components of functional composite materials and systems has been developed, consisting in the implementation of the parameters of their energy characteristics adequate to the value of the activation energy of the prevailing structural process, which determines the optimal parameters of stress-strain, adhesive and tribological characteristics, under technological effects on the components in the process of obtaining a composite and its processing. The reliability of estimating the parameters of the nanostate of material objects using an analytical expression to determine the limiting size of the transition to the nanostate of a nanoparticle or a component of the morphology of the surface layer according to the Debye temperature  $\theta_D$  criterion is theoretically and experimentally substantiated. A definition of the nanostate of material objects is proposed, characterizing the relationship between structural, morphological and energy parameters.

2) Methodological principles for the implementation of the nanostate phenomenon in materials science and technology of functional nanocomposites based on industrial thermoplastics of the polyolefin, polyamide, fluoroplastic class have been developed by optimizing the structure at the intermolecular, supramolecular and interfacial levels, ensuring the achievement of a synergistic combination of performance parameters based on:

- established crystal-chemical prerequisites for the selection of natural and synthetic carbon-containing, metal-containing and silicon-containing semi-finished products for the directed formation of active nanosized particles with specified structural, morphological and energy parameters under optimal technological action (mechanic and chemical, thermal, laser);

- implementation of the conditions for the energy compliance of nanomodifiers to the prevailing mechanism for the formation of the optimal structure of polymer, oligomeric and combined matrices at various levels of organization – molecular, supramolecular and interfacial;

- providing conditions for the manifestation of the preferred mechanisms of interfacial physicochemical interactions of components with the formation of boundary layers of optimal structure, which determine the mechanisms of destruction of nanocomposites under the influence of various operational factors.

### Acknowledgements

The given research was carried out within the framework of integrated assignment 8.4.1.51 "The concept of multilevel modification in materials science and technology of nanocomposites based on thermoplastic blends" of R&D "Mechanisms of the influence of the energy factor in the multilevel structuring of polymer nanocomposites" and R&D "Development of compositions and technology of import-substituting nanocomposite semi-finished products based on thermoplastic blends for the production of products with high parameters of characteristics using additive technologies" included in the subprogram "Multifunctional and composite materials" of the State programs for scientific research "Materials science, new materials and technologies" in 2021-2025.

### References

- [1] Anishchik V.M., Borisenko V.E., Zhdanok S.A., Tolochko N.K., Fedosyuk V.M. Nanomaterials and nanotechnologies. Minsk: Izd. Center BSU, 2008. – 372 p. (In Russian).
- [2] Edelstein A.S., Cammarata R.C. Nanomaterials: Synthesis, Properties and Applications. Bristol: J.W. Arrowsmith Ltd., 1996. – 596 p.
- [3] Pomogailo A.D., Rosenberg A.S., Uflyand I.E. Metal Nanoparticles in Polymers. Moscow: Khimiya, 2000. – 672 p. (In Russian).
- [4] Avdeichik S.V., Kostyukovich G.A., Kravchenko V.I., Lovshenko F.G., Lovshenko G.F. Nanocomposite engineering materials: experience in the development and application. Grodno, Yanka Kupala State University of Grodno, 2006. – 403 p. (In Russian).
- [5] Skaskevich A.A. Structure and technology of low-filled engineering materials based on engineering thermoplastics modified with carbon nanoclusters. *Extended abstract of candidate's thesis*. Minsk, 2000. – 18 p. (In Russian).

- [6] Weimarn P.P., von. To the doctrine of the state of matter (foundations of the crystallization theory of irreversible colloids). St. Petersburg: Econ. typo-lit., 1910. – 192 p. (In Russian).
- [7] Ajayan P.M., Schadler L.S., Braun P.V. Nanocomposite science and technology. Weinheim: Wiley-VCH, 2003. – 230 p.
- [8] Poole Ch.P., Owens F.J. Introduction to Nanotechnology. New Jersey: John Wiley & Sons, Inc., 2003. – 399 p.
- [9] Golovin Yu.I. Introduction to nanotechnology. - M.: Mashinostroenie, 2003. – 112 p. (In Russian).
- [10] Gusev A.I. Nanomaterials, nanostructures, nanotechnology. - M.: Nauka, 2007. – 416 p. (In Russian).
- [11] Avdeychik S.V., Liopo V.A., Ryskulov A.A., Struk V.A. Introduction to the physics of nanocomposite engineering materials. Grodno: Grodno State Agrarian University, 2009. – 439 p. (in Russian).
- [12] Avdeychik S.V., Struk V.A., Antonov A.S. Nanostate factor in material science of polymer nanocomposites. Saarbrücken: LAP LAMBERT Acad. Publ., 2017. – 468 p. (in Russian).
- [13] Avdeychik S., Sarokin V., Antonov A., Struk V. The compatibility factor in material science of mixed engineering nanoblends // Machines. Technologies. Materials, 2018, Vol. XII, Iss. 8. – p. 341–343.
- [14] Avdeychik S., Antonov A., Struk V., Sarokin V. Features of the structure of mixtures polymeric nanocomposites // Machines. Technologies. Materials, 2018, Vol. XII, Iss. 11. – p. 436–443.
- [15] Antonov A.S., Struk V.A., Avdeychik S.V., Abdurazakov A.A. Methodological principles of thermoplastic matrix modification to increase the parameters of performance characteristics // Mining Mechanical Engineering and Machine-Building, 2020, Vol. 1. – p. 101–108. (in Russian).
- [16] Avdeychik S., Goldade V., Struk V., Antonov A. Methodological approach to the dimension estimation of modifying particles for nanocomposites // Theoretical & Applied Science, 2020, Iss. 04, Vol. 84. – p. 638–644.
- [17] Avdeychik S., Goldade V., Struk V., Antonov A., Ikromov A. The phenomenon of nanostate in material science of functional composites based on industrial polymers // Theoretical & Applied Science, 2020, Iss. 07, Vol. 87. – p. 101–107.
- [18] Avdeichik S.V., Gol'dade V.A., Struk V.A., Antonov A.S., Ikromov A.G. Implementation of the nanostate phenomenon in materials science of functional nanocomposites based on industrial polymers // Surface Engineering and Applied Electrochemistry, 2022, Vol. 58, No. 3. – p. 211–220.
- [19] Avdeychik S., Struk V., Antonov A., Goldade V. Energy factor in technology of polymeric composites // Polymer materials and technologies, 2021, T. 7, Vol 1. – p. 60–70. (in Russian).
- [20] Liopo V.A., Struk V.A., Ryskulov A.A., Avdeychik S.V., Mikhailova L.V. Energy criterion of nanosize // Engineering Bulletin, 2009, Vol. 2(28). – p. 90–94. (in Russian).

#### **Information of the authors**

**Avdeychik Sergey Valentinovich**, PhD (Engineering), associate professor, Doctoral candidate at the Francisk Skorina Gomel State University  
e-mail: [molder.grodno@gmail.com](mailto:molder.grodno@gmail.com)

**Antonov Alexander Sergeevich**, PhD (Engineering), associate professor, Yanka Kupala State University of Grodno  
e-mail: [antonov\\_as@grsu.by](mailto:antonov_as@grsu.by)

**Struk Vasily Alexandrovich**, DSc (Engineering), professor, Yanka Kupala State University of Grodno  
e-mail: [struk@grsu.by](mailto:struk@grsu.by)

**Prokopchuk Nikolay Romanovich**, corresponding members of National Academy of Sciences of Belarus, DSc (Chemistry), professor, honored scientist of the Republic of Belarus, Belarusian State Technological University  
e-mail: [nrprok@gmail.com](mailto:nrprok@gmail.com)

**Zhang Ruoyu**, Ph.D., professor, Zhejiang International Scientific and Technological Cooperative Base of Biomedical Materials and Technology, Zhejiang Engineering Research Center for Biomedical Materials, Laboratory of Advanced Theranostic Materials and Technology, Ningbo Institute of Materials Technology and Engineering, Chinese Academy of Sciences  
e-mail: [zhangruoyu@nimte.ac.cn](mailto:zhangruoyu@nimte.ac.cn)

## Analysis of Wear Parameters of Chill Casted LM13/Zircon/Carbon Hybrid Composites Using Experimental and Statistical Approach

Ravitej Y.P.\*<sup>1</sup>, Batluri T.Ch.<sup>2</sup>, Adarsha H.<sup>3</sup>, Chandrashekar A.<sup>4</sup>, Prem C.R.<sup>4</sup>

<sup>1</sup>Dayananda Sagar University, Bengalore, India

<sup>2</sup>Sri Siddhartha Institute of Technology Tumkur, India

<sup>3</sup>Jain University, Bengalore, India

<sup>4</sup>Bangalore Institute of Technology, Bengalore, India

\*corresponding author

**Abstract:** In this article Effect of wear parameters like load, sliding speed, and sliding distance are analyzed on wear rate. The influence of the weight percentage of zircon on wear rate is studied. The wear rate analysis is done using the Analysis of variance technique (ANOVA) and SN curve with the help of MINITAB software. Specimens are prepared at the ratio of (0+3), (3+3), (3+6), (3+9) and (3+12) weight percentages of Carbon and zircon are added to Aluminum alloy (LM13) respectively. Synthesis is done using a stir casting approach and Copper chill is placed at one end of the mold before pouring the molten composite. Copper chill is placed to have unidirectional solidification and wear properties are evaluated at the chill end of the solidified composite. In the Dry Sliding Pin on Disc wear experimental, it was observed that 9wt.% of zircon shows better wear resistance than other combinations of carbon and zircon combination reinforcement. It is also seen that the wear rate increases as load, sliding speed, and sliding distance increase. The effect of wear parameters is studied and the most influencing wear parameter is analyzed. Results showed that the weight percentage of zircon exerted the greatest effect on wear rate. The wear surface morphology of the specimens is examined. Wear debris, Grooves, and delamination are observed at low Wt.% of reinforcements.

Keywords: analysis of variance technique, dry sliding pin on disc, surface morphology, wear debris, wear

### Introduction

Composites play a vital role in the selection of materials for desired applications [1], reinforcement is a crucial section in selecting a material for a composite which should provide better strength to the composite [2], Dual particle reinforcement (DRP) gives better wear results when compared to single particle reinforcement [3], It pertains high resistance to wear than a single reinforced composite [4], ceramic reinforcement is preferred as the reinforcement for structural and wear resistant applications [5]. The addition of graphite to the composite decreases the wear rate and a uniform graphite layer on the worn surface is observed in microstructural studies. Stir casting process is used synthesis of metal matrix composite for its even mixture of matrix and reinforcement [6],chill casting is a special type of casting technique which provide unidirectional solidification for the liquid composite in a mould [7], Taguchi method is used to decrease the number of experiments and decides the optimum value by using L9 orthogonal vector for wear testing condition variables[8], addition of graphite flakes to the matrix erodes the matrix material and leads to the formation of graphite holes which intern move along counterpart movement during wear[9], wear is a function of load, temperature and wt.% of reinforcement[10], SiC and ZrSiO<sub>4</sub> combination of reinforcements contributes to decrease in wear and can be applied to marine industry and marine environment[11], During initial less speed of the pin , wear is abrasive and continues to be delaminating at higher speeds[12],Thick and stable tribo layers are formed on the Graphite aluminum composite and its hardness increases for higher loads and speed [13]. Grain size affects the strength and wear properties of the composite structure, finer the grains better the properties [14], Empirical relation is established to study wear rate using statistical regression analysis and analysis of variance (ANOVA)[15], Analysis of variance (ANOVA) technique is a statistical approach used to access the most influencing parameters in the wear study [16].

### 1. Materials and experimental procedures

#### 1.1 Materials description and composition

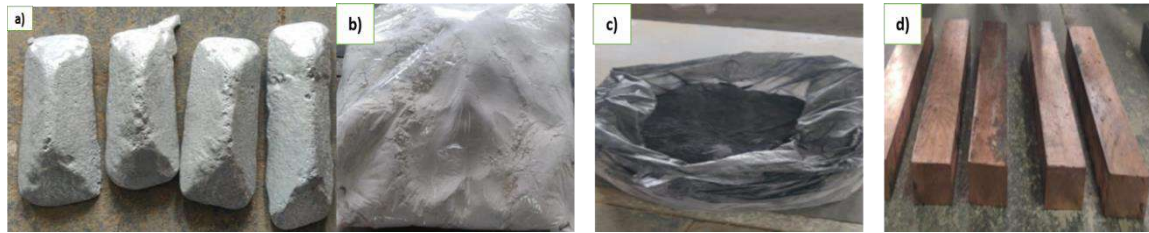
LM13, a light metal alloy is used as a metal matrix, Ceramic ZrSiO<sub>4</sub> and carbon in the form of graphite powder are used as reinforcements to the composite preparation. LM13 is selected because of its cast ability and ductile nature with 13Wt% of silicon. ZrSiO<sub>4</sub> of 1Micron is selected because of its high compressive strength. Graphite is used to study the improvisation of the properties of LM13. Copper chills are used for unidirectional solidification. The chemical composition of LM13 is shown in the table 1.

Table 1. Chemical composition of LM13

Elements	Zn	Mn	Si	Ni	Fe	Mn	Al
Wt.%	0.5	1.0	12	2.0	0.5	1.0	Bal

**Table 2.** Composition of zircon

Element	Wt.%
Zirconium dioxide (ZrO <sub>2</sub> )	64.80
Silicon dioxide (SiO <sub>2</sub> )	32.50
Ferric oxide(Fe <sub>2</sub> O <sub>2</sub> )	0.70
Titanium dioxide (TiO <sub>2</sub> )	0.15
Alumina (Al <sub>2</sub> O <sub>3</sub> )	1.20



a) aluminum alloy; b) zircon; c) carbon;d) copper chills

**Fig. 1.** - Components

### 1.2 Fabrication of the composite

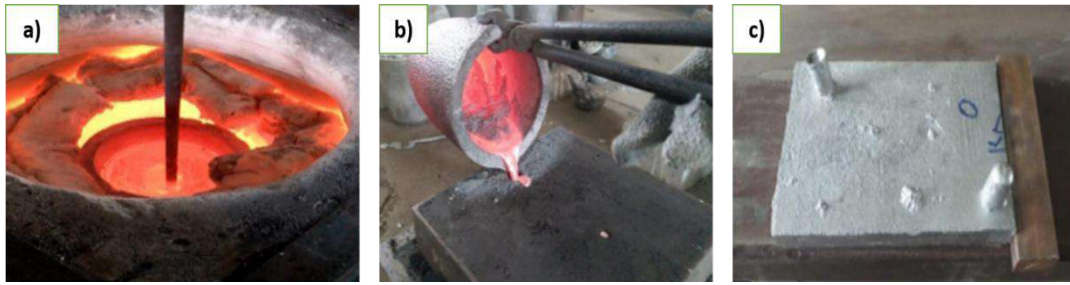
Specimens are fabricated using the stir-casting process to achieve a homogenous mixture. Reinforcements are preheated at 200 degrees Celsius for 10 minutes to remove the humidity content and avoid agglomerations in the liquid composite. LM13 aluminum alloy is melted to its melting point of 660 degrees Celsius in a graphite crucible and preheated reinforcements are added at the combinations as shown in table 2. Carbon percentage is maintained constant I,e 3wt.% throughout the sets of the experiment. Carbon provides the lubrication property to composite which resists wear. Judiciously 3wt.% is maintained because it withholds the tribo-layer formation [17]. A cast specimen is fabricated initially to find the strength of the material without adding Zircon reinforcement. In casting copper chill is placed at one end of the mold. Copper chill placed at one end provides unidirectional solidification. Hence this paper explains the influence of copper chill and Zircon percentage on the composite.

**Table 3.** Specimen with reinforcement combination

Specimen Number	Zircon (Wt.%)	Carbon (Wt.%)
1 (As cast)	0	3
2	3	3
3	6	3
4	9	3
5	12	3



**Fig.2.** - Placement of chills to the molds



a) stir casting; b) molten composite pouring to mold; c) composite part

Fig. 3 - Casting experiment

### 1.3 Wear experiments

The chill end of the specimens in disc wear test is done for the samples. Test samples of 8mm diameter and 25mm length dimension are cleaned and polished by different grit sizes of emery paper. The test steel disc surface is cleaned with acetone. The specimen is pressed against the steel disc using an attachment which is supported by an arm and lever with an incremental loaded weight. Specimens are weighed before the testing and after the testing to calculate the volumetric loss which results in loss of density of specimen due to wear.

### 1.4 Wear rate

Wear rate is the function of change in weight ( $\Delta W$ ) of the specimen before and after load, density ( $\rho$ ), load ( $F$ ), and sliding distance ( $S$ ). The relation is given by equation (1):

$$\text{Wear Rate} = \frac{\Delta W}{\rho FS} \quad (1)$$

Specific wear rate can be calculated by using the relation as shown in equation (2):

$$\text{Specific wear rate (SWR)} = \frac{M}{SL} \quad (2)$$

Wear resistance (WR) of a material is that the material offers resistance to the wear can be calculated as shown in equation (3):

$$WR = 1/\text{Wear rate} \quad (3)$$

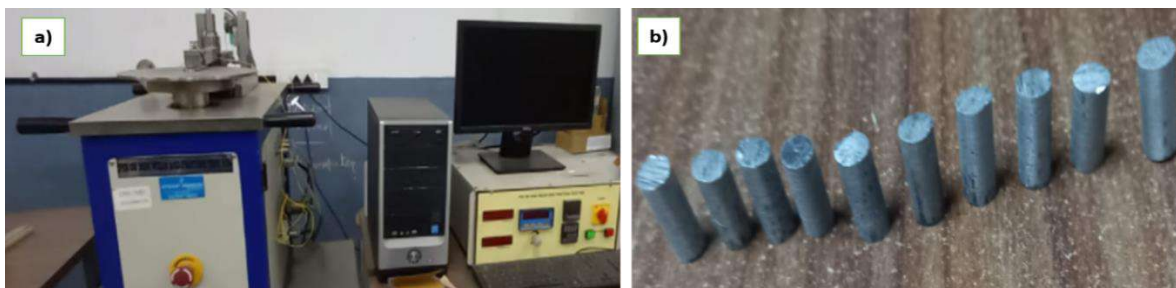
where M is the Average pin weight loss, S is the total sliding distance and L is the load applied in Newton.

### 1.5 Co-efficient of friction

It is the ratio of frictional force (F) resisting the motion to the Normal force (N) as shown in the equation:

$$\mu = F/N \quad (4)$$

Hence coefficient of friction increases as the load/Normal force acting on a pin decreases and vice-versa.



a) dry sliding wear apparatus set up; b) composite pins for experimentation

Fig. 4. - Friction experiment

Specimens are tested for wear in different conditions. All specimens indicated in Table 4 undergo a wear test for the conditions shown in Table 4.

**Table 4.** Conditions applied for the specimens for dry sliding wear test

Exp No	Condition	Applied load (N)	Sliding speed (rpm)	Sliding distance(Track radius in mm)	Exp No	Condition	Applied load (N)	Sliding speed (rpm)	Sliding distance (Track radius in mm)
1	Change in Load	30	400	30	8	Change in Speed	30	700	30
2		40	400	30	9		30	800	30
3		50	400	30	10	Change in Sliding distance	30	400	40
4		60	400	30	11		30	400	50
5		70	400	30	12		30	400	60
6	Change in Speed	30	500	30	13	30	400	70	
7		30	600	30					

**2 Experimental results**

**2.1 Effect of Applied Load and Zircon % on Wear Rate and Co-Efficient of Friction**

**2.1.1 Wear rate discussion**

As the load on the pin increases incrementally from 30 N to 70N with an increment of 10N by keeping sliding speed and sliding distance parameters constant, the wear rate gradually decreases. Also when the percentage of zircon increases gradually from 3wt.% to 12wt.% with an increment of 3wt.%, the wear rate decreases till 9wt.% of zircon and then it slightly increases as shown in Figure 5 and Table 5. Hence at 30N wear rate is the minimum and at 70N wear rate is the maximum. Also at 3wt.% of zircon wear rate is maximum and at 9wt.% wear rate is minimum.

**Table 5.** Effect of Load applied on wear loss, COF, and wear rate for copper chill end

	AL	RPM	TR	WL	WL SN	COF	COF SN	WR	WR SN
12 % chill	30	400	30	0.0078	36.8328	0.4001	0.55513	0.0056	40.381
	40	400	30	0.0081	36.1375	0.3822	0.52140	0.0058	40.184
	50	400	30	0.0092	35.5978	0.3700	0.51250	0.0059	40.026
	60	400	30	0.0105	34.8945	0.3586	0.50210	0.0061	39.785
	70	400	30	0.011	34.3793	0.3447	0.48960	0.0062	38.992
9% chill	30	400	30	0.0062	39.3315	0.3562	0.51200	0.0034	41.566
	40	400	30	0.0064	39.1721	0.3456	0.47785	0.0035	41.452
	50	400	30	0.0071	37.7211	0.3365	0.46580	0.0036	41.249
	60	400	30	0.0081	37.3933	0.3214	0.43250	0.0037	40.944
	70	400	30	0.0083	36.2496	0.3125	0.42230	0.0039	40.800
6% chill	30	400	30	0.0087	41.2096	0.4514	0.45148	0.0070	43.085
	40	400	30	0.0092	40.7242	0.4425	0.44250	0.0072	42.781
	50	400	30	0.0105	39.5762	0.4321	0.43210	0.0075	42.441
	60	400	30	0.0125	38.0618	0.4215	0.42150	0.0079	42.047
	70	400	30	0.0142	36.9542	0.4125	0.41250	0.0079	41.970
3% chill	30	400	30	0.0108	44.1522	0.512	0.35621	0.0083	49.218
	40	400	30	0.011	43.8764	0.4778	0.34560	0.0084	48.898
	50	400	30	0.013	42.9748	0.4658	0.33650	0.0086	48.659
	60	400	30	0.0135	41.8303	0.4325	0.32140	0.0089	48.427
	70	400	30	0.0154	41.6184	0.4223	0.31258	0.0091	48.178
As cast chill end	30	400	30	0.0144	42.1581	0.5551	0.40010	0.0095	44.959
	40	400	30	0.0156	41.8303	0.5214	0.38220	0.0097	44.597
	50	400	30	0.0166	40.7242	0.5125	0.37002	0.0099	44.451
	60	400	30	0.018	39.5762	0.5021	0.35860	0.0102	44.265
	70	400	30	0.0191	39.1721	0.4896	0.34470	0.0112	44.096

**2.1.2 Coefficient of friction discussion**

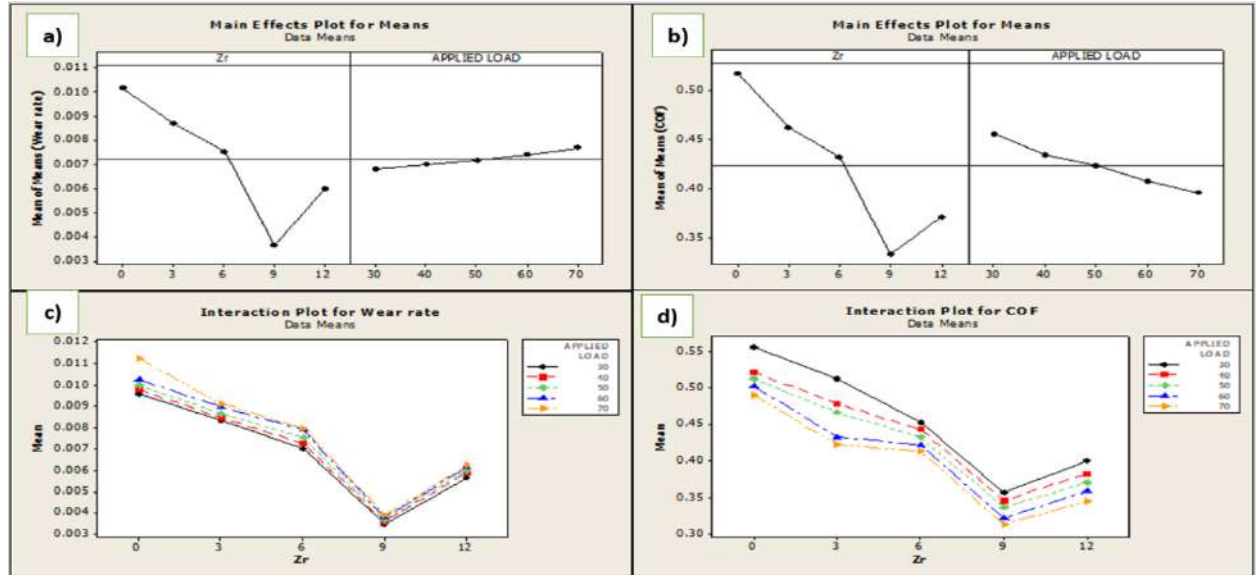
The coefficient of friction is maximum for the 30N load on the pin and it gradually decreases as the load increases to 70N as shown in figure 5. Coefficient friction is vice-versa of the wear rate as shown in equation 4. The



increase in the wear rate at 12wt.% is analyzed by its morphological study of the wear surface of the specimens. Hence 9wt.% of zircon and 12wt.% of zircon are selected for morphological analysis.

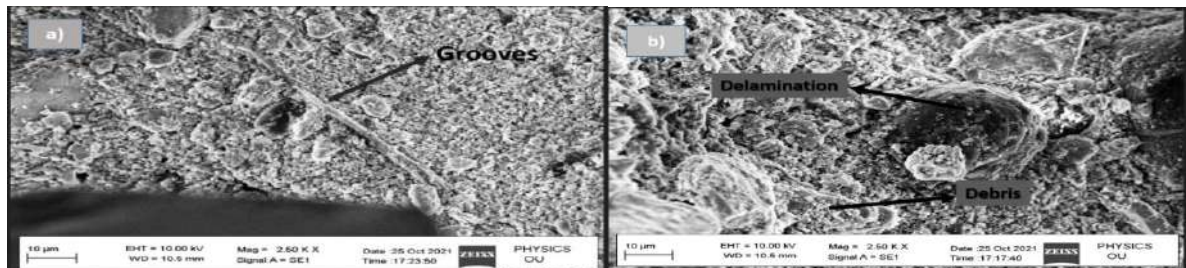
2.1.3 Morphological study

The surface morphology of the worn surface of the specimens is analyzed using FESEM at a magnification of 2.5K X resolution. It is observed that 9wt.% zircon has a homogenous mixture of matrix (LM13) and reinforcements (Zircon and carbon) but there are minor grooves observed due to sliding but there is no delamination and erosion of layers which makes composite pin withstand high wear resistance and hardness. But at 12wt.% of Zircon, it is observed that due to nucleation occurring at the interface of the matrix and the reinforcements, the tribo-layers wear out and oxidation happens which leads to delamination of the composite pin which is observed in Figure 6.



a) main effects plot for means (wear rate); b) main effects plot for means (COF); c) interaction plot for wear rate; d) interaction plot for COF

Fig. 5. - Dependence of load on wear rate, COF



a) 9wt.% of zircon, b) 12wt.% of zircon

Fig. 6. - Surface microstructure

2.1.4 Statistical analysis

For loads of 30 N and 9 Wt. % Zircon, the lowest wear rate is observed. Table 8.3 shows the effects of wear loss, COF, and wear rate on the Zircon's SN ratio values and the Load applied. It indicates that the expected and obtained results are more than 95% in agreement. In Taguchi's method, "Smaller is better" is taken into account to determine the wear rate optimal values because analysis calls for the lowest possible wear rate. The wear rate is observed to increase as the load increases, with the load of 30N and 9Wt.% Zircon showing the lowest wear rate. For various combinations of Zircon and applied force, the SN ratio of Wear loss, COF, and Wear rate is shown in Table 6.

**Table 6.** SN ratio of Wear loss, COF, and Wear rate

Wear parameter	Wear loss		COF		Wear rate	
	Zircon	Load applied	Zircon	Load applied	Zircon	Load applied
Level						
1	35.570	40.740	5.751	6.952	39.87	43.855
2	37.970	40.350	6.726	7.346	41.21	43.595
3	39.310	39.320	7.294	7.564	42.46	43.374
4	42.890	38.350	9.522	7.906	48.67	43.104
5	40.691	37.670	8.620	8.146	44.47	42.812
Delta	7.31	3.05	3.770	1.195	8.82	1.032
Rank	1.0	2.0	1.0	2.0	1.0	2.0

2.1.5 Regression analysis and analysis of variance (ANOVA)

Regression correlations have been established using the wear rate as the output and the Zircon content as the input for loads of 30N, 40N, 50N, 60N, and 70N. Equations (5), (6), and (7) indicate the regression equations for wear loss, COF, and wear rate, respectively. The Analysis of Variance (ANOVA) approach is used to assess the influence of numerous characteristics causing wear while accounting for degrees of freedom (DOF). Two-way regression analysis is taken into account for the investigation. Since both Zircon and Load effects on the wear metrics I, e Wear loss, COF, and wear rate are investigated. Table 7 shows the findings of the ANOVA test for wear rate, respectively. When performing regression investigations, the F and P values of the sources are taken into consideration. It has been observed that the value of the Load-applied source is less than the value of the Zircon content contribution. Therefore, COF, wear rate, and wear loss are influenced by Zircon content. Wear characteristics significantly benefit from the input of Zircon content. Regression correlations have been created using the wear rate as the output and the Zircon content as the input for loads of 30N, 40N, 50N, 60N, and 70N.

$$Wear\ loss = 0.0103 + 0.000111\ Applied\ load - 0.000706\ Zircon \tag{5}$$

$$COF = 0.583 - 0.00148\ Applied\ load - 0.0140\ Zircon \tag{6}$$

$$Wear\ rate = 0.00881 + 0.000021\ Applied\ load - 0.000446\ Zircon \tag{7}$$

**Table 7.** ANOVA (Two way) of Wear rate

Source	DF	Adj SS	Adj MS	F-Value	P-Value	Contribution (%)
Load applied	4.0	0.000026	0.0000007	13.65	0.000	18.72075
Zircon Content	4.0	0.0001033	0.0000314	714.20	0.000	80.65523
Error	16.0	0.0000069	0.0000000			0.546022
Total	24.0	0.0001282				100

2.1.6 Confirmative study of copper chill end specimens

A confirmative study is done based on regression equations obtained in statistical analysis using MINITAB software. Wear loss, COF, and wear rate equations give the relationship between the influencing factors and wear parameters. Since the Load applied and Zircon content influence wear parameters like wear loss, COF, and wear rate are being evaluated. The study is done by providing different values of Load and Zircon content to obtain the wear parameters in equations 5, 6, and 7. The resulting value is contrasted with the findings of the experiment. As indicated in Table 8, it can be observed that the findings obtained match each other with minimal inaccuracy.

**Table 8.** Confirmative study of copper chill end specimens

Exp No.	Load applied (N)	Zircon content (Wt. %)	Statistical results			Experimental results		
			Wear loss	COF	Wear rate	Wear loss	COF	Wear rate
1	35	3.5	0.0117	0.4534	0.00798	0.0106	0.4689	0.456
2	45	4.5	0.0121	0.4246	0.00775	0.0125	0.4365	0.4258
3	55	5.5	0.0125	0.3958	0.00751	0.0121	0.4015	0.3985
4	65	6.5	0.0129	0.367	0.00728	0.0123	0.3652	0.3645
5	75	7.5	0.0133	0.3382	0.00704	0.0135	0.3325	0.3421
6	85	8.5	0.0137	0.583	0.0068	0.0137	0.575	0.581

2.2 Effect of sliding speed

On the composite pin fabricated by copper chill casting, the impact of sliding speed is assessed. By keeping a constant track radius of 30 mm, the sliding speed is changed from 400 to 800 rpm in increments of 100 rpm. Table 9

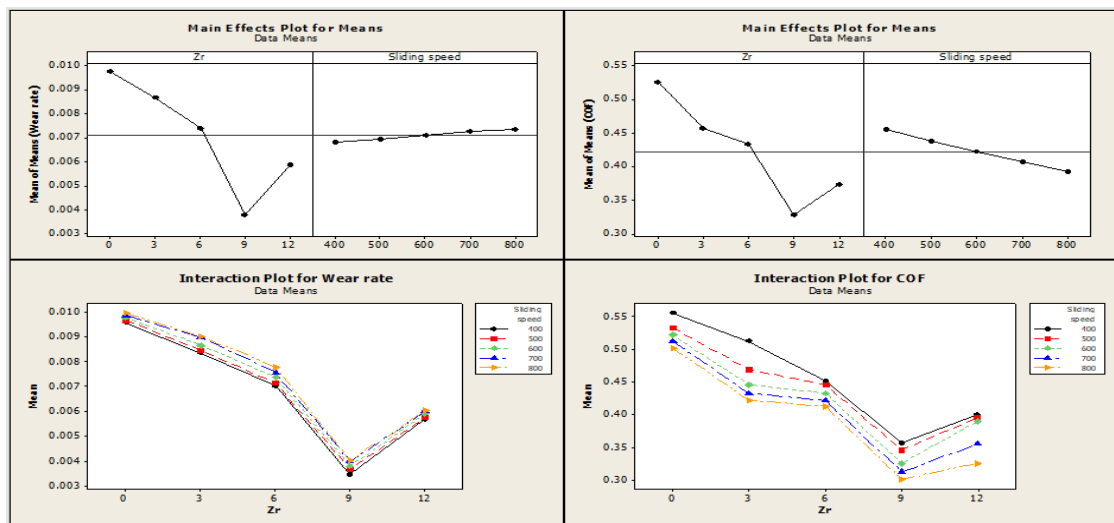
illustrates that sliding speed affects the various percentages of reinforcement samples made from the copper chill. The effect of sliding speed and Zircon is shown in Table 10 and Figure 7. Wear loss and wear rate are related to sliding speed and inversely related to Zircon content up to a Wt. % of 9; then wear loss increases.

Table 9. Taguchi method for sliding speed and zircon content

Factors /Levels	L1	L2	L3	L4	L5
Factor 1 - Zircon Content (Wt. %)	0	3	6	9	12
Factor 2 - Sliding speed (rpm)	400	500	600	700	800

Table 10. Sliding speed effect on Wear loss, COF, and wear rate for Copper chill end specimens

	AL	RPM	TR	WL	SN (WL)	COF	SN COF	WR	WR (SN)
12% chill	30	400	30	0.0078	36.832	0.4001	5.1121	0.0056	5.1121
	30	500	30	0.009	36.363	0.3952	5.4736	0.0057	5.4736
	30	600	30	0.0092	35.972	0.3896	5.6566	0.0059	5.6566
	30	700	30	0.0105	35.809	0.3548	5.8095	0.0059	5.8095
	30	800	30	0.011	35.391	0.3254	5.9998	0.0060	5.9998
9% chill	30	400	30	0.0062	39.331	0.3562	5.8146	0.0034	5.8146
	30	500	30	0.0071	39.015	0.3456	6.5821	0.0036	6.5821
	30	600	30	0.00736	38.159	0.3256	7.0211	0.0037	7.0211
	30	700	30	0.00745	37.271	0.3125	7.2803	0.0039	7.2803
	30	800	30	0.00765	36.618	0.3012	7.5061	0.0040	7.5061
6% chill	30	400	30	0.0087	41.209	0.4514	6.9072	0.0070	6.9072
	30	500	30	0.0096	40.354	0.4456	7.0211	0.0071	7.0211
	30	600	30	0.0112	39.015	0.4325	7.2803	0.0073	7.2803
	30	700	30	0.01213	38.322	0.4215	7.5040	0.0075	7.5040
	30	800	30	0.01325	37.555	0.4124	7.6936	0.0077	7.6936
3% chill	30	400	30	0.0108	44.152	0.512	8.9659	0.0083	8.9659
	30	500	30	0.0112	42.974	0.4687	9.2285	0.0084	9.2285
	30	600	30	0.01236	42.662	0.4456	9.7463	0.0086	9.7463
	30	700	30	0.01369	42.556	0.4325	10.103	0.0089	10.103
	30	800	30	0.01476	42.326	0.4214	10.422	0.0090	10.422
As cast chill end	30	400	30	0.0144	42.158	0.5551	7.9566	0.0095	7.9566
	30	500	30	0.0152	40.915	0.5325	8.0637	0.0096	8.0637
	30	600	30	0.0159	40.724	0.5214	8.1876	0.0097	8.1876
	30	700	30	0.0162	39.576	0.5123	9.0003	0.0098	9.0003
	30	800	30	0.017	39.172	0.5012	9.7516	0.0099	9.7516



a) main effects plot for means (wear rate); b) main effects plot for means (COF); c) interaction plot for wear rate; d) interaction plot for COF

Fig. 7. – Dependence of sliding speed effect on wear loss, COF, and wear rate for copper chill end specimens

2.2.1 Statistical analysis

The software MINITAB is used to statistically assess the experimental outcomes. In Taguchi's DOE, "Smaller is better" is taken into account while calculating the SN ratio for an L25 orthogonal array. It has been observed that the wear rate decreases as the sliding speed rises. Zircon and sliding speed have an impact on wear rate, COF, and wear loss. Because Zircon content delivers a higher delta value for all wear parameters, the Zircon effect has a considerable impact on wear loss, COF, and wear rate. The SN ratio of Wear rate for various combinations of Zircon and sliding speed is shown in Table 11.

Table 11. SN ratio plot for Wear rate of copper non-chill end specimens

Wear parameter	Wear loss		COF		Wear rate	
	Zircon	Sliding speed	Zircon	Sliding speed	Zircon	Sliding speed
1	36.070	40.740	5.6100	6.9510	40.210	43.840
2	38.080	39.920	6.8410	7.2741	41.220	43.650
3	39.290	39.310	7.2811	7.5780	42.660	43.430
4	42.930	38.711	9.6930	7.9390	48.460	43.191
5	40.510	38.210	8.5920	8.2751	44.640	43.090
Delta	6.86	2.52	4.083	1.324	8.25	0.75
Rank	1	2	1	2	1	2

2.2.2 Regression analysis

The equation gives a regression equation using the wear rate as an output parameter, the sliding speed, and the Zircon content as input factors. The relationship between Zircon and sliding speed is observed in Table 12. Zr content has been discovered to be a potential wear rate parameter.

$$Wear\ loss = 0.0101 + 0.000008\ Sliding\ speed - 0.000604\ Zircon \tag{8}$$

$$COF = 0.605 - 0.000154\ Sliding\ speed - 0.0143\ Zircon \tag{9}$$

$$Wear\ rate = 0.00878 + 0.000002\ Sliding\ speed - 0.000411\ Zircon \tag{10}$$

The Analysis of Variance (ANOVA) approach is used to assess the influence of numerous characteristics causing wear while accounting for degrees of freedom (DOF). Table 12 displays the findings of the ANOVA test for wear rate. The contribution of the sliding speed is significant in the wear rate.

Table 12. ANOVA (Two way) for wear rate of copper chill end

Source	DF	Adj SS	Adj MS	F-Value	P-Value	Contribution (%)
Sliding speed	4	0.0000010	0.0000003	37.30	0.000	0.890472
Zircon Content	4	0.000111	0.0000278	3978.91	0.000	98.84239
Error	16	0.0000001	0.0000000			0.089047
Total	24	0.0001123				100

2.2.3 Confirmative study for the Sliding speed effect on copper chill end specimens.

Given that the sliding speed and Zircon content are key considerations for assessing wear properties including wear loss, COF, and wear rate. The study is done by providing different values of sliding speed and Zircon content to obtain the wear parameters in equations 8, 9, and 10. The obtained value is compared with experimental results. It is observed that the obtained results match each other with negligible errors as shown in table 13.

Table 13. Confirmative study of silicon carbide chill end specimens of copper chill end

Exp No.	Sliding speed (rpm)	Zircon content (Wt. %)	Statistical results			Experimental results		
			Wear loss	COF	Wear rate	Wear loss	COF	Wear rate
1	450	3.5	0.0115	0.1381	0.0082	0.0118	0.1379	0.00842
2	550	4.5	0.0117	0.3064	0.0080	0.0011	0.3065	0.00804
3	650	5.5	0.0119	0.4747	0.0078	0.0112	0.4715	0.00783
4	750	6.5	0.0121	0.643	0.0076	0.0126	0.6415	0.00765
5	850	7.5	0.0123	0.8113	0.0074	0.0121	0.8122	0.00742
6	950	8.5	0.0125	0.9796	0.0071	0.0125	0.9725	0.00711

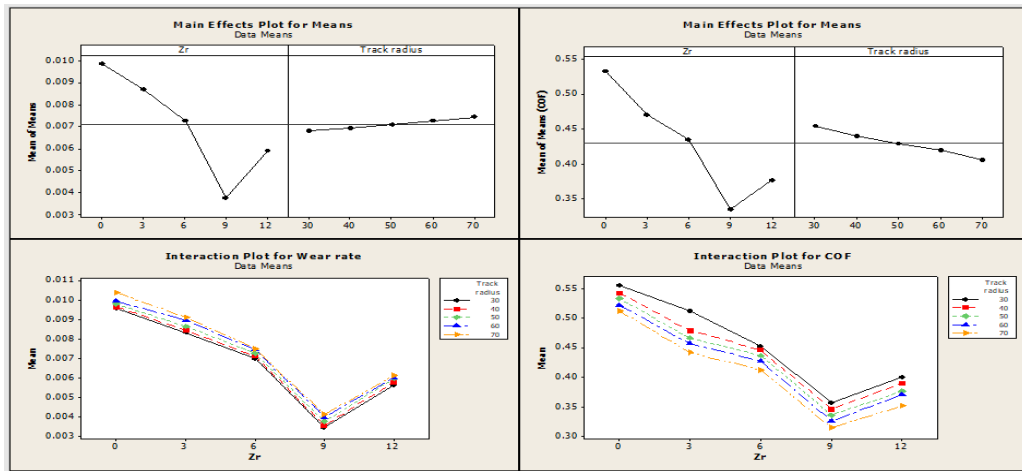
**2.3 Effect of track radius**

Wear loss, coefficient of friction, and wear rate are affected by sliding distance. The experiment is carried out with a 30 N load and 400 rpm sliding speed. With a 10 mm increment, the track radius ranges from 30 to 70 mm. It has been observed that wear rate and wear loss are inversely correlated with the coefficient of friction and proportionate to sliding distance (COF). Figure 8 depicts the sliding distance that affects the wear rate. It has been noted that as Zircon content rises from 3 Wt. % to 9 Wt. %, the wear rate lowers until it reaches 12 Wt. %. Zircon combined with 400 rpm and 9 Wt. % produces greater outcomes than other combinations. Sliding distance impact on wear rate, COF, and wear loss of the composite pin is assessed. The pin is loaded under a 30N load. The experiment is optimized using an L25 orthogonal array as given in Table 14 to evaluate the impact of sliding distance on wear behavior.

**Table 14.** Effect of track radius on wear rate

	AL	RPM	TR	WL	WL SN	COF	COF SN	WR	WR SN
12% chill	30	400	30	0.0078	36.8328	0.4001	5.1121	0.005645	40.3809
	30	400	40	0.0081	36.7129	0.3896	5.3152	0.005789	40.3059
	30	400	50	0.0085	36.5363	0.3758	5.4720	0.005969	40.1888
	30	400	60	0.009	36.4205	0.3698	5.6566	0.006012	40.0366
	30	400	70	0.0101	36.0269	0.3512	5.8061	0.006121	39.6761
9% chill	30	400	30	0.0062	39.3315	0.3562	5.8146	0.00346	41.5663
	30	400	40	0.0065	39.1721	0.3456	6.3951	0.003556	41.4608
	30	400	50	0.0068	38.3443	0.3356	6.6360	0.003756	41.2516
	30	400	60	0.0075	38.0618	0.3256	6.8036	0.003987	40.9509
	30	400	70	0.0082	37.7882	0.3145	7.1073	0.004125	40.7953
6% chill	30	400	30	0.0087	41.2096	0.4514	6.9072	0.00701	43.0856
	30	400	40	0.0089	41.0122	0.4456	7.0211	0.007123	42.9467
	30	400	50	0.0091	40.8001	0.4365	7.2003	0.007258	42.7837
	30	400	60	0.0094	40.5190	0.4269	7.3935	0.007456	42.5499
	30	400	70	0.0112	39.0156	0.4121	7.6999	0.007512	42.4849
3% chill	30	400	30	0.0108	44.1522	0.512	8.9659	0.00835	49.2185
	30	400	40	0.011	43.7417	0.4789	9.2285	0.008452	48.9808
	30	400	50	0.0121	43.3498	0.4658	9.4836	0.008658	48.5055
	30	400	60	0.0125	42.4988	0.4569	9.7463	0.008963	47.9871
	30	400	70	0.0129	41.7237	0.4412	10.047	0.009125	47.6915
As cast chill end	30	400	30	0.0144	42.1581	0.5551	7.9566	0.009571	44.9667
	30	400	40	0.0146	41.8303	0.5423	8.1876	0.009654	44.7479
	30	400	50	0.0149	41.4116	0.5326	8.5009	0.009785	44.4808
	30	400	60	0.0151	40.9151	0.5214	8.6407	0.009958	44.4189
	30	400	70	0.0158	39.9136	0.5125	9.0889	0.01038	44.2636

From Figure 8, it is observed that wear loss and wear rate are proportional to the load applied and inversely proportional to Zircon content till 9Wt.% of Zircon, with further addition of Zircon the wear loss increases.



a) main effects plot for means (wear rate); b) main effects plot for means (COF); c) interaction plot for wear rate; d) interaction plot for COF

Fig. 8. - Dependence of track radius effect of on wear rate

2.3.1 Statistical analysis

The SN ratio for wear loss, COF, and wear rate are shown in Table 15 respectively. In Taguchi's method, "Smaller is better" is taken into account to determine the wear rate's optimal values because the lowest possible wear rate is desired. The wear rate is observed to increase as the load increases, with the load of 30N and 9Wt% Zircon showing the lowest wear rate. Table 16 represents the SN ratio of Wear loss, COF, and Wear rate for different combinations of Zircon and track radius.

Table 15. SN ratio of wear loss, COF, and wear rate

Wear parameter	Wear loss		COF		Wear rate	
	Zircon	Track radius	Zircon	Track radius	Zircon	Track radius
1	36.510	40.740	5.4720	6.9510	40.120	43.840
2	38.540	40.490	6.5510	7.2300	41.210	43.690
3	40.510	40.090	7.2440	7.4590	42.770	43.440
4	43.091	39.680	9.4940	7.6480	48.480	43.190
5	41.250	38.890	8.4750	7.9500	44.580	42.980
Delta	6.59	1.84	4.022	0.999	8.36	0.86
Rank	1	2	1	2	1	2

2.3.2 Regression analysis

For track radii of 30mm, 40mm, 50mm, 60mm, and 70mm, regression correlations have been created using the wear rate as the output and the Zircon content as the input as shown in equations 11,12 and 13.

$$Wear\ loss = 0.0117 + 0.000048\ Track\ radius - 0.000599\ Zircon \tag{11}$$

$$COF = 0.583 - 0.00120\ Track\ radius - 0.0149\ Zircon \tag{12}$$

$$Wear\ rate = 0.00893 + 0.000017\ Track\ radius - 0.000423\ Zircon \tag{13}$$

Table 16 displays the findings of the ANOVA test for wear rate. The contribution of the sliding speed is significant in the wear rate.

Table 16. ANOVA (Two way) for wear rate of copper chill end

Source	DF	Adj SS	Adj MS	F-Value	P-Value	Contribution (%)
Track radius	4	0.0000014	0.0000003	49.17	0.00	1.214224
Zircon Content	4	0.0001138	0.0000284	4068.47	0.00	98.69905
Error	16	0.0000001	0.000000			0.08673
Total	24	0.0001153				100

2.3.3 Confirmative study for the Sliding distance effect on copper chill end specimens

Sliding distance and Zircon content are the influencing factors to evaluate the wear parameters like wear loss, COF, and wear rate. The study is done by providing different values of Sliding distance and Zircon content to obtain the wear parameters in equations 11, 12, and 13. The obtained value is compared with experimental results. It is observed that the obtained results match each other with negligible errors as shown in table 17.

**Table 17.** Confirmative study of silicon carbide chill end specimens of copper chill end

Exp No.	Track radius (mm)	Zircon content (Wt. %)	Statistical results			Experimental results		
			Wear loss	COF	Wear rate	Wear loss	COF	Wear rate
1	35	3.5	0.01128	0.5395	0.0080	0.0111	0.5379	0.0080
2	45	4.5	0.01116	0.5271	0.0077	0.0113	0.5265	0.0077
3	55	5.5	0.01104	0.5146	0.0075	0.0110	0.5141	0.0075
4	65	6.5	0.01092	0.5022	0.0072	0.0105	0.5015	0.0072
5	75	7.5	0.01080	0.4898	0.0070	0.0108	0.4802	0.0704
6	85	8.5	0.01068	0.4774	0.0067	0.0106	0.4725	0.0067

## Conclusion

By considering experimental, and statistical studies on LM13/Zircon/Carbon Hybrid metal matrix composites following conclusions have been made.

The Stir casting process and chill casting technique are effective methods to fabricate the hybrid metal matrix composite and to enable unidirectional solidification respectively.

9wt.% of zircon/3wt.% carbon/LM13 provides the minimal wear rate than other specimens.

Wear rate is directly proportional to the applied load, sliding speed, and sliding distance, and COF is inversely proportional to the applied load, sliding speed, and sliding distance.

By analyzing influencing wear parameters, Zircon is the prominent factor that influences the wear rate than other parameters.

The morphology of the surface of the specimens is analyzed, 9wt.% of zircon / 3wt.% of carbon / LM13 provides minimal deformation and grooves than other combination morphologies.

## Reference

- [1] R. Prem Chand, B. S. Halemani, K. M. Chandrasekhar, Y. P. Ravitej, T. Hemanth Raju, and S. Udayshankar, "Investigation and analysis for mechanical properties of banana and E glass fiber reinforced hybrid epoxy composites," *Mater. Today Proc.*, no. xx, 2021, doi: 10.1016/j.matpr.2021.05.044.
- [2] E. Omrani, A. D. Moghadam, M. Algazzar, P. L. Menezes, and P. K. Rohatgi, "Effect of graphite particles on improving tribological properties Al-16Si-5Ni-5Graphite self-lubricating composite under fully flooded and starved lubrication conditions for transportation applications," *Int. J. Adv. Manuf. Technol.*, vol. 87, no. 1–4, pp. 929–939, 2016, doi 10.1007/s00170-016-8531-6.
- [3] G. Dixit and R. Nateriya, "Microstructure and erosion wear of LM-13 alloy composites with dual reinforcement by silicon carbide and zircon sand in fine silica quartz slurry," *Usak Univ. J. Mater. Sci.*, vol. 3, no. 2, p. 226, 2014.
- [4] S. Kumar Patel, R. Nateriya, B. Kuriachen, and V. Pratap Singh, "Effect of secondary phase particles on Erosive wear characteristic of dual reinforced particle Al-alloy composites," *Mater. Today Proc.*, vol. 5, no. 9, pp. 17561–17571, 2018, doi: 10.1016/j.matpr.2018.06.073.
- [5] N. Raj and N. Radhika, "Tribological Characteristics of LM13/Si3N4/Gr Hybrid Composite at Elevated Temperature," *Silicon*, vol. 11, no. 2, pp. 947–960, 2019, doi: 10.1007/s12633-018-9893-1.
- [6] F. Author *et al.*, "Elsevier Editorial System(tm) for Materials Title: Fabrication and Characterization of hardness and microstructure of Large Sized Al2014-SiC Composite ScienceDirect Fabrication and Characterization of hardness and microstructure of Large Sized Al2014-SiC Composite." [Online]. Available: [www.sciencedirect.com](http://www.sciencedirect.com)
- [7] N. Bandekar and M. G. Anantha Prasad, "Effect of chills on tribological behavior of aluminum-garnet-carbon hybrid composites," *Int. J. Mech. Prod. Eng. Res. Dev.*, vol. 9, no. 3, pp. 761–768, 2019, doi: 10.24247/ijmperdjun201985.
- [8] A. B. Mhaske and P. K. R. Madavi, "Experimental Investigation and Optimization of Wear Properties of Aluminum Alloy LM30 Composite with Zircon Powder as Reinforcement," no. July, pp. 2062–2065, 2018.
- [9] K. Naplocha and K. Granat, "Dry sliding wear of Al/Saffil/C hybrid metal matrix composites," *Wear*, vol. 265, no. 11–12, pp. 1734–1740, 2008, doi: 10.1016/j.wear.2008.04.006.
- [10] R. S. Panwar and O. P. Pandey, "Study of wear behavior of Zircon sand-reinforced LM13 alloy composites at elevated temperatures," *J. Mater. Eng. Perform.*, vol. 22, no. 6, pp. 1765–1775, 2013, doi: 10.1007/s11665-012-0383-0.
- [11] S. K. Patel, B. Kuriachen, N. Kumar, and R. Nateriya, "The slurry abrasive wear behavior and microstructural analysis of A2024-SiC-ZrSiO4 metal matrix composite," *Ceram. Int.*, vol. 44, no. 6, pp. 6426–6432, 2018, doi: 10.1016/j.ceramint.2018.01.037.
- [12] S. Basavarajappa, G. Chandramohan, K. Mukund, M. Ashwin, and M. Prabu, "Dry sliding wear behavior of Al 2219/SiCp-Gr hybrid metal matrix composites," *J. Mater. Eng. Perform.*, vol. 15, no. 6, pp. 668–

674, 2006, doi: 10.1361/105994906X150803.

[13] A. R. Riahi and A. T. Alpas, "The role of tribo-layers on the sliding wear behavior of graphitic aluminum matrix composites *Wear*, vol. 250–251, no. PART 2, pp. 1396–1407, 2001, doi: 10.1016/s0043-1648(01)00796-7.

[14] Y. Şahin, "Abrasive wear behavior of SiC/2014 aluminum composite," *Tribol. Int.*, vol. 43, no. 5–6, pp. 939–943, 2010, doi: 10.1016/j.triboint.2009.12.056.

[15] Singh J., Chauhan A. Investigations on dry sliding frictional and wear characteristics of SiC and red mud reinforced Al2024 matrix hybrid composites using Taguchi's approach," *Proc. Inst. Mech. Eng. Part L J. Mater. Des. Appl.*, vol. 233, no. 9, pp. 1923–1938, 2019, doi: 10.1177/1464420718803126.

[16] A. Gudimetla, D. Lingaraju, and S. Sambhu Prasad, "Modelling and optimization of wear parameters of Al 4032 reinforced with coal ash using Taguchi and rsm approach *Compos. Theory Pract.*, vol. 21, no. 1–2, pp. 3–11, 2021.

[17] Wilson S., Alpas A. T. Effect of temperature on the sliding wear performance of Al alloys and Al matrix composites *Wear*, vol. 196, no. 1–2, 270–278, 1996, doi: 10.1016/0043-1648(96)06923-2.

#### Information of the author

**Ravitej Yellampalli Prakash**, PhD, assistant professor, Dayananda Sagar University  
e-mail: [ravitejyp@gmail.com](mailto:ravitejyp@gmail.com)

**Batluri Tilak Chandra**, PhD, assistant professor, Sri Siddhartha Institute of Technology  
e-mail: [batluritolakchandra@ssit.edu.in](mailto:batluritolakchandra@ssit.edu.in)

**Adarsha Hiriyannaiah**, PhD, professor, Jain University  
e-mail: [h.adarsha@jainuniversity.ac.in](mailto:h.adarsha@jainuniversity.ac.in)

**Chandrashekar Anjinappa**, PhD, assistant professor, Bangalore Institute of Technology  
e-mail: [acsmechphd@gmail.com](mailto:acsmechphd@gmail.com)

**Prem Chand R**, Ph.D, assistant professor, Bangalore Institute of Technology  
e-mail: [premchand1827@gmail.com](mailto:premchand1827@gmail.com)



## Research and Calculation of the Deformed State of the Roadway Mobile Overpass

**Ganyukov A.A., Sinelnikov K.A.\*, Kabikenov S.Zh., Karsakova A.Zh.**  
Abylkas Saginov Karaganda Technical University, Karaganda, Kazakhstan  
\*corresponding author

**Abstract.** The article proposes a new type of transport equipment that is a mobile overpass. The proposed design is used during underground repairs of urban utility networks and is a prefabricated modular bridge structure equipped with its own chassis. The overpass structure is installed through open repair trenches on highways, which will ensure continuous traffic through repair sections. The overpass is equipped with its own chassis and is mobile. The use of the overpass improves the city transport logistics during repair work: eliminates traffic jams due to the lack of need to detour repair sections, reduces the accident rate, distributes traffic flows, improves the environment, etc. It can also be used during emergency situations where it is necessary to overcome various landslides, ditches, trenches, etc. After the end of operation, the overpass structure is dismantled and can be used multiple times. The aim of the study is to calculate the deformed state of the structurally orthotropic slab of the roadway of a mobile overpass with a check for standard rigidity. Calculations of the roadway for rigidity from moving motor vehicles are performed by means of the Bubnov-Galerkin variational method. The final results include calculations of deflections in the center of the slab clamped along the contour, as well as the conditions for implementing the deflection limitation according to the standards of automobile bridge construction. Based on the results obtained, the design parameters of the slab satisfying the rigidity and strength condition are determined. The studies and calculations conducted allow for the practical design of the roadway structure of the overpass.

**Keywords:** mobile overpass, transport equipment, traffic jam elimination, mobile bridge structures, orthotropic slab, variational methods, rigidity calculations.

### Introduction

Various municipal utility networks (heating, water supply, cable, etc.) according to the planning of cities in the CIS countries are usually located under the roadways of the city's highways and lie at a certain depth. Scheduled repairs or renovation of such municipal utility infrastructure are associated with the development of repair trenches along city roads, which causes the closure of city transport arteries for a long time and the need to organize detours of repair sections. This contributes to the formation of traffic jams due to the increased concentration of cars due to detours of repair sections, increases the accident rate, worsens the city's transport logistics, its ecology, etc. [1, 2, 3]

In such conditions, instead of detours around repair areas, we propose organizing direct bridge crossings over utility network trenches, without blocking vehicle traffic on adjacent city highways.

A new type of transport equipment is proposed as such direct crossings – a mobile municipal overpass (Figure 1). The overpass is installed through the repair trenches of municipal networks and allows not to stop traffic flows for the entire period of repair of underground utility networks. The use of such overpasses improves transport logistics in the city during repair work on municipal networks: reduces the formation of traffic jams, there are no forced detours of repair sections, inconveniences for car drivers and residents of city districts are reduced, due to forced detours of transport, etc. [4, 5].

The mobile municipal overpass is assembled from standardized prefabricated modules: one orthogonally oriented module (Figure 2,a, position I) and two inclined modules (Figure 2,a, position II). The orthogonally oriented module is a spatial steel frame, the base of which is attached to the bottom of the repair trench using special methods. The upper part of the frame is a roadway in the form of an orthotropic slab with reinforcing ribs (Figure 2,a, position III). The inclined module is steel trusses equipped with a chassis and supporting the roadway also in the form of an orthotropic slab. The cantilever part of the trusses rests on the ground base, the suspended part of the trusses rests on the supporting frame of the orthogonal module. The bridge crossing is delivered to the installation site under its own power on a trailer and assembled into a single structure using special assembly methods. After using the overpass, it is disassembled into individual modules at the coupling units, placed on wheels and delivered to storage sites [6, 7, 8].

The overall dimensions of the "single-lane" modules are as follows: length of the orthogonally oriented module - 8 m; width - 3.5 m; height (taking into account their installation on the bottom of the trenches) - 3.85 m. Length of the inclined module - 4 m; width - 3.5 m; height - 0.85 m. Such dimensions provide passage of light vehicles weighing up to 3.5 tons.

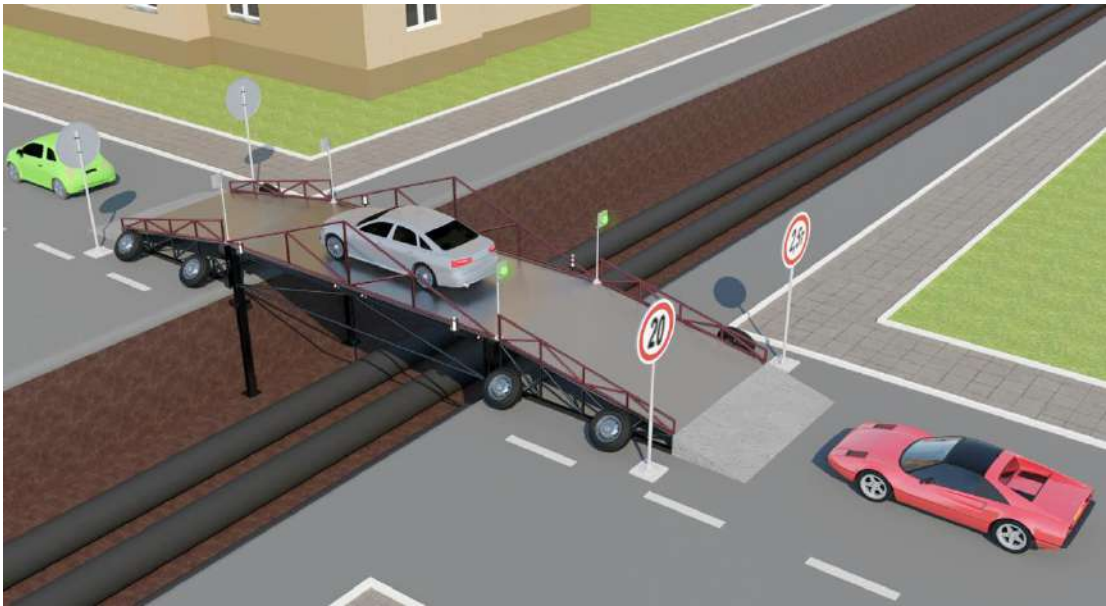
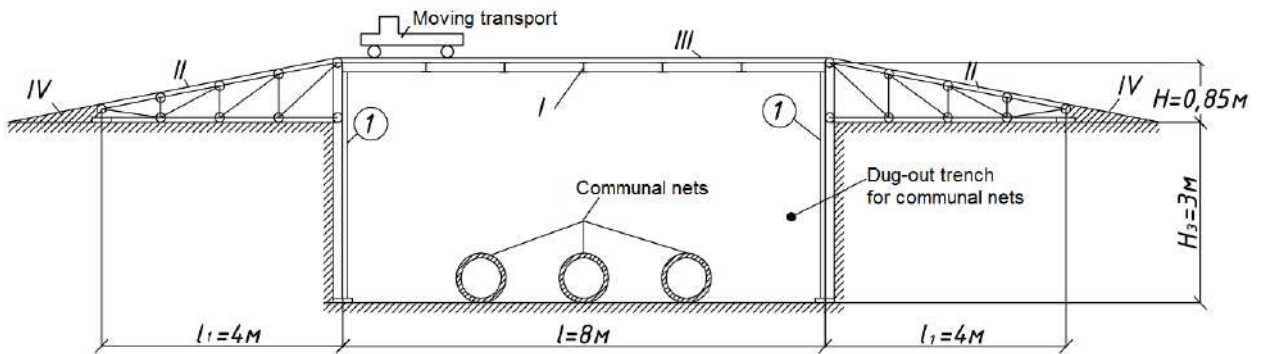
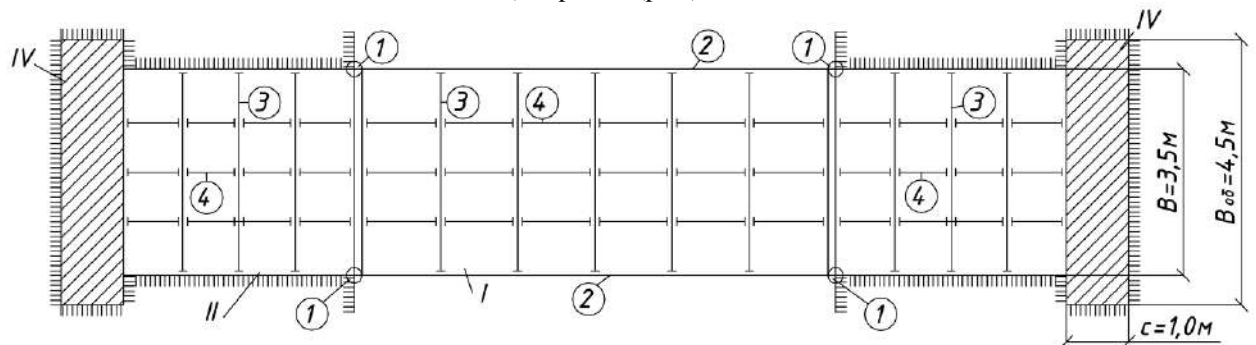


Fig. 1. – 3D model of the overpass in operational position



a) Front view (facade)

b) Top view (plan)



Explication of the elements and modules of the overpass (a, front view):

- I – Spatial frame of the structure (the orthogonal module);
- II – Pivot-nodal basic supporting-hinged rod-like frame (the inclined module);
- III – Metal roadway decking (slabs);
- IV – Access ramp.

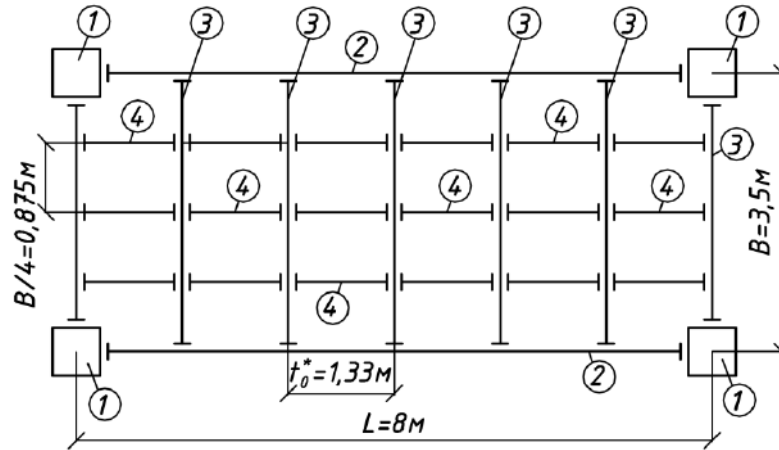
Explication of constructions of separate modules (b, top view (plan)):

- 1 – vertical posts (frame supports);
- 2 – longitudinal crossbars (beams) of the frame;
- 3 – transversal crossbars (beams) of the frame;
- 4 – longitudinal (reinforcing) ribs of the roadway.

Fig. 2. – Scheme of the mobile overpass

### 1. Materials and methods

In the design of the proposed mobile overpass, the roadway is made of steel sheets supported by a system of mutually perpendicular beams of the supporting frame (Figure 2, b, Figure 3). Such a design solution can be mathematically modeled as a structurally orthotropic plate consisting of a steel sheet interacting with mutually perpendicular stiffeners of a certain cross-section.



- 1 – vertical posts (rolled I-beam No. 50);
- 2 – longitudinal elements (beams, rolled I-beam No. 45);
- 3 – transverse elements of the plate (beams, rolled I-beam No. 30);
- 4 – reinforcing ribs of the plate (steel strip 14x3 cm).

Fig. 3. – Structural diagram of the roadway slab of the overpass

Elements 1–4 in Figure 3 were obtained separately by calculating the spatial frame of the orthogonal module and are beyond the scope of this article.

When designing engineering structures that provide for the crossing of various types of rolling stock, such as the presented overpass, special attention is paid to the design solution of their roadway. Their design solution must ensure, along with the strength of the supporting structures, the rigidity required by the operating conditions to eliminate the phenomenon of "unsteadiness" and "subsidence" [9]. In this regard, calculations are made of the deformability of the supporting structures of the roadway - calculating the displacement of the cargo belt (flooring) from the action of standard operational long-term loads. In this case, the condition of rigidity of the flooring must be met [10]:

$$\frac{W_{\max}}{L} \leq \left( \frac{1}{1000} \right), \quad (1)$$

where  $W_{\max}$  – the largest deflection of the middle surface of the deck;

$L$  – the characteristic (calculated) size (span) of the deck ( $L=8\text{m}$ ).

The calculation method for an orthotropic overpass slab must take into account the combined operation of the covering sheet, longitudinal and transverse stiffeners of the slab and the main beams of the span structure. In this case, the problem of calculating such plates in order to identify their stress and strain state arises, according to the results of which they are designed and constructed based on the requirements of rigidity and strength. This paper considers the calculation of deformations (deflections) of overpass slabs from the action of the rolling stock load using the Bubnov-Galerkin variational method for calculating the required structural rigidity according to condition (1).

The calculated rigidity characteristics of structurally orthotropic slabs with one-sided cross-arranged ribs, taking into account the combined work of the covering sheet, longitudinal and transverse ribs of the slab and the main beams of the span structure, are as follows [11, 12]:

$$D_x = \frac{Et^3}{12(1-\mu^2)} + \frac{EJ_{1y}}{t_1}; \quad D_y = \frac{Et^3}{12(1-\mu^2)} + \frac{EJ_{2y}}{t_2}; \quad D_{xy} = \frac{Gt^3}{12} + \frac{EJ_{1k}}{t_1\delta}; \quad (2)$$

$$D_{\mu} = D_1 = \mu D_x = \mu D_y; \quad \delta = 1 - \frac{t_1^2 J_{1y} (t_1 J_{2k} - t_2 J_{1k})}{t_2 J_{2k} (t_1^2 J_{1y} + t_2^2 J_{2k})}$$

where  $D_x, D_y, D_{xy}$  – cylindrical rigidities relative to axes during bending and torsion;

$D_{\mu}$  – shear cylindrical rigidity;

$\delta$  – generalized stiffness parameter;

$E, G, \mu$  – respectively, the modulus of elasticity, the shear modulus and Poisson's ratio;

$J_{1k}, J_{2k}$  – the corresponding torsional moments of elements 4 and 3 (Figure 3);

$J_{1y}, J_{2x}$  – the corresponding axial moments of inertia of elements 4 and 3, relative to their central axes, parallel to the  $x$  and  $y$  axes, respectively;  $t_1 = B/4 = 3,5/4 = 0,875m$  – step of elements “4”;  $t_2 = L/6 = 8/6 = 1,33m$  – step of elements “3”;  $t = 20mm$  – the previously accepted thickness of the metal sheet deck made of grade 09G2S steel.

For the plate shown in Figure 3, the following values were obtained using formulas (1):

$$D_x = 17,1452 \cdot 10^2 kNm; \quad D_y = 107,93 \cdot 10^2 kNm; \quad D_1 = 5,1436 \cdot 10^2 kNm; \quad D_{xy} = 3,57 \cdot 10^2 kNm. \quad (3)$$

The uniformly distributed surface load on the slab, taking into account the overload factor and the dynamic effect of movement of a mobile vehicle load weighing up to 3.5 tons along the overpass, is  $g = 52.5 kN/m^2$  [13].

To calculate the slab (Figure 3), we apply the Bubnov-Galerkin variational method [14, 15]. The desired deflection function  $W = W(x, y)$  we will look for slabs in the form:

$$W = \sum_{i=1}^n a_i \cdot \varphi_i, \quad (4)$$

where  $a_i$  – undefined coefficients;  $\varphi_i$  – approximating functions satisfying the conditions of fixing the edges of the plate. Fixing of the plate is clamping along the contour (Figure 4).

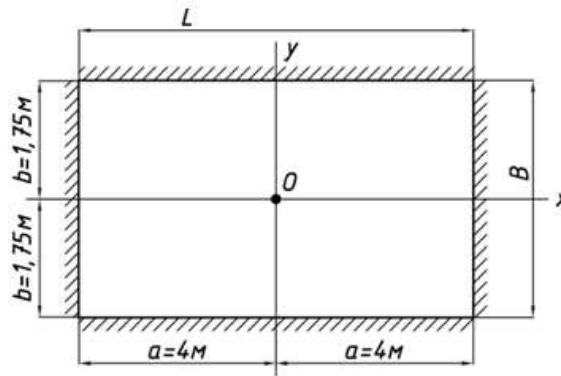


Fig. 4.– Calculation scheme of the slab

The boundary conditions (Figure 4) are written as:

- a) when  $x = \pm a$ ;  $W = 0, \partial W / \partial x = 0$ ;
- b) when  $y = \pm b$ ;  $W = 0, \partial W / \partial y = 0$ .

We will accept the approximating functions in the form of a power series:

$$\begin{aligned} \varphi_1 &= (x^2 - a^2) \cdot (y^2 - b^2); \\ \varphi_2 &= (x^2 - a^2)^2 \cdot (y^2 - b^2)^3; \\ \varphi_3 &= (x^2 - a^2)^3 \cdot (y^2 - b^2)^2. \end{aligned} \quad (6)$$



$$\delta = 20,8051a^5b^5(b^4 + 0,5714 \cdot \alpha \cdot a^2b^2 + \beta \cdot a^4), \Delta q = 1,1378a^5b^5 \frac{g}{D_x}. \quad (15)$$

Taking into account the values (8), we obtain from expressions (15), taking into account the load from transport  $g = 52.5 \text{ kN/m}^2$ :

$$\delta = 34557,73; \Delta q = 59,7345 / D_x. \quad (16)$$

Using expression (12), we calculate the value of the coefficient “ $a$ ” taking into account expression (1b):

$$a = \Delta q / \delta = \frac{59,7345}{34557,73 \cdot D_x} = 0,00173 / D_x. \quad (17)$$

Substituting the value (17) into equation (4), taking into account (11), we obtain the desired slab deflection function:

$$W(x, y) = a \cdot \varphi = \frac{0,00173}{D_x} \cdot (x^2 - a^2)^2 (y^2 - b^2)^2. \quad (18)$$

For the plate (Figure 3) ( $D_x = 17,1452 \cdot 10^2 \text{ kNm}$ ,  $a=4\text{m}$ ,  $b=1.75\text{m}$ ) at  $x=y=0$  according to equation (18) we obtain the maximum deflection:

$$W_{\max} = 0,00242\text{m} = 0,242\text{cm} = 2,42\text{mm}. \quad (19)$$

Let's consider the calculation according to option 2. In expressions (13) and (15) we take  $D_x = D_{red}$ ,  $\alpha = \beta = 1$ . Then instead of (18) we get the expression:

$$W = a_1 \cdot \varphi_1 = \frac{2,8711 \cdot (x^2 - a^2)^2 (y^2 - b^2)^2}{D_{red} (b^4 + 0,5714a^2b^2 + a^4)}. \quad (20)$$

In expression (20) the value of the reduced (conditional) cylindrical rigidity  $D_{red}$  remains undefined. To determine it, we use the theory of strength of resistance of materials. According to the hypothesis of specific potential energy of shape change, we have [16]:

$$D_{red} = \sqrt{D_x^2 + D_y^2 + 3 \cdot D_{xy}^2}. \quad (21)$$

Substituting the values of (3) into expressions (21), we obtain

$$D_{red} = 10^2 \sqrt{(17,1452)^2 + (107,93)^2 + 3 \cdot (3,57)^2} = 109 \cdot 10^2 \text{ kNm}. \quad (22)$$

Using the values (22), one can determine the reduced thickness of the roadway deck of the overpass  $t_{red}$  fictitious isotropic steel plate, equivalent in strength to a given structural orthotropic plate (Figure 3) [12]:

$$t_{red} = \sqrt[3]{\frac{12(1 - \mu^2) \cdot D_{red}}{E}} = \sqrt[3]{\frac{12(1 - 0,3^2) \cdot 109 \cdot 10^2}{2 \cdot 10^8}} = 0,0817\text{m}.$$

Comparing the result, we get that ( $t_{red} = 0,0817\text{m} = 8,17\text{mm} = 81,7\text{mm}$ )  $>$  ( $t = 20\text{mm}$ ). The actual adopted thickness of the steel plate of the roadway of the overpass is ( $t = 20\text{mm}$ ).

Substituting the values (22) into expression (20), we obtain the values of the greatest deflection in the center of the plate at  $x=y=0$ ,  $a=4\text{m}$ ,  $b=1.75\text{m}$  (Figure 4):

$$W_{\max} = \frac{2,8711 \cdot a^4 \cdot b^4}{109 \cdot 10^2 (b^4 + 0,5714a^2b^2 + a^4)} = \frac{2,8711 \cdot (4)^4 \cdot (1,75)^4}{109 \cdot 10^2 ((1,75)^4 + 0,5714 \cdot (4)^2 (1,75)^2 + (4)^4)} = 0,002155\text{m}$$

Thus

$$W_{\max} = 0,002155m = 0,2155cm = 2,155mm. \quad (23)$$

## 2. Results

By checking the values (19) and (23) according to condition (1), we obtain the required rigidity of the deflection of the roadway slab of the overpass:

$$\left( \frac{0,242}{800} < \frac{1}{1000} \right) \text{ and } \left( \frac{0,2155}{800} < \frac{1}{1000} \right). \quad (24)$$

Comparing the results of values (19) and (23), we see that they are quite close, which indicates that structurally orthotropic slabs can be calculated using the Bubnov-Galerkin variational method, both by the actual orthotropy parameters (coefficients  $\alpha$ ,  $\beta$  in expression (8)), and by the reduced (conditional) cylindrical rigidity  $D_{red}$  (expression (21)). The difference in the values of deflections  $W_{\max}$  of about 10% is explained by the small number of terms of the approximating functions adopted here, which, however, gives a good result already in the first approximation. With an increase in the number of terms of power series in the approximating functions (6), the percentage of error will decrease and at a certain stage will reach a stable final percentage of divergence.

From expressions (24) it is evident that with the adopted thickness  $t = 20mm$ . The slab decking, supported by a system of calculated stiffening ribs (elements 1-4, Figure 3), ensures the required rigidity of the slab and, accordingly, the safe operational function of the roadway of the overpass.

## 3. Discussion and conclusion

It should also be noted that it is possible to determine the value of the minimum required cylindrical rigidity  $D_x$  from the condition of the standard required rigidity of the slab (1):  $W_{\max}/L=1/1000$ . Hence  $W_{\max}^*=800/1000=0.8$  cm. Then from expression (18) at  $x=y=0$ , we obtain:

$$W_{\max} = 0,00173 \cdot a^4 \cdot b^4 / D_x. \quad (25)$$

Let's equate the values  $W_{\max} = W_{\max}^*$ , and we get the expression:

$$D_x = \frac{0,00173 \cdot a^4 \cdot b^4}{0,008} = 0,21625a^4b^4. \quad (26)$$

For  $a=4m$ ,  $b=1.75m$ , using expression (26) we obtain:

$$D_x = \frac{0,00173 \cdot (4)^4 \cdot (1,75)^4}{0,008} = 5,192 \cdot 10^2 < (D_x^* = 17,1452 \cdot 10^2),$$

where  $D_x^* = 17,1452 \cdot 10^2$  – the value adopted for the plate (Figure 3).

The method proposed in this article, applied for "manual" calculation, can be transferred to calculations using software on personal computers, which will allow performing calculations of various structural-orthotropic slabs with a wide variation of their structural and rigidity parameters with greater accuracy. This will allow selecting the structural parameters of the roadway slab of the mobile overpass to be optimal, rigid and durable. The presented studies on the calculation of the orthotropic slab by the variational method will be included in the calculation methodology of the overpass.

## Funding information

This research has been/was/is funded by the Science Committee of the Ministry of Science and Higher Education of the Republic of Kazakhstan (Grant No. AP23487832).

## References

- [1] Kadyrov A., Sarsembekov B., Ganyukov A., Suyunbaev S., Sinelnikov K. Ultrasonic Unit for Reducing the Toxicity of Diesel Vehicle Exhaust Gases // Communications - Scientific Letters of the University of Zilina, 2022, Vol. 24, no. 3. – R. B189-B198.
- [2] Kadyrov A., Kryuchkov Y., Sinelnikov K., Ganyukov A., Sakhapov R., Kukeshva A. Studying the Process of the Internal Combustion Engine Exhaust Gas Purification by an Electric Pulse // Communications - Scientific Letters of the University of Zilina. – 2022. – Vol. 24, No. 4. – R. B275-B287. DOI: 10.26552/com.C.2022.4.B275-B287
- [3] Kadyrov A., Sarsembekov B., Ganyukov A., Zhunusbekova Z., Alikarimov K. Experimental research of the coagulation process of exhaust gases under the influence of ultrasound // Communications - Scientific Letters of the University of Zilina, Vol. 23, Issue 4, 2021. – P. 288-298

- [4] Kadyrov A.S., Ganyukov A.A., Amanbayev S.Sh., Bogdanova A.A. Development of Mobile Communal Overpasses Applied During Repairing of Urban Communal Networks // *Material and Mechanical Engineering Technology*, No. 3, 2023. – P.11-14. DOI 10.52209/2706-977X\_2023\_3\_1
- [5] Kadyrov A.A., Ganyukov A.A., Balabekova K.G., Zhunusbekova Z.Z., Suleev B.D. Scientific and engineering bases for development of mobile overpasses // *Material and Mechanical Engineering Technology, №2, 2020*. – P. 7–13.
- [6] Kadyrov A., Balabekova K., Ganyukov A., Akhmediyev S. The constructive solution and calculation of elements of the unified module of the mobile bridge overcrossing // *Transport problems*. Vol. 12, Issue 3, 2017. – P. 59-69. ISSN: 1896-0596. DOI: 10.20858/tp.2017.12.3.6
- [7] Ganyukov A., Kadyrov A., Balabekova K., Kurmasheva B., Tests and calculations of structural elements of temporary bridges // *Journal Roads and Bridges*. Vol.17, No.3, 2018. – P. 215-226. DOI: 10.7409/rabdim.018.014
- [8] Kadyrov A., Ganyukov A., Imanov M., Balabekova K. Calculation of constructive elements of mobile overpass // *Current Science Journal*. Vol. 116, Issue 9, 2019. – P.1544-1550. DOI: 10.18520/cs/v116/i9/1544-1550
- [9] Bogdanov G.I. Design of bridges and pipes. - M.: Marshrut, 2009. – 350 p.
- [10] Vladimirsky S.R. Modern methods of bridge design. St. Petersburg: Papyrus, 2008. – 493 p.
- [11] Umansky A.A. Handbook of the designer of industrial, residential and public buildings and structures. Calculation and theory in 2 books. - M.: Stroyizdat, 2015. – 600 p.
- [12] Weinberg D.V. Handbook on strength, stability and vibrations of plates. Kyiv: Budivelnik, 2010. – 488 p.
- [13] Gordeev V.N. Load and impact on buildings and structures; edited by Perelmutter A.V. - M.: ASV Publishing House, 2009. – 528 p.
- [14] Pratushevich Ya.A. Variational methods in structural mechanics. - M.: Gostekhizdat, 1998. – 418 p.
- [15] Varvak P.M., Ryabov A.F. Handbook on the Theory of Elasticity. - Kyiv: Budivelnik, 2012. – 421 p.
- [16] Lyuboshits M.I., Itskovich G.M. Handbook on Strength of Materials. - Minsk, 2002. – 464 p.

#### **Information about the authors**

**Ganyukov Alexander Anatolyevich**, PhD, acting associate professor, Abylkas Saginov Karaganda Technical University  
e-mail: [sgn2002@mail.ru](mailto:sgn2002@mail.ru)

**Sinelnikov Kirill Anatolyevich**, PhD, engineer, Abylkas Saginov Karaganda Technical University  
e-mail: [coolzero7777@gmail.com](mailto:coolzero7777@gmail.com)

**Kabikenov Sapar Zhomartovich**, c. t. s., associate professor, Abylkas Saginov Karaganda Technical University  
e-mail: [sapargk@mail.ru](mailto:sapargk@mail.ru)

**Karsakova Akbope Zholaevna**, PhD, acting associate professor, Abylkas Saginov Karaganda Technical University  
e-mail: [karsakova84@mail.ru](mailto:karsakova84@mail.ru)



## Remaining Useful Life Prediction Method For Different Types Of Rolling Bearings Based On Bi-Lstm Quantification

Kondhalkar Ganesh Eknath\*, Dr. G. Diwakar

Koneru Lakshmaiah Education Foundation (Deemed to be University), Vaddeswaram, India

\*corresponding author

**Abstract.** The remaining Useful Life (RUL) forecast for rolling bearings is still the crucial part of condition-based maintenance (CBM) for mechanical systems. To predict the RUL, the existing research utilized traditional Deep Learning techniques, however, it has trouble quantifying uncertainty. Therefore, this research suggested a novel DL model to improve RUL prediction. Initially, to define the degree of rolling bearing deterioration and comprehend the non-linear qualities, time domain features, frequency domain features, & time-frequency domain features are removed. Then, this study suggested using a Bi-LSTM - RF framework to predict the RUL, this framework has an LSTM layer in a combination of forward and backward motion, a fully connected layer, an RF classifier, & a dropout layer. As a result, our proposed deep learning-based RUL prediction obtains the Accuracy of 0.9845, Precision of 0.93, Recall of 1.0, & F1-score of 0.9656.

**Keywords:** bidirectional long short term memory (Bi-LSTM), deep learning, degradation features extraction, normalization, remaining useful life (RUL) prediction

### Introduction

Due to their significant impact on safety, production, and financial efficiency, equipment stability, and reliability are essential in many industrial domains. Reduced maintenance costs and unneeded downtime are advantages of Prognostic and Health Management (PHM), which is further known as terms like Condition-Based Maintenance (CBM) & predictive maintenance (PdM) [1-2]. In rotating equipment, rolling bearings are a common mechanical component that must frequently sustain a variety of mechanical and thermal pressures. Bearing problems account for more than 40% of motor failures. RUL forecasting, fault locating, and anomaly detection are all components of PHM for rolling bearings [3]. Utilizing historical trajectory data, one may evaluate and project roller bearings' RUL, it is crucial for maintaining mechanical material effectively during its service life. It is suggested to develop structure accessibility, dependability, & less expensive equipment maintenance. The Remaining Service Life (RSL) of the linked equipment before failure is considered to have happened is precisely specified as RUL [4]. Each of the maximum essential elements of spinning machinery, rolling bearings frequently has a straight effect on the security of the mechanical system's overall operation. As a result, production safety may be ensured and significant economic benefits can be realized through actual & precise RUL prediction of rolling bearings [5].

Three general categories may be used to classify RUL prediction approaches: physics model-based techniques, data-driven techniques, & hybrid techniques. To create a physical model, methodologies based on physical models investigate the components' damage mechanisms & the rules of degradation for certain fault modes. This typically calls for a variety of previous information, making it challenging to exactly create a deterioration model in difficult situations [6–9]. Data-driven techniques goal to change the information given by IoT into dependent models, either parametric or non-parametric, which only use sufficient previous data and do not require knowledge of specific deterioration processes [10,11]. They can show the fundamental relationships and causes between RUL and the raw sensor data. Data-driven methods are frequently utilized in industrial applications as a result of the quick development of intelligent technology [12].

The RUL is predicted using machine learning techniques that identify features from raw sensor data using signal processing methods and expert knowledge [13–16]. As a result, deep learning technology offers a potentially effective way to raise RUL prediction accuracy. To extract features from high-dimensional data, deep learning techniques like Recurrent Neural Networks (RNN), Long Short-Term Memories (LSTM), Gated Recurrent Units (GRU) for time series modeling, and convolutional neural networks (CNN) have been extensively used. Even though the deep learning neural network has demonstrated tremendous potential for RUL prediction, there are a few data- and practically-related difficulties that merit more thought. Since physical equipment operates under complicated settings, noise fluctuations and measurement mistakes must be present in the sensor streaming data. Therefore, the RUL prediction and feature extraction are greatly impacted by the changing variations.

The studies mentioned above have confirmed the potential of DL-based approaches for RUL prediction. But, the majority of these techniques use deterministic neural networks as their implementation, which eventually produces RUL point estimation. There are several different kinds of forecast ambiguities, including quantification uncertainty caused by interference from noise, model uncertainty relating to the forecast model, and unreliability environments caused by operation irrationality, which have an impact on RUL prediction in real applications [17]. Many important judgments are founded on the quantification of uncertainty. The anticipated cost of the RUL prediction point struggles to provide adequate direction for the maintenance strategy in real-world situations if the

uncertainty is not quantified. Therefore, this research proposed a bearing RUL prediction approach to address these issues. The following is the primary contribution of this study:

For RUL prediction, this research proposed a BiLSTM – RF framework, which consists of the following steps:

- the first step of this framework is the extraction of degradation features in rolling bearing. Here, we extract 13 frequency domain features to analyze the vibration signal, 12 time-domain features to represent the degree of rolling bearing degeneration, and 5 time-frequency domain features to comprehend its nonlinear characteristics;

- then, the extracted features are get normalized, then we create the sample data by using the sliding time window approach. Then, for prediction, this work employs a Bi-LSTM model, which employs LSTM layers in both forward and backward directions, a fully connected layer, an RF classifier, & a dropout layer.

As a result, when compared to the current methodologies, this suggested RUL prediction offers greater accuracy.

This research project is organized as follows: Segment 2 investigates an artificial intelligence-based method to predict the RUL. Following that, Segment 3 describes a proposed deep learning model to predict the RUL, and Segment 4 contains the simulation findings and comparison analysis of the suggested method. This research study is concluded in Segment 5.

## **1. Literature survey**

Statistical models or Artificial Intelligence are typically used in data-driven ways to predict RUL. The construction of statistical models using empirical knowledge is the basis of statistical model-based approaches. A Wiener process-based real-time prognostic strategy for wind turbine bearing was introduced by Hu et al. [18]. The parameters of a Wiener process model are determined using maximum likelihood estimation. When combined the reverse Gaussian distribution, the RUL of a wind turbine bearing may determine. It is difficult to choose the right parameters for a given scenario because the statistical models' parameters vary depending on the scenario. An adaptive network-based fuzzy inference system (ANFIS)-based prognostic technique was presented by Wu et al. [19]. After the data pre-processing is complete, statistical features from the multi-sensor data are extracted. ANFIS and polynomial curve fitting is then used to fuse data from many sensors and estimate the RUL. For bearing under various operational circumstances, an RUL prediction technique was suggested by Kundu et al. [20]. This method establishes a Weibull accelerated failure time regression (WAFTR) model that acknowledges together operational state variables & monitoring signals. In conclusion, the outcomes demonstrate this strategy takes better forecast presentation. While allowing them to examine enormous amounts of data, the standard AI model's shallow designs restrict their capacity to learn complicated non-linear correlations.

Deep learning is already becoming a powerful technique for pattern detection and data prediction. DL is an addition of ANN that can extract data features from input data by performing deep analysis and mining using several hidden layers & nonlinear transformations [21]. Due to its remarkable representative feature capture capacity, it has established extensive use in the area of roller bearings RUL prediction. Hu et al. [22] utilized the DBN to construct the rolling bearing health index extractor, combining the network because of the diffusion process technique to forecast RUL. Deep convolution neural networks (DCNN), which can use several convolutional and pooling layers to extract hidden features from input data, were employed by Cheng et al. [23] to accomplish RUL prediction of rolling bearing. The RUL estimation issue was seen by the RNN network as a time series regression problem, which makes it a prime choice for DL techniques to analyze time series data and solve. According to CNN & the Bi-LSTM network, Zhao C. et al. [24] built the hybrid two-channel prediction model. Since multivariate degradation equipment stores information about various elements of degradation, degradation laws, life contribution rates, and coupling relationships between the various aspects are all diverse. The aforementioned model will inevitably have limitations when used to anticipate data from a single network. As a normal RNN, Bi-LSTM may successfully overcome the Temporal Convolution network's limitations, However, compared to convolution operation, its short-term memory is slower and less precise. The LSTM model & the AdaBoost regression model were combined to create a hybrid data-driven RUL prediction technique by Zhu et al. [25] depending on data trajectory expansion. The studies mentioned above have confirmed the potential of DL-based approaches for RUL prediction. RUL prediction in practical applications is impacted by a variety of prediction uncertainties, including measurement uncertainty caused by noise interference, model uncertainties relevant to the prediction model, & uncertainty conditions affected by operation haphazardness. The predicted RUL prediction point value struggles to provide adequate guidance for the preservation approach in real-world presentations if the uncertainty is not defined [26]. According to Li et al. [27], to deal with uncertainty in deep learning, Bayesian inference can be utilized as a learning method. A possible way for measuring uncertainty is the Bayesian approach.

Eknath et al. [28] DCNN & Gated Recurrent Units (GRU) are used in a unique prediction approach that uses feature extraction to derive vibration signal properties. Simultaneously, to estimate a rolling bearing's remaining usable lifespan, the Gated recurrent unit (BiGRU) has been used. However, its sluggish convergence rate and learning efficiency lead to an excessively extended training period.

According to the study and description above, it can be said that both traditional deep learning techniques are hindering RUL prediction at the moment and common uncertainty measurement techniques have a hard time

adapting to RUL prediction methods. These challenges must be overcome; this research suggests a bearing RUL prediction technique depends on RNN & unreliability quantification.

## 2. Proposed approach

RUL prediction is a crucial component to increase the dependability & availability of machines. The bearing deterioration rule was mined from operational data in the current study using DL to get the RUL. However, building a suitable DL model for precise RUL prediction is typically challenging due to the complexity of operating data. Also, external uncertainties have a big impact on bearing degradation, to overcome that existing research utilized traditional deep learning techniques, however, it has trouble quantifying uncertainty, and conventional approaches to measuring uncertainty have limited ability to accommodate RUL prediction techniques. In addition, the Bi-GRU model is used in the existing RUL prediction, due to difficulties including a poor convergence rate and low learning efficiency, training times are excessively long [28]. Therefore, this research proposed a novel DL-based RUL prediction which was described in the following section.

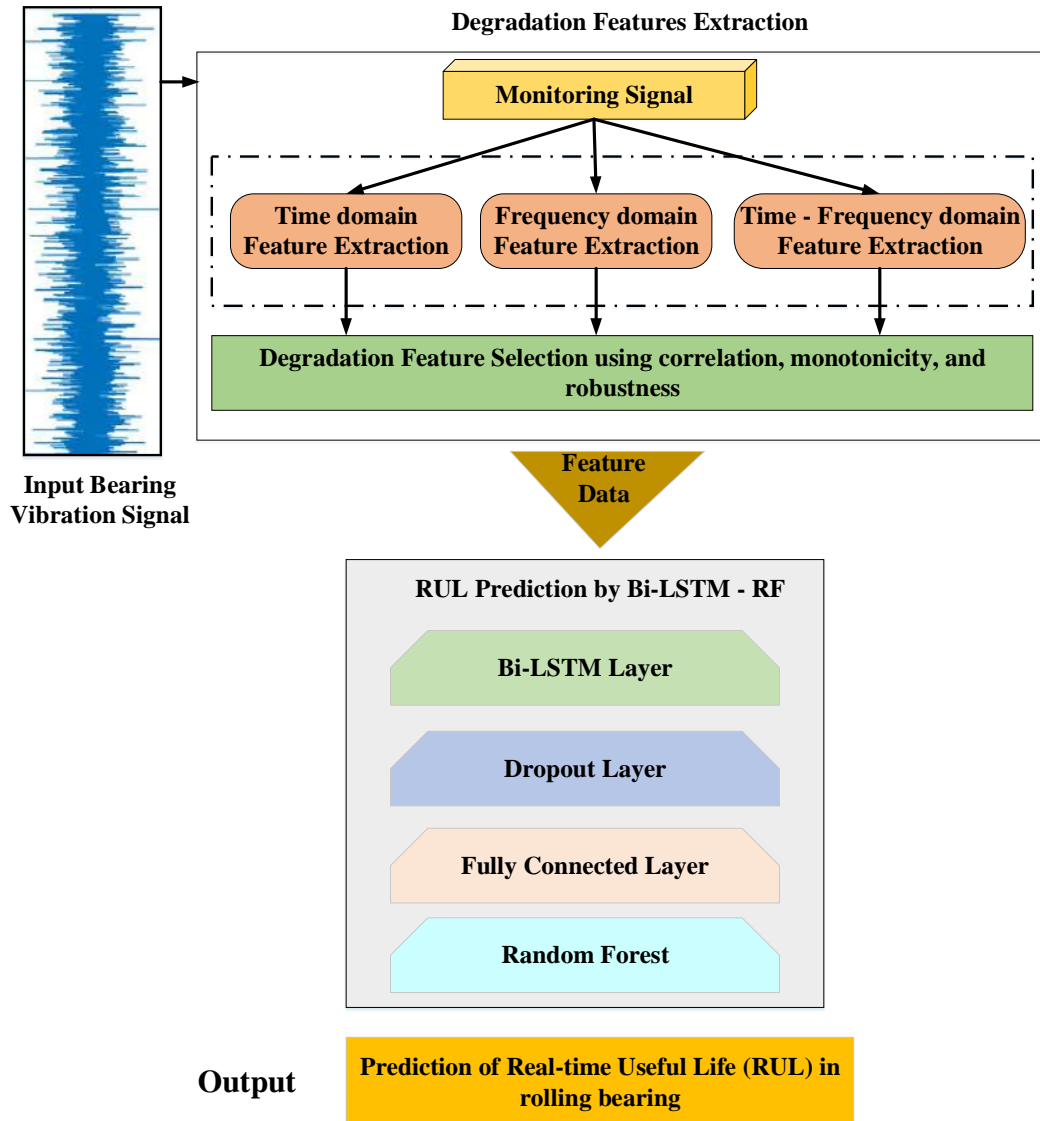


Fig. 1. - Architecture of the proposed RUL prediction approach

### 2.1 Building Feature Set

Since vibration signals may include a wealth of information, they are frequently chosen for rolling bearing deterioration process monitoring. Since the vibration signal cannot automatically portray the bearing's deteriorating method, the degradation characteristics must be removed from the raw vibration data. To replicate the degrading method of rolling bearings from various dimensions, time-domain features, frequency-domain features, & time-frequency domain features were retrieved in this research.

Different techniques may be used to obtain the deterioration characteristics of bearings in different domains. Even though frequency domain characteristics were typically statistical features depending on the Fast Fourier transform, which is useless for explaining how a single frequency changes over time, bearing deterioration is a non-

stationary dynamic method with substantial time correlation. Time-frequency domain features were chosen to take the transitory peculiarities in the bearing deterioration.

In contrast to its role in fault detection, RUL prediction must be compatible with the degradation process, which is impacted by failure types. As a result, some other characteristics that are only appropriate for certain failure modes remain not appropriate for RUL prediction. The characteristics that may accurately depict the deterioration process and have predictability are screened using three feature assessment indices: a correlation indicator, a monotonicity indicator, and a robustness indicator.

2.1.1 Time domain feature extraction

One of the easiest and most efficient techniques for analyzing vibration signals is the time domain deterioration characteristic. The vibration signal was statistically analyzed to determine the time-domain deterioration features. To represent the degree of rolling bearing degradation, 12 time-domain degradation characteristics are removed and displayed.

**Table 1.** Time domain degradation features

S.No	Name	Formula
1	Absolute Mean	$T_1 = \frac{1}{N} \sum_{t=1}^N  x(t) $
2	Root Mean Square	$T_2 = \sqrt{\frac{1}{N} \sum_{t=1}^N x(t)^2}$
3	Peak	$T_3 = \max(x(t))$
4	Square Root Amplitude	$T_4 = \left[ \frac{1}{N} \sum_{t=1}^N \sqrt{ x(t) } \right]^2$
5	Skewness	$T_5 = \frac{1}{N} \sum_{t=1}^N (x(t) - \bar{x})^3$
6	Kurtosis	$T_6 = \frac{1}{N} \sum_{t=1}^N (x(t) - \bar{x})^4$
7	Waveform Indicator	$T_7 = \frac{T_2}{ \bar{x} }$
8	Peak Indicator	$T_8 = \frac{T_3}{T_2}$
9	Impulse Indicator	$T_9 = \frac{T_3}{ \bar{x} }$
10	Margin Factor	$T_{10} = \frac{T_3}{T_4}$
11	Kurtosis Factor	$T_{11} = \frac{T_6}{T_2}$
12	Skew Factor	$T_{12} = \frac{T_5}{T_2}$

Table 1. T1–T12 in the table stand for time domain deterioration characteristics,  $x(t)$ ,  $t=1,2,..N$ . N, where N is the total number of signal data values, stands for the signal data points in vibration signals. This characteristic capture the altering regulations of various bearing health states. For instance, the RMS value primarily imitates the amplitude of the overall energy of the entire bearing monitoring signal, whereas the maximum value depicts the effect force on the bearing at the specific value of failure, the peak factor can be used to define the signal's peak level for bearing monitoring.

2.1.2 Frequency domain feature extraction

It is required to do frequency domain analysis on the vibration signal to acquire the frequency domain deterioration aspect since the error features of rolling bearings were typically concealed in frequency domain information. Here, the monitoring signal is transformed into a frequency spectrum using the fast Fourier transform, & 13 frequency domain characteristics were then retrieved from the monitoring signal's frequency spectrum.

**Table 2.** Frequency domain degradation features

S.No	Formula
1	$F_1 = \frac{\sum_{i=1}^K s(i)}{K}$
2	$F_2 = \frac{\sum_{i=1}^K (s(i) - F_1)^2}{K - 1}$
3	$F_3 = \frac{\sum_{i=1}^K (s(i) - F_1)^3}{K(\sqrt{F_2})^3}$
4	$F_4 = \frac{\sum_{i=1}^K (s(i) - F_1)^4}{K(F_2)^2}$
5	$F_5 = \frac{\sum_{i=1}^K f_i s(i)}{\sum_{i=1}^K s(i)}$
6	$F_6 = \sqrt{\frac{\sum_{i=1}^K f_i^4 s(i)}{\sum_{i=1}^K f_i^2 s(i)}}$
7	$F_7 = \sqrt{\frac{\sum_{i=1}^K f_i^2 s(i)}{\sum_{i=1}^K s(i)}}$
8	$F_8 = \sqrt{\frac{\sum_{i=1}^K (f_i - F_5)^2 s(i)}{K}}$
9	$F_9 = \frac{\sum_{i=1}^K f_i^2 s(i)}{\sqrt{\sum_{i=1}^K s(i) \sum_{i=1}^K f_i^4 s(i)}}$
10	$F_{10} = \frac{F_6}{F_5}$
11	$F_{11} = \frac{\sum_{i=1}^K (f_i - F_5)^3 s(i)}{K F F_6^3}$
12	$F_{12} = \frac{\sum_{i=1}^K (f_i - F_5)^4 s(i)}{K F F_6^4}$
13	$F_{13} = \frac{\sum_{i=1}^K (f_i - F_5)^{\frac{1}{2}} s(i)}{K F F_6}$

These frequency domain properties are listed in Table 2, in which the vibration signal's frequency spectrum is depicted by  $s(i)$ .  $x(t)$ ,  $i = 1, 2, 3, \dots, K$ , the amount of spectral lines is  $K$ , & the frequency of the  $i^{\text{th}}$  spectral line is represented by  $f_i$ . Features  $F_1 - F_5$  characterize alterations in the major frequency band location of the recorded signal in the frequency domain. The aspect domain spectral energy distribution's dispersion level is described by the values of  $F_6 - F_{13}$ .

### 2.1.3 Time - Frequency domain feature extraction

Rolling bearing monitoring signals are often non-linear and non-stationary during real operation. Due to the complex interaction between time, frequency, and amplitude, the Time-Frequency (TF) domain analysis of bearing monitoring signals was used to identify the features of changes in bearing health status. In this work, a three-level wavelet packet decomposition technique called the Haar wavelet was utilized to break down the vibration signal into a collection of wavelet nodes.

Entropy is suggested as a way to gauge both the complexity of the data and the likelihood that a new signal model will emerge. The aim of assessing the sparsity is to provide a purpose, which expresses the sparse distribution of energy. The KL divergence of the multivariate joint probability density & its marginal probability density product was used to characterize the mutual information of several variables. A physical quantity called kurtosis has been presented as a way to assess how much a random variable has a Gaussian distribution.

Where  $TF_1$  is represented as energy entropy, the percentage of each value in the time-frequency energy histogram is called  $p_i$ , the energy entropy can also show the degree of uncertainty in the energy distribution. The time-frequency energy histogram is divided into  $m$  parts according to frequency, &  $TF_2$  is shown as the energy correlation coefficient. Where  $corcoef(\cdot)$  is the cross-correlation function.  $TF_3$  is represented as energy Sparsity, where the sparsity is determined using  $x$ .  $TF_4$  is represented as Energy Mutual Information,  $p(x)$  and  $q(x)$  are two distinguish probability density functions of the random vector  $x$ .  $TF_5$  is represented as Energy Kurtosis, where  $\mu$  means data mean, &  $\sigma$  means standard deviation, and  $x_i$  is the random variable with  $N$  observations ( $i=1, 2, \dots, N$ ).

**Table 3.** Time-Frequency domain degradation features

S.No	Name	Formula
1	Energy Entropy	$TF_1 = - \sum_{i=1}^n p_i \log(p_i)$
2	Energy Correlation Coefficient	$TF_2 = [corcoef(1), corcoef(2), \dots, corcoef(m)]^T$
3	Energy Sparsity	$TF_3 = \frac{\ X\ _p}{n^{1/p-1/2} \cdot \ X\ _2}$
4	Energy Mutual Information	$TF_4 = \int P(x) \log \frac{P(x)}{q(x)} dx$
5	Energy Kurtosis	$TF_5 = \frac{\sum_{i=1}^N (x_i - \mu)^4 / N}{\sigma^4} - 3$

#### 2.1.4 Degradation feature selection

RUL prediction, in contrast to its function in fault detection, must be compatible with the deterioration process, which failure modes affect. As a result, a few different characteristics that are only appropriate for certain failure modes were not appropriate for RUL prediction. Using a correlation indicator and three feature evaluation indices  $Corr(f, t)$ , monotonicity indicator,  $Mon(f)$ , and robustness indicator,  $Rob(f)$ , were employed to identify characteristics that can accurately and predictably reflect the deterioration process [29].

First, when assessing the monotonic growing or reducing the development of the degradation characteristics, the monotonicity is stated as:

$$Mon = \left| \frac{no.of\ dF>0}{L-1} - \frac{no.of\ dF<0}{L-1} \right| \quad (1)$$

$L$  denotes the amount of signal models, & the derivative of the aspect sequence is called  $dF$ .  $Mon$  denotes a quantity between 0 and 1, where 1 means the character is fully monotonous and 0 means it is constant.

The connection between the rolling bearing degradation characteristics and the degradation period is then evaluated using the Pearson correlation coefficient (PCC), which is written as:

$$PCC = \frac{|\sum_{t=1}^T (F_t - \bar{F})(L_t - \bar{L})|}{\sqrt{\sum_{t=1}^T (F_t - \bar{F})^2 \sum_{t=1}^T (L_t - \bar{L})^2}} \quad (2)$$

Where  $F_t$  represents the current value of the deterioration feature  $t$  &  $L_t$  displays the time value associated with the signal sample. The amount of signal samples is  $T$ . The PCC also has a 0–1 range. 1 indicates that the degradation characteristic and the degradation time are perfectly connected:

$$Robustness = Robustness = \frac{1}{T} \sum_{t=1}^T \exp\left(-\left|\frac{F_t}{\bar{F}}\right|\right) \quad (3)$$

To identify deterioration characteristics that can precisely depict the deterioration procedure of rolling bearings, three pointers are linearly integrated to create selection criteria (SC). The SC formula is shown as:

$$SC = \omega_1 Mon + \omega_2 PCC + \omega_3 Robustness \quad (4)$$

Where  $\omega_i$  is the weighting coefficient.

## 2.2 Standardizing Features and Constructing Samples

The comparative size of various aspect measures has a significant impact on training. The characteristics with big magnitudes would be crucial in model training if screened features weren't regular. The characteristics with modest magnitudes, however, have trouble making it easier to update model parameters. As a result, since some crucial properties were not included in the model training process, it is problematic to train the model to its optimum form. Additionally, this would result in frequent gradient direction oscillations in the process of model optimization, which would hinder convergence and lengthen training. As a routine pre-processing step, normalizing the input characteristics into a machine learning model is done most frequently by employing the mean and standard deviation. The Z-score standardization criteria are requested to handle partitioned characteristics. The formulation of the Z-score standardization criterion is:

$$X_{stand} = \frac{X_{orig} - \mu}{\sigma} \quad (5)$$

where  $X_{stand}$  and  $X_{orig}$  are the original signal & the standardized signal, and the original signal's variance & mean, respectively.

In this research, model information that satisfies the input specifications of Bi-LSTM is created using the sliding time window approach in addition to normalizing the aspect signals. The input size and length of the sequence must be specified in the model input for the Bi-LSTM prediction model. After processing in the preceding stages, the sample data constitute a two-dimensional array of size  $N_{sample\_point} \times N_{feature}$ , where  $N_{sample\_point}$  and  $N_{feature}$  is the quantity of features and sampling points, respectively. It is necessary to first identify the sample length that corresponds to the sequence length. The input sample is the distance of the sample,  $N_{length}$ , the information related to the model positions 0- $N_{length}$ , and the sample label is the RUL of the  $N_{length}$ -th sampling point. To get a sequence of input samples, after that, a single unit is added to the sampling time axis to advance the interception window, & the previous action is frequent. Since neighboring samples built using sliding time windows overlap, the training set of data can be perfectly fitted using Bi-LSTM.

### 2.3 RUL prediction based on Bi-LSTM – RF Model

An LSTM layer, a fully connected layer, an RF classifier, & a dropout layer make up the proposed Bi-LSTM-RF-based prediction model in this research. The Bi-LSTM - RF's suggested design is seen in Figure 2.

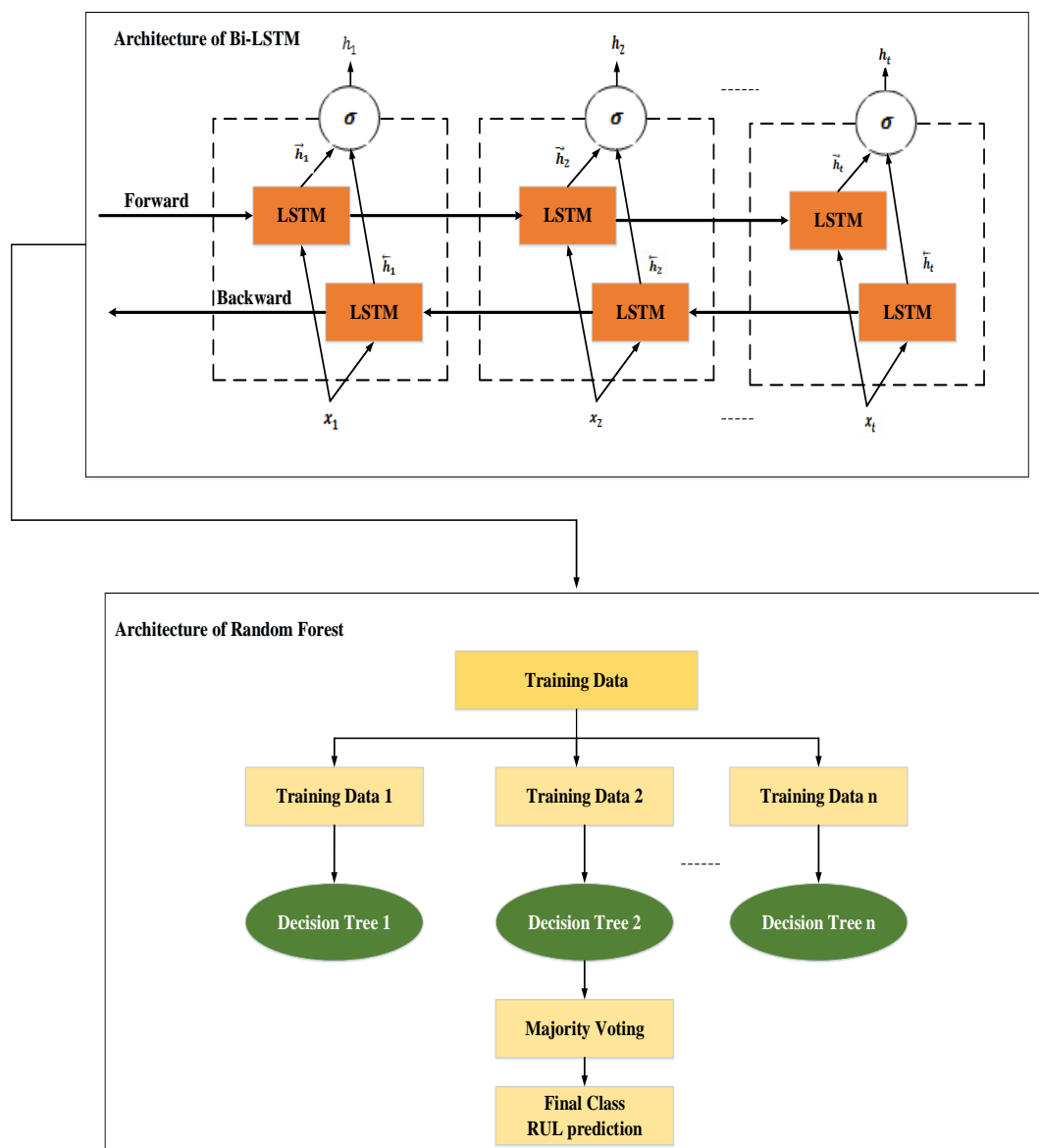


Fig. 2. - Architecture of the Bi-LSTM – RF

A Bi-LSTM is a bidirectional variation of the LSTM that can analyze lengthy data sequences by learning in each direction, including forward and backward. To efficiently learn the long-term data sequences in both forward and backward orientations, Bi-LSTM uses two distinct hidden layers. To access long-range information, it is desirable to

record two-direction contextual relationships. It is made up of two LSTMs, the first of which feeds the learning process in an onward manner, and the second of which is utilized to learn from the inputs in a backward (reverse) way.

Here,  $\vec{h}$  and  $\overleftarrow{h}$  are utilized to signify the onward and reverse hidden layers' respective outputs separately. The training method for both LSTM units makes use of the ordered input data sequences. The forward  $\vec{h}_t$  and  $\overleftarrow{h}_t$  LSTM layers' output is estimated using a recursive technique. The merge property, which includes the following potential merging approaches: average, sum, multiplied, and concat, is used to combine the output of both LSTM layers.

The design we've suggested calls for an average mode to combine results from onward and reverse LSTM units. In conclusion, the combined output is obtained using a flattened layer  $f_{layer}$  which is then converted into a one-dimensional vector  $v$  and passed to the softmax function to get the desired result.

Equation 6 shows how the layer of Bi-LSTM concatenates the output sequences of both LSTM units using the merge mode approach to produce a two-dimensional output vector,  $Y$ , which is used to build bi-directional sequences.

$$y_t = \alpha (\vec{h}_t, \overleftarrow{h}_t) \tag{6}$$

Where  $\alpha$  denotes the merge mode approach applied to the  $\vec{h}_t$  and  $\overleftarrow{h}_t$  output sequences, respectively. To combine the output sequences of both the onward and reverse LSTM units, the symbol  $\alpha$  denotes an average mode method. The multiplication function, summation function, averaging function, or concatenating function can be used as the merge mode technique. The final result of the two LSTM units is shown as a one-dimensional vector,  $Y = [y_1, y_2, \dots, y_t]$ , where the last component,  $y_t$ , is the best-predicted value for the following time iteration.

A tanh function serves as the activation function after the LSTM layer, followed by two linked layers on top of each other. The dropout layer was employed in the testing step to measure the prediction uncertainty and avoid over-fitting. LSTM between two layers, and two completely connected layers in this investigation, a dropout layer is placed.

Then, the RFC was utilized for the final RUL prediction. The ensemble learning idea, which is useful for prediction issues, is the foundation of RF. The ensemble learning idea, which is useful for prediction issues, is the foundation of RF. As the name suggests, RF is a classifier that improves classification accuracy by using multiple decision trees on different dataset subsets. Instead of relying just on one decision tree, the random forest together forecasts from all decision trees & predicts the eventual decision made based on the majority of estimates. As the number of trees rises, so does the precision and danger of over-fitting. As the number of trees rises, so does the precision and danger of over-fitting. Finally, to reduce the cost function, the Adam optimizer is utilized, & associated learning rate is set to 0.001.

**Table 4.** Results of the proposed method with different epochs

Epoch	Learning rate	Dropout	MSE`	MAE
10	0.001	0.2	2.3850	1.3009
20	0.001	0.2	2.3850	1.3009
30	0.001	0.2	2.12	1.2950
40	0.001	0.2	1.28	1.10
50	0.001	0.2	1.170	0.95

Additionally, for the suggested prediction model, the RUL point estimates & kernel distributions are obtained by calculating the uncertainty using nonparametric kernel density estimation and dropout. The dropout procedure resembles parallel network training with a predetermined network topology. As a consequence, when the same data are repeatedly input into a Bi-LSTM-based prediction model with operational dropout, approximately alternative forecast outcomes may be obtained, indicating the quantification of uncertainty. The mean value may be thought of as the RUL's point estimation. These prediction findings may be processed using the nonparametric kernel density estimation to get the kernel density distributions of the RUL at various model locations, which could have been utilized to provide judgments with a strong basis in uncertainty.

### 3. Result and discussion

This segment discusses the performance of our suggested explanation as well as the implementation results. Also mentioned are the comparison outcomes from the baseline method.

Tool: PYTHON 3

OS: Windows 7 (64-bit)

Processor: Intel Premium

RAM : 8GB RAM



### 3.1 Dataset Description

The IMS Bearing dataset, which was produced by the NSF I/UCR Centre for Intelligent Maintenance System (IMS), was used in this study.

#### 3.1.1 Experimental Setup

A shaft has four bearings placed on it. An AC motor connected to the shaft by rub belts controlled the revolution speed to remain constant at 2000 RPM. A spring mechanism provides a radial force of 6000 lbs on the shaft & bearing. All bearings were greased by force. As seen in Figure 3, Rexnord ZA-2115 double-row bearings were mounted on the shaft. PCB 353B33 The bearing housing was equipped with High Sensitivity Quartz ICP accelerometers (two accelerometers for all bearing (x- & y-axes) for data set 1, and one accelerometer for every bearing for data sets 2 & 3). Figure 1 illustrations display the positioning of the sensors. All failures happened next to the bearing had completed more than its intended lifetime above 100 million revolutions.

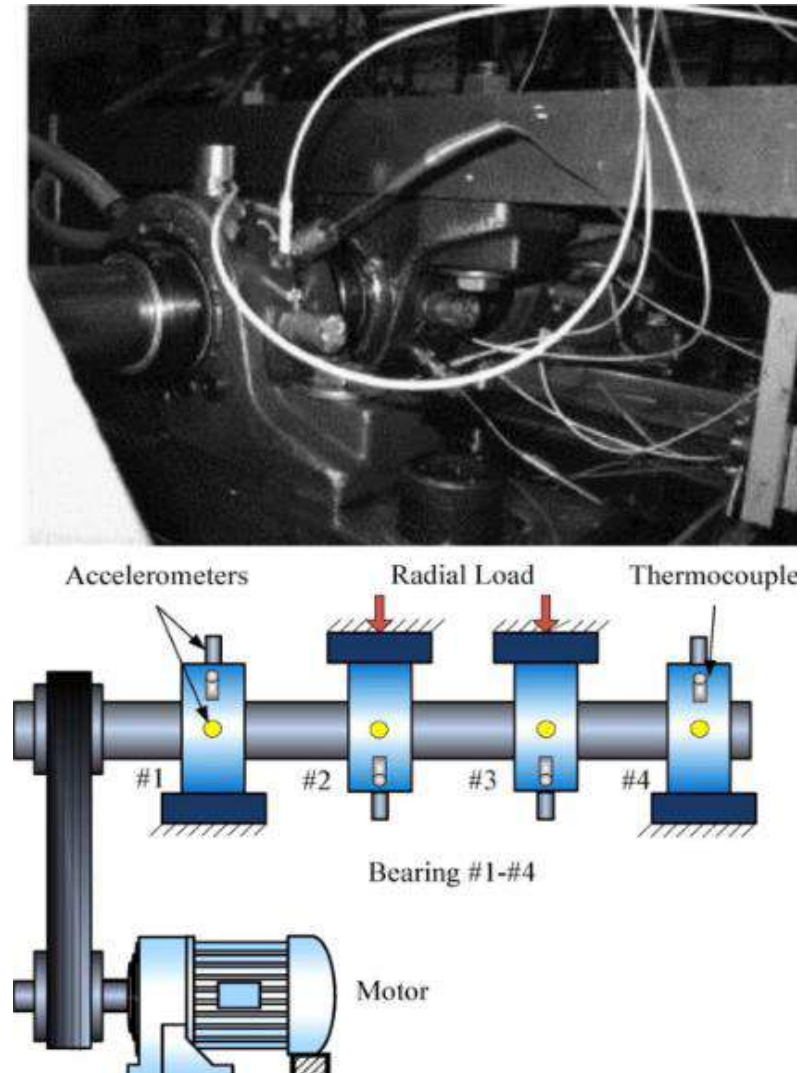


Fig. 3. Experimental Setup

#### 3.1.2 Structure of IMS data

The data packet contains three (3) data sets. A test-to-failure experiment is described in each piece of data. Every data set was composed of separate files that are snapshots of a 1-second vibration signal taken at predetermined intervals. All file has a sampling rate of 20 kHz & a total point count of 20,480. The document name displays the date of data gathering. A record (row) in a file that contains information is known as a data point. NI DAQ Card 6062E enabled data collecting. The research was restarted the following working day, as shown by longer time stamp intervals (seen in file names).

Table 5. Dataset Details

Parameters	Set No.1	Set No.2	Set No.3
Recording Duration	October 22, 2003 12:06:24 to November 25, 2003 23:39:56	February 12, 2004 10:32:39 to February 19, 2004 06:22:39	March 4, 2004 09:27:46 to April 4, 2004 19:01:5
No. of files	2,156	984	4448
No. of channels	8	4	4
Channel Arrangement	Bearing 1 – Ch 1&2; Bearing 2 – Ch 3&4; Bearing 3 – Ch 5&6; Bearing 4 – Ch 7&8.	Bearing 1 – Ch 1; Bearing 2 – Ch 2; Bearing 3 – Ch 3; Bearing 4 – Ch 4;	Bearing 1 – Ch 1; Bearing 2 – Ch 2; Bearing 3 – Ch 3; Bearing 4 – Ch 4;
File Recording Interval	Except for the first 43 files, which were captured every 5 minutes, every 10 minutes.	Every 10 minutes	Every 10 minutes
File Format	ASCII	ASCII	ASCII
Description	An inner race flaw and a roller element defect both appeared in bearings 3 and 4 after the test-to-failure experiment.	After the test-to-fail experiment, bearing 1 experienced outer race failure.	After the test-to-fail experiment, bearing 3 experienced outer race failure.

3.1.3 Training and Testing Loss of Dataset

The training loss & testing loss of dataset 1 is 0.0278, and 0.0275 at epoch 34, dataset 2 is 0.0038 and 0.0037 at epoch 42, and dataset 3 is 0.0255 and 0.0252 at epoch 41 by using our proposed Bi-LSTM – RF which is presented in figure 4 (a), (b) and (c). As a result, dataset 2 has less training and testing loss when compared to the existing dataset.

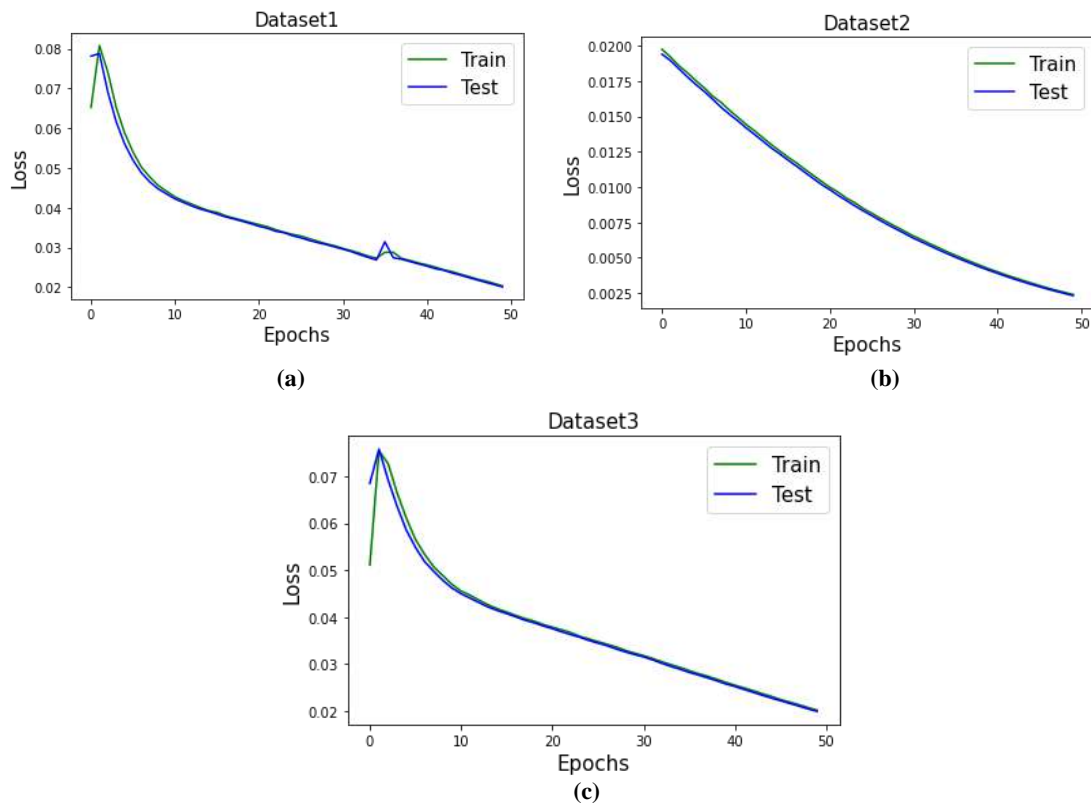


Fig. 4. Train and Test Loss of the dataset

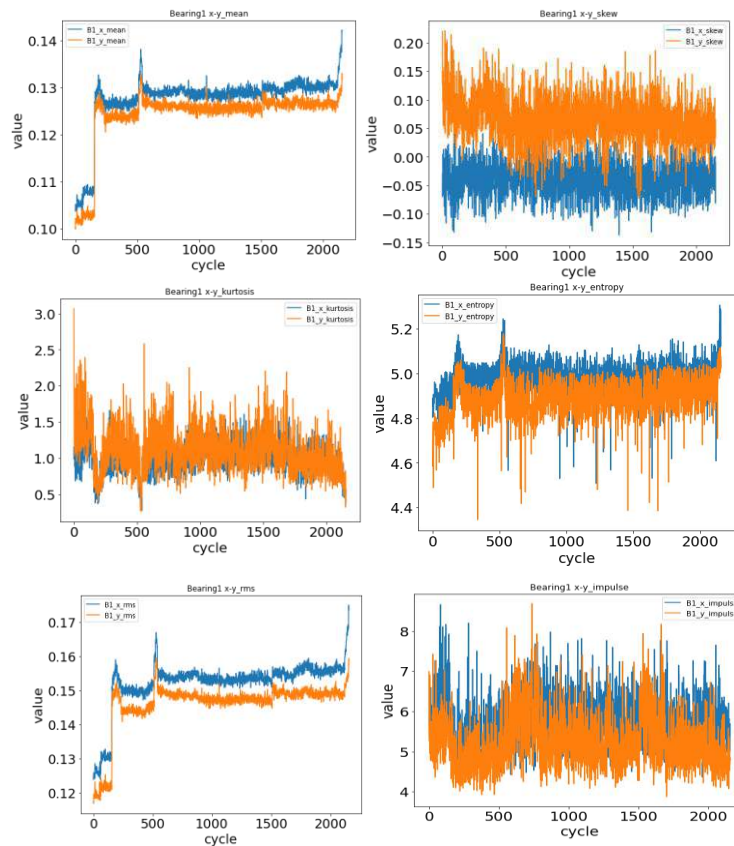
### 3.2 Parameter Settings

**Table 6.** Parameter Settings of the proposed approach

Algorithm	Parameters	Value
	Learning rate	0.001
	Batch Size	64
	Dropout	0.2
	Testing Size	0.25
	Training Size	0.75
Bi-LSTM	Input Size	64×25×9
	LSTM	(9,9)
	Dropout	0.2
	LSTM	(9,9)
	Dense	(9× 25 × 100), linear
	Dropout	0.2
	Dense	(100,1)
	Output	(64,1)
	Optimizer	Adam
RF	Random state	1
	Max_depth	2
	Max_features	30

### 3.3 Experimental Results

#### 3.3.1 Results of degradation features



**Fig. 5.** Results of degradation features

This research presented some of the degradation features which are depicted in Figure 5. To define the degree of rolling bearing degeneration and comprehend its nonlinear characteristics, these features are retrieved. The chosen degradation features can adequately capture the deterioration of rolling bearings. Hence, the identified features are accurate and predictable depicting the deterioration process.

3.3.2 RUL Prediction Results

Table 7. RUL prediction results

S.No	Bearing No	Cycle	Prediction	Is valid	(Normal / Suspected)
(a)	Bearing 1	2206	1950	False	Suspected
(c)	Bearing 2	2156	1800	False	Suspected
(b)	Bearing 3	2231	2281	False	Imminent failure
(d)	Bearing 4	2256	2256	False	Suspected

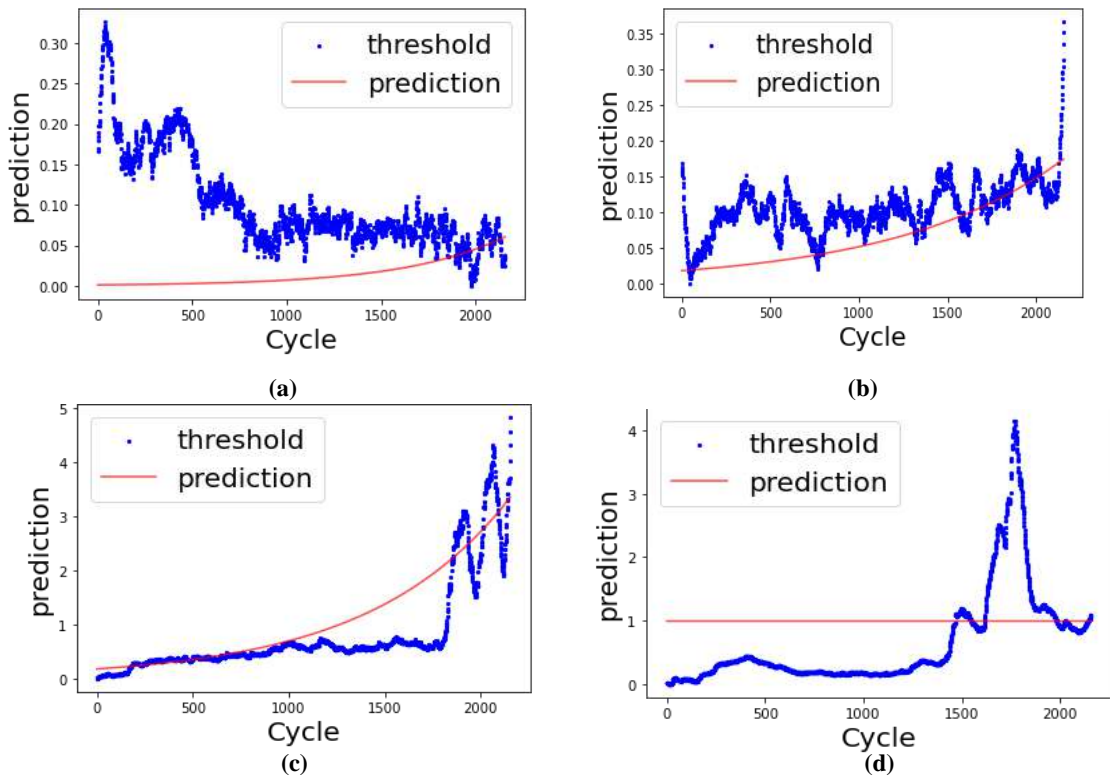


Fig. 6. Results of RUL Prediction

The RUL prediction consequences are exposed in Figure 6. To predict the RUL this research utilized a Bi-LSTM model, which employs LSTM layers in both forward and backward directions, a dropout layer, an RF classifier, & a fully connected layer. The Adam Optimizer is utilized to modify the Bi-LSTM network's parameters. Additionally, dropout & nonparametric kernel density estimation is combined for the proposed prediction model to quantify the uncertainty, results in the kernel distributions, and RUL point predictions.

3.4 Performance Parameters

Stated figure 7 is a performance measurement for the proposed Bi-LSTM - RF. The following equations are used to obtain the f1-score, which is very helpful for assessing accuracy, recall, precision, and other metrics.

$$\text{Accuracy} = \frac{\text{True Positive} + \text{True Negative}}{\text{True Positive} + \text{True Negative} + \text{False Positive} + \text{False Negative}} \tag{7}$$

$$\text{Precision} = \frac{\text{True Positive}}{\text{True Positive} + \text{False Positive}} \tag{8}$$

$$\text{Recall} = \frac{\text{True Positive}}{\text{True Positive} + \text{False Negative}} \tag{9}$$

$$F1\ Score = \frac{2*Precision*Recall}{Precision+Recall} \tag{10}$$

Several metrics, including Accuracy, F1 score, precision, & recall have been used to evaluate the effectiveness of our suggested method's performance in forecasting RUL.

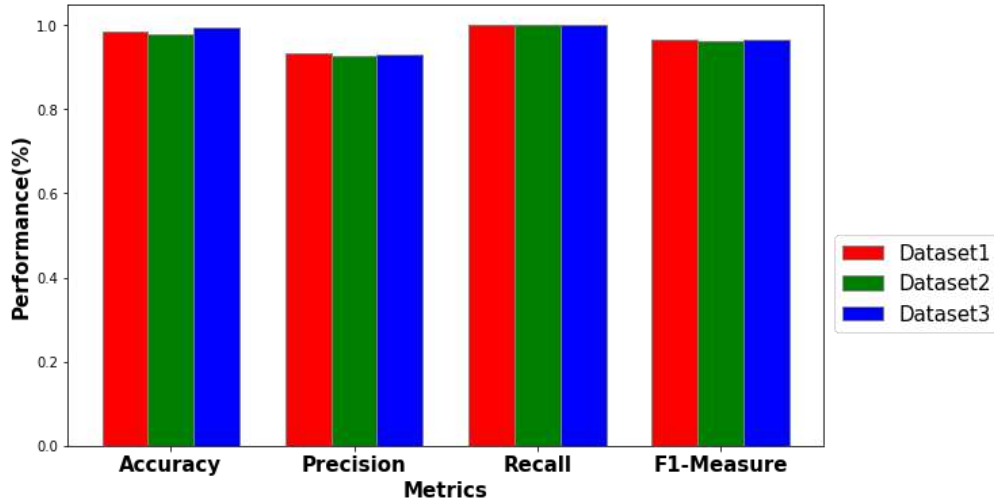


Fig. 7. - Performance metrics of the proposed approach

The suggested method's presentation evaluation measures are shown in Figure 7. Accuracy, Precision, Recall, and F1-score were measured and found to be respectively 0.9845, 0.93, 1.0, and 0.9656 (dataset 1). The obtained values (dataset 2) of Accuracy, Precision, Recall, and F1-score are 0.9786, 0.912, 1.0, and 0.952. The obtained values (dataset 3) of accuracy, precision, recall, and f1-score are 0.9953, 0.93, 1.0, and 0.965. By utilizing a unique Bi-LSTM - RF methodology for RUL prediction in rolling bearings, our suggested method performs better in terms of Accuracy, F1 score, Precision, & Recall.

The following formula is used to assess index model parameters like MAE and RMSE:

$$MAE = \frac{\sum_{i_z=1}^{m_z} |y_{zi_z, f_z} - \overline{y_{zf_z}}|}{m_z} \tag{11}$$

where  $y_{zi_z, f_z}$  = prediction,  $\overline{y_{zf_z}}$  = true value,  $m_z$  = there are a total of N data points.

$$RMSE = \sqrt{\frac{\sum_{i_z=1}^{m_z} (x_{zi_z, f_z} - \overline{x_{zf_z}})^2}{m_z}} \tag{12}$$

where  $x_{zi_z, f_z}$  = actual observation time series,  $m_z$  = number of non-missing data points,  $\overline{x_{zf_z}}$  = estimated time series,  $i_z$  = variable  $i_z$

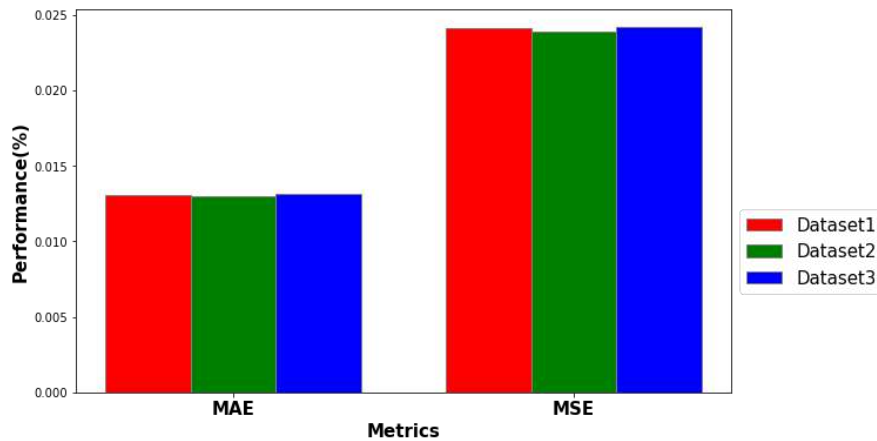


Fig. 8. Error analysis of the proposed approach

Figure 8 illustrates the comparison using sample assessment indices such as MAE. The suggested method reduces the error by incorporating Bidirectional LSTM with RFC. For dataset 1, the MAE and RMSE errors are 0.012 and 0.0243, for dataset 2, 0.011 and 0.0239, and dataset 3, 0.013 and 0.0245.

### 3.5 Comparison analysis

This segment compares the current methodologies, putting the suggested method up to standard methods like LSTM with random features [29], Convolutional Neural Network [29], Adaptive Kalman Filter (AKF) [29], LSTM with uncertainty quantification [29], and DCNN-Bi-GRU [28].

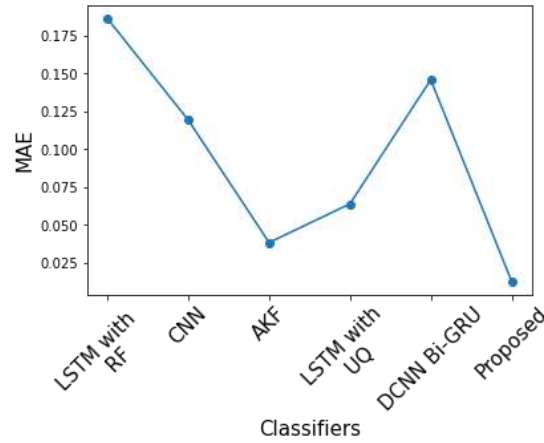


Fig. 9. Comparison analysis of MAE

Figure 9 illustrates the MAE of the suggested approach. By combining Bi-LSTM with a Random Forest classifier, a suggested method lowers the error. Our suggested method related to the baseline LSTM with random features, Convolutional Neural Network, AKF, LSTM, and DCNN-Bi-GRU with uncertainty quantification such as 0.1864, 0.1613, 0.0640, 0.0567, and 0.146. The MAE of the proposed approach is 0.013. As a consequence, our suggested strategy makes improved than the current methods.

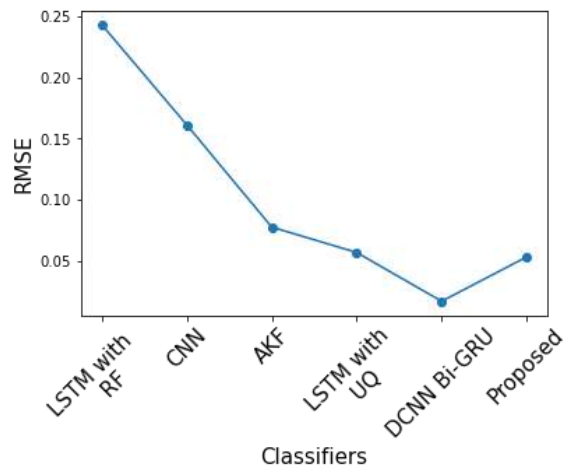


Fig. 10. - Comparison analysis of RMSE

Figure 10 illustrates the RMSE of the suggested approach. By combining Bi-LSTM with a Random Forest classifier, the suggested method lowers the error. Our suggested method related to the baseline LSTM with random features, Convolutional Neural Network, AKF, LSTM with uncertainty quantification, and DCNN-Bi-GRU such as 0.2463, 0.1613, 0.0775, 0.0567, and 0.167. The RMSE of the proposed approach is 0.053. As a result, our suggested strategy performs better than the current methods.

### Conclusion

This research suggested a unique dL model develop the RUL prediction model's accuracy. To predict the RUL, Bi-LSTM – RF and uncertainty quantification is proposed. Initially, to define the level of rolling bearing degradation, in this study, 12 time-domain features, 13 frequency-domain features, & 5 time-frequency domain features were retrieved. Moreover, to identify features that may accurately depict the deterioration process, three

feature assessment indices correlation, monotonicity, and robustness are used. The proposed Bi-LSTM - RF model is then fed the normalized input characteristics to most accurately forecast the RUL. As a result, this proposed approach obtained a greater accuracy, precision, recall, & f1-score of 0.9845, 0.93, 1.0, & 0.9656. Moreover, this research obtained a lesser error such as MAE of 0.013, and RMSE of 0.053 when compared to the existing approaches. In the future, this research may concentrate on a hybrid deep learning-based framework to predict the RUL with the highest accuracy.

## References

- [1] de Pater, I., Reijns, A., & Mitici, M. Alarm-based predictive maintenance scheduling for aircraft engines with imperfect Remaining Useful Life prognostics. *Reliability Engineering & System Safety*, 221, 2022, 108341.
- [2] Kondhalkar, G. E., & Diwakar, G. Crest factor measurement by experimental vibration analysis for preventive maintenance of bearing. In *ICRRM 2019–System Reliability, Quality Control, Safety, Maintenance, and Management: Applications to Civil, Mechanical and Chemical Engineering*, 2020, 133-138
- [3] Kondhalka, G., & Diwakar, E. Effect of various defects in roller bearings and ball bearings on vibration. *Int. J. Innov. Technol. Explor. Eng*, 8(12), 2019, 5137-5141.
- [4] Zhang, P., Gao, Z., Cao, L., Dong, F., Zou, Y., Wang, K. & Sun, P. Marine systems and equipment prognostics and health management: a systematic review from health condition monitoring to maintenance strategy // *Machines*, 10(2), 2022, 72.
- [5] Cao, Y., Ding, Y., Jia, M., & Tian, R. A novel temporal convolutional network with residual self-attention mechanism for remaining useful life prediction of rolling bearings // *Reliability Engineering & System Safety*, 2021, 215, 107813.
- [6] Cao, Y., Jia, M., Ding, P., & Ding, Y. Transfer learning for remaining useful life prediction of multi-conditions bearings based on bidirectional-GRU network // *Measurement*, 178, 2021, 109287.
- [7] Chen C, Liu Y, Wang S, Sun X, Di Cairano-Gilfedder C, Titmus S, et al. Predictive maintenance using Cox proportional hazard deep learning // *Adv Eng Informatics*, Volume 44, April 2020, 101054
- [8] Aremu O.O., Hyland-Wood D, McAree PR. A Relative Entropy Weibull-SAX framework for health indices construction and health stage division in degradation modeling of multivariate time series asset data // *Adv Eng Informatics* 2019.
- [9] Caravaca CF, Flamant Q, Anglada M, Gremillard L, Chevalier J. Impact of sandblasting on the mechanical properties and aging resistance of alumina and zirconia-based ceramics // *J Eur Ceram Soc*, 2017, 38(3)
- [10] Ding P, Jia M, Yan X. Stationary subspaces-vector autoregressive with exogenous terms methodology for degradation trend estimation of rolling and slewing bearings // *Mech Syst Signal Process*, 202, 150.
- [11] Ding P, Jia M, Wang H. A dynamic structure-adaptive symbolic approach for slewing bearings' life prediction under variable working conditions // *Struct Heal Monit* 2020, Volume 20, Issue 1
- [12] Meissner, R., Rahn, A., Wicke, K. Developing prescriptive maintenance strategies in the aviation industry based on a discrete-event simulation framework for post-prognostics decision-making. *Reliability Engineering & System Safety*, 214, 2021, 107812.
- [13] C. Ordoñez, F. S. Lasheras, J. Roca-Pardinas, F. J. de Cos Juez, A hybrid arima–svm model for the study of the remaining useful life of aircraft engines // *Journal of Computational and Applied Mathematics* 346, 2019, 184–191.
- [14] Z. Chen, Y. Li, T. Xia, E. Pan, Hidden Markov model with auto-correlated observations for remaining useful life prediction and optimal maintenance policy // *Reliability Engineering & System Safety* 184, 2019, 123–136.
- [15] Yang, B., Liu, R., & Zio, E. Remaining useful life prediction based on a double-convolutional neural network architecture // *IEEE Transactions on Industrial Electronics*, 66(12), 2019, 9521-9530.
- [16] Z. Liu, Y. Cheng, P. Wang, Y. Yu, Y. Long, A method for remaining useful life prediction of crystal oscillators using the Bayesian approach and extreme learning machine under uncertainty // *Neurocomputing* 305, 2018, 27–38.
- [17] Liu, Z.; Cheng, Y.; Wang, P.; Yu, Y.; Long, Y. A Method for Remaining Useful Life Prediction of Crystal Oscillators Using the Bayesian Approach and Extreme Learning Machine under Uncertainty. *Neurocomputing* 2018, 305, 27–38.
- [18] Hu Y., Li H., Shi P., Chai Z., Wang K., Xie X., Chen Z. A prediction method for the real-time remaining useful life of wind turbine bearings based on the Wiener process // *Renew Energ* 127, 2018, 452–460.
- [19] Wu J., Su Y., Cheng Y., Shao X., Deng C., Liu C. Multi-sensor information fusion for remaining useful life prediction of machining tools by adaptive network-based fuzzy inference system // *Appl Soft Comput* 68, 2018, 12–23.
- [20] Kundu P, Darpe AK, Kulkarni MS Weibull accelerated failure time regression model for remaining useful life prediction of bearing working under multiple operating conditions // *Mech Syst Signal Process*, 2019, 134:106302.
- [21] Cheng Y, Hu K, Wu J, Zhu H, Shao X. Auto-encoder quasi-recurrent neural networks for remaining useful life prediction of engineering systems // *IEEE/ASME Trans Mechatron*,
- [22] Hu C., Pei H., Si X., Du D., Pang Z., Wang X.A. prognostic model based on DBN and diffusion process for degrading bearing. *IEEE Trans Ind Electron* 67(10), 2020, 8767–8777.
- [23] Cheng H., Kong X., Chen G., Wang Q., Wang R. Transferable convolutional neural network based remaining useful life prediction of bearing under multiple failure behaviors // *Measurement*, 168, 2020, 108286.

- [24] Zhao, C., Huang X., Li, Y., Yousaf Iqbal M. A. double-channel hybrid deep neural network based on CNN and Bi-LSTM for remaining useful life prediction //Sensors 2020, 20, 7109.
- [25] Zhu X., Zhang P., Xie M. A Joint Long Short-Term Memory and AdaBoost Regression Approach with Application to Remaining Useful Life Estimation //Measurement 2020, 170, 108707.
- [26] Biggio, L., Wieland, A., Chao M.A., Kastanis, I., Fink O. Uncertainty-aware Remaining Useful Life predictor. arXiv 2021, arXiv:2104.03613.
- [27] Li G., Yang L., Lee C.G., Wang X., Rong M. A Bayesian Deep Learning RUL Framework Integrating Epistemic and Aleatoric Uncertainties //IEEE Trans. Ind. Electron. 2020, 68, 8829–8841
- [28] Eknath K. G., Diwakar G. Prediction of Remaining useful life of Rolling Bearing using Hybrid DCNN-BiGRU Model //Journal of Vibration Engineering & Technologies, 2022, 1-14.
- [29] Yang J., Peng Y., Xie J., Wang P. Remaining Useful Life Prediction Method for Bearings Based on LSTM with Uncertainty Quantification //Sensors, 22(12), 2022, 4549.

#### **Information of the authors**

**Kondhalkar Ganesh Eknath**, PhD, professor, Koneru Lakshmaiah Education Foundation (Deemed to be University)

e-mail: [kondalkarganeshknath@gmail.com](mailto:kondalkarganeshknath@gmail.com)

**Garikapati Diwakar**, PhD, professor, Koneru Lakshmaiah Education Foundation (Deemed to be University)



## Comparative Analysis of Fits of Parts with Guaranteed Interference on Shafts of Annular and Solid Sections

Mustafin A., Sadykov N.\*, Kabylkaiyr D., Shaimardan A., Sadykova A.

Toraighyrov University, Pavlodar, Kazakhstan

\*corresponding author

**Abstract.** The main feature of the proposed work is a comparative analysis of the use of a gear landing with guaranteed tension on hollow and solid-section shafts. In order to reduce the stress concentration and increase the malleability of the joint, it is also proposed to reduce the thickness of the hub. The conclusions of the research in the form of calculated data confirm the effectiveness of the proposed measures. As a result of these structural changes, the cross-section of the joint becomes smaller: for the structure under study compared to the basic assembly, i. e. with a wheel with a conventional hub and a solid-section shaft, 1.7 times. Consequently, the metal consumption of the unit decreases, the loads on the shaft supports and the drive decrease, and the energy efficiency of the device increases.

**Key words:** shafts, sections, pressing, guaranteed tension, wheel hub.

### Introduction

The work examines the features of fitting a gear with guaranteed interference on the shaft. The advantage of an interference fit when installing a wheel on a shaft is the manufacturability and economy of the process of manufacturing and assembling parts. The design, in comparison with keyed or splined types of connections, does not contain additional elements in the form of shaft steps that fix the wheel on the shaft, grooves and splines on the shaft that weaken the section. To reduce metal consumption and increase energy efficiency, the technology of mounting a wheel on a shaft with a ring cross-section rather than a solid one is being explored. Strengthening the section under the wheel is achieved by using an interference connection, when the hollow shaft and the wheel hub are one part with diameters  $d_2/d_1$ . Due to the interference, initial stresses arise in the connection [1], the nature of which is shown in Figure 1.

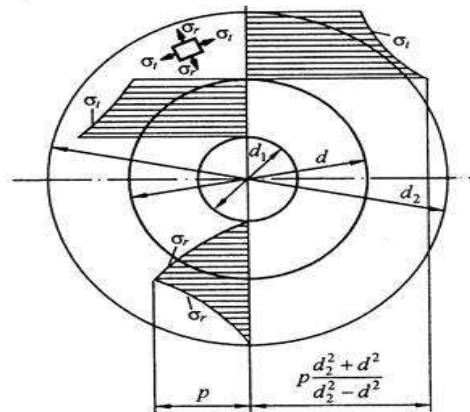


Fig. 1. - Character of changes in radial and circumferential stresses in connection with interference

### 1. Research methodology

As a rule, the highest stresses occur at the inner surface of the female part, the highest equivalent stress

$$\sigma_e = \sigma_z - \sigma_{z1} = \frac{2 \cdot p}{1 - (d/d_2)^2} \leq [\sigma]_T \quad (1)$$

The greatest stresses of the covered part also occur on the inner surface and are compressive

$$\sigma_{z1} = \frac{2 \cdot p}{1 - (d/d_2)^2} \leq [\sigma]_T \quad (2)$$

The optimal value of the radius of the contact surface can be determined from the condition of the greatest reduction in the equivalent voltage at the dangerous point [2]. In accordance with this, the optimal diameter of the contact surface is:

$$d = 2 \cdot \sqrt{d_1 \cdot d_2} \quad (3)$$

Using the specified dependence, the diameter of the hole  $d_1$  is determined. According to the recommendations of the technical literature [3], the outer diameter of the hub and its length

$$d = (1.5 \div 1.55) \cdot d, l_{hub} = (1 \div 1.2) \cdot d \quad (4)$$

The size of the outer circumference of the surface of a thick-walled pipe, the diameter of which  $d = 60$  mm, is taken as the optimal diameter. The diameter of the outer circle of the hub is  $d_2 = 1.55 \cdot 60 = 93$  mm, then according to the formula for the optimal diameter of the contact surface, the diameter of the inner surface of the pipe is found

$$d_1 = d^2/d_2 = 60^2/93 = 38,7 \text{ mm} \quad (5)$$

A thick-walled pipe with a diameter ratio of 38/60 and a wall thickness of 11 mm is used as a blank for the manufacture of the shaft. For a narrow hub, the pressure distribution over the contact surface is more uniform, so the hub length is assumed to be  $l_{hub} = d$  [1].

In order to increase the compliance of the connection with interference and reduce the stress concentration, the thickness of the hub is reduced to 10 mm, and the diameter ratio is taken  $d/d_2 = 60/80 = 0.75$ . The strength of the connection is checked using the following input data:

Shaft power  $P_2=6$  kW; rotation speed  $n=120$  min<sup>-1</sup>; pitch wheel diameter  $D_2=350$  mm; tooth angle  $\beta=12$ mm; module  $m=3$  mm; shaft material is steel 45 with limits of endurance and strength for workpieces up to 80mm  $\sigma_{temp}=900$  MPa,  $\sigma_{-1}=410$  MPa.

Torque

$$T = P_2/\omega = 9,55P_2/n = 9,55 \cdot 6 \cdot 10^3/120 = 477,5 \text{ N}\cdot\text{m} \quad (6)$$

Based on the results of the calculation of the loads acting on the shaft, diagrams of bending moments are constructed and the equivalent moment is determined (taking into account the moment from the axial force) in the section in the middle of the wheel hub:

$$M_e = 533.08 \text{ N}\cdot\text{m} \quad (7)$$

Bending stress from equivalent load

$$\sigma_e = M_e/W_x \quad (8)$$

where  $W_x$  is the axial moment of resistance, determined by the extreme section of the hub, i. e. along the cross section of the shaft.

The bending moment  $M_e$  in this section, due to the small width of the wheel, is taken to be the same as the moment in the middle section. Allowable bending stresses for shafts experiencing alternating stresses are determined by the endurance limit. The use of an interference fit is taken into account by the corresponding values of the stress concentration coefficients [4].

$$[\sigma]_{-1} = \sigma_{-1} \cdot k_F \cdot k_d / k_\sigma \quad (9)$$

where the ratio of the stress concentration coefficient to the scale factor during interference fit at  $\sigma_{temp} = 900$  MPa and  $d=60$  mm  $\cdot k_\sigma / k_d = 4.5$ ; surface roughness coefficient  $k_F = 0,8 \div 0,91$ ;  $[\sigma]_{-1} = 410.90/4.5=82$  MPa.

Bending stress from equivalent load

$$\sigma_e = M_e/W_x \quad (10)$$

Allowable torsional stresses from empirical dependence

$$[\tau]_{-1} = [\sigma]_{-1}/\sqrt{3} \quad (11)$$

Torsional stress:

$$\tau = T/W_p \quad (12)$$

The strength is checked according to the safety factor, which must exceed the permissible  $[n]=2\div 3$ . Calculations for shaft bending are currently automated and can be performed on-line [5].

After checking the strength of the connection, the calculation of the press connection and selection of fits is carried out using a well-known method [3].

With simultaneous action on the connection of torque  $M_k$  and axial force  $A$ , the calculation is carried out using the resultant axial and circumferential force:

$$T = \sqrt{\left(\frac{2 \cdot M_k}{d}\right)^2 + A^2}; \quad (13)$$

According to the contact pressure formula:

$$p \geq T \cdot k / \pi \cdot f \cdot l \cdot d, \quad (14)$$

where  $k$  - safety factor, to prevent corrosion, is taken for connection at the outlet with the coupling  $k = 3$ ;  $f$  - adhesion coefficient, for a steel pair material  $f = 0.14$ .

The section of the shaft under the bushing takes up the pressure from the bending moment, the pressure is redistributed - on one side of the bushing it is added to the tension pressure, on the other it is subtracted. The pressure difference must ensure that the joint of the parts being connected cannot be opened. The pressure diagram  $p_1$  from the moment of bending changes according to a linear law, the highest pressure in the connection

$$p_1 = 4 \cdot M_x / 2 \cdot W_y \cdot \pi, \quad (15)$$

where  $4/\pi$  - factor, taking into account the crescent shape of the pressure change;

$W_y = b^2 \cdot (d - d_1) / 6$  – moment of resistance to bending of the diametrical section of the bushing;

$b$  - width of the shaft section for the hub.

The diagram of pressure  $p_1$  from the moment of bending, changing according to a linear law, on one side of the bushing has a negative value and helps to reduce the total pressure [6]. On the landing surface it can drop to  $0.25 \cdot p$  (i. e.  $p_1 \approx 0.25 \cdot p$ ) and the interference in the pipe connection will not be guaranteed. Based on this condition, it is necessary to check that the tension pressure is not less than  $p = p_1 / 0.25$ .

## 2. Results and discussion

The results of calculation and testing of the section strength in the connection of a gear with a hollow and solid shaft, performed according to formulas (8), (9), (10), (11), are presented in Table 1.

Table 1. Results of strength calculations for shaft sections

Parameters	Ring $d_1/d = 38/60$	Circular disk $d = 60$
$[\sigma]_{-1}, MPa$	82	82
$W_x, mm^3$	17790	21600
$\sigma_e, MPa$	29,96	25,72
$n_\sigma$	2,73	3,19
$[\tau]_{-1}, MPa$	47,4	47,4
$W_p, mm^3$	35580	43200
$\tau, MPa$	13,42	11
$n_\tau$	3,5	4,31

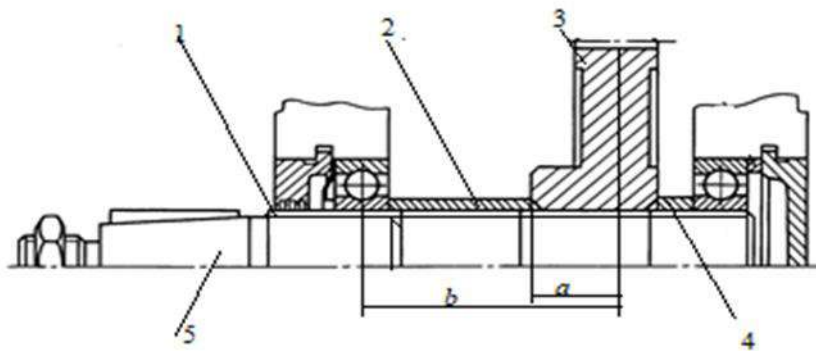
As follows from the analysis, the maximum values of normal and tangential stresses are several times higher than the permissible stresses determined by the endurance limit. When calculating the strength of the shaft, the dangerous sections were taken to be those located at the ends of the wheel hub, i.e., along the sections of the shafts. It should be noted that for the sections under consideration, the safety factors are greater than the permissible standards, which are accepted within the range  $[n] = 2\div 3$  and confirm a sufficient safety margin for shafts of two types of sections.

Next, using the well-known method for calculating interference joints [3], calculations are carried out for both shafts, the results of which are presented in Table 2.

**Table 2.** Results of calculating connections with interference of a gear wheel with a hollow and solid shaft

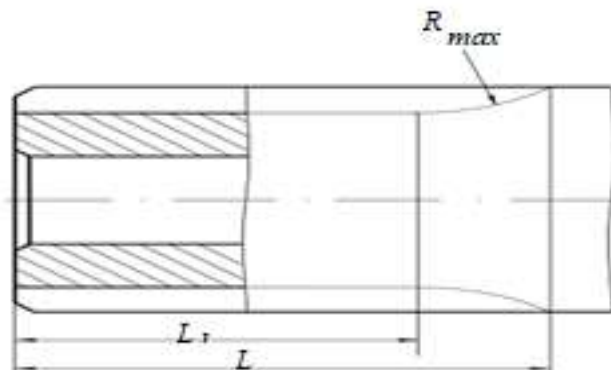
Parameters	Ring $d_1/d = 38/60$	Circular disk $d = 60$
$p, MPa$	28,17	28,17
$p_1/0.25, MPa$	11,10	2,39
$\delta, \mu m$	46,14	22,73
$p_{max1}, MPa$	121,6	320
$[p_{max2}, MPa$	143	186,8
$N_{min}, \mu m$	63,4	35,73
$N_{max}, \mu m$	232,7	163,79
interference	H7/u7	H8/u6
$t, ^\circ C$	183	199
[t]	230	230

The contact pressure  $p$  is determined and a check is made to ensure that the joint in the connection cannot be opened from a bending moment  $p_1 \approx 0.25 \cdot p$ . Next, the values of interference  $\delta$  are determined, taking into account the height of micro-irregularities, the minimum  $N_{min}$  and maximum interference  $N_{max}$  are calculated, according to which the fits are selected wheels on the shaft. Fits H7/u7 and H8/u6 are considered heavy press fits, providing guaranteed tension of connections with variable and dynamic loads. They also apply to recommended plantings, since the technology for their provision is available and well known. Next, based on the maximum tension  $N_{max}$ , from the condition of the strength of the covered part, excluding the occurrence of plastic deformation, the heating temperature of the part  $t \text{ } ^\circ C$  is determined. For both options for pressing wheels onto the shaft, it turned out to be lower than the permissible value recommended for steel parts. As shown in Figure 2, spacer bushings 2 and 4 are installed on shaft 1 and wheel 4 is pressed in, the hub of which can serve as a bushing that increases the cross-section of the shaft.



**Fig. 2.** - Gear pressed onto an annular shaft

To transmit rotation from the output end of the shaft 5 to the actuators, keyed or splined connections of the parts are used. If the wall thickness is sufficient, spline grooves can be cut at the output end of the tubular shaft (Fig. 3).



**Fig. 3.** - Output end of a hollow shaft.

The length of the working section of the output end of the shaft is determined from the crushing strength condition

$$L \geq 2 \cdot M \cdot \frac{k}{d_{avg}} \cdot z \cdot h \cdot \psi \cdot [\sigma]_{cr}, \quad (16)$$

where  $[\sigma]_{cr}$  – permissible crumbling stresses on the working surfaces of the teeth, MPa;

$M$  – transmitted torque, N·mm;  $z$  – number of teeth in the connection;

$h$  – height and length of the working surface of one shaft tooth, mm;

$\psi$  – load distribution unevenness coefficient;

$d_{avg}$  – average connection diameter, mm;

$k$  – safety factor

$$L \geq 2 \cdot 533.08 \cdot 10^3 \cdot 2 / (282) \cdot 28 \cdot 2 \cdot 0.7 \cdot 120 = 8 \text{ mm}$$

## Conclusions

Thus, the main feature of the proposed work is a comparative analysis of the installation of a gear with guaranteed interference on hollow shafts and a solid section. The diameter ratio of the recommended shaft section is 38/60, the wall thickness is 11 mm, these dimensions are typical for thick-walled pipes that are used in production and have sufficient strength. In order to reduce the stress concentration and increase the compliance of the connection, it is proposed to reduce the thickness of the hub, as recommended by a number of authoritative sources [7], [8]. The basic connection is taken to be the fit of the wheel hub on the shaft with a hub thickness of 16.5 mm. In the proposed design, it is reduced to 10 mm and the ratio of the diameters of the outer circumferences of the hub and shaft becomes equal to 80/60. The results of the study in the form of calculated data confirm the effectiveness of the proposed measures. As a result, the cross-section of the connection becomes smaller: for the investigated hollow shaft design with a reduced hub compared to the basic installation, i. e. for a wheel with a conventional hub on a solid shaft, 1.7 times. Consequently, the metal consumption of the unit is reduced, the load on the shaft supports and drive is reduced, and the energy efficiency of the device is increased.

## References

- [1] Birger I. A., Shorr B. F., Iosilevich G. V. Raschety na prochnost detaley. Spravochnik [Calculations for the strength of parts. Handbook]. Moscow, Mashinostroenie, 1993. - 702 p.
- [2] V. F. Pershin, Yu. T. Selivanov Raschet na prochnost tonkostennyih obolochek vrascheniya i tolstostennyih tsilindrov [Calculation of the strength of thin-walled shells of revolution and thick-walled cylinders]. Tambov, GTU, 2002. - 20 p.
- [3] Dunaev P.F., Lelikov O.P. Konstruirovaniye uzlov i detaley mashin Design of machine components and parts. - M.:Academiya, 2008. - 496 p.
- [4] V.I. Anurev Spravochnik konstruktora-mashinostroytelya [Handbook of mechanical engineering designer]. Mashinostroenie, 2001. - 897 p.
- [5] Raschet balok iz trub, kruglogo, kvadratnogo, shestigrannogo i pryamougolnogo prokata na izgib i progib — kalkulyator onlayn (Calculation of beams made of pipes, round, square, hexagonal and rectangular rolled products for bending and deflection - online calculator) Available at: <https://trubanet.ru>
- [6] Ivanov A.S., Ermolaev M.M. Interference operation during transmission bending moment connection //Vestnik mashinostroeniya Machinery Engineering Bulletin, 2009, 5, pp. 45-48.
- [7] Kutz M. (Ed.) Mechanical Engineers' Handbook. 3rd Edition. Four Volume Set. - John Wiley & Sons, Inc., 2005. - 4200 p.
- [8] Childs Peter R.N. Mechanical Design Engineering Handbook. Amsterdam: Elsevier, 2014. - 817 p.

**Mustafin Adilbek**, c.t.s., professor, Toraighyrov University

e-mail: [mustafin-51@mail.ru](mailto:mustafin-51@mail.ru)

**Sadykov Nursultan**, master of science, senior lecturer, Toraighyrov University

e-mail: [sadykov.n@teachers.tou.edu.kz](mailto:sadykov.n@teachers.tou.edu.kz)

**Kabylkaiyr Dauren**, master of science, senior lecturer, Toraighyrov University

e-mail: [kabylkair.d@teachers.tou.edu.kz](mailto:kabylkair.d@teachers.tou.edu.kz)

**Shaimardan Aruan**, master of science, lecturer (assistant), Toraighyrov University

e-mail: [aruan.shaimardan97@mail.ru](mailto:aruan.shaimardan97@mail.ru)

**Sadykova Aigerim**, master of science, lecturer (assistant), Toraighyrov University

e-mail: [aygerim.sadykova.86@bk.ru](mailto:aygerim.sadykova.86@bk.ru)